The Numerical Modelling of Steep Waves Interacting with Structures

Michael Stuart Turnbull

Jesus College

Trinity Term, 1999

A thesis submitted in partial fulfilment of the requirements

for the degree of Doctor of Philosophy at the University of Oxford

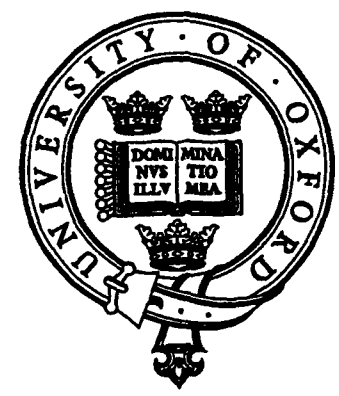

University of Oxford

Department of Engineering Science

Parks Road, Oxford. OX1 3PJ

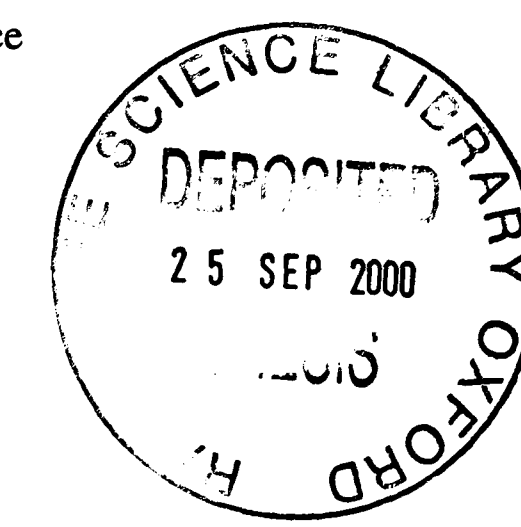

The Numerical Modelling of Steep Waves Interacting With Structures

Michael Stuart Turnbull
Jesus College
Trinity Term 1999

A thesis submitted in partial fulfilment of the requirements for the degree of Doctor of Philosophy at the University of Oxford

ABSTRACT

The interaction of steep waves with structures is a complex problem which is still not fully understood, and is of great importance for the design of offshore structures. A particular problem of interest is the phenomenon of ringing which is highly nonlinear.

In this thesis a number of inviscid free surface flow problems are simulated using a finite element model. The free surface boundary condition is fully nonlinear, meaning nonlinear effects up to very high order can be simulated, depending on mesh resolution. The model uses a fully automatic unstructured mesh generator; this allows the mesh to change its shape and structure as the free surface deforms.

Two unstructured mesh generators have been developed, one based on the advancing front method, the other on the Voronoi technique. Variations of each method are examined. Both methods give good quality meshes. The advancing front technique is found to be faster, but the Voronoi method is more robust and reliable.

In addition to the standard finite element method, a sigma transformed version of the finite element formulation has been developed as an alternative. Both techniques have been used for the numerical simulations. The sigma transformation involves stretching of the mesh between the bed and free surface, and so has the advantage that remeshing is avoided. The standard finite element method is straightforward to apply to problems involving submerged arbitrary shaped bodies.

Simulations have been performed of a number of test cases, such as a standing wave of large amplitude, a base excited tank and steep travelling waves. Convergence tests were carried out and results found to be in close agreement with analytical and alternative numerical solutions of Wu and Eatock Taylor (1994), Wu *et al.* (1998) and Chern *et al.* (1999).

The force on a submerged horizontal cylinder due a travelling wave has been calculated. First and second order components have been obtained by Fourier analysis. The results have been compared with the theoretical predictions of Ogilvie (1963), Vada (1987) and Wu and Eatock Taylor (1990) and the experimental results of Chaplin (1984).

ACKNOWLEDGEMENTS

I would like to thank my supervisors, Dr Alistair G.L. Borthwick and Prof. Rodney Eatock Taylor for their advice, guidance and encouragement over the course of my study. I would also like to express my gratitude to Dr D. M. Greaves, Dr Q. Ma and Dr G.X. Wu of University College London for their helpful suggestions. Thanks are particularly due to Dr G.X. Wu for the use of his finite element code.

I had helpful discussions with my colleagues at the Ocean Engineering and Dynamics group, such as Koo-Yong Park, Ming-Jyh Chern, Abhi Sarkar, Sergio Cruz and Cedric Yiu.

The support of the Engineering and Physical Sciences Research Council, who provided funding for my studies, is gratefully acknowledged.

CONTENTS

		Page
Chapter 1	**INTRODUCTION**	**1**
Chapter 2	**LITERATURE REVIEW**	**9**
2.1	Introduction	9
2.2	Mesh Generation	9
2.3	Wave Loading on Cylinders	15
	2.3.1 Vertical Cylinders	15
	2.3.2 Horizontal Cylinders	18
2.4	Numerical Modelling of Waves	17
Chapter 3	**UNSTRUCTURED MESH GENERATION**	**24**
3.1	Introduction	24
3.2	Advancing Front	25
	3.2.1 Method One	26
	3.2.2 Method Two	27
	3.2.3 Special Cases	28
	3.2.4 Domain Control	29
3.3	Voronoi Method	29
3.4	Smoothing	31
3.5	Performance	32
3.6	Efficiency and Speed Comparison	37
3.7	Conclusions	38

Chapter 4 STANDARD FINITE ELEMENT FORMULATION 61

4.1 Introduction 61

4.2 Governing Equations 62

4.3 Finite Element Discretisation 64

4.3.1 Velocity Potential Calculation 64

4.3.2 Velocity Calculation 68

4.3.3 Updating the free surface 72

4.3.4 Smoothing 74

4.4 Accuracy Tests 75

4.5 Final Remarks 77

Chapter 5 SIGMA TRANSFORMED FINITE ELEMENT FORMULATION 80

5.1 Introduction 80

5.2 Mathematical Formulation 80

5.2.1 Velocity Potential Calculation 80

5.2.2 Velocity Calculation 86

5.3 Final Remarks 88

Chapter 6 RESULTS OF TEST CASES WITHOUT A CYLINDER 90

6.1 Introduction 90

6.2 Standing Wave 91

6.3 Sloshing Wave Motion in a Base-excited tank 98

6.4 Travelling Wave without Cylinder 100

6.5 Focused Wave 108

6.5 Conclusions 109

Chapter 7 **RESULTS : THE FORCE ON A HORIZONTAL SUBMERGED CYLINDER DUE TO A TRAVELLING WAVE** **151**

7.1 Travelling Wave with Cylinder 151

7.2 Conclusions 158

Chapter 8 **CONCLUSIONS AND RECOMMENDATIONS** **181**

8.1 Introduction 181

8.2 Mesh Generation 181

8.3 Finite Element Simulations 182

8.4 Recommendations for Future Work 184

REFERENCES **186**

CHAPTER 1

INTRODUCTION

The purpose of the work presented in this thesis is to develop a reliable and accurate numerical technique for predicting the forces imposed on structures by steep water waves. Knowledge of wave-induced forces is essential for the proper design of offshore structures under operating and extreme wave conditions.

A two dimensional finite element potential flow solver has been developed which uses unstructured meshes. The resulting numerical wave tank is capable of modelling small or large amplitude waves and regular or random waves; it can simulate focused waves and solitary waves. Complicated obstacle geometries can be inserted into the numerical wave tank, including multiple cylinders of arbitrary shape. The bottom of the tank can be horizontal or sloped or indeed can comprise any combination of surfaces at any angle. For future work, the method may be readily extended to three dimensions, thus permitting simulation of multi-directional spread seas and the calculation of wave-induced forces on arbitrarily inclined cylinders, in particular surface piercing vertical cylinders. Of course, a three dimensional model would require greater computational resources.

Steep free surface waves are non-linear, and so cannot be solved easily by analytical methods. Normally solutions are restricted to special cases, for example small amplitude waves. It is extremely difficult, if not impossible, to obtain analytical solutions for more complicated problems, such as wave motions over a sloping bed, large amplitude waves, or wave-induced forces on multiple cylinders of large diameter. In such situations, it is

necessary to turn to physical (experimental) or numerical modelling. This thesis chooses the latter course of action, whereby complex two-dimensional wave-structure interaction problems are simulated using the finite element method.

A particularly important consequence of steep waves interacting with structures, which is still not fully understood, is the phenomenon of ringing. It is an example of a problem where high order effects due to the steepness of the waves are important, and which in the future could be simulated using a three dimensional extension of the method used here. By examining ringing, it can be seen that non-linear effects can be highly significant; numerical time domain analysis of the kind used in this thesis will be useful in obtaining accurate simulations and hence a greater understanding of the non-linear wave-structure interaction.

Ringing is the transient high frequency oscillation of a structure and is particularly relevant for floating structures containing large diameter thin-walled cylinders, such as tension leg platforms (TLPs). Tension leg platforms consist of a floating platform attached to the sea bed by tethers which are under high tension due to the platform buoyancy being larger than the platform weight; the high tension thus restricts the vertical oscillation of the platform. TLPs are used in deep water, where having a structure built on the sea bed, such as a jacket or gravity platform would not be feasible.

The period of oscillation of ringing is at the resonant period of the structure which tends to lie between 2 and 5 seconds, which is substantially smaller than the dominant wave period which typically is 3 to 5 times the resonant periods. Ringing excites the vertical modes of vibration of the platform, which can be considered as a mass on elastic springs (the

tethers). Figure 1.1, reproduced from Faltinsen *et al.* (1995), illustrates a characteristic ringing event observed in scale-model experiments of a tension leg platform with four columns. The upper curve is the time history of the free surface elevation of the incident wave, measured at a point alongside the structure; it can be seen that the wave elevation is relatively small to begin with, and then increases rapidly to a much larger value. The lower curve is the measured tension in the tether; a rapid increase in tension is observed, followed by a decaying resonant high frequency oscillation.

Observations on instrumented platforms and in model experiments suggest that ringing occurs when the waves are steep and the wave height is comparable to cross-sectional dimensions of the structure. There is no evidence that significant viscous effects or flow separation occur during ringing, or that wave breaking or slamming impacts are involved.

Problems in incompressible fluid dynamics are governed by the Navier Stokes equations, which are essentially an expression of the conservation of mass and momentum for a small element of fluid. The forces acting on the fluid are taken to be gravity, acting at the centre of the fluid element, a pressure force, acting normal to each face of the fluid element, and a shear force proportional to the viscosity of the fluid. A great simplification is made by neglecting viscosity and surface tension and assuming irrotational flow. The result is potential theory, where the entire flow at a given time can be fully described by the velocity potential and the location of the fluid boundary. Phenomena such as boundary layers, flow separation, viscous drag and turbulence cannot be described by potential theory. For an offshore structure, viscous effects are important when the ratio between the wave height and a characteristic cross-sectional dimension of the structure is large; the value of the ratio

depends on the structure, but typically it is between three and six. For large diameter structures, potential flow theory will suffice. For example, many TLPs have cylindrical surface piercing columns with a diameter of between 10 and 20 metres; the most probable largest wave height in 100 years can be more than 30 metres in hostile areas like the North Sea, but generally will be much smaller. It therefore would be appropriate to use potential theory to simulate problems involving TLPs.

Potential flow of a liquid with a free surface is a non-linear problem, i.e. the sum of two different solutions for the free surface elevation (for example) does not result in a third solution. The non-linearity is due to the non-linear dynamic and kinematic free surface boundary conditions (see equations 4.3 and 4.4). The dynamic boundary condition is obtained by applying Bernoulli's equation at the free surface; the non-linear term in the equation is proportional to the square of the magnitude of the velocity. For small variations in the free surface relative to the mean water level, the problem can be linearised by neglecting the non-linear terms, which are extremely small relative to the other terms in this case, and applying the free surface boundary conditions at the mean water level. This approach is clearly not suitable for steep waves.

To account for the finite amplitude of the waves, second order corrections can be made to the linear potential. This second order term is proportional to the square of the linear wave amplitude and has twice the frequency and half the wavelength of the linear term. Stokes (1847) used this approach for water waves, and the resulting mathematical approximation is referred to as a second order Stokes wave. Fenton (1985) has derived a fifth order Stokes approximation for regular waves. More recently, the technique of separating the

potential into first, second and sometimes higher order components has been used for the calculation of higher order force components on structures, particularly cylinders; for example the third order forces on a vertical cylinder were calculated by Malenica and Molin (1995).

When second and higher order terms are taken into account, the analysis becomes increasingly complex and unmanageable, and assumptions still need to be made about the relative sizes of the wave height, wave length and structure. For example, Faltinsen *et al.* (1995) assume the cylinder radius is small relative to the wavelength, but of comparable size to the wave amplitude, whereas Malenica and Molin (1995) assume that the cylinder radius is comparable to the wavelength, but much larger than the wave amplitude.

An alternative approach to the above, adopted in this work, is to solve the fully non-linear problem in the time domain using a numerical technique. Here, a two dimensional model has been developed, based on the finite element code used by Wu and Eatock Taylor (1994). This model is used to calculate the forces exerted by steep waves on horizontal cylinders, located beneath the free surface of the water. The results are compared to those produced by others, particularly Ogilvie (1963), Wu and Eatock Taylor (1990) and Chaplin (1984). The accuracy of the model is assessed and recommendations are made for future three dimensional work.

The finite element method has been used, rather than the more usual boundary element method, as comparisons made by Wu and Eatock Taylor (1995) showed that the solution time was shorter in spite of the larger number of nodes, due to the entire domain being discretised, rather than just the boundary. This is due to the finite element method requiring the solution

of a system of equations with a banded matrix, rather than a full matrix in the case of the boundary element method.

Having chosen the finite element method, a means of discretising the domain into a suitable boundary-fitted mesh is required. A simple regular, structured mesh will suffice for those cases where a wave is travelling in a domain without a structure. In the presence of a structure, a more sophisticated method of mesh generation is required, due to the domain constantly changing shape as the free surface distorts above the structure. Two mesh generating strategies have been used here, the advancing front method, and the Voronoi technique. A comprehensive overview of mesh generation techniques is given by George (1990).

An alternative to changing the mesh as the free surface changes is to map the physical domain on to a fixed computational domain. Curvilinear coordinate systems achieve this aim, as does the sigma transformation. A version of the finite element using the sigma transformation has been developed and its performance is compared with the standard version.

This thesis is structured in the following way. Chapter two contains a literature review which surveys mesh generation and hydrodynamic force theories. The third chapter deals with mesh generation techniques, including detailed descriptions of the advancing front and Voronoi methods and examples of the meshes produced by them. A potential flow numerical wave tank based on the standard finite element method is described in chapter four; the formulation is given, and its efficiency is examined. Chapter five describes a version of the finite element model which used a sigma domain transformation. In the sixth chapter, results

obtained using both versions of the finite element method are presented and compared. Three test cases are examined; the standing wave, a sloshing wave in a tank and the progressive wave without a cylinder. Results for forces on a submerged horizontal cylinder due to a progressive wave are given in chapter seven. The eighth chapter gives the conclusions and recommendations for future work.

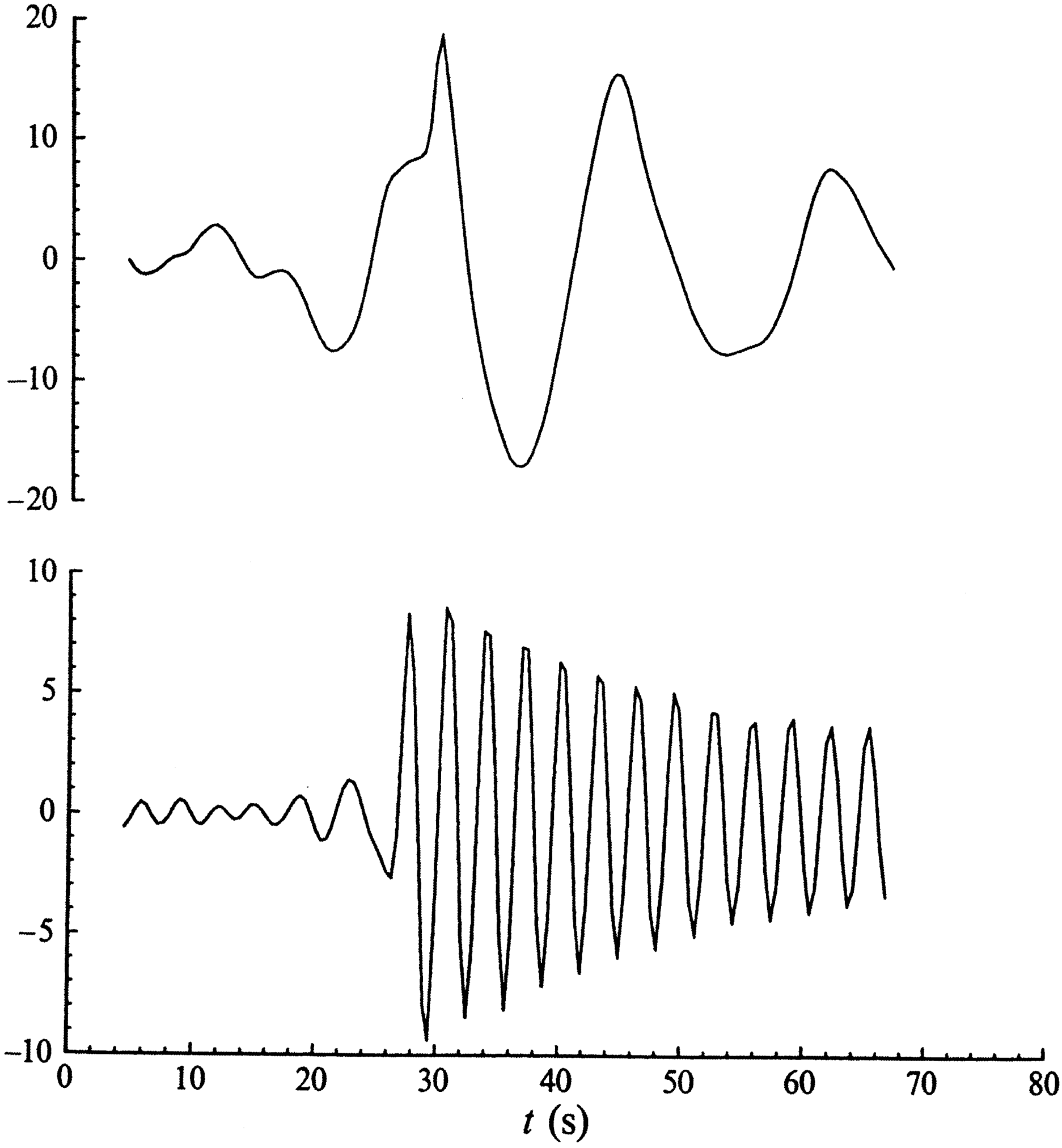

Figure 1.1 Experimental data showing the occurrence of ringing

Upper graph : time history of incident wave
Lower graph : measured tension in tethers

CHAPTER 2

LITERATURE REVIEW

2.1 Introduction

The finite element method is used with unstructured meshes in this thesis to model steep waves interacting with cylindrical structures. Conceptual developments relevant to this work are examined in turn in the literature review.

The next section details typical mesh generation techniques used in computational fluid dynamics, concentrating particularly on the advancing front and Voronoi methods used herein. Literature is reviewed on approaches to calculating forces on horizontal and vertical cylinders. Next, a review of the engineering literature is given. Finally, a survey is given on the development of numerical techniques for modelling free surface waves.

2.2 Mesh Generation

An Eulerian numerical solution to a physical problem consists of the values of dependent variables at specified discrete points within the domain. These points together with their connectivity make up the mesh. The simplest form of mesh is the Cartesian mesh; for the two dimensional case, nodes lie along lines of constant x and y and are uniformly spaced. This leads to difficulties in representing curved or irregular boundaries.

One approach that allows boundaries to be accurately represented is that of body-fitted curvilinear meshes. Here, the mesh can be considered to be equivalent to a transformed coordinate system, where the boundaries of the domain correspond to constant values of one of the coordinates. It is then possible to solve the problem on the transformed computational domain directly. The relationship between the physical and transformed domain can be described by a set of analytical equations or implicitly by requiring the new coordinate system to satisfy a set of partial differential equations. Among the first to use the analytical approach were Zienkiewicz and Phillips (1971), who used an isoparametric mapping, Gordon and Hall (1973), who used a transfinite mapping, and Cook (1973), who used the approach in three dimensions.

An alternative method for coordinate transformation is to solve a set of partial differential equations, usually an elliptic system. The most common approach is to ensure that each transformed variable satisfies Laplace's equation. When the outer boundary does not need to be fully specified, such as in external aerodynamic problems, hyperbolic equations may be used. The use of curvilinear coordinates has been developed extensively by Thompson *et al.* (1974, 1982, 1985). Johnson and Thompson (1978) discussed the applicability of curvilinear coordinates to the numerical modelling of hydraulic problems. More recently, Borthwick and Kaar (1993) used the curvilinear approach for shallow water modelling.

Cartesian and curvilinear meshes are both structured; that is, their elements can be arranged into rows and columns or in some other logical pattern. The alternative is unstructured meshes, where the elements and nodes are connected without any particular

pattern, allowing greater flexibility in meshing complex geometries; they can be made finer in areas of interest and coarser elsewhere. Unstructured meshes readily allow adaptivity. A problem can be simulated, and the numerical truncation errors through the domain estimated. An unstructured mesh can then be made finer where large errors were found. Making a mesh finer by adding extra nodes and elements cannot be easily achieved with structured meshes, though efforts have been made in the direction of nested meshes.

Yerry and Shephard (1983,1984) developed a method of hierarchical mesh generation based on the quadtree in two dimensions and the octree in three dimensions. Here, the domain is recursively subdivided into quadrants down to a prescribed resolution; a quadtree is used to store and manipulate the mesh information. The nodes of the quadtree provide the nodes of the mesh, which has an unstructured appearance. At the boundaries the quadtree nodes are displaced to coincide with the boundary. Triangular elements are formed by subdivision of the quadtree cells. Quadtree meshes have been used to solve a variety of fluid problems. Van Dommelen and Rundensteiner (1989) used quadtrees to model vortex shedding from a cylinder; Young *et al.* (1991) modelled compressible flow; De Zeeuw and Powell (1993) used quadtrees adaptively. The quadtree and curvilinear approaches were combined by Evans *et al.* (1991). Yiu *et al.* (1996) examined a number of quadtree techniques and their application to vortex shedding behind a square cylinder and a standing wave above a submerged cylinder. Greaves and Borthwick (1999) created two and three dimensional finite element meshes using quadtrees and octrees respectively. Free surface flow involving a submerged horizontal cylinder and a surface piercing vertical cylinder was simulated.

A related idea to the quadtree is that of the tritree. This concept has been developed by Wille (1992). The method uses a search tree based on triangles in two dimensions and tetrahedra in three dimensions. The density of elements in the resulting mesh can be varied throughout the computational domain. Wille (1997) recently used a tritree multigrid technique for a Navier-Stokes equation solver.

Early attempts at creating unstructured meshes were made by Frederick *et al.* (1970) and Cavendish (1974), who developed methods of connecting together pre-existing nodes. Another method of this kind was suggested by Lo (1985) who was the first to use an advancing front technique (one of the two techniques used in the present work). The front separated the part of the domain which had been meshed from the part which had not. A new element was created by connecting a node to an edge on the front; the new element would form part of the advanced front. Peraire *et al.* (1987) extended the technique to include a node creation algorithm, which created the nodes as the front advanced.

Advancing front techniques have often been used for constructing meshes of tetrahedra for three dimensional domains. Lohner and Parikh (1988) and Lo (1991) were among the first to use the advancing front method for three dimensional domains. Subsequently, Jin and Tanner (1993) developed a three dimensional algorithm, as did Moller and Hansbo (1995). Lohner (1996) demonstrated the large range of applicability of the advancing front method, describing how it could be used to generate elements with high aspect ratio for Navier Stokes applications, as well as quadrilateral and hexahedral elements. The discretization of a multiconnected volume was described by Chan and Anastasiou (1997); in their method the interior nodes were created using an inverse power interpolation technique. Rassineux (1998)

used an octree method to create a well distributed set of nodes from which a mesh was generated using the advancing front method. Parallel processing was used by Wilson and Topping (1998). They used a coarse background mesh of tetrahedra for their initial finite element simulation from which adaptive parameters were calculated. The domain was divided into subdomains which were refined concurrently using the advancing front technique. Kwak and Pozrikidis (1998) meshed three dimensional surfaces in order to model the large deformation of a viscous drop subjected to a shear flow. Most recently Lee and Hobbs (1999) used the advancing front technique for an adaptive finite element method, using triangular and quadrilateral elements.

The other kind of unstructured mesh generation technique used in the present work is the Voronoi method. This method results in a Delaunay triangulation, which is sometimes referred to as a Dirichlet tessellation. Dirichlet (1850), Voronoi (1908) and Delaunay (1934) each analyzed the space discretisation subsequently named after them. A Delaunay triangulation is one such that for each pair of adjacent triangles the minimum angle is larger than the case where the four vertices of the pair are connected in the alternative way. Each node of a Delaunay triangulation has an associated Voronoi region, every point inside of which is closer to the node of interest than any other. The edges of the Voronoi regions intersect the edges of the Delaunay triangles at right angles.

Lawson (1972) proposed an algorithm based on edge swapping to create Delaunay triangulations. This method was reviewed and implemented by Sibson (1978) and Green and Sibson (1978). A more efficient algorithm was proposed by Bowyer (1981) and Watson (1981). This method is based on node insertion. Each node is inserted into an existing mesh

of triangles. Remeshing is performed locally around the new node in order to incorporate it. This algorithm is described in detail in chapter three and is referred to as the Voronoi method.

Mavriplis (1990) used Voronoi meshes adaptively for viscous flow in two dimensions. Baker (1989) used the point insertion process to create Voronoi meshes in three dimensions. Examples of Voronoi meshes for aerospace geometries were given by Weatherill (1992). Further use of the Bowyer-Watson algorithm was made by Rebay (1993). Several automatic point creation techniques were compared by Weatherill and Hassan (1994) who presented statistics of measurements of mesh quality for several meshes. Borouchaki and Lo (1995) described a method where the tetrahedron containing a point was located by a random walk. This work was developed further by Borouchaki *et al.* (1996) and Borouchaki and George (1997). Rivara and Inostroza (1997) compared two longest side bisection techniques for the automatic refinement of Delaunay triangulations. Xu *et al.* (1998) presented an automatic mesh coarsening procedure.

Several papers have presented mesh generation techniques which combine aspects of the advancing front and Voronoi methods. One of the earliest to do this was by Muller *et al.* (1993). George and Seveno (1994) used a background Voronoi mesh which governed an advancing front algorithm. Mavriplis (1995) used the point placement technique of the advancing front together with a Voronoi triangulation algorithm. A similar approach was used by Frey *et al.* (1998).

Mesh generators based on the advancing front and Voronoi techniques have been developed by the present author and are described and compared in chapter three. The

performance of the mesh generators is assessed and timing comparisons are made.

2.3 Wave Loading on Cylinders

This review only deals with inertia loading on cylinders, not viscous drag effects. Inertia loading will tend to dominate the drag when the cylinder radius is large. For a cylinder in deep water, the wave height would typically have to be over three times the cylinder diameter, for viscous effects to be important. First, wave loading on vertical cylinders will be examined, followed by wave loading on horizontal cylinders.

2.3.1 Vertical Cylinders

The first attempts to use potential flow to find the force exerted by a free surface wave on a structure were based on linear theory, which assumes the wave amplitude is small. Havelock (1940) found the force on a vertical surface piercing cylinder in water of infinite depth. Diffraction was taken into account, with the cylinder affecting the flow around it. The theory predicted dynamic loads with peak values occurring at the wave frequency and proportional to the wave amplitude. MacCamy and Fuchs (1954) extended the solution to the more general case of finite depth.

When the wave amplitude increases, the second order force becomes significant. The second order force has a frequency twice that of the incident wave and is proportional to the square of the wave amplitude. The second order diffraction force on a vertical cylinder due to regular waves in water of infinite depth was derived by Lighthill (1979). He obtained an

explicit expression for the second order force without explicitly deriving the second order potential. Instead, an assisting potential was used which satisfied the homogenous form of the second order free surface boundary condition. Molin (1979) carried out the corresponding analysis for finite water depth. A difficulty with these formulations was the presence of a free surface integral which oscillated rapidly and converged slowly. The difficulty was overcome by Eatock Taylor and Hung (1987) who developed a closed form expression for the evaluation of the integral in the far field.

Kim and Yue (1989) used the integral equation formulation with Green functions to solve the second order problem. The second order potential throughout the domain was calculated by Chau and Eatock Taylor (1992). Further work on the second order wave force on a vertical cylinder was carried out by Newman (1996) who derived the second order potential using a Weber transformation of the forcing function on the free surface.

The third order load on a vertical cylinder was calculated by Malenica and Molin (1995) using an integral equation technique with a Green function expressed in cylindrical coordinates. They assumed that the wave amplitude is small relative to the wave length and the cylinder diameter. Faltinsen *et al.* (1995) used a different approach to obtain the second and third order loads. They assumed that the wave amplitude and the cylinder radius are of comparable size, but are both much smaller than the wave length.

Rainey (1989) developed a general wave loading technique for slender cylinders. In this method, the incident wave is described by a time varying velocity field, and the body is free to move in response to the waves. The wave loads are derived from arguments based

on energy conservation, with the assumption that the position of the wave surface is unaffected by the presence of the structure.

Experimental work was carried out by Chaplin *et al.* (1997) in order to investigate the phenomenon of ringing. The loading on a fixed vertical cylinder due to a steep focused wave was recorded. The response of a cylinder able to move was measured. The measured response was compared to the response calculated on a quasi-static basis from the measured loading history. Good agreement was found. Other experimental work on ringing has been performed by Grue *et al.* (1993), who generated large waves by frequency focusing, and by Stansberg *et al.* (1995) who identified extreme events by inspection of a long sequence of irregular waves.

2.3.2 Horizontal Cylinders

Now the case of the horizontal cylinder will be examined. Dean (1948) used a conformal mapping technique to demonstrate that the reflection coefficient of a submerged cylinder is zero. The first complete solution for waves travelling over a submerged horizontal cylinder in an infinite depth, for the linear case, was given by Ursell (1950) who used a multipole expansion method. Yu and Ursell (1961) extended the solution for the finite depth case.

Ursell's procedure was used by Ogilvie (1963) who calculated the first and second order forces on a submerged circular cylinder by sinusoidal waves in infinite depth. Vada (1987) used an integral equation method based on Green's theorem to calculate the first and

second order force components for infinite depth. A solution for the second order force on a horizontal submerged cylinder in finite depth was obtained by Wu and Eatock Taylor (1990) using a similar approach to the one used by Eatock Taylor and Hung (1987) for the vertical cylinder.

Chaplin (1984) carried out experimental work which measured forces on a submerged horizontal cylinder in deep water with its axis parallel to the crests of the wave. Non linear components with frequencies up to three times the fundamental wave frequency were found. Agreement was found with the theoretical results of Ogilvie (1963) for the linear oscillatory and second order steady forces. Later, Vada (1987) found agreement with Chaplin for the second order oscillatory force. Experimental work was also carried out by Grue (1992) who measured the first and second order wave elevation components either side of a submerged cylinder. The results were found to be in agreement with computations by Cointe (1989) based on potential flow theory.

2.3 Engineering Literature

Design methods used for calculating wave forces on offshore structures, use either Stokes waves or linear waves with a transformation applied, i.e. Wheeler stretching (see Wheeler (1970) or δ-stretching. Conte and Marshal (1994) demonstrate that Wheeler and δ-stretching schemes result in significant differences in response when used to calculate low-frequency drag forces on a fixed vertical cylinder. Couch and Conte (1997) compared the calculated responses of an offshore tower using kinematics based on various stretching schemes to the measured response. The Wheeler stretching technique was found to be the most effective.

Wang and Li (1997) used a Wheeler stretching approach when calculating hydrodynamic forces due to waves and a current.

Morison's equation is an empirical equation which bases the force calculation on the fluid speed and acceleration (see Morison *et al.* (1950)). Data from a slender compliant cylinder in random waves was analysed by Burrows *et al.* (1997) to obtain Morison wave force coefficients. Wolfram and Naghipour (1999) made an assessment of the various methods that may be used to analyse experimental data on the force experienced by a circular cylinder in combined wave and current flows to estimate drag and inertia coefficients for use in Morison's equation. It was found that the weighted least square method gave the best predictive accuracy.

Vugts *et al.* (1998) used a quasi-static approach to calculate the dynamic response of a structure. An 'inertial load set' is determined that accounts for the effects of the dynamic response and this is added to the applied loading; the quasi-static design wave method is then used.

The measured response of the Heidrun TLP was compared to a second order time domain model by Teigen and Haver (1998). Fairly good agreement between the observations and the model were found.

2.4 Numerical Modelling of Waves

A variety of techniques has been used to numerically model free surface waves, the most common of which is the boundary element method. The fully non linear problem in the time domain was first solved using this method by Longuet-Higgins and Cokelet (1976). At each time step the Laplace equation was solved, and the free surface was updated in a Lagrangian way by integrating the fully non linear kinematic and dynamic free surface boundary conditions with respect to time. With the assumption of periodicity, Longuet-Higgins and Cokelet (1976) were able to simulate propagating steep Stokes waves in infinite depth, as well as realistic overturning and plunging of the wave crest when an asymmetric surface pressure was applied. A similar method was applied by Faltinsen (1977) to study the non linear waves inside and outside moving bodies. Vinje and Brevig (1981) retained the assumption of periodicity and extended the approach of Longuet-Higgins and Cokelet (1976) to the case of finite depth with floating bodies; they used a complex potential formulation to improve the efficiency and accuracy of the method. The technique of formulating the problem in the complex plane and using a stream function was used for two dimensional problems by Dold and Peregrine (1986), Lin *et al.* (1984) and Dommermuth *et al.* (1988).

Dommermuth and Yue (1987) solved three dimensional axisymmetric problems, including the heaving of a floating vertical cylinder and the heaving of an inverted vertical cone. Rankine ring sources were used in a Green's theorem boundary integral formulation to solve Laplace's equation; the free surface was again treated in a Lagrangian way, and stepped forward in time. Green's function techniques were subsequently used by Grilli *et al.* (1989), and Cointe (1990) for the numerical simulation of tank wavemaking.

Cao *et al.* (1990,1991,1992) have used a time stepping technique with the Desingularized Boundary Integral Equation Method (DBIEM) to study various non-linear free surface problems including the non-linear waves generated by free surface pressure disturbances. The DBIEM uses Rankine sources outside the solution domain, and therefore does not require any special analysis or numerical technique to integrate the singularities over the boundary surfaces. This method was used by Celebi *et al.* (1997,1998) to investigate fully non-linear wave interactions with a stationary vertical cylinder in a three dimensional numerical wave tank with side and end beaches. Kim *et al.* (1998) used the method for the case with waves and currents.

Alternative Eulerian boundary element approaches have been used for non-linear wave problems. Yang and Ertekin (1992) simulated non-linear wave diffraction by a vertical cylinder as did Boo and Kim (1996); two and three dimensional numerical wave tanks were developed by Contento and Casole (1995) and Boo *et al.* (1994) respectively, the latter examining irregular waves. Ferrant (1996,1997) used a three dimensional mixed Euler Lagrange approach to model non linear wave current body interactions in the time domain. Other potential based boundary element methods used for computing wave body interactions include the two dimensional model of Clement (1996) and the three dimensional model of Beck (1994). A subdomain approach has been developed by Wang *et al.* (1995).

All of the above methods are fully non-linear. An alterative approach is to apply the Stokes perturbation expansion to the problem and to solve the problem to second order in the time domain. An advantage of this approach is that it avoids the need for remeshing, and so it has been used to solve several two dimensional wave structure interaction problems.

Isaacson and Cheung (1990,1991) used it for a wave diffraction problem, Isaacson and Ng (1993) applied it to wave radiation and Ng and Isaacson (1993) solved a combined radiation diffraction problem using the perturbation technique. A second order numerical wave tank was developed by Zhang and Williams (1996). First and second order forces due to waves and current were found by Isaacson and Cheung (1993). This was extended to three dimensions by Cheung *et al.* (1996), which in turn was extended to second order in wave height by Buchmann *et al.* (1998).

A completely different approach from the boundary element method is that of the volume of fluid (VOF) method, first developed by Hirt and Nichols (1981). Here, a background stationary Eulerian grid is used. The location of the fluid free surface is given by specifying the fraction of fluid in each cell of the grid. For this reason, the method can be used for a wide variety of fluid configurations and can easily deal with wave breaking. Finite differences are used to discretise the Navier-Stokes equations. The volume of fluid method has been used more recently by Ng and Kot (1992). A finite element volume of fluid model which uses adaptive meshing has been developed by Jeong and Yang (1998).

A related method to that of the volume of fluid uses a density function to specify the free surface. Miyata (1986) developed such a method using finite differences on a rectangular mesh. Subsequently the method has been developed further, and Miyata *et al.* (1996) use the density function technique with finite difference and finite volume methods, using both rectangular and curvilinear coordinate systems; Miyata *et al.* apply the method to three dimensional breaking waves around ships and to wave diffraction around offshore structures. The most recent version of the technique has been used by Park *et al.* (1999) to calculate the

interaction of a vertical truncated cylinder with waves in a tank.

Finally, the finite element method can be used to simulate non-linear free surface potential flow as demonstrated by Wu and Eatock Taylor (1994,1995) who considered the standing wave in a rectangular tank, waves generated by a vertical wave maker, and waves generated by an oscillating cylinder below the free surface. Wu and Eatock Taylor (1995) showed that the finite element method could be more efficient than the boundary element method as it led to a banded matrix equation which could be solved more easily than the full matrix produced by the boundary element method.

The finite element method is ideally suited for use with unstructured meshes; given the nodal coordinates and connectivity, the finite element matrix equation can be calculated automatically. The use of unstructured meshes allows complex geometries to be modelled; single and multiple submerged bodies of arbitrary shape can be included in the fluid domain. An automatic mesh generator can be used to remesh the domain, meaning that problems where significant changes in the shape of the domain can be solved; this is the case with steep free surface gravity waves. Because of the reasons of efficiency and flexibility described, the finite element method with unstructured meshes seems ideal for the difficult problem of calculating forces on structures due to steep waves, and has therefore been used for the work in this thesis. The next chapter describes advancing front and Voronoi unstructured mesh generation techniques used herein. Details of the finite element formulation are given in chapter four.

CHAPTER 3

UNSTRUCTURED MESH GENERATION

3.1 Introduction

The finite element method allows numerical solutions to be obtained for problems with complex domains. The method requires the domain to be divided into a tiled mesh, usually of triangular elements. For a large domain with a complex geometry, the generation of the mesh is an important part of the computational procedure. For cases involving moving boundaries, where the domain is continually changing shape, remeshing may be done many times. It is therefore necessary to have a mesh generator which is computationally quick and efficient.

The mesh generator should be able to produce a mesh with varying density whereby the elements are of different sizes in different parts of the domain. It is important the mesh is fine enough to give sufficient resolution in areas of interest, such as where there are large changes in a variable over a short distance. The finer the mesh is, the more elements there are; there is more computation to be done, requiring more memory and longer run times. Clearly, the mesh should only be fine where necessary, not throughout the domain.

Adaptive remeshing is a process where the mesh is refined in some places, and possibly made coarser in others, based on the solution resulting from the previous mesh. A new solution is obtained using the new mesh; the procedure may be repeated many times. There are many criteria that may be used for adaptive remeshing. In one approach, an

estimate of the error is made; where the error is too high, the mesh fineness is increased. The Courant number ($u\Delta t/\Delta x$) may be used. It is effectively the ratio of the physical speed to the maximum speed that information can cross the computational domain. The Courant number places a limit on how fine the mesh can be for a given time step. The Courant number must be less than 1 everywhere in order that instabilities do not occur. Remeshing may be done on the basis of the magnitude of a non-dimensional physical parameter, or the magnitude of a physical property such as free surface elevation or water depth. Mixed grid and physical variables may be used, such as the product of vorticity and element area which gives the element circulation.

The mesh needs to be produced automatically, otherwise the user is required to make some additional decisions before the method can proceed. For example, with a curvilinear boundary fitted mesh, the user may have to decide the shape of the untransformed computational domain. The method should be robust and reliable, being able to successfully mesh any domain with which it is presented.

For this purpose, two unstructured mesh generators have been developed for the discretisation of two dimensional domains, based on the advancing front method and the Voronoi method. One of the earliest papers dealing with the advancing front technique is by Lo (1985). The first paper to present the algorithm described here as the Voronoi method is by Bowyer (1981).

3.2 Advancing Front

Two versions of the advancing front method have been used. One merely requires information about the x and y coordinates of the boundary nodes; the other requires additional information about the desired mesh density within the domain. During the mesh generation process there are one or more fronts where new elements are created. These fronts separate the areas of the domain where elements have been created and those where they have not (see figure 3.1). A new element is created such that one or two of its edges is supplied by the front. The method progresses along the front, examining each node in turn, determining on the basis of the angle between adjacent line segments at the node, what kind of element to create.

3.2.1 Method One

Figures 3.2 to 3.4 show the three different ways in which new elements are introduced at the front. Figure 3.2 shows pattern **a**. Here, the angle between two sides on the front, α, is less than or equal to $\pi/2$, therefore nodes A and C are joined to make element ABC. A variable e is defined such that if e equals 1, this case is dealt with first, along the entire front, until all angles less than or equal to $\pi/2$ are eliminated; otherwise, e equals 0 and pattern **a** triangles are only created as they are encountered by the method as it progresses along the front. Unless otherwise stated e, is set equal to 1. Pattern **b** is illustrated in figure 3.3. Here, α is greater than $\pi/2$ and less than or equal to $2\pi/3$ and the angles either side, β and γ are greater than $8\pi/15$. In this case, two new elements are created, ABP and BCP. The line BP bisects α and the length of BP is given by

$$BP = \frac{1}{6}(l_1 + 2l_2 + 2l_3 + l_4) \quad . \tag{3.1}$$

The final case is pattern **c**, shown in figure 3.4. One new element, an equilateral triangle *ABP*, is created when the angles α and β are both greater than $2\pi/3$. Method one is given by George (1990) in his description of the advancing front technique.

3.2.2 Method Two

This method is very similar to the first. It is defined in terms of the same three basic patterns, but the positions of the new nodes are determined differently, using information about the required mesh density in the region of the node. The mesh density can be specified in various ways. Here, analytical formulas are used which, given the x and y coordinates of a point in the domain, return the required distance, l, between two nodes.

Equations 3.2 to 3.4 give the formulas used for the case of a domain with a rectangular outer boundary with a circular inner boundary. The rectangle has uniform node spacing on its upper and lower boundaries, with variable spacing on the left and right.

$$f = 1 - \frac{y}{h}, \qquad g = 1 - \frac{r}{R}, \tag{3.2}$$

$$A = \left(\frac{t}{b}\right)^{\left(\frac{d}{d-1}\right)} + 1, \qquad B = \frac{\log_{10}(f^A + 1)}{\log_{10}(2)}, \tag{3.3}$$

$$l_a = t\left(\frac{b}{t}\right)^B \quad \text{and} \quad l_b = b\left(\frac{c}{b}\right)^g , \tag{3.4}$$

where t, b and c are the lengths of the line segments on the top and bottom of the domain and the cylinder; y and r are the positions of the point relative to the bottom of the domain and the cylinder and h is the height of the domain at the point (see figure 3.5); R is a constant, representing a distance measured from the circle; d is the number of line segments on the left and right boundaries; A, B, f and g are intermediate values. If c is smaller than either t or b, then l equals the smaller of l_a and l_b, otherwise, l equals the larger of l_a and l_b. The value l_a is calculated such that it corresponds to the left and right of the domain, where the ratio of lengths of successive segments is constant. Equations 3.2 to 3.4 were devised by the author.

Pattern **a** is dealt with as before. For pattern **b**, BP again bisects α, but the length BP equals l. In the case of pattern **c**, the length AP is equal to l, unless l is less than $AB/2$, in which case, AP equals 0.6 AB. This method is of the author's own devising.

3.2.3 Special Cases

When a possible new node position is calculated by one of the above methods, it must be checked whether the new node lies within an existing element or outside the domain (see figure 3.6). If so, this node and its associated elements are not created. If a node already exists within a certain specified small distance of the proposed node, then this node is used instead (see figure 3.7). The specified distance is a fraction, m, of the desired distance between two nodes, l, in that part of the domain. In most cases, m is set equal to 0.3. When an existing node is used as described, the front will be split into two. Each front is then dealt

with in turn. For a domain with an inner boundary (a hole) as well as an outer, each front is dealt with alternately until the two are joined by the method just described. When the front only consists of five nodes, a node is created at the average position of these five nodes and connected to each of them to create five new elements (see figure 3.8).

3.2.4 Domain control

As described in the previous section, when a new node is proposed, the surrounding elements and nodes need to be checked. In order that this checking process may be done efficiently, the domain is split into a number of square regions and each element and each node is assigned to one of these regions as it is created. Only the elements assigned to the region of the new node or the eight surrounding regions are checked (see figure 3.9).

3.3 Voronoi method

This method generates a mesh using a node insertion technique. At any stage during the mesh generation procedure, a valid mesh exists. When a new node is inserted, the existing elements in the region of the new node are eliminated and new elements are created connecting the new node to the rest of the existing mesh.

As with the advancing front technique, the mesh generator requires information about the boundary of the computational domain, in the form of the positions of the nodes on the boundary. An initial mesh is used, larger than the computational domain, consisting of two triangular elements and four nodes. Figure 3.10 shows an example for a domain with a

square outer boundary and a circular inner boundary. The nodes of the computational boundary are then inserted into this larger domain using the following method.

Each element has an associated circumcircle. This is the circle with a boundary that intersects the three nodes of the element (see figure 3.11). If a new node lies within the circumcircles of existing elements, then these elements are removed. New elements are created in the space left by the removed elements by connecting the surrounding nodes to the new node (see figure 3.12).

Following the insertion of the boundary nodes, elements have been created both inside and outside the computational domain. Those outside the domain are removed; figure 3.13 shows an example for the same domain as in figure 3.10.

Further nodes are now created inside the domain. At this stage, the elements of the mesh have a variety of sizes and shapes. For each element that is too large, a new node is created. The size of each element is checked to determine whether a node should be created. All the new nodes are then inserted. Every element is then checked again and the procedure repeats. There are a number of different measurements of the size of an element: (1) the area of the element; (2) the radius of the circumcircle of the element; (3) the length of the shortest side of the element. The new node can be positioned in a number of different ways relative to the large element: (1) at the centroid of the element; (2) at the centre of the circumcircle of the element; (3) such that the node makes an equilateral triangle when joined to the shortest side (see figure 3.14). In the latter case, it must be checked that no two nodes are created at the same position.

An element is considered to be too large if its size is larger than a specified size. For a uniform mesh, this size is constant throughout the domain. For a mesh with variable density, an analytical formula gives the desired length of a line segment at a particular point in the domain (see equations 3.2 to 3.4). The upper limit on the size of an element will be given by pl^2 if the area is used as the size measure and pl for the other two size measures; p is an adjustable parameter. The finer the mesh, the smaller the specified size is. When no more elements can be found which are too large, the Voronoi method terminates.

The application of a further two rules has been found to improve mesh quality. Before a new node is incorporated into the mesh, it is checked whether it lies closer than ql to an existing node. If the smallest side of an element is larger than rl then no node is inserted into that element regardless of its size. This rule is useful when the third node positioning technique is used, and prevents nodes being created too far from the boundary initially. The values of p, q and r can all be adjusted in order optimize the quality of the mesh produced.

3.4 Smoothing

In order to improve mesh quality, smoothing is performed. This alters the node positions while maintaining the node connectivity. Each node is repositioned so that it lies at the average location of the nodes to which it is connected (see figure 3.15). A node is considered to be connected to another node if they both belong to the same element. After each node has been repositioned once, each node is not necessarily at the average location of its surrounding nodes which have since been relocated also. Smoothing takes very little computational work, therefore it is performed four times for each mesh.

lack of uniformity, but there are no large regions of differing density. The result of positioning nodes so as to make equilateral triangles is illustrated in figure 3.16 (*c*). Close to the boundary the mesh is very regular, with equilateral triangles arranged such six elements together make a regular hexagon. Towards the centre this regularity is lost, but the mesh remains reasonably uniform.

For the first three cases, the rule preventing a node being created when the shortest side of an element is too large, is not applied. This is because r is set equal to a large number, 10000. In Figure 3.16 (*d*), method 3 for node positioning is again used, but r is equal to 1.5. It can be seen that the mesh retains its regular nature throughout the domain, not just near the boundary. This is because, initially, nodes are prevented from being created, except close to the boundary. Method 3 has been shown to produce good quality meshes with the required mesh density, with certainty of good quality near the boundaries, which is important when the mesh is for the use of the finite element method. For these reasons, method 3 is used in subsequent examples. For a uniform mesh, good meshes have been seen to be obtained with r equal to 1.5. When the mesh density varies, better results are achieved with r equal to 10; being too strict in preventing the insertion of nodes can mean the mesh density does not vary smoothly.

In the remaining examples of the Voronoi method given here and the later examples of the advancing front method, the mesh density varies throughout the domain. All the domains consist of an outer rectangular boundary and an inner circular boundary. The rectangle has uniform node spacing on its upper and lower boundaries, with variable spacing on the left and right. The circle has uniform node spacing on its boundary. This type of

domain is used for illustration as it is clearly applicable to the problem of wave forces on a submerged horizontal cylinder, where a finer mesh will be required near the free surface and close to the cylinder.

Figure 3.17 shows the results of the Voronoi method, with the same square boundary as before, but with an inner circular boundary also. The analytical formulas (3.2 to 3.4) were used to specify the mesh density, with R equal to twice the circle radius. For the uniform square, t equals b. In figure 3.17 (a), the mesh is uniform, with 32 segments on the circle and c equal to t. Figure 3.17 (b) has a circle with 64 segments and c equal to half of t. This results in a circle with the same radius as before, but with a finer mesh in the region around it. The mesh around the circle is coarser in figure 3.17 (c), with only 16 segments around the circle and c equal to $2t$. In figure 3.17 (d), the mesh is uniform, but the circle is not at the centre of the domain. In all these cases, the Voronoi method can be seen to have produced good results, creating elements of good quality and producing the correct mesh density where specified.

Figure 3.18 shows further examples of the Voronoi mesh generator. Here, the domain is twice as wide as it is high, and figures 3.18 (b) to (d) have a sinusoidal variation on the upper boundary. A circle is again present as the inner boundary, close to the upper boundary. These figures illustrate the kinds of mesh that are produced during the finite element simulation of waves passing over a submerged horizontal cylinder. In each case the cylinder has 32 segments and $c = 0.5$. The number of segments vertically, d, is 16. In figures 3.18 (a) and (b), $t = b = 1.0$; in figure 3.18 (c), $t = 0.5$ and $b = 1.0$; in figure 3.18 (d), $t = 0.5$ and $b = 2.0$. Figure 3.18 (d) shows the kind of mesh that is used for finite element simulations,

with a finer mesh close to the free surface and the cylinder, the areas of interest, and a coarser mesh towards the bottom of the domain, where velocities are expected to be smaller.

Examples of the advancing front technique are presented next. As for the Voronoi technique, the results of different versions of the advancing front mesh generator are given (in figure 3.19) for a square domain with 32 segments on each side. Figure 3.19 (*a*) shows a mesh created using method one, where no use is made of the desired mesh density; the size of new triangles is entirely determined by the size of the segments on the front. The mesh is not uniform, with some small regions of higher mesh density and some regions of lower density. Method two has been found to give better control of mesh density and is used in all further examples. In figure 3.19 (*b*), e equals 0, so that angles less than $\pi/2$ are not eliminated first along the entire front, but only as they are encountered as the method progresses along the front. The number m, which determines whether an existing node is used instead of a new one being created, is usually equal to 0.3, but in figure 3.19 (c), m is put equal to 1.5. This makes it much more likely that an existing node is used. Figure 3.19 (*d*) illustrates the results of method two in its standard form ($e = 1$ and $m = 0.3$). This is clearly the most symmetrical mesh of the three using method two, but its quality is not significantly superior to the other two.

Figures 3.20 and 3.21 show the results of the advancing front mesh generator on the same boundaries as were used by the Voronoi method in figures 3.17 and 3.18. Equations 3.2 to 3.4 were used to specify the mesh density, with R equal to the circle radius. These domains all contain a circle as the inner boundary. For this case it has been found that good results are given if e equals 1 initially, but when the inner front is connected to the outer, e

is set equal to 0. The latter approach is more effective when the remaining space available for the creation of new elements is long and narrow. If angles less than $\pi/2$ are eliminated as soon as they are created, triangles much larger than required are created (see figure 3.22). With an inner boundary, the value of m chosen has a greater effect on the results. A value of m equal to 0.3 has been found to give the best results. The meshes in figures 3.20 and 3.21 can all be seen to be of good quality with the required mesh density. There is very little difference in appearance of the meshes created by the advancing front technique and those created by the Voronoi method.

A number of stages of the generation of the mesh in Figure 3.21 (*d*) by the advancing front method are illustrated in figure 3.23. In figure 3.23 (*a*), the inner front has recently joined the outer front. After the method has progressed further, one large front remains in the left part of the domain and a number of very small fronts in the rest of the domain, as can be seen in figure 3.23 (*b*). Figure 3.23 (*c*) shows the final mesh before smoothing. The quality of the mesh is good in most parts of the domain, but there are four elements with an unacceptably high aspect ratio. After smoothing, the mesh quality can be seen to be improved, with the removal of these high aspect ratio elements (see figure 3.23 (*d*) or 3.21 (*d*)).

Similar stages in the Voronoi mesh generation are illustrated in figure 3.24, for the same domain. Figure 3.24 (*a*) shows the situation after two node insertion stages. Approximately equilateral triangles have been created close to the boundaries, with many high aspect ratio triangles further in the domain and a number of large triangles. The method has progressed further in figure 3.24 (*b*) and the final mesh before smoothing is shown in figure

3.24 (*c*). The mesh before smoothing is noticeably poorer than the corresponding advancing front mesh. However, after smoothing, the meshes are of similar quality as can be seen by comparing figure 3.23 (*d*) to figure 3.24 (*d*).

3.6 Efficiency and speed comparison

The efficiency of the advancing front and Voronoi techniques can be compared by examining the time taken by the methods to mesh a particular domain. The domain chosen for these tests is a square. Tables 3.1 and 3.2 show the time taken in seconds when the fortran programs are run on a Sun Sparc Unix Workstation. The left column indicates the number of line segments on each side of the square. Figure 3.25 shows these results in graphical form, with time taken plotted against the number of elements. The results are plotted in logarithmic form in figure 3.26, where the lines are those of best fit. In both cases, the dotted line is for the Voronoi method and the solid line is for the advancing front.

It can be seen that the advancing front method is considerably faster than the Voronoi method; for the 50 by 50 domain it is nearly ten times faster. For both methods the relationship between the time taken to the number of elements produced is not linear. If we express the relation as $t = A\ E^n$, where t is the time taken, E is the number of elements, and A and n are constants, then n can be found from the logarithmic graph (figure 3.26). For the advancing front, n is found to be approximately 1.3. For the Voronoi method, n is about 1.8. This means that for larger domains, the ratio of the time taken by the advancing front method to the Voronoi method will be smaller, and the advancing front technique will have the advantage.

For the Voronoi method, most of the run time is spent determining which element a new node lies in, prior to incorporating it into the mesh. This search procedure could perhaps be made much more efficient by using quadtrees when finding elements in which particular nodes are located. The advancing front technique performs a number of checks before a new node is created, such as ensuring that the new node does not lie in an existing element. These checks seem to be efficient, taking about 15% of the total run time.

3.7 Conclusions

Two mesh generator programs have been written, one based on the advancing front method, the other based on the Voronoi method. Both methods have been found to mesh successfully domains of arbitrary size and shape with varying mesh density. The meshes produced have been seen to be of good quality, with very few triangles with a high aspect ratio, thus making them suitable for use with the finite element method. The methods are automatic, only data about the boundary and a specification of the required mesh density are needed. The mesh generators are robust and flexible, and are able to deal with a variety of domains.

Each mesh generator has a number of different versions. These versions have been implemented and compared; the version giving the best mesh quality has been chosen in each case. The advancing front and Voronoi meshes have been compared and found to be of similar quality. Smoothing has been found to improve the meshes, eliminating elements with a high aspect ratio.

The efficiency of each technique has been examined. The advancing front mesh

generator has been found to be faster than the Voronoi mesh generator in its present form. During testing, the Voronoi method was found to be invariably robust, whereas the advancing front method occasionally broke down due to difficulties encountered in checking overlapping elements. For future work, a combined approach, making use of the advantages of each method could be adopted. The advancing front technique could be used initially, but if the method breaks down, the Voronoi could be used instead. The approach would require an error detection routine to determine whether the method has failed.

In chapters six and seven, wherever unstructured meshes are needed, the Voronoi method is used, because it is robust and reliable.

Table 3.1 Time taken by advancing front method to mesh a square domain.

Line segments	No. of nodes	No. of elements	Time (seconds)
10	132	222	0.03
20	496	910	0.24
30	1093	2064	0.73
40	1917	3672	1.64
50	2977	5752	2.83

Table 3.2 Time taken by Voronoi method to mesh a square domain.

Line segments	No. of nodes	No. of elements	Time (seconds)
10	137	232	0.16
20	504	926	1.07
30	1096	2070	4.86
40	1928	3694	20.21
50	2988	5774	44.68

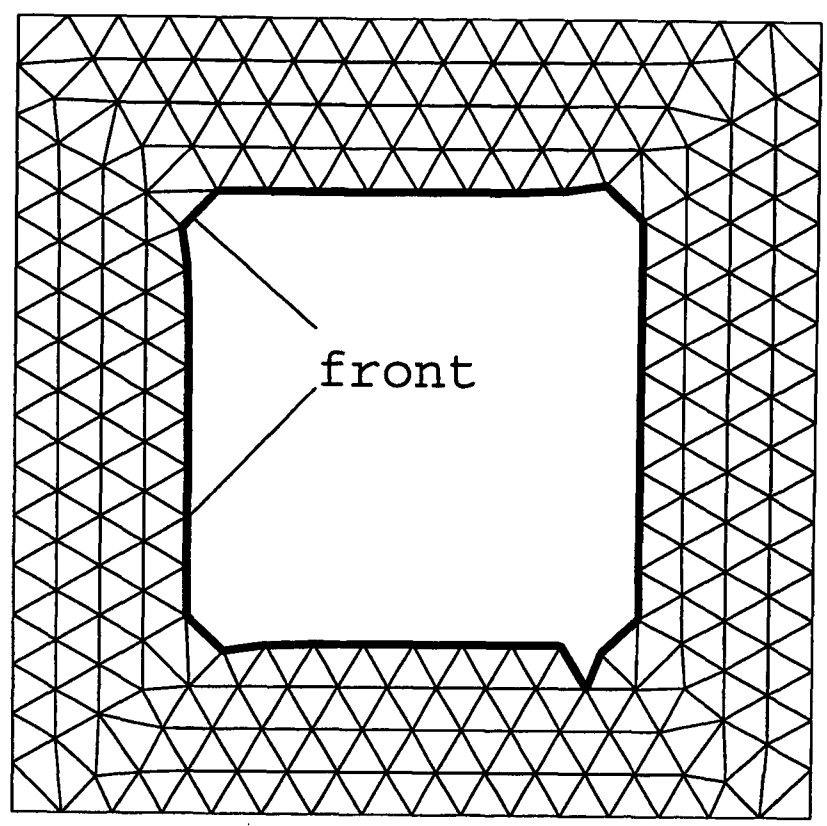

Figure 3.1 Example of a front in the advancing front method

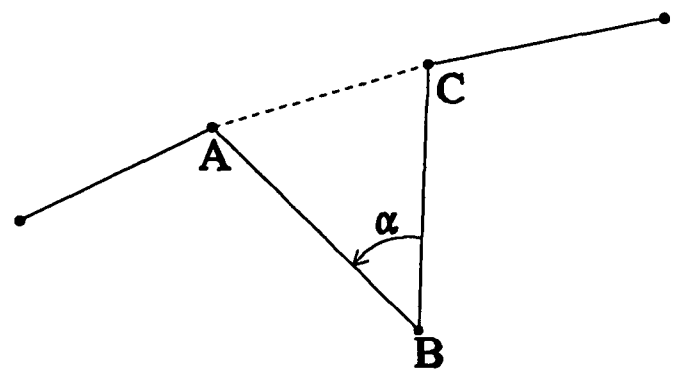

Figure 3.2 Pattern **a**

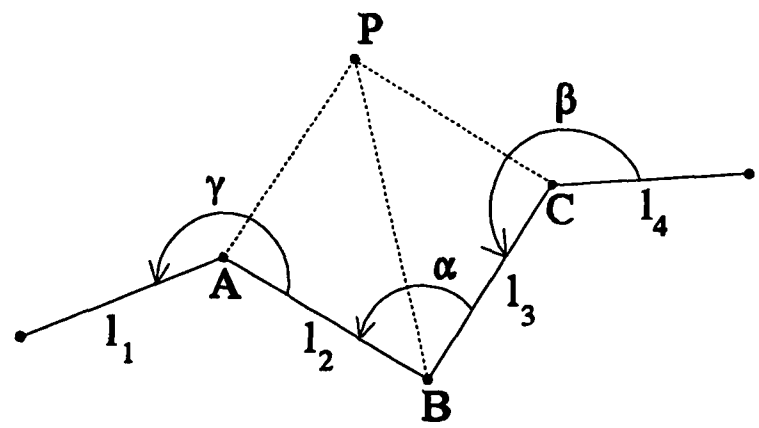

Figure 3.3 Pattern **b**

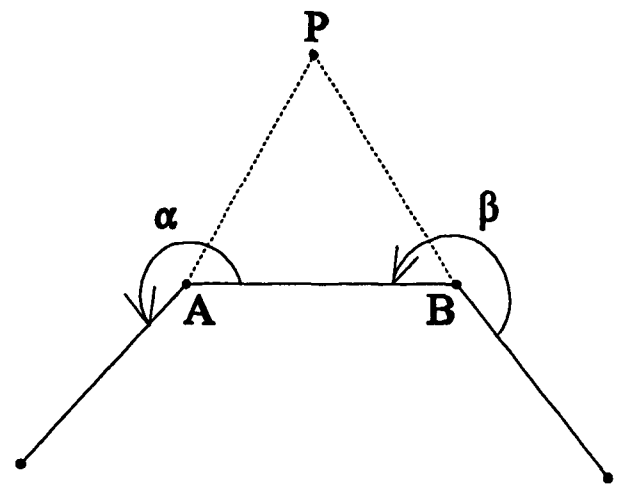

Figure 3.4 Pattern **c**

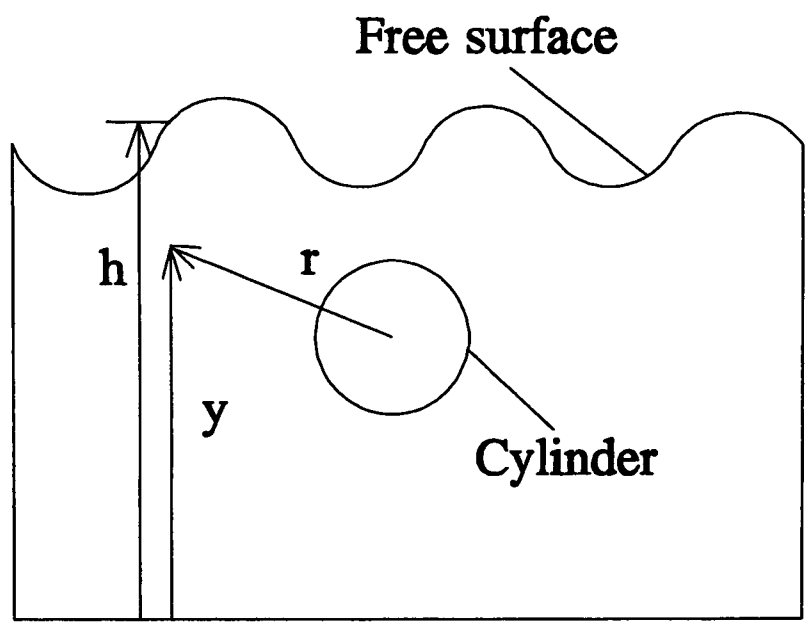

Figure 3.5 Definition of h, y and r

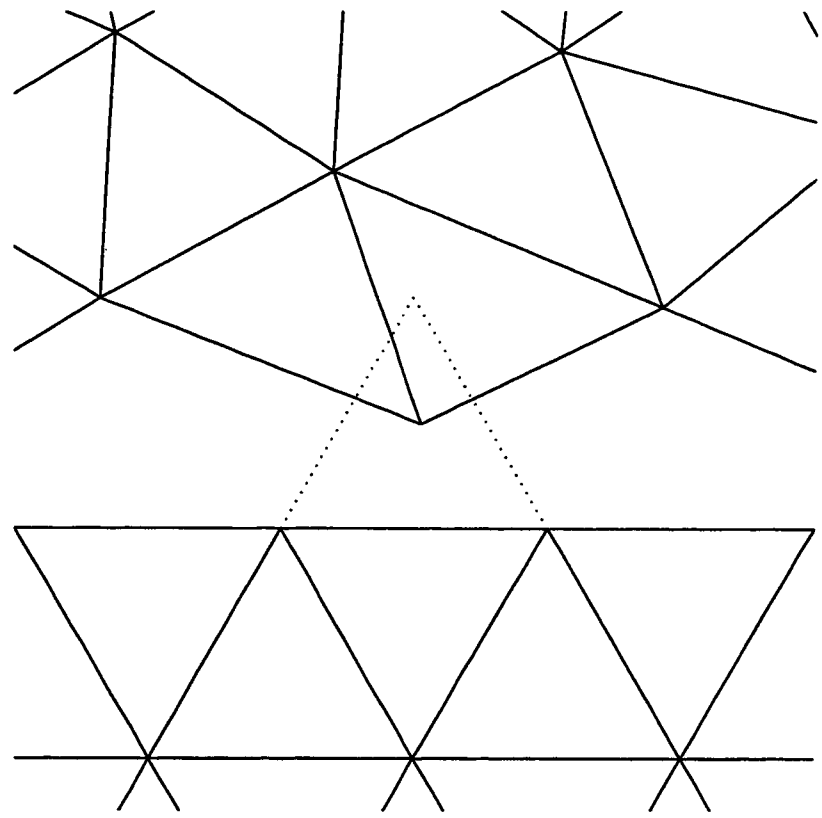

Figure 3.6 Node located in existing element

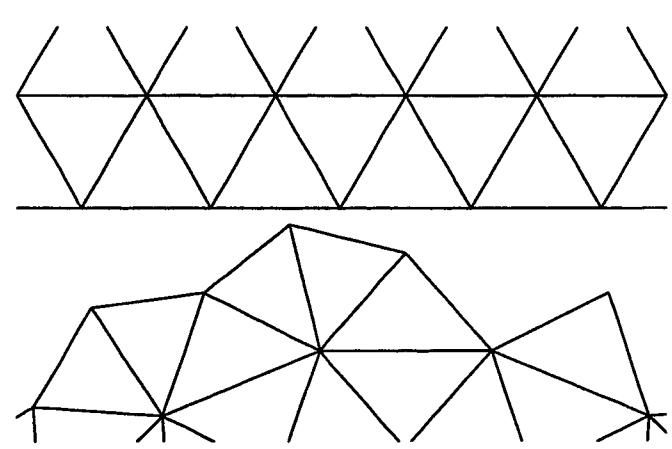

(a)

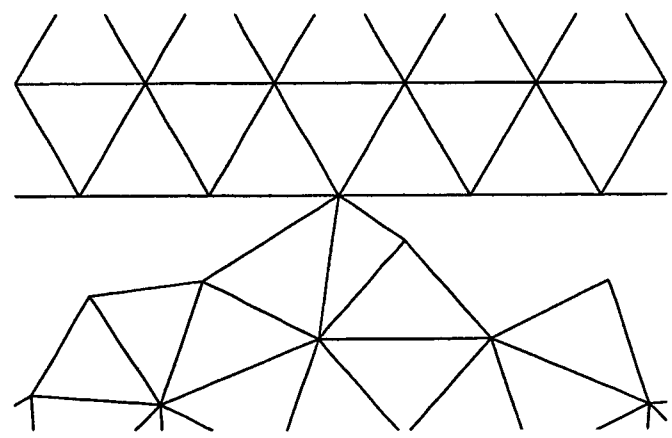

(b)

Figure 3.7 An existing node is used instead of creating a new node.

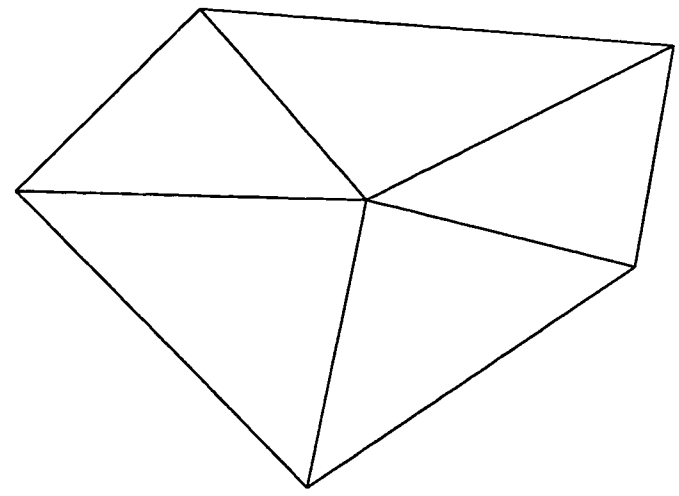

Figure 3.8 Creation of five new elements

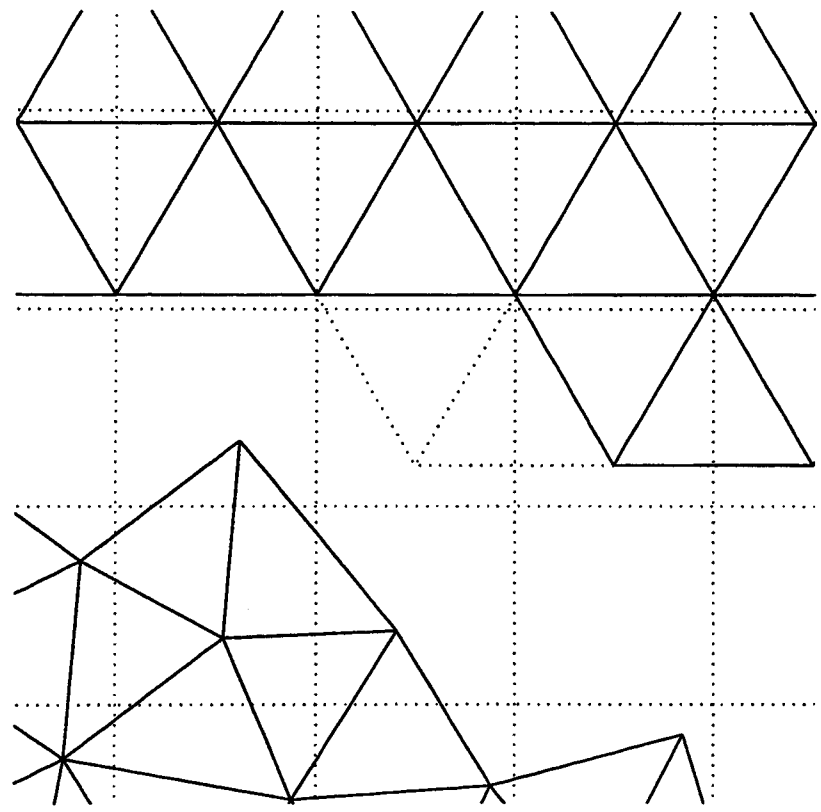

Figure 3.9 Domain is split up in order to perform search more efficiently

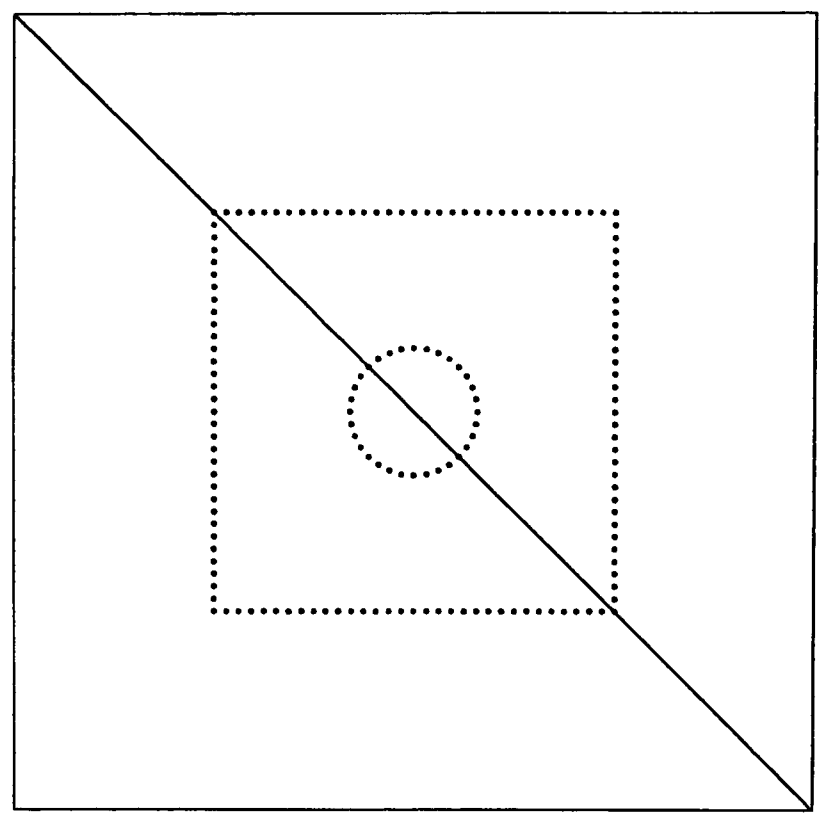

Figure 3.10 Initial Grid for Voronoi Method

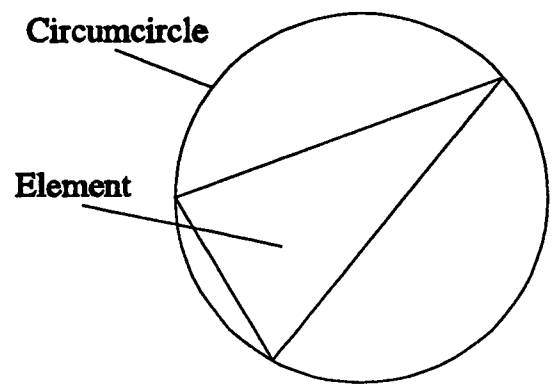

Figure 3.11 Example of a circumcircle

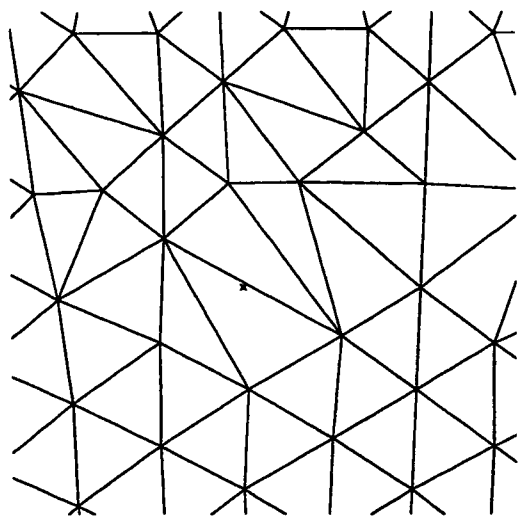

(a)

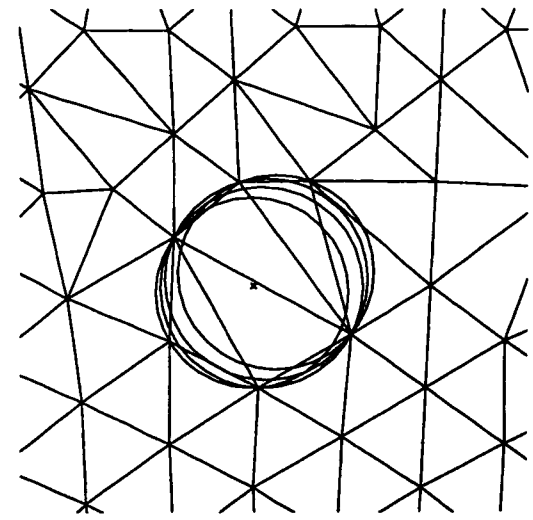

(b)

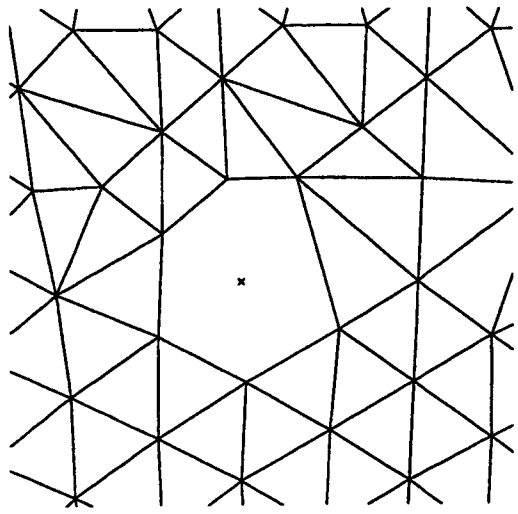

(c)

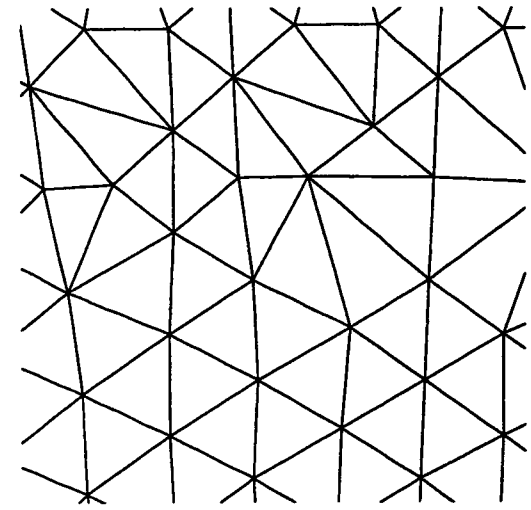

(d)

Figure 3.12 The Node Insertion Process for the Voronoi Method

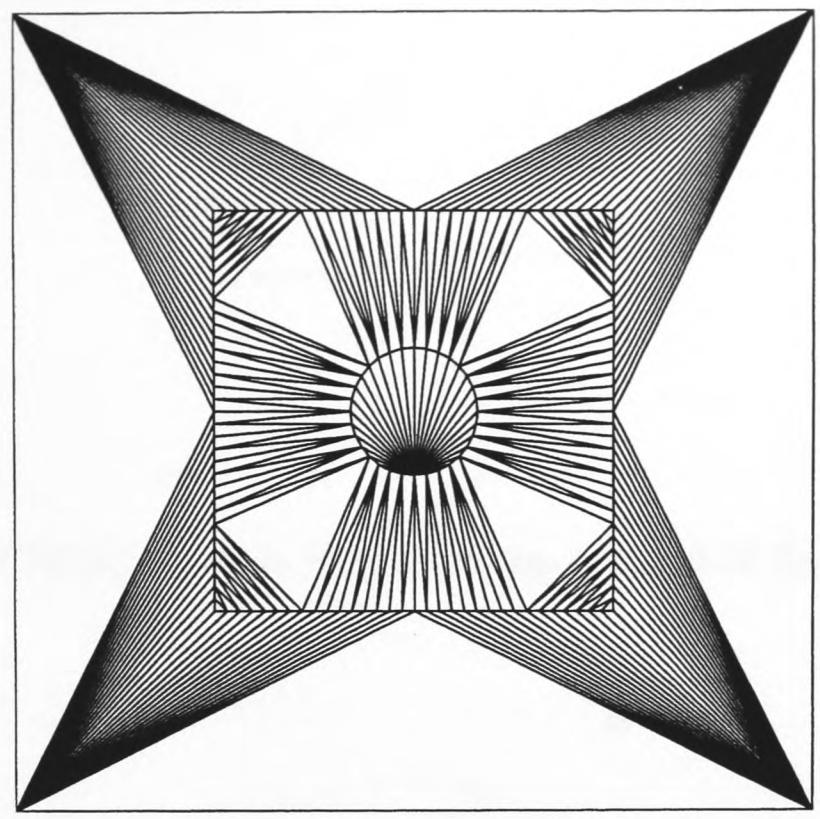

(a)

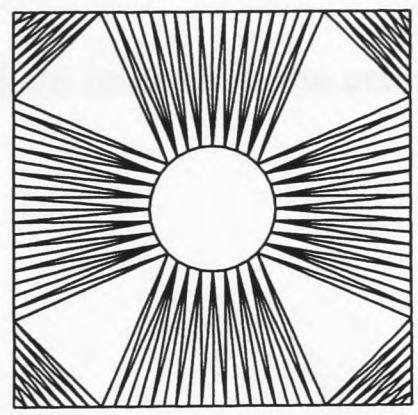

(b)

Figure 3.13 Removal of External and Internal Elements for the Voronoi Method

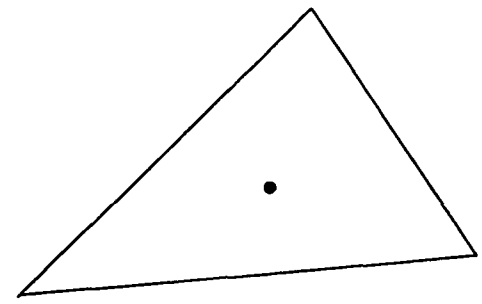

Figure 3.14 (a) Node inserted at the centroid of the element

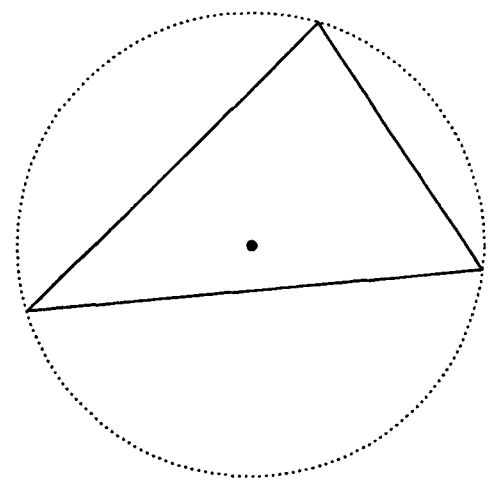

Figure 3.14 (b) Node inserted at the centre of the circumcircle

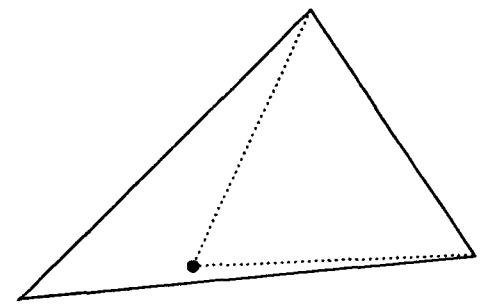

Figure 3.14 (c) Node inserted such that it creates an equilateral triangle

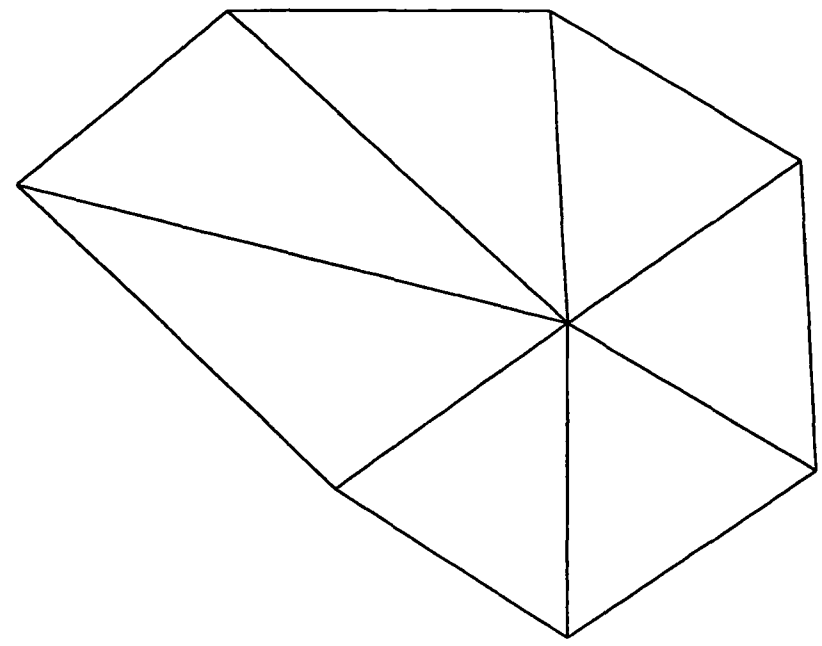

Figure 3.15 (a) Before smoothing

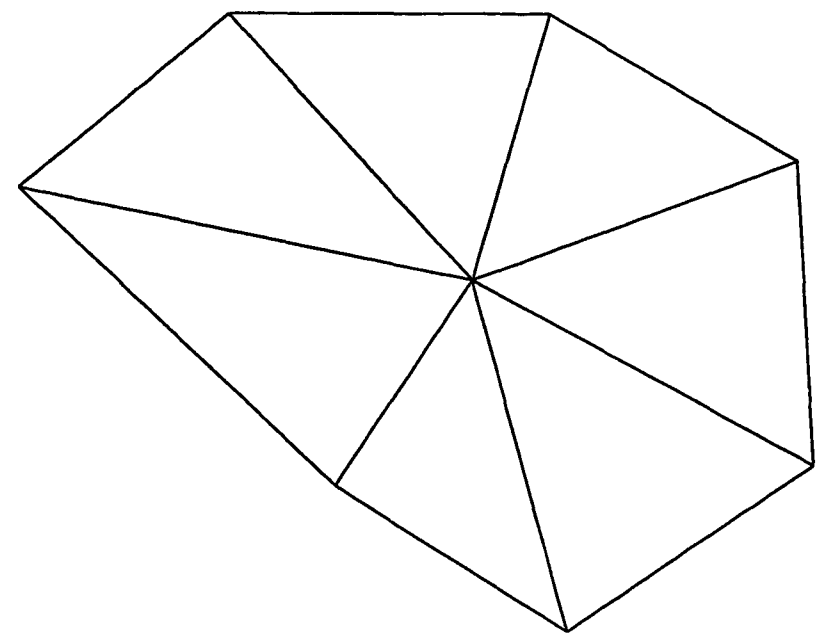

Figure 3.15 (b) After Smoothing

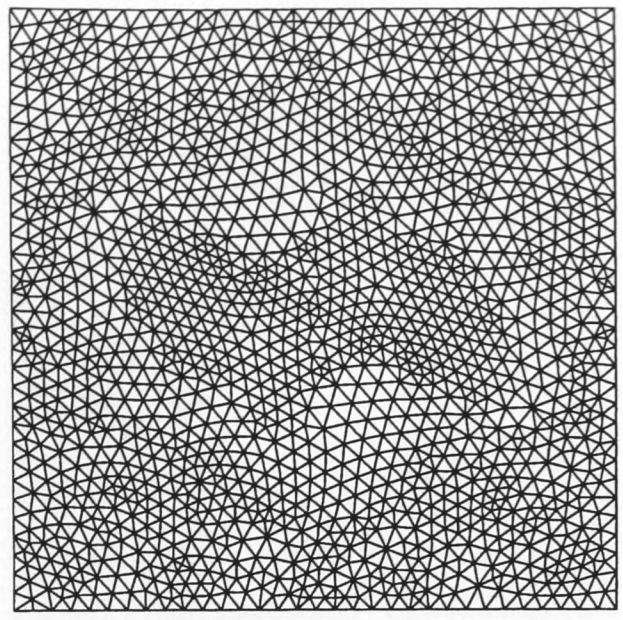

(*a*)

$p = 0.6$
$q = 0.5$
$r = 10000$
Node position = 1

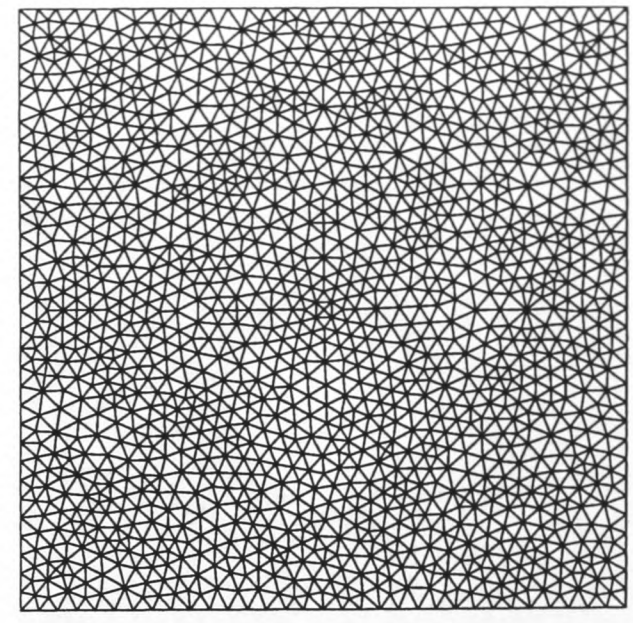

(*b*)

$p = 0.6$
$q = 0.5$
$r = 10000$
Node position = 2

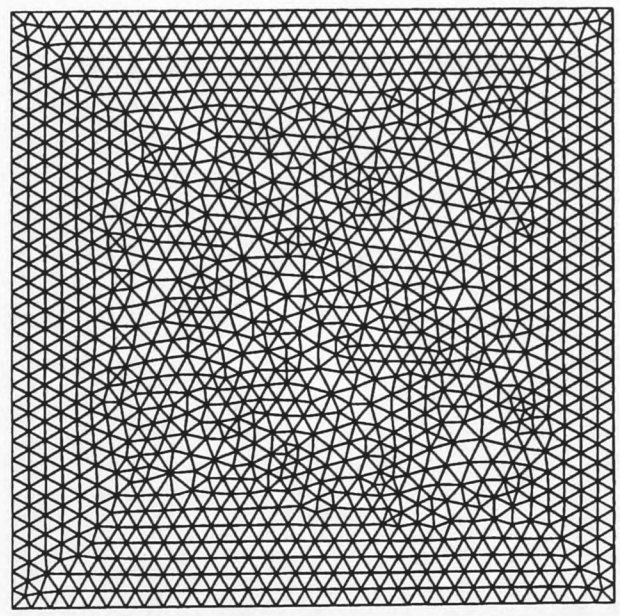

(*c*)

$p = 0.6$
$q = 0.5$
$r = 10000$
Node position = 3

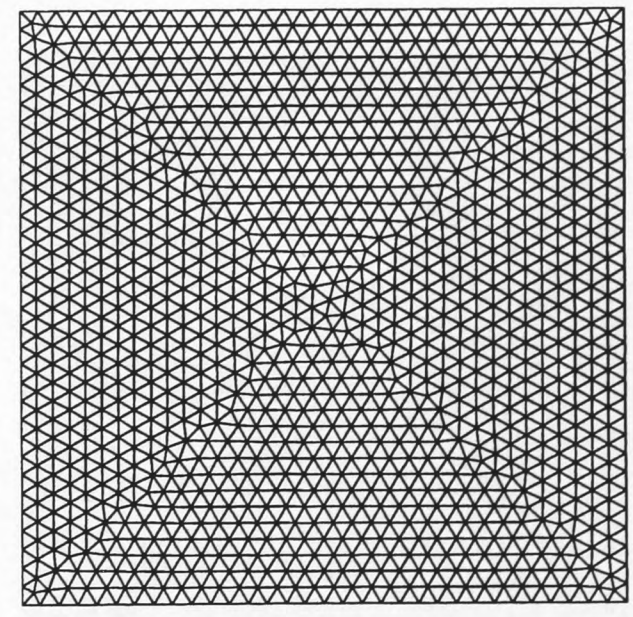

(*d*)

$p = 0.6$
$q = 0.5$
$r = 1.5$
Node position = 3

Figure 3.16 Voronoi meshes generated within a square domain

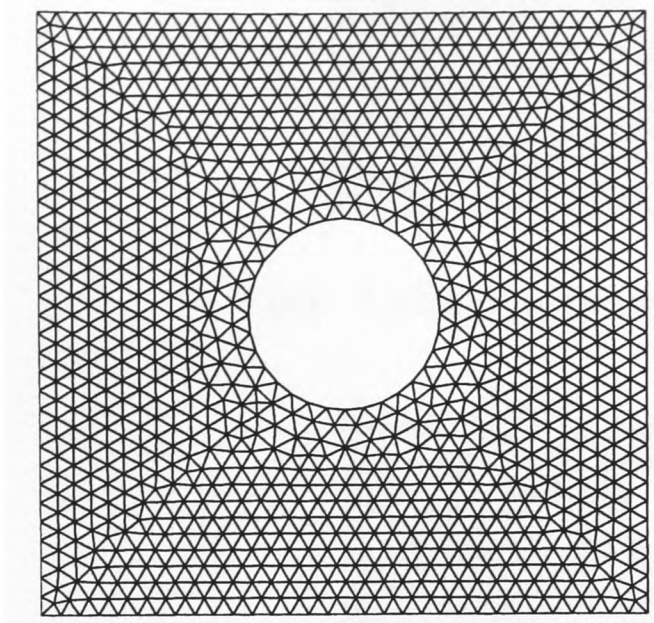

(*a*)

32 Circle segments

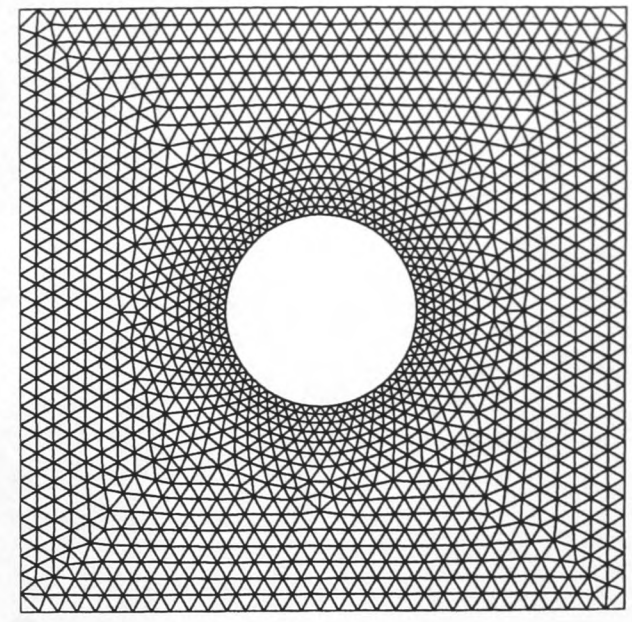

(*b*)

64 Circle segments

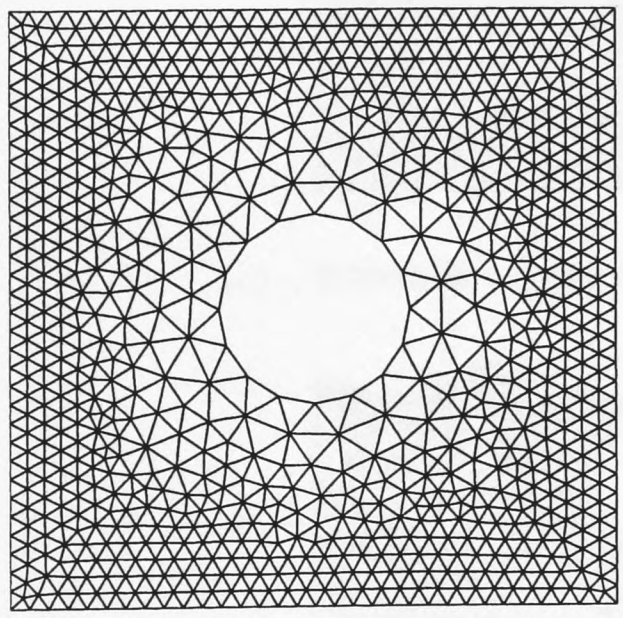

(*c*)

16 Circle segments

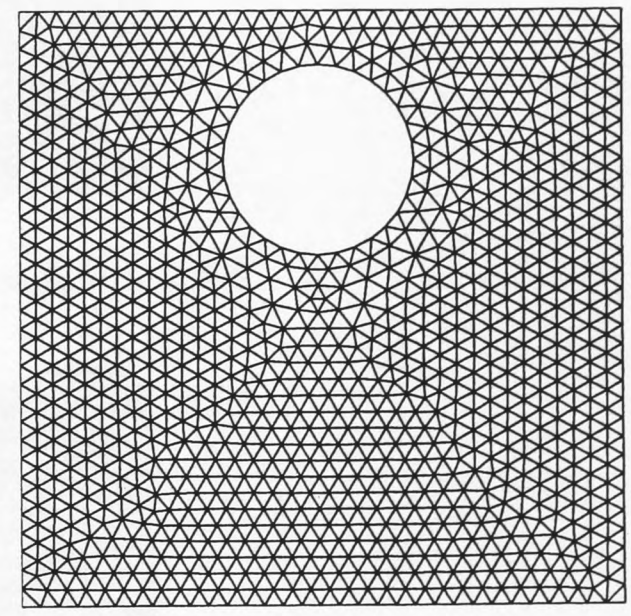

(*d*)

32 Circle segments

Figure 3.17 Voronoi meshes generated around a circle inside a square domain
Note that for all above figures, $p = 0.5$, $q = 0.6$, $r = 10.0$, node position = 3.

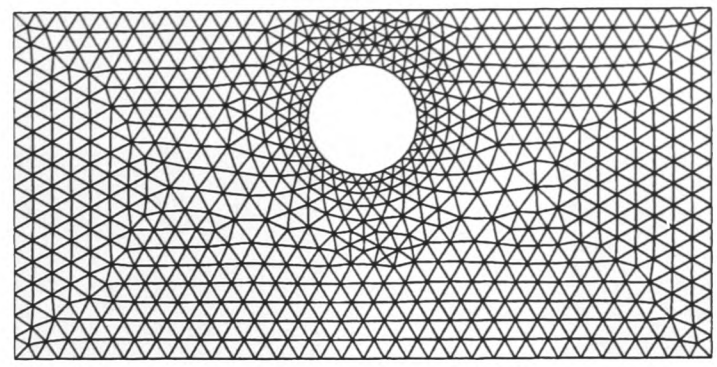

(*a*) Uniform upper boundary, $t = 1.0$, $b = 1.0$

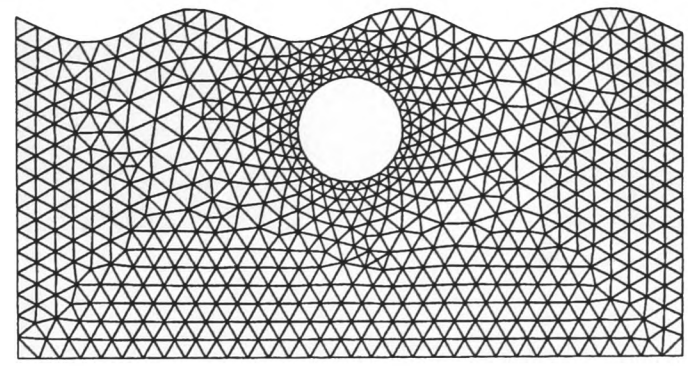

(*b*) Sinusoidal upper boundary, $t = 1.0$, $b = 1.0$

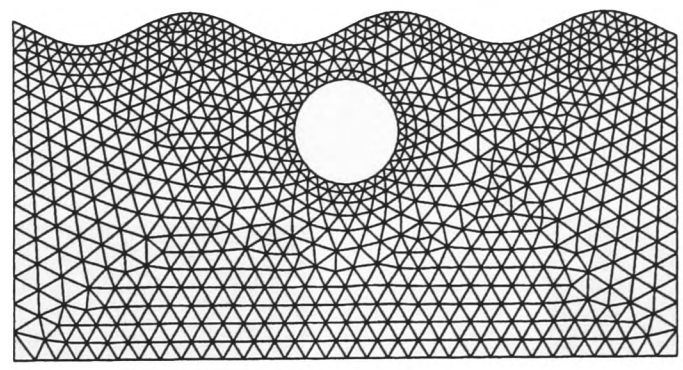

(*c*) Sinusoidal upper boundary, $t = 0.5$, $b = 1.0$

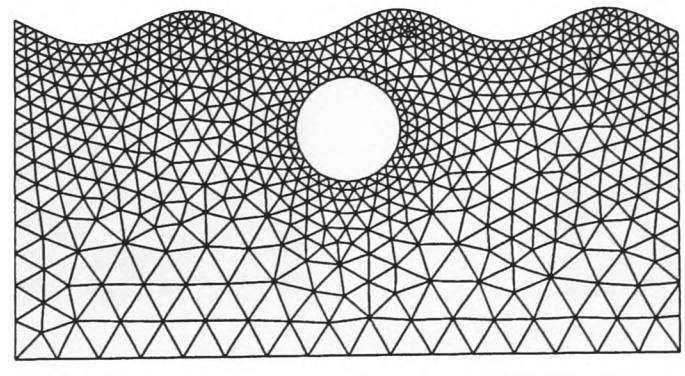

(*d*) Sinusoidal upper boundary, $t = 0.5$, $b = 2.0$

Figure 3.18 Voronoi method for domains with circular inner boundary and varying mesh density.

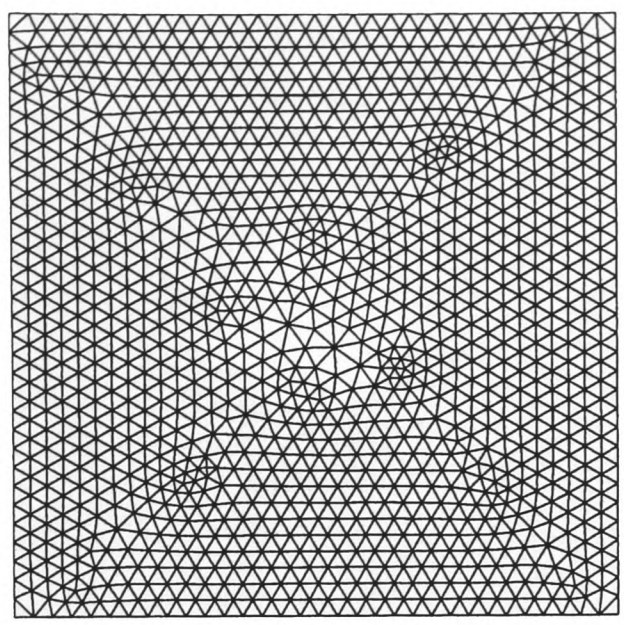

(*a*)

Method One
$e = 1$, $m = 0.3$

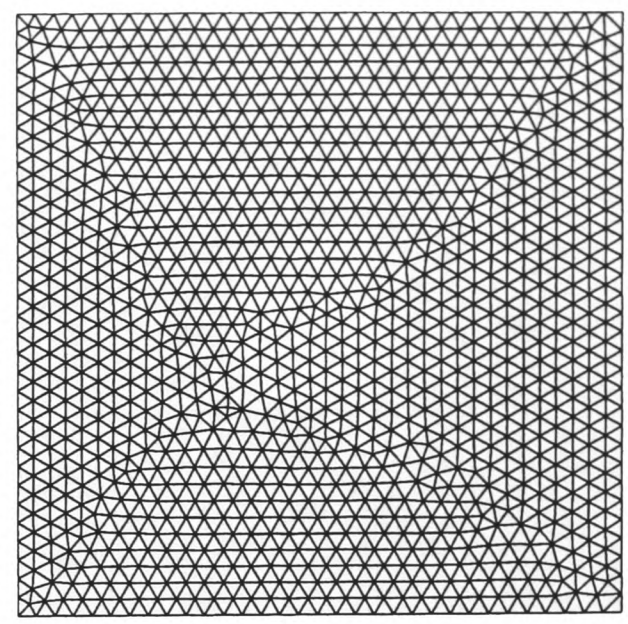

(*b*)

Method Two
$e = 0$, $m = 0.3$

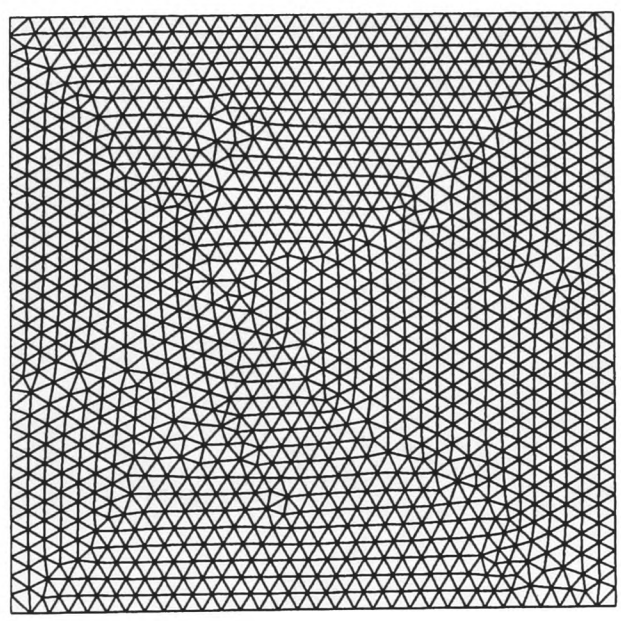

(*c*)

Method Two
$e = 1$, $m = 1.5$

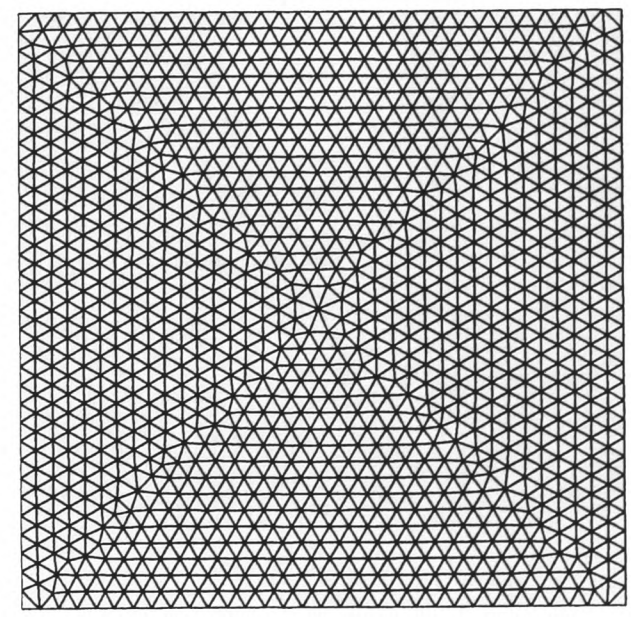

(*d*)

Method Two
$e = 1$, $m = 0.3$

Figure 3.19 Advancing front meshes generated within a square domain

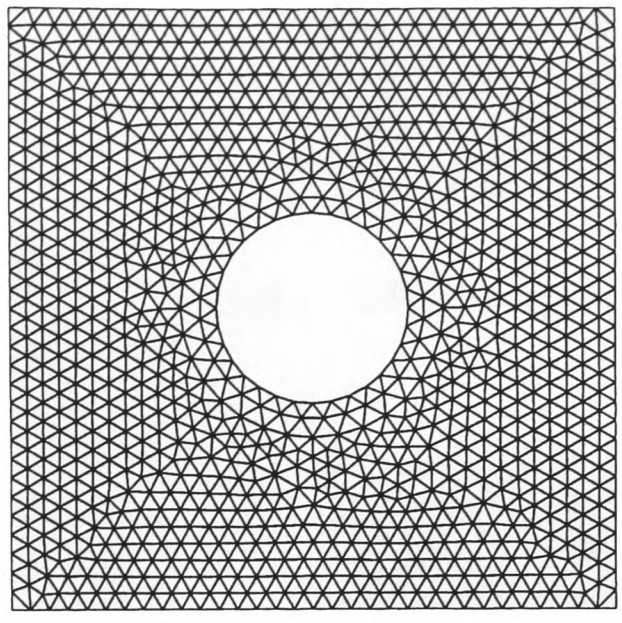

(*a*)

32 Circle segments

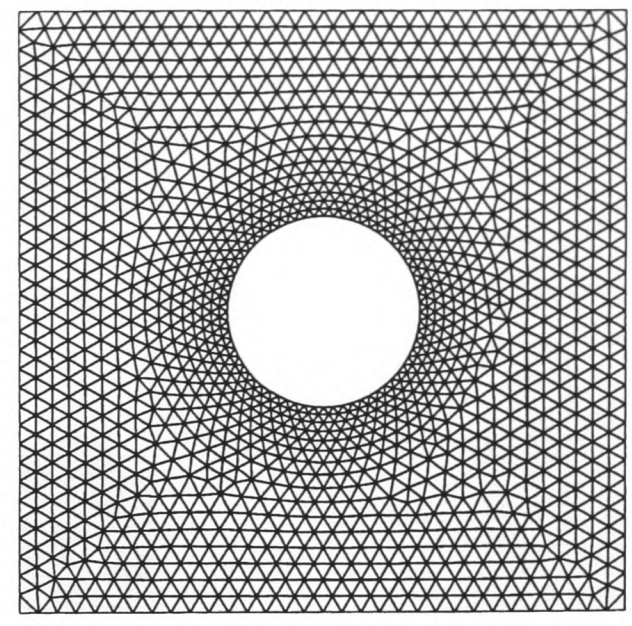

(*b*)

64 Circle segments

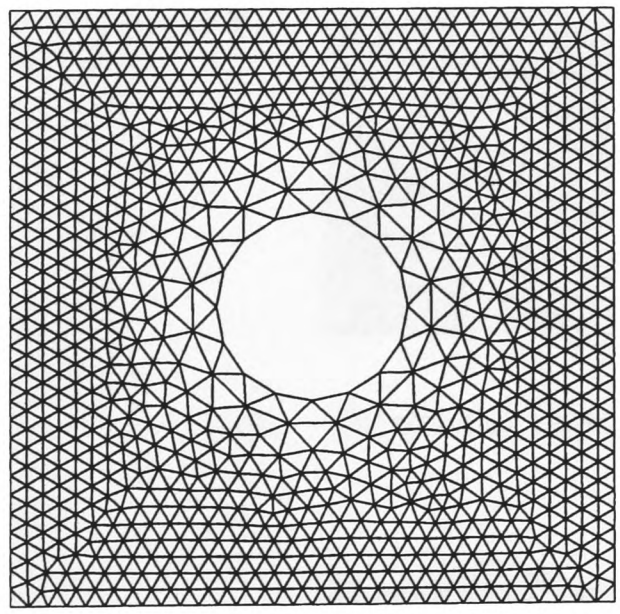

(*c*)

16 Circle segments

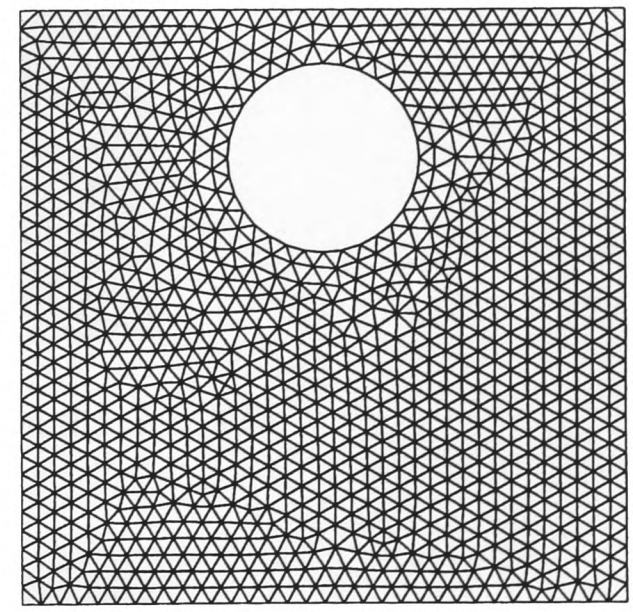

(*d*)

32 Circle segments

Figure 3.20 Advancing front meshes generated around a circle inside a square domain For all cases $e = 1$ initially and later is set equal to 0; $m = 0.3$

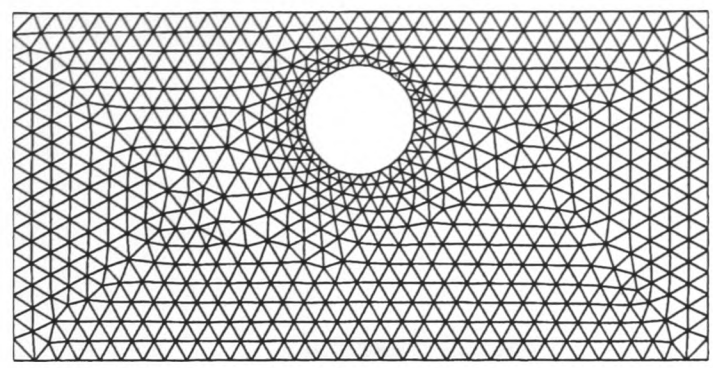

(*a*) Uniform upper boundary, $t = 1.0$, $b = 1.0$

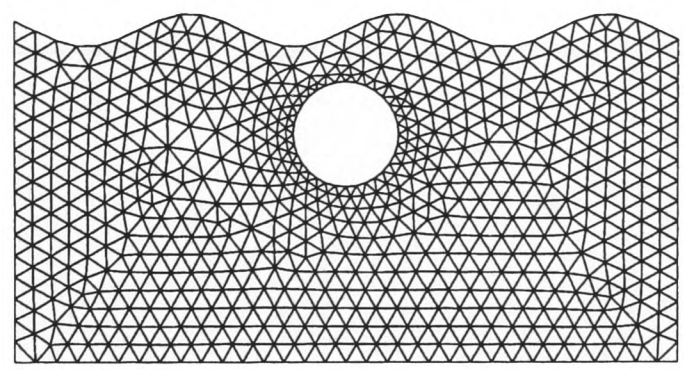

(*b*) Sinusoidal upper boundary, $t = 1.0$, $b = 1.0$

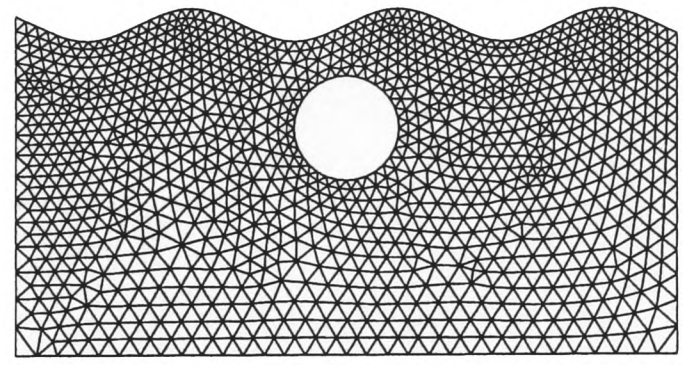

(*c*) Sinusoidal upper boundary, $t = 0.5$, $b = 1.0$

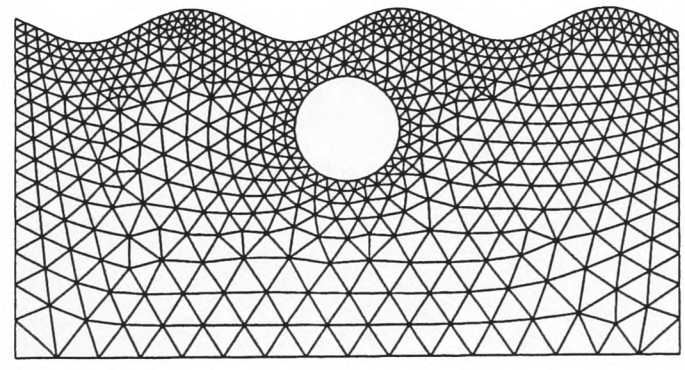

(*d*) Sinusoidal upper boundary, $t = 0.5$, $b = 2.0$

Figure 3.21 Advancing front method for domains with circular inner boundary and varying mesh density

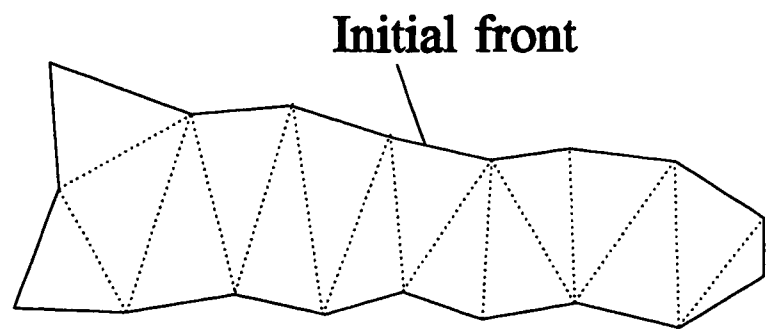

Figure 3.22 Final stages of advancing front method

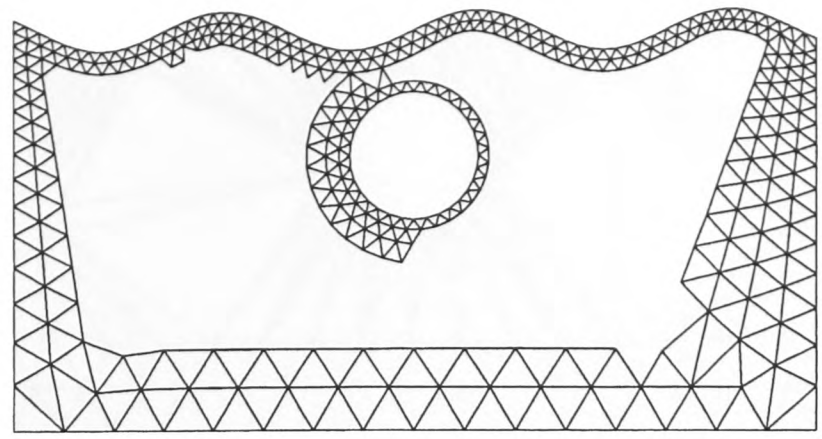

(*a*)

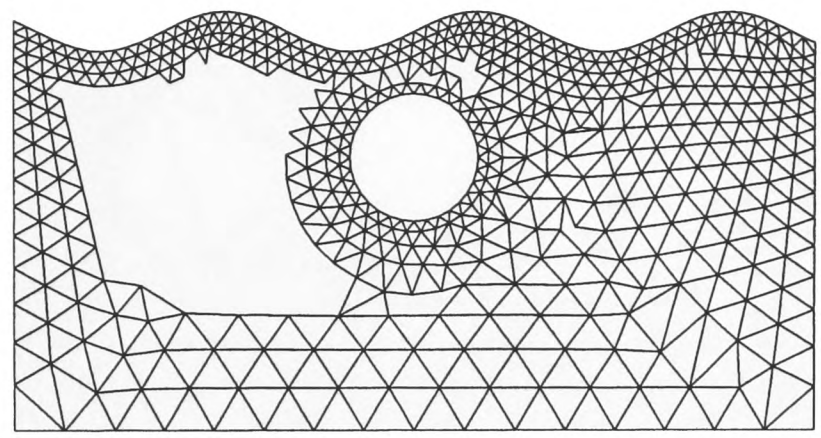

(*b*)

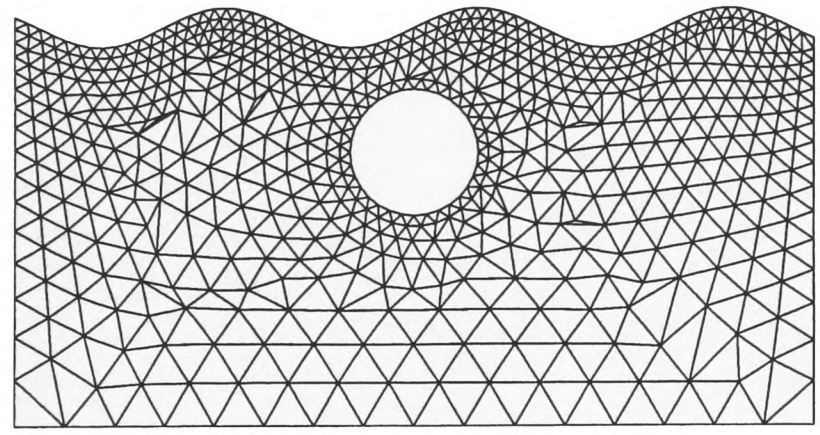

(*c*)

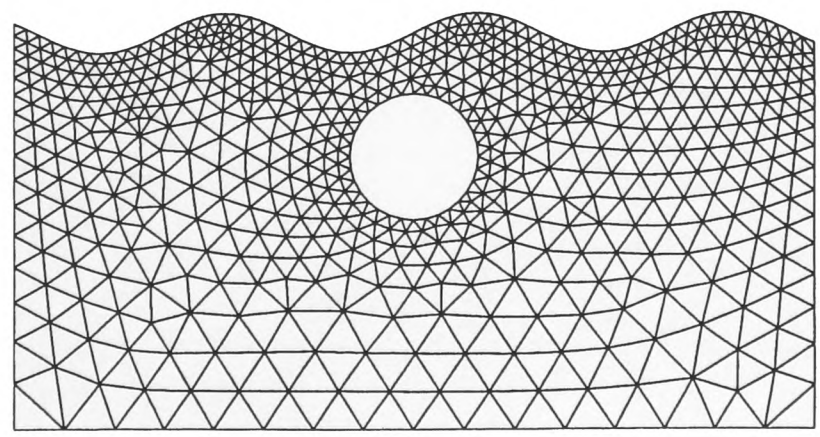

(*d*)

Figure 3.23 Stages in generation of an advancing front mesh

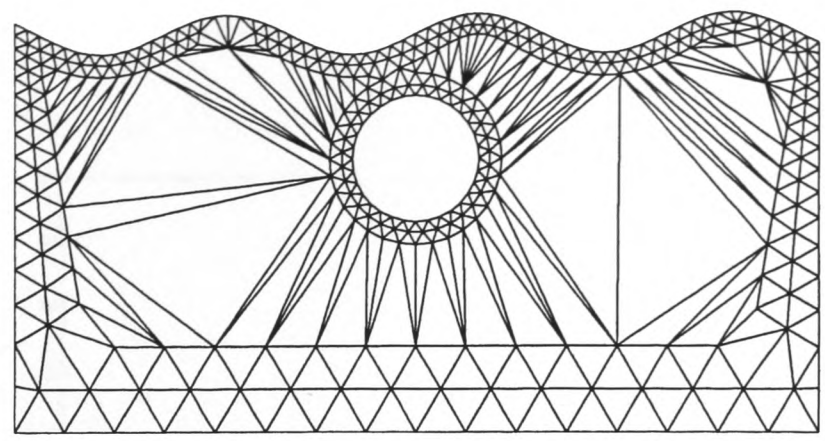

(*a*)

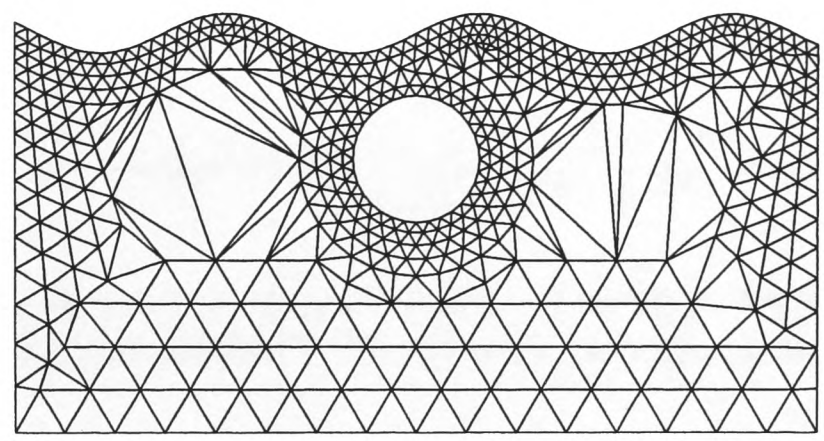

(*b*)

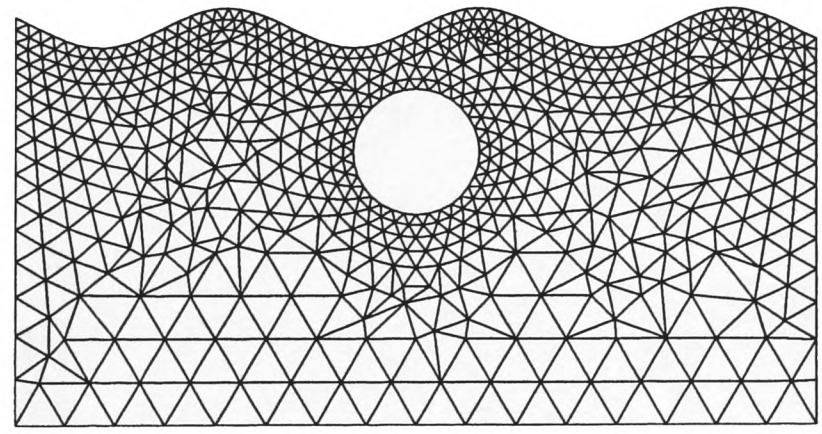

(*c*)

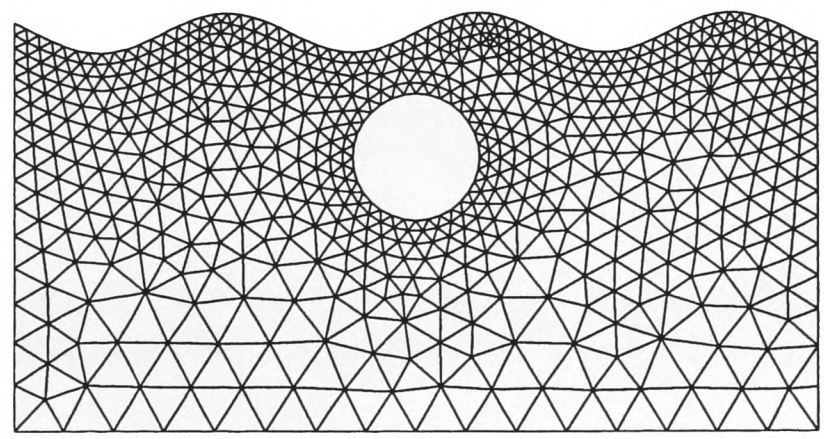

(*d*)

Figure 3.24 Stages in generation of a Voronoi mesh

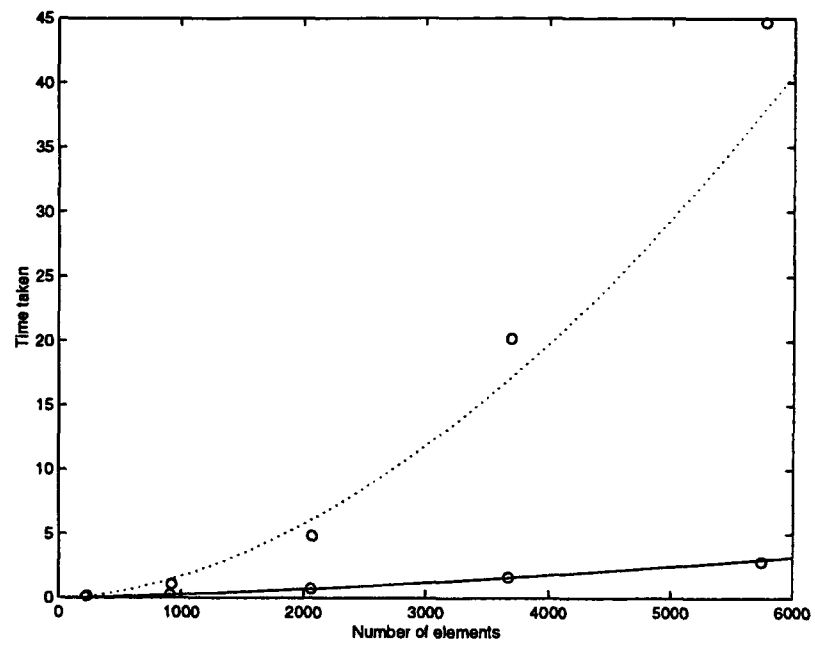

Figure 3.25 The time taken against number of elements for the advancing front and Voronoi (dashed line) methods for a square domain.

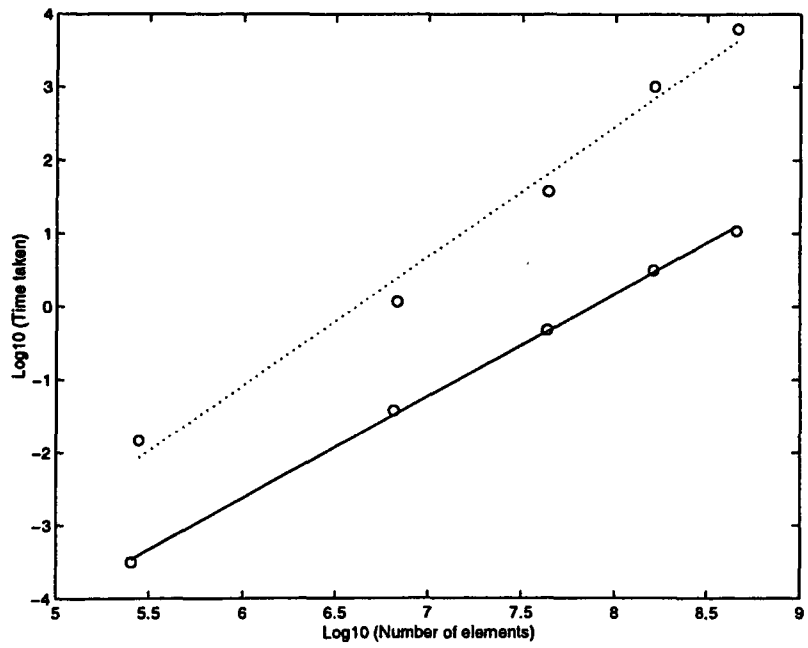

Figure 3.26 Log_{10} of time taken against log_{10} of the number of elements for the advancing front and Voronoi (dashed line) methods for a square domain.

CHAPTER 4

STANDARD FINITE ELEMENT FORMULATION

4.1 Introduction

A finite element program has been developed to investigate a number of two dimensional potential flow problems involving an inviscid liquid with a free surface. These problems include steep sloshing waves in a tank, steep progressive waves in a flume and the calculation of forces exerted on a horizontal cylinder, situated beneath a progressive wave. Results are presented in chapters six and seven.

The finite element program used is a modified version of that written by Dr G. X. Wu of University College London. The theory upon which the program is based is described by Wu and Eatock Taylor (1994).

The basic method used is as follows. The domain is discretised into triangular elements, with nodes at the vertices. The finite element program solves the Laplace equation to give the values of the potential at each node in the computational mesh, given the potential on the free surface and the velocities of the solid boundaries of the domain. Nodal potential values are used to calculate the fluid velocity at each node on the free surface, and the rate of change of potential with time on the free surface. These derivatives can then be used in a time stepping technique, to find the position of the free surface and the potential on the free surface. At each time step, remeshing is performed.

4.2 Governing Equations

Let there be a Cartesian coordinate system O - xz such that the origin is on the mean free surface and z is vertically upwards. The fluid is assumed to be inviscid and incompressible. Hence the flow is irrotational and a velocity potential ϕ exists which satisfies Laplace's equation,

$$\nabla^2\phi = 0 \quad . \tag{4.1}$$

Everywhere on the boundary, either the velocity potential or the normal velocity component is specified. The potential is specified at the free surface and at a Sommerfeld radiation boundary in the case of an infinite flume (see section 6.4). The velocity is specified at container walls, the surface of a body in the fluid and in cases where a wave generator is required. The boundary condition on the velocity boundary is,

$$\frac{\partial\phi}{\partial n} = f_2 \quad , \tag{4.2}$$

where f_2 is the normal velocity at the boundary and n is normal to the boundary and is directed out of the fluid domain.

The two-dimensional dynamic and kinematic free surface boundary conditions are, respectively,

$$g\eta + \frac{\partial\phi}{\partial t} + \frac{1}{2}\nabla\phi\cdot\nabla\phi = 0 \tag{4.3}$$

and

$$\frac{\partial \phi}{\partial z} = \frac{\partial \eta}{\partial t} + \frac{\partial \phi}{\partial x}\frac{\partial \eta}{\partial x} \quad , \tag{4.4}$$

where η is the free surface elevation vertically above the still water level, g is the acceleration due to gravity and t is time. The dynamic free surface boundary condition comes from Bernoulli's equation with relative pressure equal to zero. The kinematic condition is effectively a statement that particles on the free surface remain on the free surface.

Equations (4.3) and (4.4) are Eulerian as the time derivatives refer to changes in the variables at a fixed point in space. In order to update the free surface, the rates of change of the x and z coordinates of the free surface nodes are required, along with the rate of change of velocity potential at a free surface node; a Lagrangian approach or a mixed Euler-Lagrange approach can be adopted for this purpose.

In a Lagrangian approach, the time derivatives give the rate of change of a variable for a particle of fluid as it moves with the flow. In Lagrangian form, the dynamic boundary condition is

$$\frac{\mathrm{d}\phi}{\mathrm{d}t} = \frac{1}{2}\nabla\phi\cdot\nabla\phi - g\eta \quad . \tag{4.5}$$

From the definition of velocity potential,

$$\frac{\mathrm{d}x}{\mathrm{d}t} = \frac{\partial \phi}{\partial x} \quad \text{and} \quad \frac{\mathrm{d}z}{\mathrm{d}t} = \frac{\partial \phi}{\partial z} \tag{4.6}$$

everywhere in the domain.

Equations (4.5) and (4.6) give the Lagrangian formulation, allowing the nodes on the free surface to be moved as though they were fluid particles.

The nodes are moved only vertically when using the mixed Euler-Lagrange approach. The equations for updating the free surface position and velocity potential are:

$$\left.\frac{\partial x}{\partial t}\right|_{EL} = 0 \tag{4.7}$$

$$\left.\frac{\partial z}{\partial t}\right|_{EL} = \frac{\partial \phi}{\partial z} - \frac{\partial \phi}{\partial x}\frac{\partial \eta}{\partial x} \tag{4.8}$$

$$\left.\frac{\partial \phi}{\partial t}\right|_{EL} = -g\eta - \frac{1}{2}\nabla\phi\cdot\nabla\phi + \frac{\partial \phi}{\partial z}\frac{\partial z}{\partial t} \tag{4.9}$$

or in terms of the velocity components:

$$\left.\frac{\partial z}{\partial t}\right|_{EL} = w - u\frac{\partial \eta}{\partial x} \tag{4.10}$$

and

$$\left.\frac{\partial \phi}{\partial t}\right|_{EL} = -g\eta - \frac{1}{2}(u^2+w^2) + w\left.\frac{\partial z}{\partial t}\right|_{EL} \quad . \tag{4.11}$$

4.3 Finite Element Discretisation

4.3.1 Velocity Potential Calculation

An approximation to the velocity potential can be made in terms of the values of the potential ϕ_j at each node in the finite element mesh and corresponding linear shape functions $N_j(x,z)$.

The continuous velocity potential is therefore given by

$$\phi = \sum_{j=1}^{n} \phi_j N_j(x,z) \tag{4.12}$$

where n is the number of nodes. The use of shape functions is described by any standard finite element text, such as the one by Zienkiewicz (1994).

Each shape function is described by a different linear function in each element to which its node is attached. Therefore, for a particular element, the shape function for node i is:

$$N_i = \frac{\alpha_i + \beta_i x + \gamma_i z}{2\ \Delta} \tag{4.13}$$

where

$$\begin{aligned} \alpha_1 &= x_2 z_3 - x_3 z_2 \\ \alpha_2 &= x_3 z_1 - x_1 z_3 \\ \alpha_3 &= x_1 z_2 - x_2 z_1 \end{aligned} \tag{4.14}$$

and

$$\begin{aligned} \beta_1 &= z_2 - z_3 & \qquad \gamma_1 &= x_3 - x_2 \\ \beta_2 &= z_3 - z_1 & \qquad \gamma_2 &= x_1 - x_3 \\ \beta_3 &= z_1 - z_2 & \qquad \gamma_3 &= x_2 - x_1 \end{aligned} \tag{4.15}$$

and Δ is the area of the element. In the definitions of α, β and γ, the subscripts refer to the three nodes of the element.

A solution of the Laplace equation is required at each time step. This is achieved

using the Galerkin technique. The Laplace equation is multiplied by each shape function in turn and integrated over the entire domain (see Wu and Eatock Taylor 1995), resulting in n equations, as follows.

$$\int_R N_i \nabla^2 \phi \, dR = 0 \tag{4.16}$$

or

$$\int_R (\nabla \cdot (N_i \nabla \phi) - \nabla N_i \cdot \nabla \phi) \, dR = 0 \tag{4.17}$$

or

$$\int_S N_i \frac{\partial \phi}{\partial n} \, dS - \int_R \nabla N_i \cdot \nabla \phi \, dR = 0 \tag{4.18}$$

where S is the boundary of R.

Replacing ϕ with its approximation and the potential derivative with f_2, gives

$$\int_R \nabla N_i \cdot \sum_{j=1}^{n} \phi_j \nabla N_j dR|_{j \in S_1} = -\int_R \nabla N_i \cdot \sum_{j=1}^{n} \phi_j \nabla N_j dR|_{j \in S_1} + \int_{S_2} N_i f_2 dS \tag{4.19}$$

where S_1 and S_2 are the surfaces on which the potential and its normal derivative are specified, respectively. The terms on the right hand side of the equation can be calculated from the boundary conditions. The equation can be written in matrix form,

$$[A]\{\phi\} = \{B\} \quad , \tag{4.20}$$

where $\{\phi\}$ is the vector of the nodal velocity potentials and the coefficients of $[A]$ and $\{B\}$ are given by

$$A_{ij} = \int_R \nabla N_i \cdot \nabla N_j \, dR \tag{4.21}$$

or

$$\begin{aligned} A_{ij} &= 1 \quad \text{if } i=j \text{ and } i \in S_1 \\ A_{ij} &= 0 \quad \text{if } (i \in S_1 \text{ or } j \in S_1) \text{ and } i \neq j \end{aligned} \tag{4.22}$$

and

$$B_i = -\int_R \nabla N_i \cdot \sum_{j=1}^{n} \phi_j \nabla N_j \, dR \Big|_{j \in S_1} + \int_{S_2} N_i \, f_2 \, dS \tag{4.23}$$

or

$$B_i = \phi_i \quad \text{if } i \in S_1 \tag{4.24}$$

Integrating the above terms, using the linear shape functions, yields algebraic expressions for equations (4.21) and (4.23):

$$A_{ij} = \sum_e \frac{\beta_i \beta_j + \gamma_i \gamma_j}{4 \Delta} \tag{4.25}$$

and

$$B_i = \sum_e \left(-\sum_{j=1}^{k} \left(\frac{\phi_j \, (\beta_i \beta_j + \gamma_i \gamma_j)}{4 \Delta} \right) \Bigg|_{j \in S_1} + \frac{|z_i - z_I| \, (f_2)_i}{2} \Bigg|_{i, I \in S_2} \right) \tag{4.26}$$

where k is the number of nodes linked to node i, and I is a node on S_2, linked to node i. The second term in equation (4.26) is valid when S_2 is a vertical boundary. In both equations the first summation is performed over all elements, e, attached to the node or nodes in question.

Solution of the matrix equation provides an approximation to the velocity potential. The matrix equations are solved at each time step by reordering the nodes to minimise the bandwidth of the matrix, and then applying Gaussian elimination.

4.3.2 Velocity Calculation

Three different techniques have been used for calculating the fluid velocity, given the solution for the velocity potential, ϕ. The first two techniques (proposed by Eatock Taylor *et al.* (1996) and Wu and Eatock Taylor (1994)) are suitable for either structured or unstructured meshes. The third (suggested by the present author) is only applicable to structured meshes.

(a) Least Squares Method

Each node, P_j, is connected to p other nodes by the finite element mesh. Let the position vector of the k^{th} node relative to P_j be denoted by $\boldsymbol{l}^k$. The x and z components of $\boldsymbol{l}^k$ divided by the magnitude of $\boldsymbol{l}^k$, i.e $dx/d\boldsymbol{l}^k$ and $dz/d\boldsymbol{l}^k$, are written l_x^k and l_z^k. The rate of change of potential with distance between two nodes is related to the horizontal and vertical velocity components u and w by the following equation.

$$u l_x^k + w l_z^k = \frac{\partial \phi}{\partial l^k} \tag{4.27}$$

When a node is connected to more than two other nodes, there will be more equations available than unknowns. This is resolved by using the least squares method. The expression,

$$E = \sum_{k=1}^{p} \left(\frac{\partial \phi}{\partial l^k} - u l_x^k - w l_z^k \right)^2 \tag{4.28}$$

is minimised by solving the following matrix equation:

$$\begin{pmatrix} \sum_{k=1}^{p} l_x^k l_x^k & \sum_{k=1}^{p} l_x^k l_z^k \\ \sum_{k=1}^{p} l_x^k l_z^k & \sum_{k=1}^{p} l_z^k l_z^k \end{pmatrix} \begin{Bmatrix} u \\ w \end{Bmatrix} = \begin{Bmatrix} \sum_{k=1}^{p} l_x^k \frac{\partial \phi}{\partial l^k} \\ \sum_{k=1}^{p} l_z^k \frac{\partial \phi}{\partial l^k} \end{Bmatrix} \tag{4.29}$$

This gives estimates for u and w. This method is described by Eatock Taylor *et al.* (1996).

(b) Galerkin Method

As described by Wu and Eatock Taylor (1994), the Galerkin method approximates the relationship

$$\nabla \phi = \boldsymbol{u} \tag{4.30}$$

in the form

$$\int_R N_i (\nabla \phi - \boldsymbol{u}) \, dR = \mathbf{0} \quad . \tag{4.31}$$

Substituting expressions for the velocity components and the potential in terms of linear shape functions leads to the following matrix equations for the horizontal and vertical velocity components, u and w:

$$[C]\{u\} = [D_1]\{\phi\} \quad \text{and} \quad [C]\{w\} = [D_2]\{\phi\} \quad . \tag{4.32}$$

The coefficients of $[C]$, $[D_1]$ and $[D_2]$ are given by

$$C_{ij} = \int_R N_i N_j dR \tag{4.33}$$

$$D_{1\,ij} = \int_R N_i \frac{\partial N_j}{\partial x} dR \tag{4.34}$$

and

$$D_{2\,ij} = \int_R N_i \frac{\partial N_j}{\partial z} dR \quad . \tag{4.35}$$

N_i and N_j refer to the same linear functions as before. Therefore, after integration, the following algebraic expressions are obtained:

$$\begin{aligned} C_{ij} &= \sum_e \frac{\Delta}{6} \qquad \text{if } i = j \\ C_{ij} &= \sum_e \frac{\Delta}{12} \qquad \text{if } i \neq j \end{aligned} \tag{4.36}$$

$$D_{1\,ij} = \sum_e \frac{\beta_j}{6} \tag{4.37}$$

and

$$D_{2\,ij} = \sum_e \frac{\gamma_j}{6} \quad . \tag{4.38}$$

(c) Higher Order Velocity Calculation

For the structured meshes used in this thesis, each node on the free surface will have a number of nodes vertically beneath it with the same x coordinate. This allows a better

estimate of the vertical velocity to be made using the nodal values of potential at a series of nodes below the free surface.

In the following analysis, subscript 1 refers to the free surface node, and subscripts 2 and higher refer to subsequent nodes beneath the free surface node. The z coordinate is measured upwards from the free surface and is expressed as a multiple of the spacing Δz between the top two nodes.

$$\begin{aligned} \Delta z &= z_2 - z_1 \\ z_1 &= 0 \\ z_2 &= \Delta z \\ z_3 &= \alpha \Delta z \\ z_4 &= \beta \Delta z \end{aligned} \qquad . \tag{4.39}$$

If the vertical variation of the potential is assumed to be quadratic, then it can be written as:

$$\phi = A\left(\frac{z}{\Delta z}\right)^2 + B\left(\frac{z}{\Delta z}\right) + C \tag{4.40}$$

Putting in values for z and ϕ at three nodes (one on the free surface and two nodes vertically beneath) gives three simultaneous equations, which can be expressed in matrix form:

$$\begin{bmatrix} 0 & 0 & 1 \\ 1 & 1 & 1 \\ \alpha^2 & \alpha & 1 \end{bmatrix} \begin{Bmatrix} A \\ B \\ C \end{Bmatrix} = \begin{Bmatrix} \phi_1 \\ \phi_2 \\ \phi_3 \end{Bmatrix} \tag{4.41}$$

or

$$\begin{Bmatrix} A \\ B \\ C \end{Bmatrix} = \frac{1}{\alpha(1-\alpha)} \begin{bmatrix} -\alpha+1 & \alpha & -1 \\ \alpha^2-1 & -\alpha^2 & 1 \\ \alpha(1-\alpha) & 0 & 0 \end{bmatrix} \begin{Bmatrix} \phi_1 \\ \phi_2 \\ \phi_3 \end{Bmatrix} \quad . \tag{4.42}$$

Differentiating equation (4.40) and using $z = z_1 = 0$, gives a value for the vertical velocity at the free surface.

$$w = \frac{\partial \phi}{\partial z} = \frac{2Az_1}{\Delta z^2} + \frac{B}{\Delta z} = \frac{B}{\Delta z} \quad . \tag{4.43}$$

Therefore:

$$w = \frac{(1-\alpha^2)\phi_1 + \alpha^2\phi_2 - \phi_3}{\alpha(\alpha-1)\,\Delta z} \quad . \tag{4.44}$$

If the nodes are evenly spaced, then α equals 2 and the velocity is:

$$w = \frac{-3\phi_1 + 4\phi_2 - \phi_3}{2\,\Delta z} \quad . \tag{4.45}$$

A higher order formula, assuming variation to the power of four, and using five nodes can be obtained by a similar procedure. For the case of evenly spaced nodes:

$$w = \frac{-25\phi_1 + 48\phi_2 - 36\phi_3 + 16\phi_4 - 3\phi_5}{12\,\Delta z} \quad . \tag{4.46}$$

4.3.3 Updating the free surface

Knowing the velocity and potential on the free surface, the solution can be advanced forward in time by updating the position of the free surface and the potential on the free surface using

either the Lagrangian approach or the mixed Euler-Lagrange method. In the case of the Euler-Lagrange method, there is no need to alter the x coordinates.

The finite difference procedure used to advance the solution in the time domain is the fourth order Runge-Kutta technique. Let the values of x, z and ϕ at node i and time step k, be denoted x_i^k, z_i^k and ϕ_i^k. The equations below show how the updated nodal value z_i^{k+1} is calculated. Similar equations apply for x_i^{k+1} and ϕ_i^{k+1}.

$$z_i^A = z_i^k + \frac{1}{2}\left(\frac{dz}{dt}\right)_i^k \Delta t \tag{4.47}$$

$$z_i^B = z_i^k + \frac{1}{2}\left(\frac{dz}{dt}\right)_i^A \Delta t \tag{4.48}$$

$$z_i^C = z_i^k + \left(\frac{dz}{dt}\right)_i^B \Delta t \tag{4.49}$$

and

$$z_i^{k+1} = z_i^k + \frac{\Delta t}{6}\left(\left(\frac{dz}{dt}\right)_i^k + 2\left(\frac{dz}{dt}\right)_i^A + 2\left(\frac{dz}{dt}\right)_i^B + \left(\frac{dz}{dt}\right)_i^C\right) \quad . \tag{4.50}$$

The labels A, B and C refer to intermediate states. At time step k, the finite element program will calculate values for $(dx/dt)_i^k$, $(dz/dt)_i^k$ and $(d\phi/dt)_i^k$. Equations similar to (4.47) are used to find x_i^A, z_i^A and ϕ_i^A which define the intermediate state A. The finite element program again finds the derivatives, this time corresponding to state A. The process is repeated using equations (4.48) and (4.49). The result is four estimates of the derivatives for each variable within the time interval. These estimates are used to give x_i^{k+1}, z_i^{k+1} and ϕ_i^{k+1} on the free surface in the way shown in (4.50). For each Runge-Kutta time step, the finite element

program solves the Laplace equation four times.

When the Lagrange approach is used, the free surface nodes are moved from their original x positions. After many time steps, this may lead to nodes on the free surface becoming too close together in some places, and too far apart in others. In order to prevent this from happening, the nodes are returned to their original x coordinates, and new values of y and ϕ are assigned using linear interpolation.

4.3.4 Smoothing

In some cases, in order to prevent instabilities developing, smoothing is performed on the free surface. This involves assigning new values to the nodal values of z and ϕ based on a weighted average of the previous nodal values. Two smoothing formulae have been used, one based on five nodes:

$$z_i^* = \frac{1}{16}\left(-z_{i-2} + 4z_{i-1} + 10z_i + 4z_{i+1} - z_{i+2}\right) \tag{4.51}$$

and the other based on a template of seven nodes:

$$z_i^* = \frac{1}{32}\left(-z_{i-3} + 9z_{i-1} + 16z_i + 9z_{i+1} - z_{i+3}\right) \quad . \tag{4.52}$$

Similar formulae apply for ϕ.

4.4 Accuracy Tests

At each time step, the finite element program returns values for the horizontal and vertical velocity components on the free surface. By applying the method to a case where the solution is known, an estimate of the accuracy of the solution for the velocities can be obtained. For the following results, a rectangular domain was used, with a height of 1 unit, and a length of 8 units. A structured mesh was used. Using a coordinate system originating at the top left corner of the domain, the potential was specified on the boundaries of the domain by:

$$\phi = \frac{\sin(kx)\ \cosh(k(d+z))}{\cosh(kd)} \quad . \tag{4.53}$$

Therefore, the horizontal and vertical velocities on the free surface are given by:

$$u = \frac{\partial \phi}{\partial x} = k\ \cos(kx) \tag{4.54}$$

and

$$w = \frac{\partial \phi}{\partial z} = k\ \sin(kx)\ \tanh(kd) \quad . \tag{4.55}$$

Subtraction of the finite element solution from the values obtained by the above formulae, gives a smooth sinusoid like curve, the maximum value of which, gives a measure of the error of the finite element calculation. The error is a smooth sinusoid in this case because of the sinusoidal boundary condition and the regular nature of the mesh.

Table 4.1 shows the errors for four different velocity calculation techniques and seven different cases. In the standard case, the mesh had 16 elements vertically and 128

horizontally; the vertical spacing of the nodes was uniform; the wavelength λ was half the length of the tank, meaning $k = \pi/2$ and $\lambda = 4$. The table indicates the way in which the other cases differ from the standard case. When the vertical node spacing is not uniform, r gives the ratio of the node spacing at the bottom to that at the top, for the 16 by 128 mesh.

Two values have been given for the error in the horizontal velocity with the Galerkin method. This is because the error at the ends is much greater than the rest of the free surface. The error at the ends using the Galerkin method is about twice that for the least squares method. The Galerkin method's error at the middle is at least 100 times smaller than the least squares error. The least squares and Galerkin methods give very similar results for the error in the vertical velocity, with the least squares value usually being slightly larger. The higher order technique was used to obtain two further estimates of the vertical velocity, one using 3 nodes, the other 5 nodes. The 3 node calculation gives errors between 10 and 30 times smaller than the least squares method. The 5 node method gives errors smaller by a further factor of between 3 and 4. This demonstrates that the higher order technique gives more accurate results.

For the least squares method, doubling the number of nodes on the free surface halves the error for the horizontal velocity. Doubling the number of nodes vertically approximately halves the error for the vertical velocity. Varying the vertical distribution of nodes, such that the nodes are closer together nearer the free surface, reduces the error on the vertical velocity, but has little effect on the horizontal velocity.

Table 4.2 shows the ratio of the error to the amplitude of the velocity for the four

calculation methods and the same seven cases. For the least squares and the Galerkin methods, the fractional error halves as the wavelength doubles. For the higher order calculations, the fractional error approximately divides by four as the wavelength doubles. This suggests that for larger wavelengths, the higher order technique has an even greater advantage over the other two.

4.5 Final Remarks

The standard finite element method has been described in this chapter. The higher order velocity calculation works very well and the possibility of extending the idea to unstructured meshes should be investigated; the method would clearly be more complicated for an unstructured mesh. Results for this method applied to a number of test cases are presented in chapters six and seven. In the next chapter, the formulation of the sigma transformation version of the finite element method is described.

Table 4.1 Errors for velocity at free surface

	Least Squares		Galerkin			3 nodes	5 nodes
	u	w	u (end)	u	w	w	w
16x128	4.00e-2	6.70e-2	6.87e-2	7.28e-5	6.11e-2	5.42e-3	1.18e-3
32x256	2.01e-2	3.37e-2	3.39e-2	9.22e-6	3.04e-2	1.40e-3	2.91e-4
32x128	4.21e-2	2.76e-2	6.77e-2	4.80e-5	4.67e-2	1.83e-3	7.25e-4
$r = 4$	4.18e-2	2.37e-2	6.73e-2	4.58e-5	4.47e-2	6.86e-4	2.88e-4
$r = 16$	3.95e-2	6.06e-3	6.65e-2	3.61e-5	3.94e-2	1.32e-3	3.36e-3
$\lambda = 2$	0.170	0.272	0.283	1.21e-3	0.256	4.46e-2	1.08e-2
$\lambda = 8$	7.92e-3	1.37e-2	1.69e-2	3.63e-6	1.34e-2	4.94e-4	1.04e-4

Table 4.2 Ratio of errors to velocity amplitude at free surface

	Amplitude		Least Squares		Galerkin		3 nodes	5 nodes
	u	*w*	*u*	*w*	*u*	*w*	*w*	*w*
16x128	1.57	1.44	0.026	0.047	4.6e-5	0.042	3.8e-3	8.2e-4
32x256	1.57	1.44	0.013	0.023	5.9e-6	0.021	9.7e-4	2.0e-4
32x128	1.57	1.44	0.027	0.019	3.1e-5	0.032	1.3e-3	5.0e-4
$r = 4$	1.57	1.44	0.027	0.017	2.9e-5	0.031	4.8e-4	2.0e-4
$r = 16$	1.57	1.44	0.025	4.2e-3	2.3e-5	0.027	9.2e-4	2.3e-3
$\lambda = 2$	3.14	3.13	0.054	0.087	3.9e-4	0.082	0.014	3.5e-3
$\lambda = 8$	0.785	0.515	0.010	0.027	4.6e-6	0.026	9.6e-4	2.0e-4

CHAPTER 5

SIGMA TRANSFORMED FINITE ELEMENT FORMULATION

5.1 Introduction

The standard finite element program, described in chapter four, uses Cartesian coordinates for its formulation. As the free surface changes its position with time, a new mesh is required at each time step. By using an alternative sigma transformed coordinate system it is possible to use the same mesh at each time step, thus eliminating the need for remeshing. As before, the problem is that of potential flow of an inviscid liquid with a free surface.

5.2 Mathematical Formulation

5.2.1 Velocity Potential Calculation

Instead of using the Cartesian coordinates x and z, two new coordinates X and σ are used. They are defined as follows:

$$X = \frac{x}{l} \tag{5.1}$$

$$\sigma = \frac{z+d}{h} \tag{5.2}$$

where l is the length of the domain, d is the depth of the domain (the distance from the sea bed to the mean free surface) and h is the distance of the sea bed to the actual free surface

(see figure 5.1). Thus, X is the new horizontal component and σ is the new vertical component. This coordinate transformation is known as the sigma transform; it was originally proposed by Phillips (1957) for meteorological forecasting and has subsequently been used by Mellor and Blumberg (1985) to model oceanic and coastal flows and by Stansby and Lloyd (1995) for shallow water flow.

X and σ are non dimensional. It can be useful to define non-dimensional variables for time and velocity potential also:

$$T = \left(\frac{g}{l}\right)^{\frac{1}{2}} t \tag{5.3}$$

$$\Phi = \frac{\phi}{g^{\frac{1}{2}} l^{\frac{3}{2}}} . \tag{5.4}$$

For convenience, the present method uses $T = t$ and $\Phi = \phi$, in order to keep the transformed equations reasonably simple.

Derivatives with respect to the new variables need to be found. Hence,

$$\frac{\partial}{\partial x} = \frac{\partial X}{\partial x}\frac{\partial}{\partial X} + \frac{\partial \sigma}{\partial x}\frac{\partial}{\partial \sigma} + \frac{\partial T}{\partial x}\frac{\partial}{\partial T} \quad . \tag{5.5}$$

Therefore, after substitution

$$\frac{\partial}{\partial x} = \frac{1}{l}\frac{\partial}{\partial X} + \left(\frac{\partial \sigma}{\partial x}\right)\frac{\partial}{\partial \sigma} \quad . \tag{5.6}$$

Also

$$\frac{\partial}{\partial z} = \frac{\partial X}{\partial z}\frac{\partial}{\partial X} + \frac{\partial \sigma}{\partial z}\frac{\partial}{\partial \sigma} + \frac{\partial T}{\partial z}\frac{\partial}{\partial T} \quad , \tag{5.7}$$

Therefore

$$\frac{\partial}{\partial z} = \frac{1}{h}\frac{\partial}{\partial \sigma} \quad . \tag{5.8}$$

Finally,

$$\frac{\partial}{\partial t} = \frac{\partial X}{\partial t}\frac{\partial}{\partial X} + \frac{\partial \sigma}{\partial t}\frac{\partial}{\partial \sigma} + \frac{\partial T}{\partial t}\frac{\partial}{\partial T} \tag{5.9}$$

which becomes, again after substitution

$$\frac{\partial}{\partial t} = \frac{\partial}{\partial T} + \left(\frac{\partial \sigma}{\partial t}\right)\frac{\partial}{\partial \sigma} \quad . \tag{5.10}$$

The derivative of σ with respect to x is found from

$$\frac{\partial \sigma}{\partial x} = \frac{\partial}{\partial x}\left(\frac{z+d}{\eta+d}\right) = \frac{1}{h}\left(\frac{\partial d}{\partial x}\right) - \frac{z+d}{h^2}\left(\frac{\partial \eta}{\partial x} + \frac{\partial d}{\partial x}\right) \tag{5.11}$$

$$= \frac{1}{h}\left(\frac{\partial d}{\partial x}\right) - \frac{\sigma}{h}\left(\frac{\partial \eta}{\partial x} + \frac{\partial d}{\partial x}\right) = \frac{1}{h}\left(-\sigma\frac{\partial \eta}{\partial x} + (1-\sigma)\frac{\partial d}{\partial x}\right) \tag{5.12}$$

$$= \frac{1}{lh}\left(-\sigma\frac{\partial \eta}{\partial X} + (1-\sigma)\frac{\partial d}{\partial X}\right) \tag{5.13}$$

where η is the free surface elevation measured from the mean free surface ($h = \eta + d$). Similarly,

$$\frac{\partial \sigma}{\partial t} = \frac{1}{h}\left(-\sigma\frac{\partial \eta}{\partial T} + (1-\sigma)\frac{\partial d}{\partial T}\right). \tag{5.14}$$

Equations (4.20) to (4.24) are still valid for the domain transform formulation, but the integrations of equations (4.21) and (4.23) are performed differently.

A general term in the finite element matrix is of the form (see equation (4.21)),

$$\int_R \nabla N_i \cdot \nabla N_j \, \mathbf{d}R \, . \tag{5.15}$$

In order to integrate this using the new variables, the Jacobian is required.

$$\frac{\partial(X,\sigma)}{\partial(x,z)} = \begin{vmatrix} \frac{\partial X}{\partial x} & \frac{\partial X}{\partial z} \\ \frac{\partial \sigma}{\partial x} & \frac{\partial \sigma}{\partial z} \end{vmatrix} = \begin{vmatrix} \frac{1}{l} & 0 \\ \frac{\partial \sigma}{\partial x} & \frac{1}{h} \end{vmatrix} = \frac{1}{lh} \quad , \tag{5.16}$$

and so

$$\mathbf{d}R = \mathrm{d}x\mathrm{d}z = lh \; \mathrm{d}X\mathrm{d}\sigma. \tag{5.17}$$

The gradient operator can be expressed in terms of the new coordinates.

$$\nabla = \begin{pmatrix} \frac{\partial}{\partial x} \\ \frac{\partial}{\partial z} \end{pmatrix} = \begin{pmatrix} \frac{1}{l}\frac{\partial}{\partial X} + \left(\frac{\partial \sigma}{\partial x}\right)\frac{\partial}{\partial \sigma} \\ \frac{1}{h}\frac{\partial}{\partial \sigma} \end{pmatrix}. \tag{5.18}$$

The general form of a linear shape function is:

$$N_i = \frac{\alpha_i+\beta_i X+\gamma_i \sigma}{2\Delta} \tag{5.19}$$

where α_i, β_i and γ_i are as defined previously (see equations (4.14) and (4.15)) with X and σ instead of x and z respectively.

The spatial derivatives of the shape functions become:

$$\frac{\partial N_i}{\partial X} = \frac{\beta_i}{2\Delta} \quad \text{and} \quad \frac{\partial N_i}{\partial \sigma} = \frac{\gamma_i}{2\Delta} \; . \tag{5.20}$$

Therefore, for a particular element,

$$\nabla N_i \cdot \nabla N_j = \frac{1}{l^2}\frac{\beta_i\beta_j}{4\Delta^2} + \frac{1}{l}\left(\frac{\partial \sigma}{\partial x}\right)\frac{(\beta_i\gamma_j+\beta_j\gamma_i)}{4\Delta^2} + \left(\frac{\partial \sigma}{\partial x}\right)^2\frac{\gamma_i\gamma_j}{4\Delta^2} + \frac{1}{h^2}\frac{\gamma_i\gamma_j}{4\Delta^2} \; . \tag{5.21}$$

Integrating equation (5.21) over the element gives:

$$\frac{1}{l}\frac{\beta_i\beta_j}{4\Delta^2}\int_e h \, dX d\sigma + \frac{\beta_i\gamma_j+\beta_j\gamma_i}{4\Delta^2}\int_e \left(\frac{\partial \sigma}{\partial x}\right) h \, dX d\sigma \tag{5.22}$$

$$+ \frac{l\gamma_i\gamma_j}{4\Delta^2}\int_e \left(\frac{\partial \sigma}{\partial x}\right)^2 h \, dX d\sigma + \frac{l\gamma_i\gamma_j}{4\Delta^2}\int_e \frac{1}{h} dX d\sigma \; . \tag{5.23}$$

The integral expressions can be evaluated using a cubic numerical formula which takes four values of the integrated function in each element. Formulas such as the one used here, were first derived by Hammer *et al.* (1956); a comprehensive list of higher-order formulas were derived by Cowper (1973). The x coordinates at which the function is evaluated are given

by,

$$x_A = \frac{(x_1+x_2+x_3)}{3} \tag{5.24}$$

$$x_B = 0.6x_1 + 0.2x_2 + 0.2x_3 \tag{5.25}$$

$$x_C = 0.2x_1 + 0.6x_2 + 0.2x_3 \tag{5.26}$$

and

$$x_D = 0.2x_1 + 0.2x_2 + 0.6x_3 \quad . \tag{5.27}$$

The subscripts 1, 2 and 3 refer to three nodes of an element. The σ coordinates are given by similar expressions.

The integral of the general function, f,

$$\int_e f \, dX d\sigma \tag{5.28}$$

has the following cubic approximation:

$$\frac{\Delta}{48}(-27f_A + 25f_B + 25f_C + 25f_D) \tag{5.29}$$

where f_A is evaluated at x_A and σ_A and so on.

Summation over each element yields the required integration over the entire domain.

The surface integral from the untransformed version of the finite element program (see equation (4.23)) can be expressed in terms of the transformed variables, provided the surface

is vertical, as

$$\int_{S_2} N_i f_2 \, dS = \int_0^1 N_i f_2 h \, d\sigma \tag{5.30}$$

where f_2 is the outward velocity of the fluid at the surface.

Equation (5.30) is evaluated by the following analytical expression:

$$\sum_e \left(\frac{|\sigma_i - \sigma_I| (f_2)_i}{2} \Big|_{i, I \in S_2} \right) \tag{5.31}$$

where S_2 refers to the part of the boundary where the velocity is imposed, and I refers to a node on S_2, linked to node i.

With the coefficients known, the matrix equation can then be solved by Gaussian elimination as before.

5.2.2 Velocity Calculation

Once the potential is known at all the nodes, the potential gradients can be found in the X and σ directions using one of the velocity calculation methods described in Chapter 4. The horizontal and vertical velocities, u and w can be found from the potential gradients.

$$u = \frac{\partial \phi}{\partial x} = \frac{1}{l} \frac{\partial \phi}{\partial X} + \frac{1}{lh} \left(-\sigma \frac{\partial \eta}{\partial X} + (1 - \sigma) \frac{\partial d}{\partial X} \right) \frac{\partial \phi}{\partial \sigma} \tag{5.32}$$

$$w = \frac{\partial \phi}{\partial z} = \frac{1}{h}\frac{\partial \phi}{\partial \sigma} . \tag{5.33}$$

These velocities are used to find the rates of change of the free surface elevation and free surface potential with time. The free surface kinematic boundary condition gives:

$$\frac{\partial \eta}{\partial T} = w - u\frac{\partial \eta}{\partial x} = w - \frac{u}{l}\frac{\partial \eta}{\partial X} . \tag{5.34}$$

For the case of a uniform sea bed,

$$\frac{\partial \sigma}{\partial t} = -\frac{\sigma}{h}\frac{\partial \eta}{\partial t} . \tag{5.35}$$

Therefore,

$$\frac{\partial \Phi}{\partial T} = \frac{\partial \Phi}{\partial t} + \frac{\sigma}{h}\frac{\partial \eta}{\partial t}\frac{\partial \Phi}{\partial \sigma} = \frac{\partial \Phi}{\partial t} + \sigma\frac{\partial \eta}{\partial t}\frac{\partial \Phi}{\partial z} . \tag{5.36}$$

At the free surface, $\sigma = 1$. Using the dynamic free surface boundary condition gives,

$$\frac{\partial \Phi}{\partial T} = -g\eta - \frac{1}{2}(u^2+w^2) + \frac{\partial \eta}{\partial T}w \tag{5.37}$$

where the rate of change of η was calculated in equation (5.34).

The rates of change of free surface elevation and free surface potential are used to step these values forward in time, using a Runge-Kutta scheme, as described in Chapter 4. The option of smoothing is again available to prevent instabilities developing.

5.3 Final Remarks

The finite element method using a domain transformation has been described. The concept of a sigma transformed finite element technique is original and has been devised by the author. The results of applying this method to a number of test cases are given in chapters six and seven.

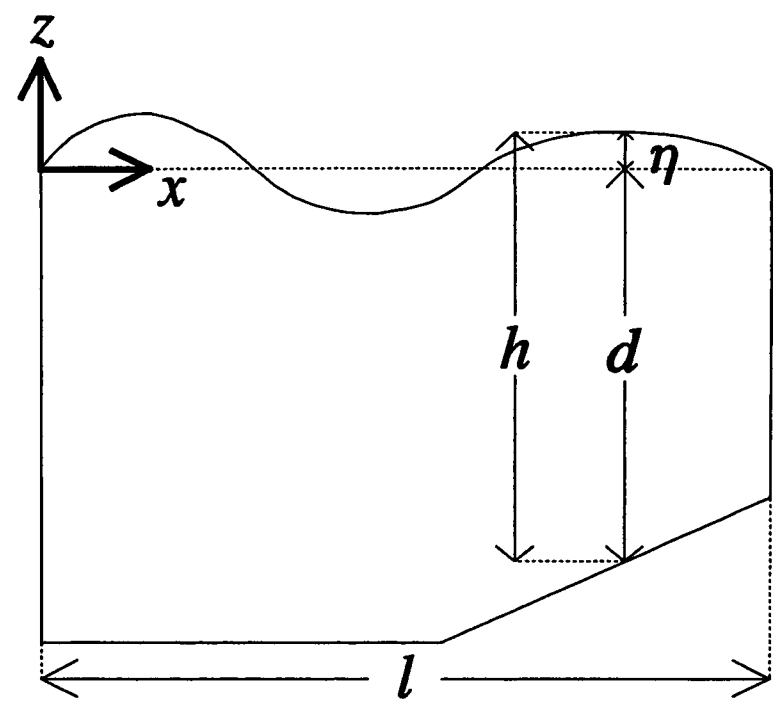

(*a*) Physical domain

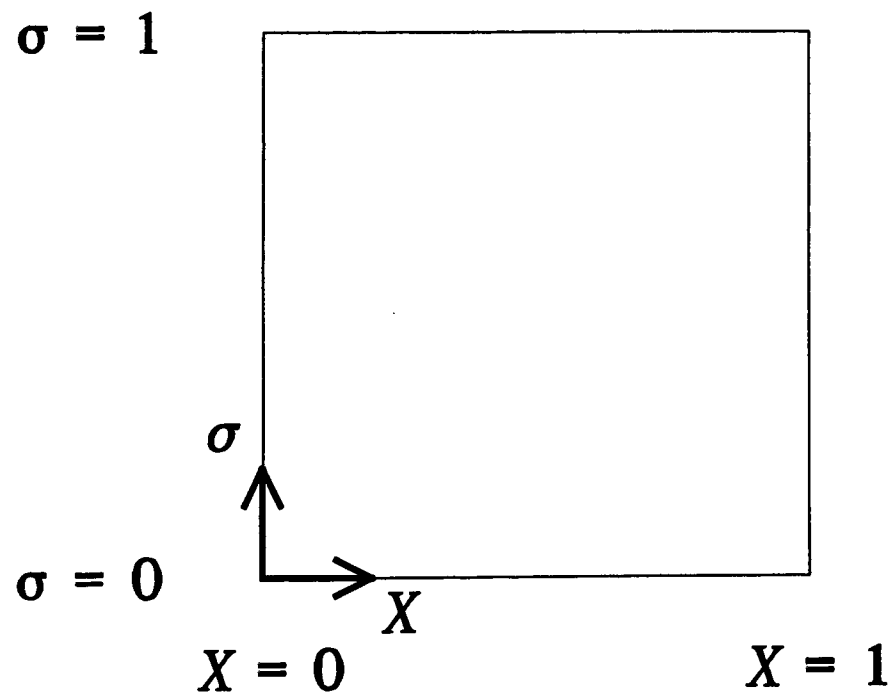

(*b*) Transformed domain

Figure 5.1 The sigma transformation

CHAPTER 6

RESULTS OF TEST CASES WITHOUT A CYLINDER

6.1 Introduction

The standard finite element method described in chapter four and the sigma transform version described in chapter five have been used to generate results for a number of test cases. In all the cases, an inviscid liquid with a free surface is modelled.

In this chapter, cases with no cylinder in the flow will be examined. The results will be compared with analytical solutions and with other numerical results. In chapter seven, the results for forces on a horizontal submerged cylinder due to a progressive wave will be presented.

Four cases are examined in this chapter: a standing wave in a fixed rectangular tank; sloshing waves in a base-excited tank; a travelling regular wave with no cylinder in the flow; and a focused wave.

In generating the following results, the mean water depth d, and the gravitational acceleration, g have both been set equal to 1. This is equivalent to supposing that distance and time have been non-dimensionalised in the following way.

$$x' = \frac{x}{d} \qquad z' = \frac{z}{d} \qquad \text{and} \qquad t' = t\left(\frac{g}{d}\right)^{\frac{1}{2}} \tag{6.1}$$

where the dashed symbols are the new non-dimensional variables. The non-dimensional

velocity potential is:

$$\phi' = \frac{\phi}{d(gd)^{\frac{1}{2}}} \quad . \tag{6.2}$$

6.2 Standing Wave

For this problem, the standing wave is generated in a liquid initially at rest. Although, the term standing wave is used here, it should be noted that when the wave amplitude is large relative to the wavelength, the free surface profile will not remain sinusoidal and will not be precisely the same from one wave period to the next. The initial sinusoidal free surface elevation is such that one wavelength fits the length of the tank. The initial elevation is given by

$$\eta = a\cos(2\pi x/l) \tag{6.3}$$

where η is the elevation, a is the wave amplitude, l is the length of the tank and x is the horizontal distance from the origin, which is located at the mean free surface position at the far left of the domain (see figure 6.1).

For all the results presented in this section, the length of the tank, l, equals 2. Structured meshes are used; the nodes are spaced uniformly horizontally, and the node spacing at the free surface is four times as small as at the base of the tank. Figure 6.2 shows a mesh at $t = 0$ for an initial wave amplitude of 0.1; there are 32 elements along the length of the tank, and the liquid is 16 elements deep. Unless stated otherwise, the Higher-Order velocity calculation is used to calculate the vertical velocity component, and the Least-Squared-Method is used to calculate the horizontal component (both velocity components are

needed regardless of the method chosen to update the free surface); smoothing is not applied and as a mixed Euler-Lagrange formulation is used, interpolation is not needed to bring the nodes back to their original horizontal position. The reason for the choices is explained below.

To prevent the solution becoming unstable, the free surface may be smoothed, as described in section 4.3.4. The effect of smoothing every time step has been investigated for the case of a 32 by 16 mesh, with a time step of 0.1, and an initial wave amplitude of 0.1, using the standard finite element method described in chapter 4. It can be seen in figure 6.3 that smoothing does not cause significant damping, but does reduce the troughs and most of the peaks relative to the case without the smoothing. Smoothing clearly has an undesirable effect on the solution and is not used, unless necessary.

When recalculating the free surface, a Lagrangian approach can be adopted, whereby the nodes are moved horizontally and vertically and then repositioned at their original horizontal location using interpolation. Alternatively, a mixed Euler-Lagrangian method can be used, where the nodes are only moved vertically. It has been found that when the method with interpolation is used, smoothing is needed to prevent instabilities building up; therefore a case with interpolation and smoothing is compared to the equivalent case without interpolation but with smoothing, referred to in the previous paragraph. The standard finite element scheme is used. The two time histories at the centre of the tank are plotted in figure 6.4. Interpolation causes damping, with a significant reduction in the amplitude of oscillation with time and a phase shift. The mixed Euler-Lagrange method is therefore used for all subsequent simulations.

Three different velocity calculations were described in section 4.2.2. These were the Galerkin method, the Least-Squared method and the Higher-Order method (the version using 5 nodes has been used throughout). Figure 6.5 shows the time history of the free surface elevation at the centre of the tank for these three methods, using the standard finite element method. The initial non-dimensional wave amplitude is 0.1. A mesh with 32 elements along the length and 16 elements deep is used; the time step is 0.05. The Galerkin and the Least-Squares method exhibit a phase shift relative to the Higher Order method, with the phase shift of Least-Squares method being greater. None of the methods exhibit a reduction in the amplitude of oscillation. The Galerkin and the Least- Squares method both require smoothing at every time step to prevent the solution becoming unstable. However, even with smoothing, by t = 80, both methods have begun to exhibit instability with very erratic free surface profiles. After a few oscillations, the Galerkin and Least-Squares method show a noticeable asymmetry in the free surface profile, with the oscillation amplitude at one end of the tank being greater than the other; it is likely that this asymmetry is due to the asymmetry of the computational mesh, as seen in figure 6.2. This is all in agreement with the test results presented in section 4.3, which suggested that the Higher-Order method was more accurate. The Higher-Order method is therefore used for all subsequent results in this section.

When the initial amplitude of the free surface elevation is small, it can be expected that the subsequent oscillation at the centre of the tank will be perfectly sinusoidal. This is indeed the behaviour shown by the finite element model. For all discussions of the small amplitude case, the initial amplitude, a, equals 0.001. Convergence tests have been performed, where it has been seen how the results depend on the mesh density and the time step. For a mesh 32 elements long and 16 elements deep, three time steps have been used:

0.2, 0.1 and 0.05. As the time step is decreased, the results do not change greatly; the results of the smaller two time steps are virtually identical. Therefore, for this mesh, the most appropriate time step is 0.1.

Two further simulations of the small amplitude standing wave were done, with smaller time steps and finer meshes. The time history of the free surface elevation at the centre of the tank, for these two cases, together with the coarser mesh result with a time step of 0.1, can be seen in figure 6.6. There is virtually no difference between the three cases up to a time of 20, and even after 80 time units have elapsed, only a very small phase difference is evident between the coarser mesh result and the other two. There is no distinguishable difference between the two finer mesh results.

The first order analytical solution for the free surface elevation at the centre of the tank is

$$\eta_1 = -a\cos(\omega_2 t) \tag{6.4}$$

where $\omega_2 = (g\ k_2 \tanh(k_2\ d))^{1/2}$ and $k_2 = 2\ \pi\ /\ l$.

This analytical solution between times 70 and 80 is plotted in figure 6.7, along with the intermediate of the three finite element results plotted in figure 6.6. There is very close agreement; the amplitude is virtually identical and the phase difference is virtually zero. Therefore, the finite element method gives very good results when the amplitude is small.

Now, the case of a standing wave with a larger amplitude ($a = 0.1$) is examined. As with the small amplitude case, convergence tests have been performed. The standard finite

element method is used with a 32 by 16 mesh; it can be seen in figure 6.8 that there is no visible difference in the result when the time step is decreased from 0.1 to 0.05. Therefore, a time step of 0.1 is the most appropriate for this mesh. Figure 6.9 shows this result with those obtained using two finer meshes. The finer mesh results are slightly different to the coarse mesh result and virtually identical to each other. Therefore, for this case, there is no advantage in having a mesh resolution higher than 64 by 32.

The simulations described in the previous paragraph were repeated using the sigma transform version of the finite element method and the results presented in figure 6.10. The results are almost identical to those in figure 6.9.

The finite element results for the standing wave case can be compared to an analytical solution which is accurate up to second order. The second order contribution to the wave elevation at the centre of the tank (see Wu and Eatock Taylor (1994) for the derivation) is

$$\eta_2 = \frac{1}{8g}\left(2(\omega_2 a)^2\cos(2\omega_2 t) + \frac{a^2}{\omega_2^2}(g^2k_2^2+\omega_2^4) - \frac{a^2}{\omega_2^2}(g^2k_2^2+3\omega_2^4)\cos(\omega_4 t)\right) \quad (6.5)$$

where $\omega_4 = (g\ k_4\ \tanh(k_4\ d))^{1/2}$ and $k_4 = 4\ \pi/\ l$.

The total wave elevation is given by

$$\eta_t = \eta_1 + \eta_2 \quad (6.6)$$

Figure 6.11 shows the converged sigma transform result and the standard finite element result for the same mesh and time step, together with the analytical solution given

by equation (6.6). The two finite element results can be seen to be identical to each other and to match the analytical solution quite closely. Both numerical solutions remain in phase with each other, whereas the analytical solution has a clear phase difference. It is much greater than the phase difference seen in the small amplitude case. The non-linearities due to the greater amplitude cause a change in the oscillation frequency. Denoting the frequency predicted by linear theory as ω_0, the ratio ω/ω_0 is found to be 0.990. When the amplitude, a is increased to 0.13, the ratio ω/ω_0 becomes 0.982. This compares with a value of $\omega/\omega_0 =$ 0.978 found by Greaves *et al.* (1997) using a similar finite element method with quadtree meshes. Tsai and Jeng (1994) obtained a value of 0.979 using a truncated double Fourier series for the velocity potential which satisfied Laplace's equation; they developed an algorithm involving Newton's iteration method to calculate the unknown Fourier coefficients.

Greaves *et al.* (1997) simulated the same standing wave problem, as did Chern *et al.* (1999) who used a pseudospectral method. They both produced figures which can be compared to figure 6.11. All three results are found to be very similar. In all cases the first and second peaks are virtually identical to the second order solution, the third peak is larger and the fourth peak is smaller. For the troughs, the first is deeper, the second is shallower, the third is similar and the fourth is deeper.

A series of wave profiles is shown in figure 6.12 for the case where the initial wave amplitude is small (a = 0.001). For this and subsequent figures, the labels for each time are positioned next to the peak or trough of the corresponding wave profile. As time varies from 0 to 1.6, the trough in the centre of the tank approaches a peak. At all times, the free surface profile remains sinusoidal, and non-linear effects are unimportant. There all two well defined

nodes at $x = 0.5$ and $x = 1.5$, where there is no variation in elevation. The equivalent plot is shown in figure 6.13 for a case with large amplitude ($a = 0.1$). Here, after half a period, the free surface is clearly not sinusoidal, with the peak at the centre being narrower than the small amplitude case. At a later time (see figure 6.14), the central peak is even narrower, and the subsequent trough is wider than it would be for a sinusoidal shape. The fixed positions of nodes that existed for the small amplitude case are not present with the larger amplitude, as can be seen in figure 6.13 and to a much greater extent in figure 6.14. This result agrees closely with that of Chern *et al.* (1999).

Two typical velocity vector plots are shown in figures 6.15 and 6.16 for the case where $a = 0.1$. As the central peak grows, fluid flows in from the sides (see figure 6.15). The reverse is true as the peak falls, as seen in figure 6.16.

Double standing waves have been simulated, i.e. waves where the wavelength of the initial sinusoidal free surface elevation is half the width of the tank. Here, the initial elevation is given by

$$\eta = a\cos(4\pi x/l) \quad . \tag{6.7}$$

Again, the length of the tank, l, equals 2. The standard finite element program with a structured mesh of the kind described previously was used for all these simulations. Figure 6.17 shows the time history of the central free surface elevation for the case where $a = 0.05$, meaning the ratio of the amplitude to wavelength is the same as for the single wave. The results for three different meshes are plotted. The coarsest mesh is 128 elements by 32 elements; the other two have either twice as many elements vertically or twice as many

horizontally. For the coarsest mesh, a time step of 0.1 was used; for the other two, the time step was halved. All the results are extremely similar, so the 128 by 32 mesh with a time step of 0.1 was used for the other simulations.

Figure 6.18 shows the time history of the free surface elevation at the centre of the tank for the case where $a = 0.03$. Figure 6.19 displays the free surface space profiles at five times from $t = 26$ to $t = 30$ for the same case. Both these figures can be compared with those presented by Chern *et al.* (1999). Good agreement is found. Free surface profiles for the larger amplitude case of $a = 0.05$ are given in figure 6.20. The crests are clearly sharper and the troughs are shallower than for the smaller amplitude case shown in figure 6.19.

6.3 Sloshing Wave Motion in a Base-excited tank

Sloshing wave motion can be generated in a rectangular tank by oscillating the entire tank horizontally. For small amplitudes this is equivalent to imposing the same horizontal velocity on both the side walls. If the frequency of this imposed motion is similar to the natural sloshing frequency then resonance will occur.

For all simulations in this section, the standard finite element method was used with a structured mesh; the mesh is 64 elements by 32 elements and the time step is 0.1; the length of the tank, l equals 2. The initial free surface elevation is zero. The velocity of the side walls is given by

$$u = a\omega\sin(\omega t)$$

where ω is the frequency of oscillation and a is the effective amplitude of oscillation of the side walls.

Wu *et al.* (1998) derive the linear solution for this problem. It is presented again here. The free surface elevation is given by

$$\eta = \eta_1 + \eta_2 \quad , \tag{6.9}$$

where

$$\eta_1 = \frac{a}{g}\left(x\omega^2 + \sum_{n=0}^{\infty} C_n \omega \sin(k_n x)\right)\sin(\omega t) \tag{6.10}$$

and

$$\eta_2 = -\frac{a}{g}\sum_{n=0}^{\infty} \omega_n\left(C_n + \frac{H_n}{\omega^2}\right)\sin(k_n x)\sin(\omega_n t) \tag{6.11}$$

and

$$k_n = \frac{(2n+1)\pi}{b}\ , \quad \omega_n = (gk_n\tanh(k_n d))^{\frac{1}{2}}\ , \quad H_n = \frac{(-1)^n 4\omega^3}{bk_n^2}\ , \quad C_n = \frac{H_n}{\omega_n^2 - \omega^2}\ .$$

Using the above equations, the natural sloshing frequency ω_0 is found to be 1.2. Figure 6.21 displays the time history of the free surface elevation at the left hand wall of the tank, where the excitation frequency, $\omega = 0.999\omega_0$. The amplitude of oscillation steadily increases with time. The analytical solution given by equation (6.9) is also plotted in figure 6.21; close agreement is observed. The frequency, ω, is increased to $1.1\omega_0$; figure 6.22 shows the time history of the elevation. Now, the elevation increases in amplitude to begin with,

decreases to zero, and then starts to increase again. Again, this is in close agreement with the analytical solution. A series of wave profiles is given in figure 6.23, corresponding to $\omega = 0.999\omega_0$. Figures 6.21 to 6.23 show very close agreement to the results presented by Chern *et al.* (1999)

6.4 Travelling Wave without Cylinder

The finite element program has been used to simulate a travelling free surface wave in an infinitely long flume. The wave is generated by imposing the horizontal component of the velocity at the left hand boundary of the domain. This velocity varies sinusoidally with time and can be constant with respect to depth or can vary to match approximately the expected vertical variation of the velocity. According to linear wave theory, for a travelling wave of height H, frequency, ω and wavenumber, k, the free surface elevation, η, is

$$\eta = \frac{H}{2}\cos(kx-\omega t) \tag{6.12}$$

where x is the horizontal distance and t is the time.

The horizontal component of the velocity, u, is given by

$$u = \frac{H\omega}{2}\frac{\cosh(k(d+z))}{\sinh(kd)}\cos(\omega t) \tag{6.13}$$

in which d is the still water depth.

Therefore, in most cases, the velocity imposed at the left hand boundary was chosen to have the form,

$$u = U_0 \frac{\cosh(k(d+z))}{\sinh(kd)} \cos(\omega t) \tag{6.14}$$

where U_0 is a measure of the size of the input wave and k is related to the frequency, ω, by the dispersion relation:

$$\omega^2 = gk \tanh(kd) \quad . \tag{6.15}$$

The waves need to be absorbed at the far end of the tank. There are a number of approaches to wave absorption, many of which are reviewed by Romate (1992). Orlanski (1976) proposed the use of a Sommerfeld radiation condition, which was subsequently used by Chan (1977) and others. Another method is to use an absorbing layer which can be implemented by adding a damping term to the field equation or the free surface condition; the former kind of absorbing layer was used by Israeli and Orszag (1981), and the latter by Baker *et al.* (1981) and Cointe *et al.* (1990). Here, the Sommerfeld radiation condition is used, together with an absorbing layer implemented by modifying the free surface boundary conditions.

In the absorbing layer, the time derivatives of the free surface elevation, η, and the velocity potential, ϕ, are modified by the following formulas:

$$\frac{\partial \eta}{\partial t} = \frac{\partial \eta_p}{\partial t} - S\omega \left(\frac{x - x_s}{x_e - x_s} \right)^3 \eta_p \tag{6.16}$$

and

$$\frac{\partial \phi}{\partial t} = \frac{\partial \phi_p}{\partial t} - S\omega \left(\frac{x - x_s}{x_e - x_s} \right)^3 \phi_p \tag{6.17}$$

where x_s and x_e are the x coordinates of the start and end of the absorbing layer respectively, the subscript p denotes the values predicted by the finite element model; the coefficient S is chosen to be 3, as this value has been found to give good results.

The Sommerfeld boundary condition is implemented at the right hand end of the tank. For a wave travelling in the x direction, the Sommerfeld boundary condition is:

$$\frac{\partial \phi}{\partial t} = -c \frac{\partial \phi}{\partial x} \tag{6.18}$$

where c is the wave celerity. For a linear wave, the wave celerity is:

$$c = \frac{\omega}{k} = \frac{\sqrt{gk \tanh(kd)}}{k} \quad . \tag{6.19}$$

Therefore, at the right hand boundary, the velocity potential can be stepped forward in time, using equation (6.18). Figure 6.24 shows the various components of the model.

For the standard case, against which the other simulations will be compared, the tank is of non-dimensional length 40 and depth 1; the wave frequency, ω, is 2, meaning it is effectively a deep water case; the wavelength, λ, is approximately 1.57 ($\pi/2$); the absorbing layer is 10 units long. The mesh is structured, 640 elements long, and 16 elements deep; therefore the horizontal distance between two nodes is 0.0625. The node spacing varies vertically, such that the node spacing at the free surface is four times as small as at the bottom of the tank (see figure 6.25). The Runge-Kutta non-dimensional time step is 0.15707 ($\pi/20$); therefore there are 20 time steps per wave period. The Higher-Order velocity calculation is used, based on 5 nodes. The free surface is updated using the mixed Euler-

Lagrange method. No smoothing is performed on the free surface. The input velocity at the left hand boundary is multiplied by a ramp function. This will be explained further below.

When the Lagrange approach with linear interpolation is used, a significant loss in wave amplitude with distance occurs. Similarly, when smoothing is performed on the free surface at every time step, there is a loss in amplitude. However, in the standard case, described in the previous paragraph, the wave propagates with no loss of amplitude. Figure 6.26 shows the free surface profile after 60 wave periods (i.e. $t = 60\ \pi$), for a small amplitude wave, with U_0 equal to 0.01. From $x = 30$ onwards, there is the absorbing layer, which accounts for the amplitude of the wave reducing to zero after that point. Because of the effect on the wave amplitude, linear interpolation is not used and smoothing is avoided wherever possible. Figure 6.27 shows an enlarged view, in the range $x = 20$ to $x = 30$.

The three methods of calculating the velocity are compared. Again, the comparison is made for a small amplitude wave, with U_0 equal to 0.01. For all three results, smoothing was performed every time step, as otherwise the Galerkin and Least-Squares methods give unstable solutions. With the Higher-Order velocity calculation, the amplitude of the wave remains constant. The Galerkin method results in a significant drop in amplitude and the Least-Squares method results in a significant gain in amplitude. These undesirable alterations in amplitude can be made less severe by decreasing the time step, but cannot be eliminated completely. As with the standing wave, the Higher-Order method gives the best results.

The sensitivity of the result to time step and mesh density has been examined. Figure 6.28 shows the effect of halving the time step from $\pi/20$ to $\pi/40$. The results remain very

similar, with the amplitude being constant with respect to distance. There is a very small reduction in wavelength which can be detected by comparing the expanded space profiles in the range $x = 25$ to $x = 30$. In figure 6.29, the space profiles for a number of different meshes are displayed. As in the previous figure, the profiles only differ in their wavelength, and the difference is still very small.

The standard finite element result is compared with an analytical solution in figure 6.30. The analytical solution is a second order Stokes wave, although in this case, the second order component is negligible, due to the small amplitude. The solutions can be seen to agree closely.

The reason for imposing a velocity which varies with depth at the left boundary can be seen by examining figure 6.31, which compares the wave profile of the standard case to that obtained when a velocity $u = U_0 \cos(\omega t)$ is imposed (u does not vary with depth). The wave amplitude of the latter case is approximately twice that of the standard case. This is in agreement with wavemaker theory as described by Dean and Dalrymple (1984). More importantly, the wave profile is not uniform close to the wave generator; there is clear increase in wave amplitude due to the standing wave, or evanescent component. This deviation from a pure travelling wave is undesirable and is larger for cases with a higher wave frequency, so a velocity which varies with depth is imposed in all other cases.

The effect on the initial wave front of the ramp function can be seen in figure 6.32; the space profile at two times is shown. The ramp function is initially 0 and gradually increases up to 1 as time elapses. Therefore, if the imposed velocity is multiplied by the

ramp function, the amplitude will gradually increase from 0 up to the steady state value,

$$u_r = u \tanh(t/20) \tag{6.20}$$

where u_r is the velocity with the ramp function and u is given by equation (6.14). Without the ramp function, the wave amplitude increases up to a peak, before reducing again to a steady value; with the ramp function, there is no peak. The ramp function reduces the possibility of spurious oscillations developing.

Figure 6.33 demonstrates the effectiveness of the absorbing layer. A simulation with a tank length of 80 is compared to that with the standard length of 40. It can be seen that for the case with the longer tank, the wave has not yet reached the far end of the tank, so no reflections will have occurred. For the shorter tank, the waves have entered the absorbing layer (which starts at $x = 30$). There is virtually no difference in the wave profiles to the left of the absorbing layer of the shorter tank, as can be seen in the lower of the two graphs in figure 6.33. This suggests that the absorbing layer is successful in preventing reflections.

The progression of the wave along the tank is shown in figure 6.34. The wave front travels at the group velocity. This example is effectively a deep water case, with the dispersion relation approximating closely to,

$$\omega^2 = gk \tag{6.21}$$

therefore,

$$c = \frac{\omega}{k} = \frac{2}{4} = 0.5 \tag{6.22}$$

and

$$c_g = \frac{d\omega}{dk} = \frac{g}{2\omega} = \frac{\omega}{2k} = 0.25 \qquad (6.23)$$

where c is the phase velocity and c_g is the group velocity. The group velocity is therefore half the phase velocity and in this example equals 0.25. Every 10π time units, the wave front advances 10π x 0.25 = 2.5π = 7.85 distance units; this can be seen in figures 6.34.

Another representation of the evolution of the free surface with time is given in figure 6.35. The space profile is shown at time intervals of twice the wave period. At a given point in the domain, the wave amplitude grows until it reaches a steady value. Once the steady value has been reached, the wave profile remains virtually identical from one wave period to the next.

Figure 6.36 shows the time history of the free surface profile at the centre of the tank. The amplitude grows gradually before reaching a constant value. The lower of the two graphs shows that the wave amplitude is virtually identical from one wave period to the next.

Larger amplitude simulations have been performed using the sigma transformed finite element program. As with the small amplitude simulations, the wave frequency, ω, is 2. All other parameters are as for the standard case, described earlier, except that for the very highest amplitudes, smoothing is performed to prevent instabilities. The results are compared with Stokes fifth order theory for regular travelling waves, as derived by Fenton (1985). For deep water, the expression for the free surface elevation is:

$$\begin{aligned}\eta(x,t) = {} & (\epsilon - 0.375\epsilon^3 - 1.099\epsilon^5)\cos(k(x-ct)) \\ & + (0.5\epsilon^2 + 0.333\epsilon^4)\cos(2k(x-ct)) \\ & + (0.375\epsilon^3 + 0.773\epsilon^5)\cos(3k(x-ct)) \\ & + (0.333\epsilon^4)\cos(4k(x-ct)) \\ & + (0.326\epsilon^5)\cos(5k(x-ct))\end{aligned} \tag{6.24}$$

where the wave steepness, $\varepsilon = kH/2$ (k is the wave number and H is the wave height).

Twelve simulations have been performed, with the amplitude of the imposed velocity, U_0, ranging from 0.125 to 0.3, being incremented by 0.125 for each successive run. For each simulation, the surface profile at a typical time has been analysed to obtain the Fourier components at the wavelength and half the wavelength. These two components are plotted in figure 6.37(*a*), together with the corresponding curve for Stokes fifth order theory. It can be seen that there is very close agreement up to a value of 0.06 for component 1. A small degree of divergence between the two curves can be seen as the amplitude increases further. Figure 6.37(*b*) shows the wavenumber plotted against component 1 for the finite element results and Stokes fifth order theory. The wave number decreases as the wave amplitude increases, corresponding to an increase in the wavelength. Again, there is close agreement between the finite element results and Stokes theory up to the very highest amplitudes where the two curves become noticeably different.

Two examples of free surface profiles are shown in figure 6.38. The upper graph is for a steepness of 0.37; good agreement between the finite element solution and Stokes fifth order theory can be seen. The lower graph is for a steepness of 0.43. This is very close to the theoretical limiting steepness of 0.44. In this case the agreement is not as good, with some asymmetry visible in the wave crest.

6.5 Focused Wave

A focused wave can be generated by imposing a velocity which contains a number of different frequency components. Here, the velocity at the wave maker is given by the following equation:

$$u = \frac{U_0}{1001} \frac{\cosh(k_p(d+z))}{\sinh(k_p d)} \sum_{n=1}^{1001} e^{\left(-\left(\frac{k_n - k_p}{8}\right)^2\right)} \cos(-k_n x_f - \omega_n (t - t_f)) \qquad (6.25)$$

where

$$k_n = 0.04(n-1) - 16$$
$$\omega_n = \sqrt{g k_n \tanh k_n d} \quad .$$

The peak value of the wave number, $k_p = 4$. The position and time of linear focus are given by x_f and t_f. Here, $x_f = 12.5$ and $t_f = 75.4$.

Results using the standard finite element program were obtained, with the measure of velocity amplitude, U_0, ranging from 0.5 to 4.0. The resulting wave focused as a peak. By changing the sign of U_0, a further set of runs were performed with a focused trough. All other physical and numerical parameters were as for the standard case described previously. In figure 6.39, results are presented for U_0 = 1.0, 2.0, 3.0 and 4.0 and the corresponding trough cases. The free surface profile is shown at the time of focus, *i.e.* the time of maximum (or in the case of the trough, minimum) free surface elevation. Also shown, are the envelopes of maximum elevation over time for the peak case and minimum elevation for the trough case.

For $U_0 = 1.0$, the focus occurs at a distance of 12.5 from the wavemaker, as predicted by linear theory. For the larger amplitudes, the focus event occurs progressively further away from the wavemaker and at a later time. Up to $U_0 = 3.0$, the crest focus and the corresponding trough focus, occur at the same position and time, even though non-linearities are present; the crest has a larger magnitude than the trough in each case. For $U_0 = 4.0$, non-linear effects are very great; the crest and trough focus are no longer in line with each other.

Figure 6.40 plots the maximum value of $(c\text{-}t)/2$ over all time and space against the wave generator velocity amplitude, U_0 (c is the elevation of the crest and t is the elevation of the trough). This gives a good indication of the level of non-linearity of the result. For U_0 higher than 2.0, a deviation from the linear relationship can be seen.

6.5 Conclusions

The finite element method has been used to simulate four potential flow problems involving a free surface. For all four cases, good results have been obtained. The standing wave results have been found to agree well with the analytical solution of Wu and Eatock Taylor (1994) and the numerical results of Chern *et al.* (1999). The results for the base-excited tank correspond closely to the analytical solution of Wu *et al.* (1998) and the numerical results of Chern *et al.* (1999). The travelling wave was simulated with little or no loss of amplitude, and with great consistency in the wave profile over many time periods. The wave absorption technique was found to be very effective. The large amplitude waves were in close agreement with Stokes fifth order theory. Focused waves with significant non-linearity were simulated. The sigma transformed finite element method was found to produce results

virtually indistinguishable from the standard method. However, the run times were slightly longer due to the extra computation needed to calculate the matrix coefficients. The next chapter presents results for the force on a horizontal submerged cylinder due to a travelling wave.

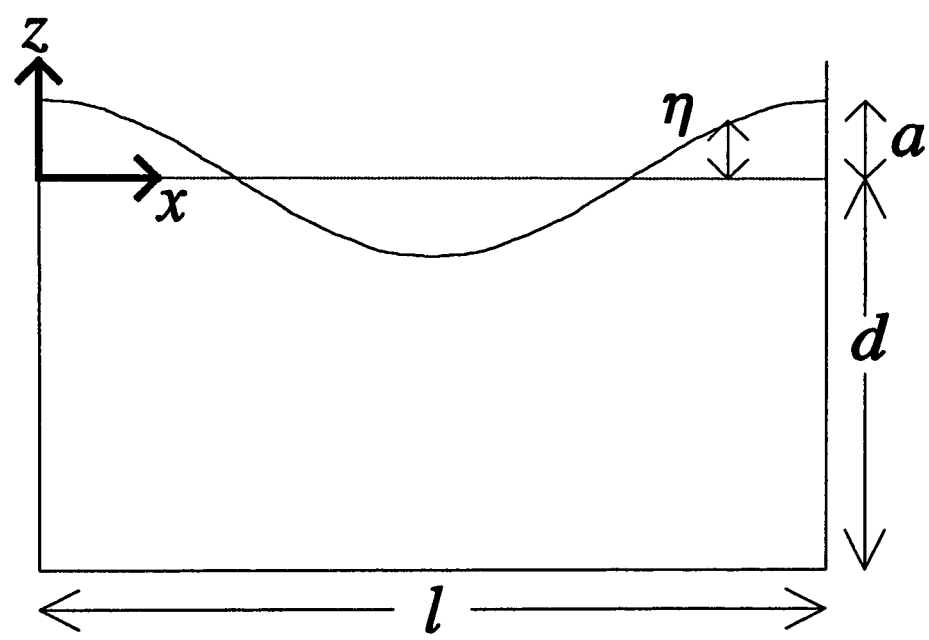

Figure 6.1

Model diagram for standing wave case

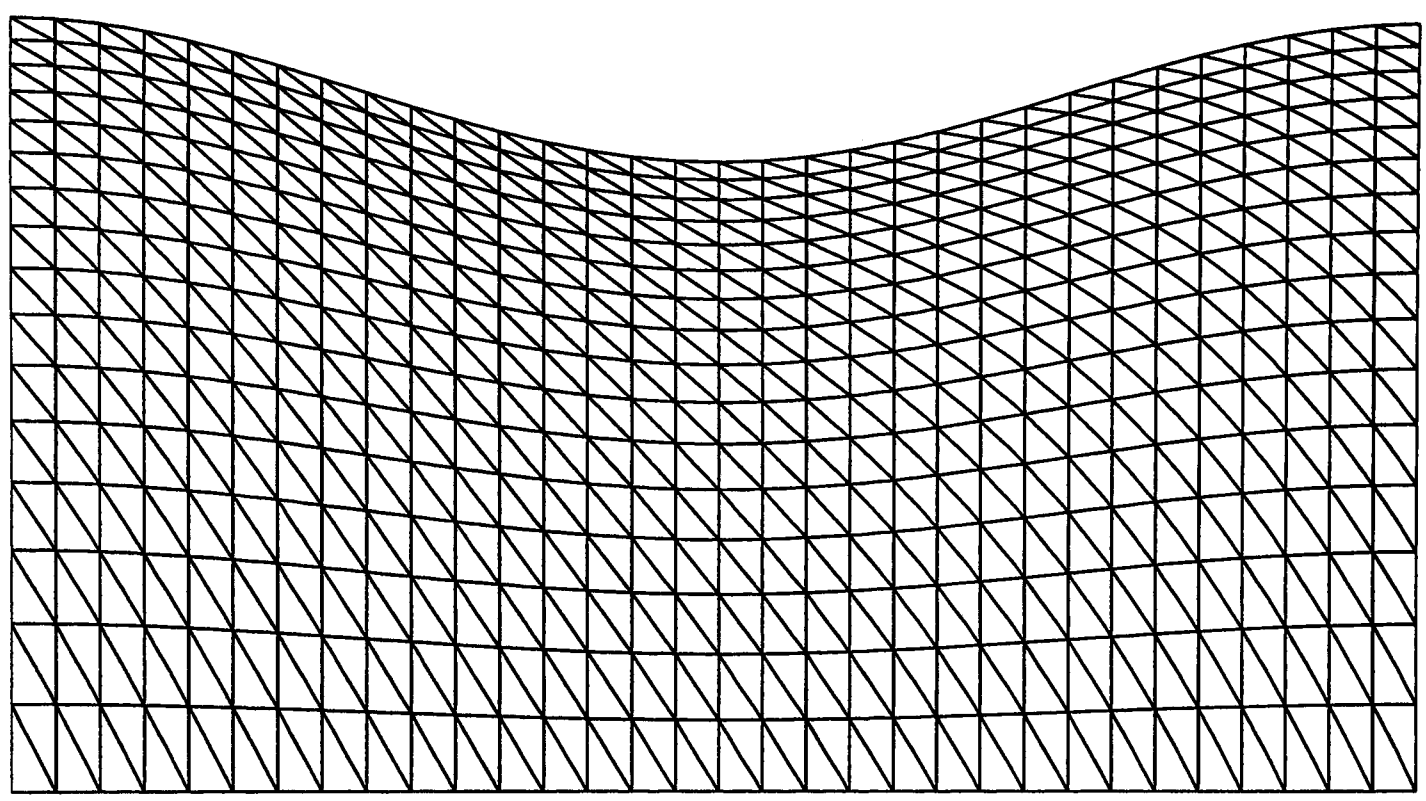

Figure 6.2

Structured mesh at start of simulation

32 elements long and 16 elements deep

Initial wave amplitude, $a = 0.1$

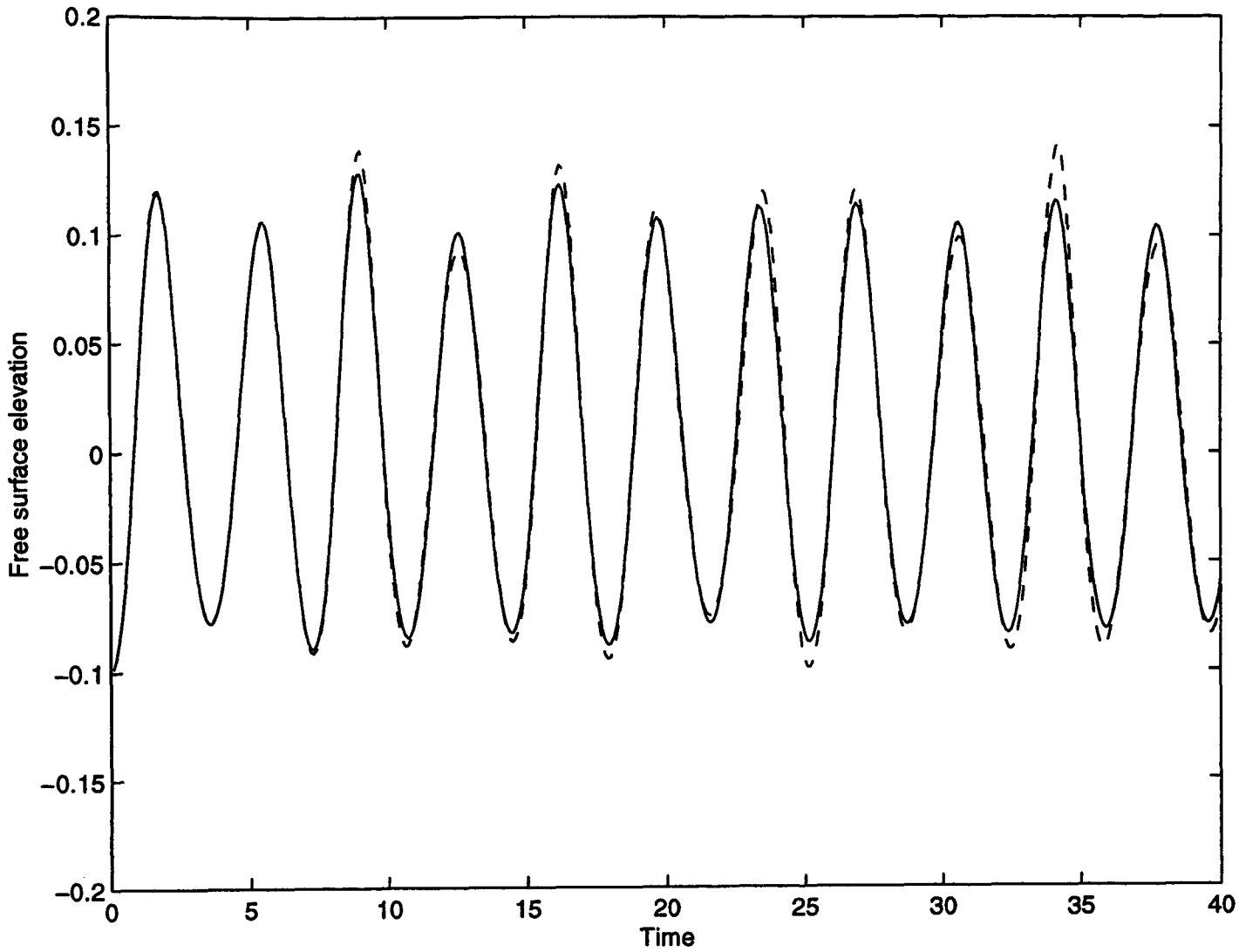

Figure 6.3 Time history of the free surface elevation at the centre of the tank

Standing wave with initial amplitude, $a = 0.1$

Time step = 0.1 Mesh is 32 elements long and 16 elements deep

Dashed line : Without smoothing
Solid line : With smoothing

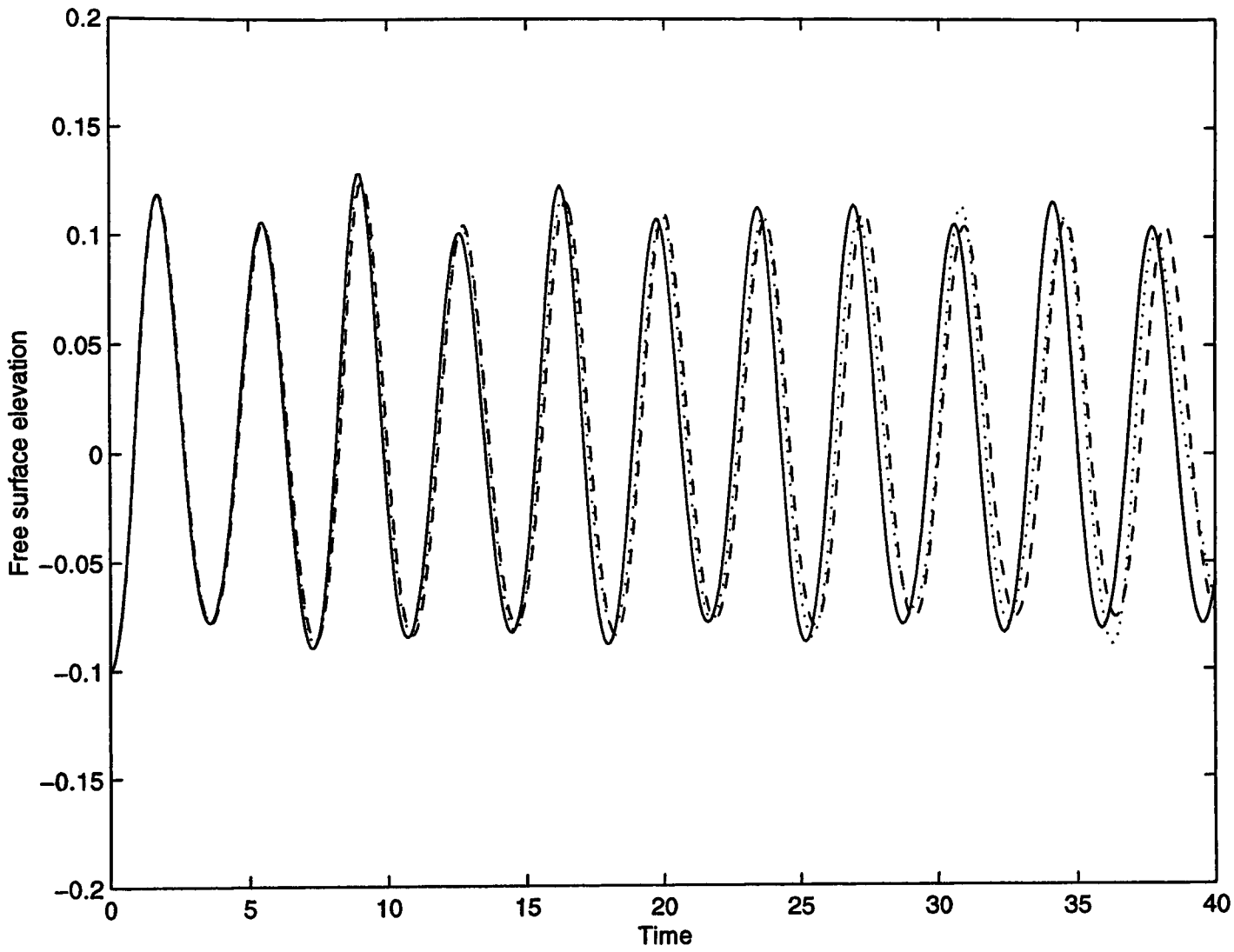

Figure 6.5 Time history of the free surface elevation at the centre of the tank

Standing wave with initial amplitude, $a = 0.1$

Time step = 0.05 Mesh is 32 elements long and 16 elements deep

Dotted line : Galerkin velocity calculation
Dashed line : Least Squares velocity calculation
Solid line : Higher Order velocity calculation

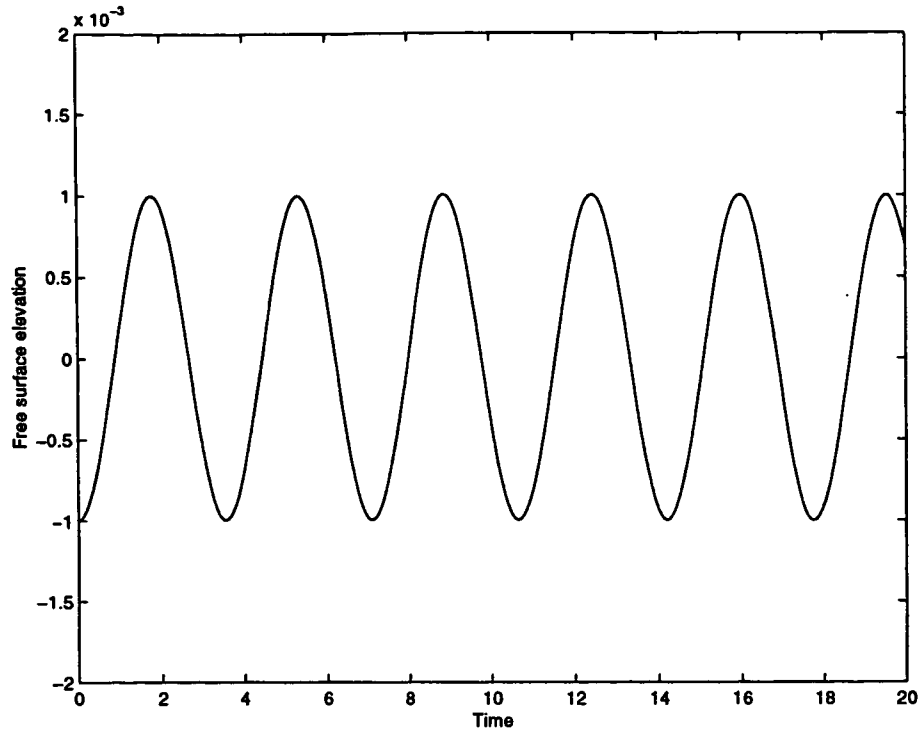

(*a*) Time history: t = 0 to 20

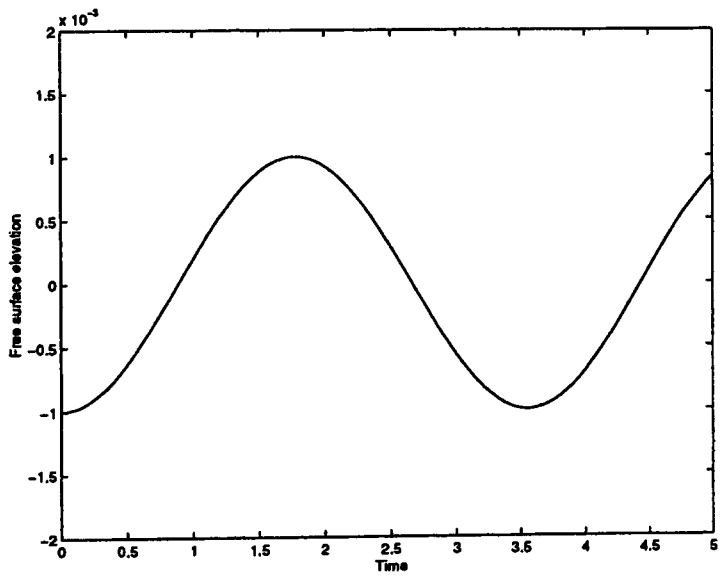

(*b*) Time history: t = 0 to 5

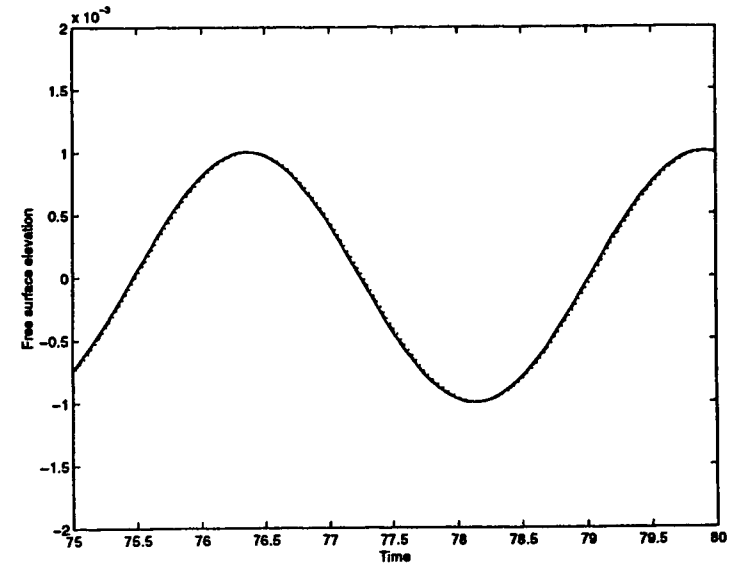

(*c*) Time history: t = 75 to 80

Figure 6.6 Time history of the free surface elevation at the centre of the tank

Standing wave with initial amplitude, a = 0.001

Dotted line : Time step = 0.1, Mesh : 32 by 16
Dashed line : Time step = 0.05, Mesh : 64 by 32
Solid line : Time step = 0.025, Mesh : 128 by 64

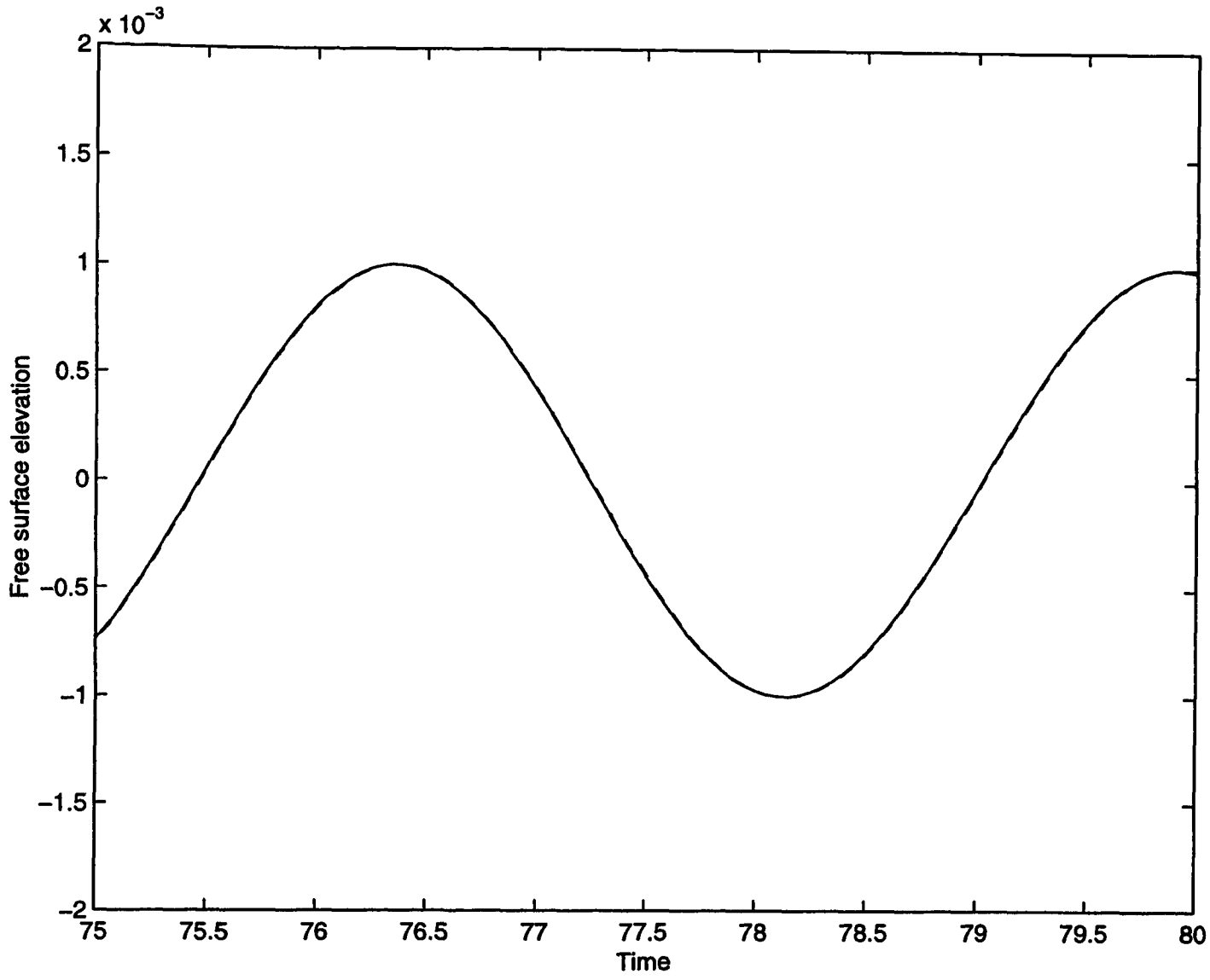

Figure 6.7 Time history of the free surface elevation at the centre of the tank

Standing wave with inital amplitude, a = 0.001

Dashed line : Finite Element Model. Time step = 0.05, Mesh : 64 by 32
Solid line : Analytical solution

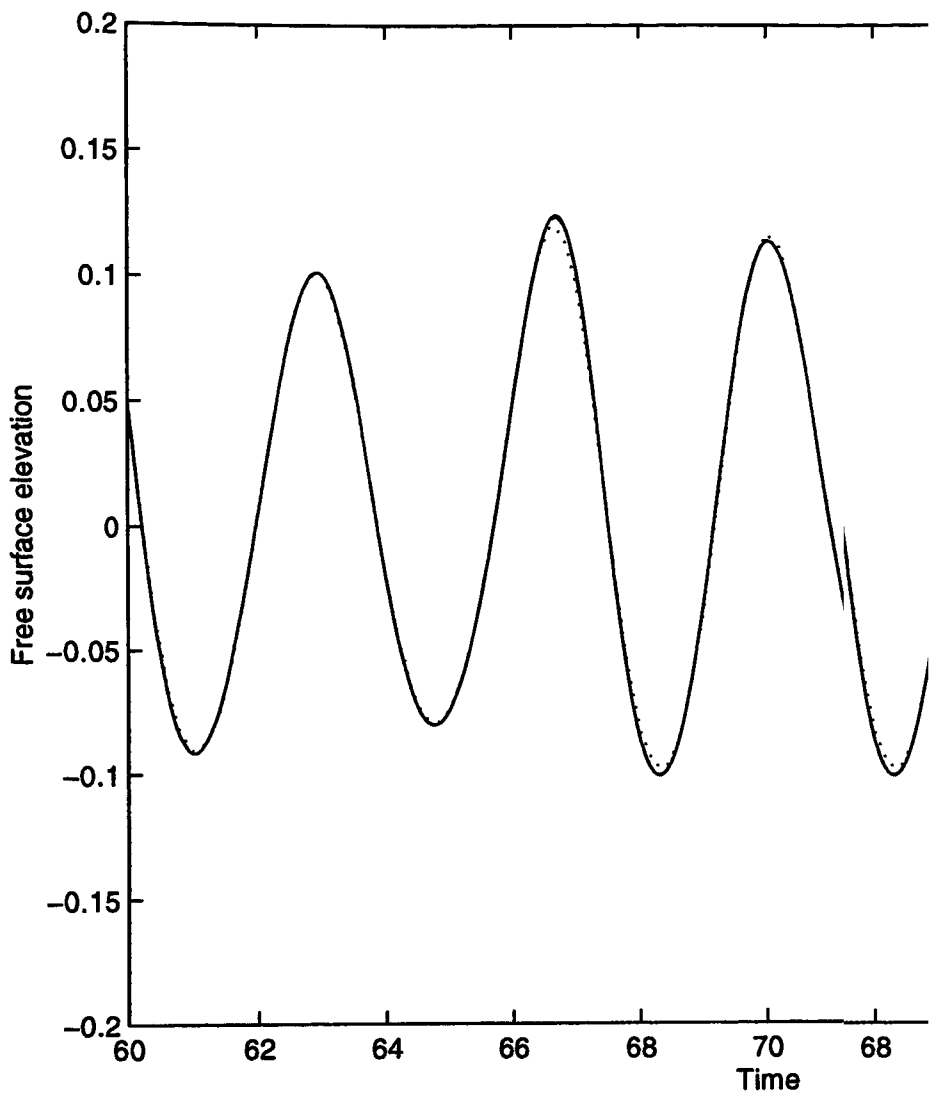

Figure 6.8 Time history of the free surface ‹free

Standing wave with initial amvith i

Mesh is 32 elements long and nts l‹

Dotted line : Time stine :
Dashed line : Time stine :
Solid line : Time stee : 1

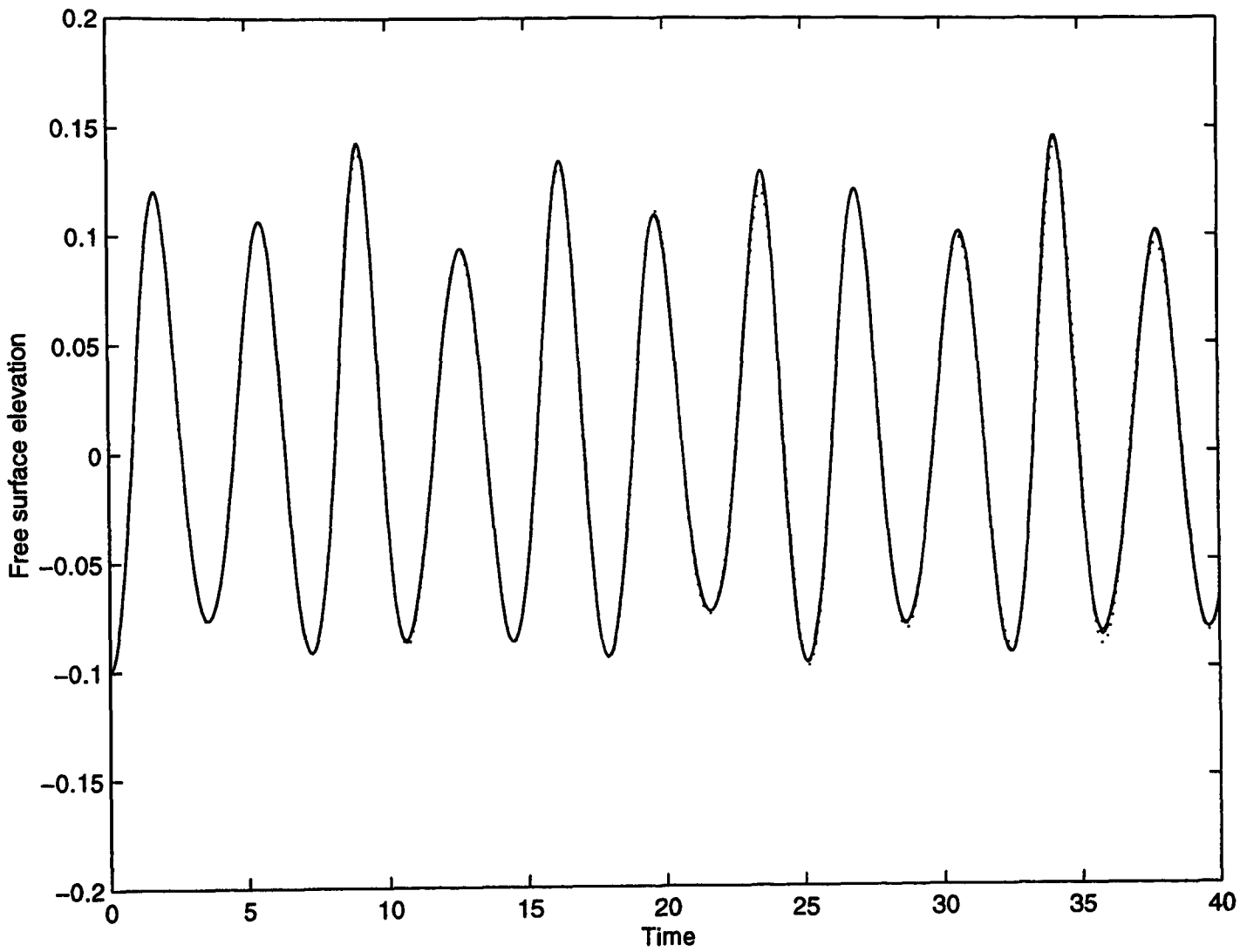

Figure 6.9 Time history of the free surface elevation at the centre of the tank

Standing wave with initial amplitude, $a = 0.1$

Standard Finite Element Method

Dotted line : Time step = 0.1, Mesh : 32 by 16
Dashed line : Time step = 0.05, Mesh : 64 by 32
Solid line : Time step = 0.025 , Mesh : 128 by 64

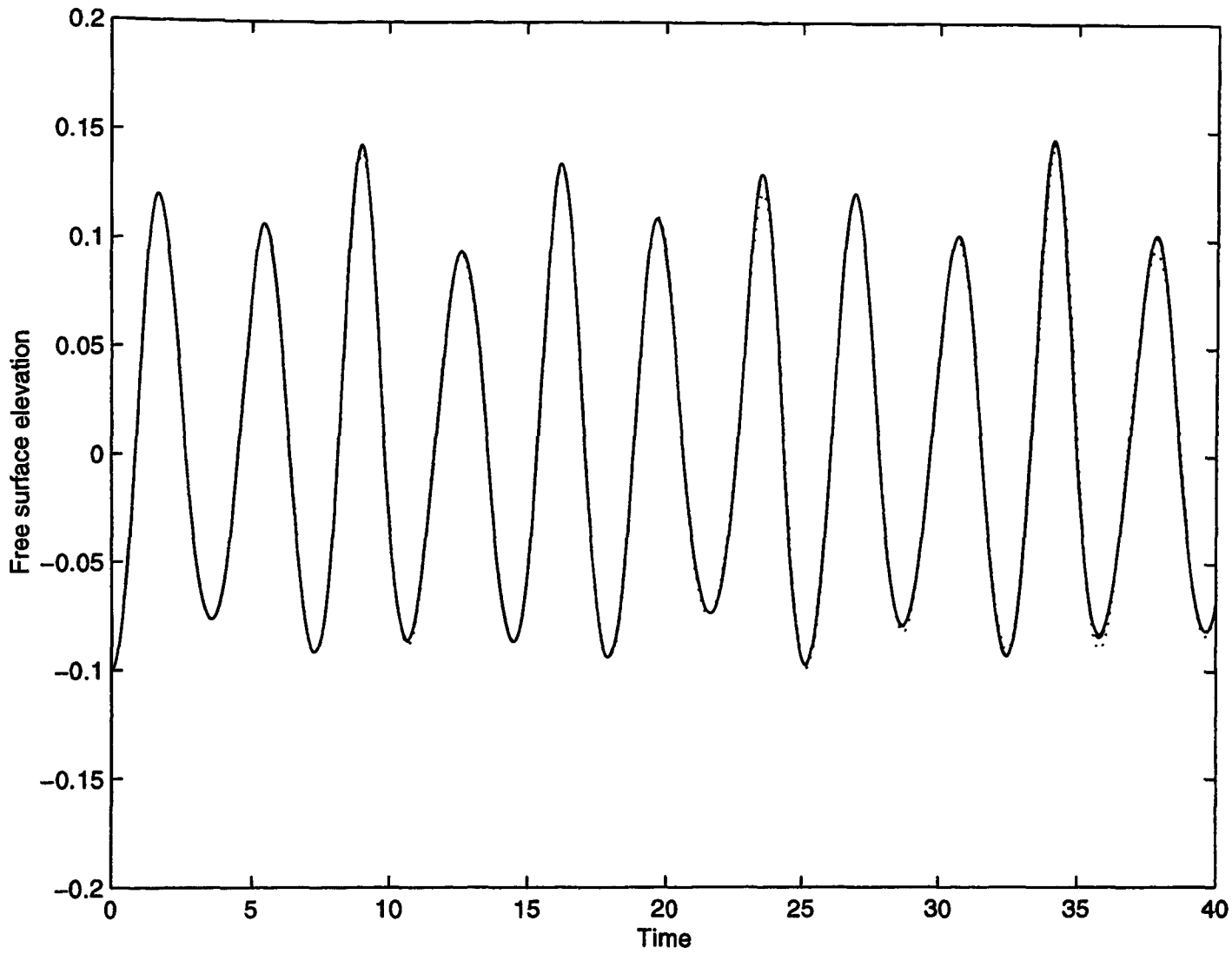

Figure 6.10 Time history of the free surface elevation at the centre of the tank

Standing wave with initial amplitude, $a = 0.1$

Sigma Transform Finite Element Method

Dotted line : Time step = 0.1, Mesh : 32 by 16
Dashed line : Time step = 0.05, Mesh : 64 by 32
Solid line : Time step = 0.025, Mesh : 128 by 64

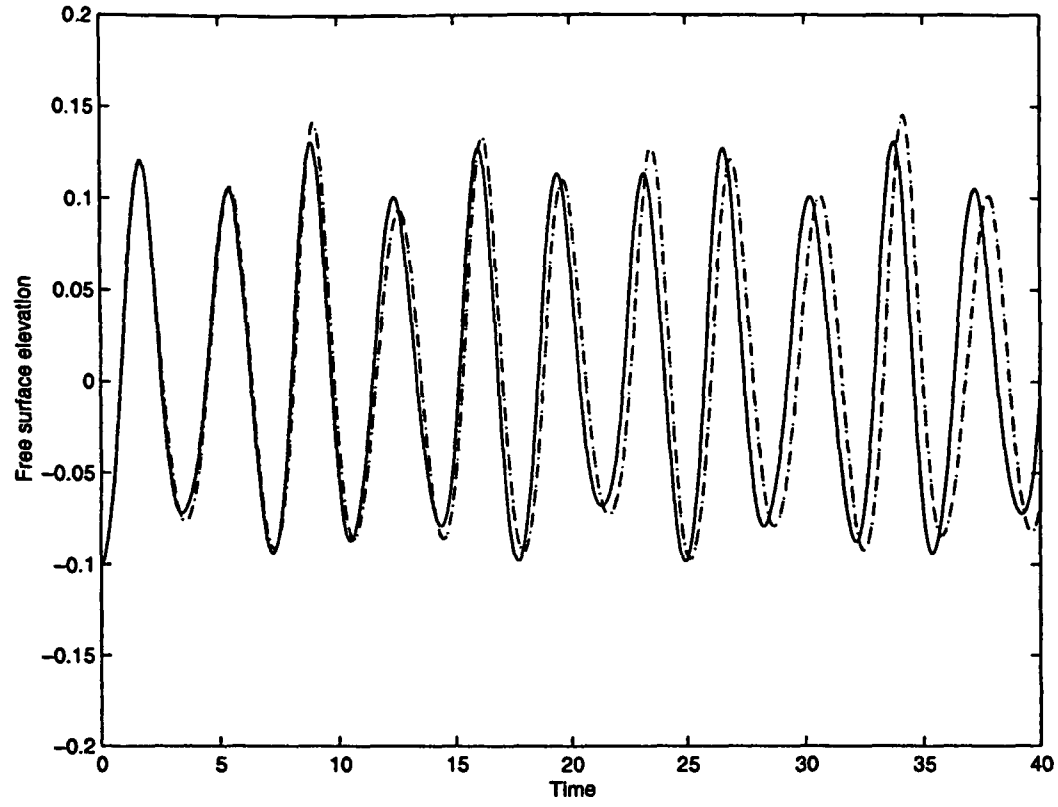

(*a*)

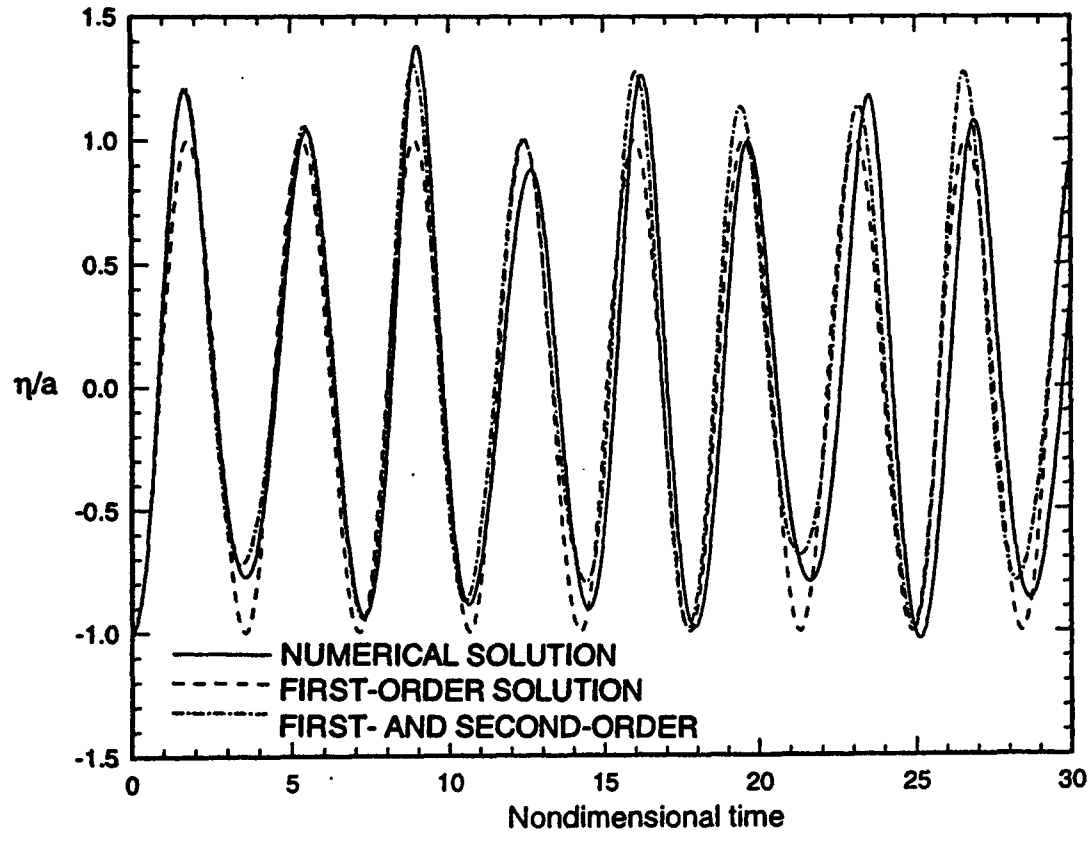

(*b*)

Figure 6.11(*a*) Time history of the free surface elevation at the centre of the tank

Standing wave with initial amplitude, $a = 0.1$

Time step = 0.05 Mesh is 64 elements long and 32 elements deep

Dotted line : Standard Finite Element Method
Dashed line : Sigma Transform Finite Element Method
Solid line : Analytical solution

(*b*) Corresponding result of Chern *et al.* (1999)

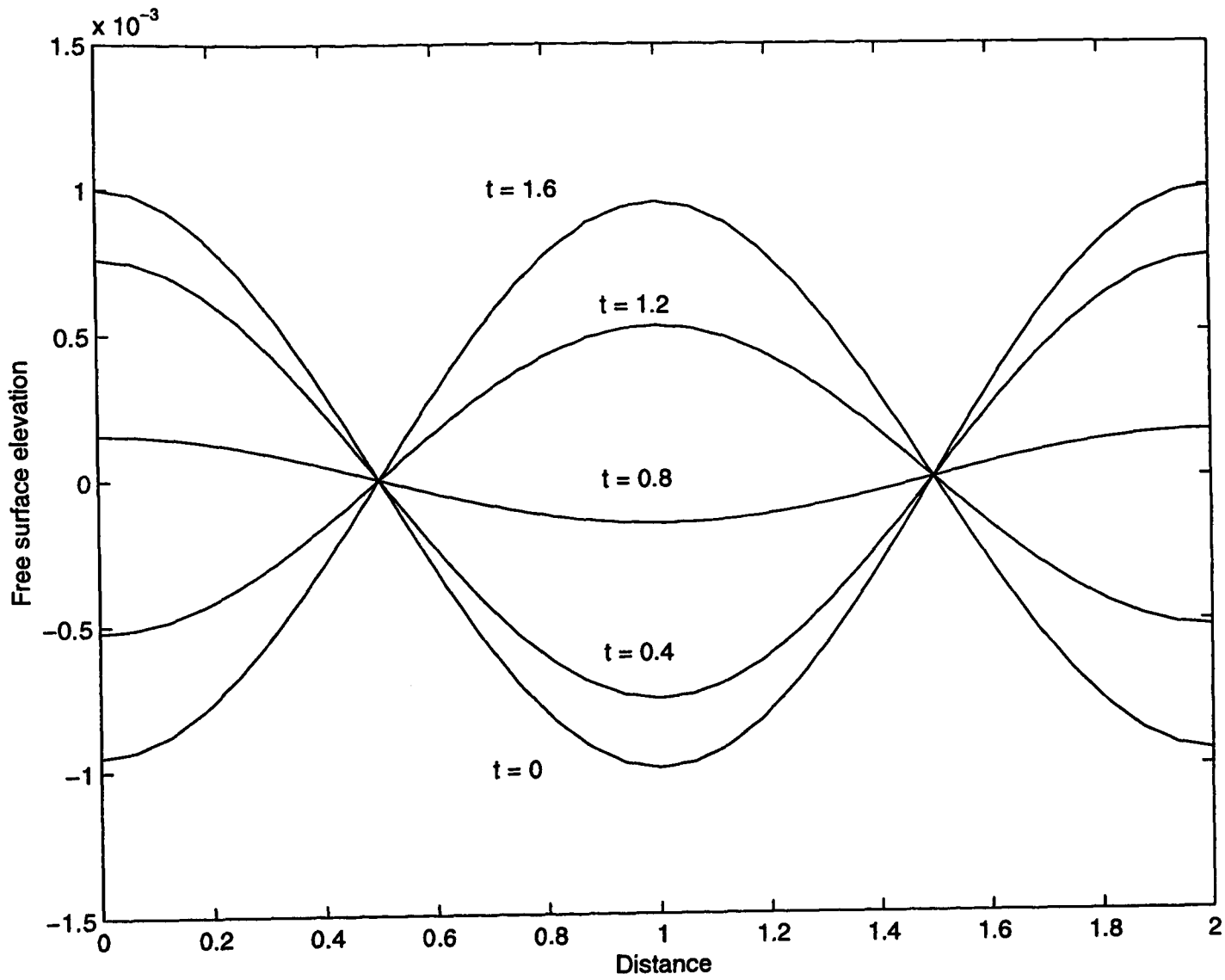

Figure 6.12 A series of wave profiles from $t = 0$ to $t = 1.6$

Standing wave with initial amplitude, $a = 0.001$

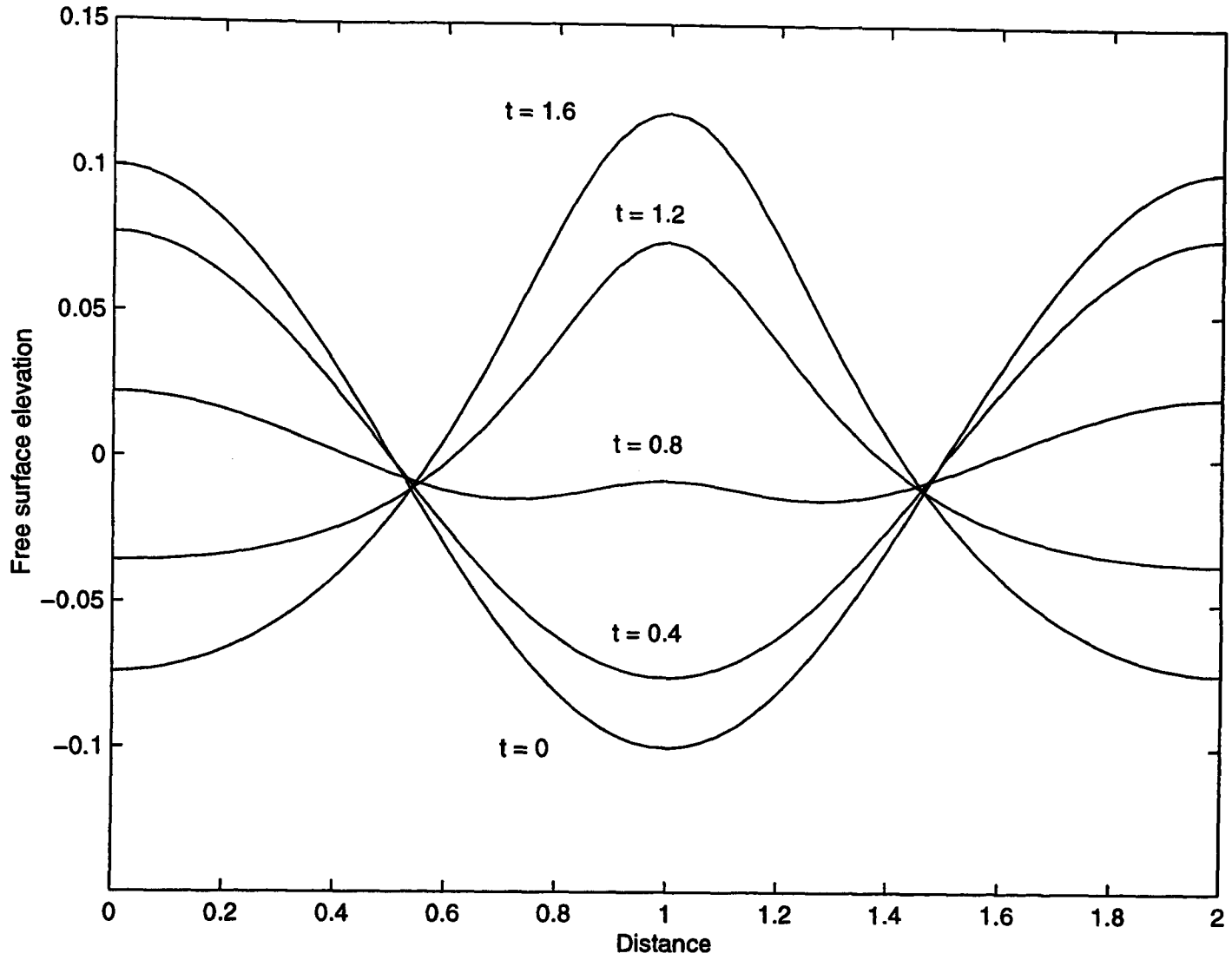

Figure 6.13 A series of wave profiles from $t = 0$ to $t = 1.6$

Standing wave with initial amplitude, $a = 0.1$

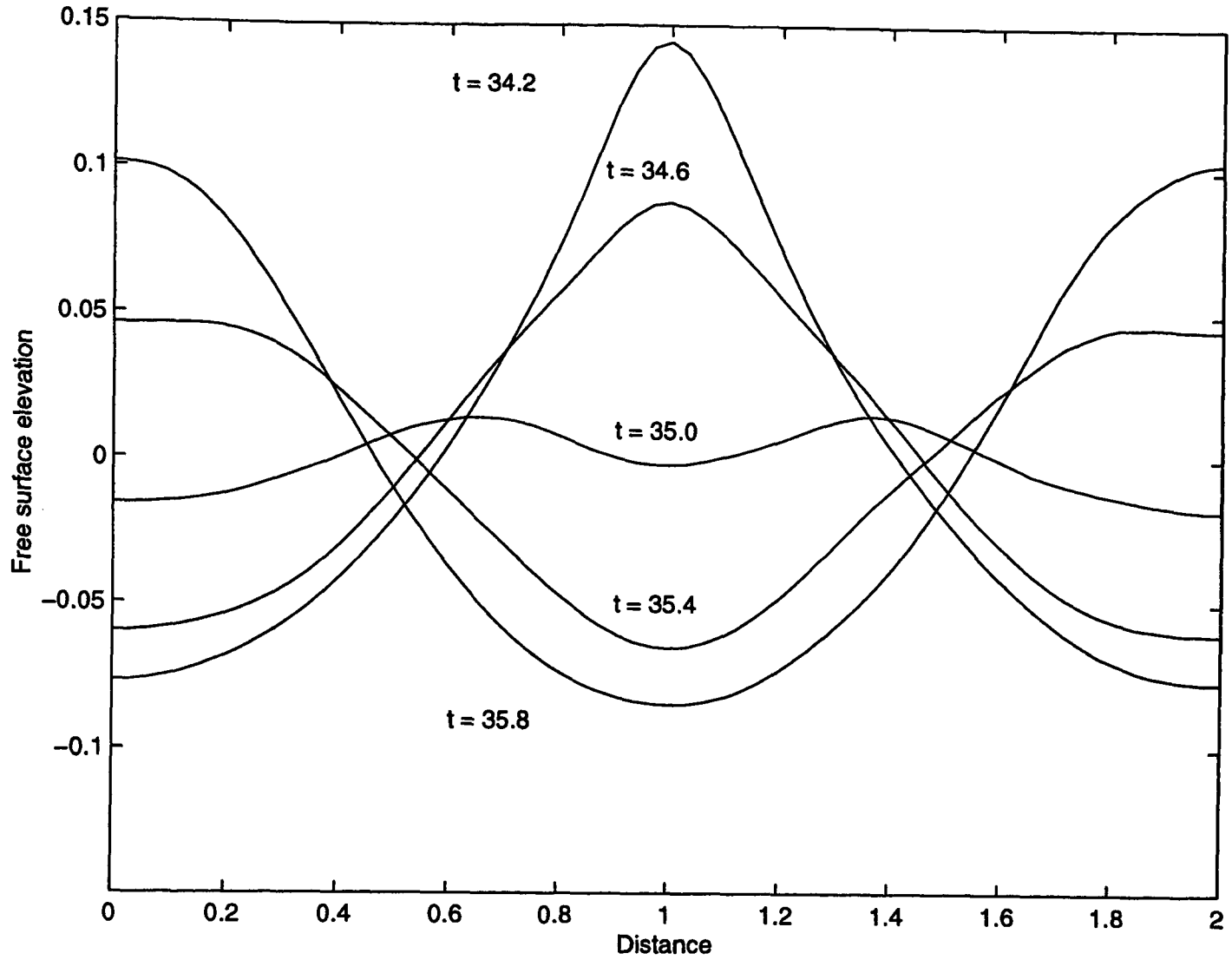

Figure 6.14 A series of wave profiles from $t = 34.2$ to $t = 35.8$

Standing wave with initial amplitude, $a = 0.1$

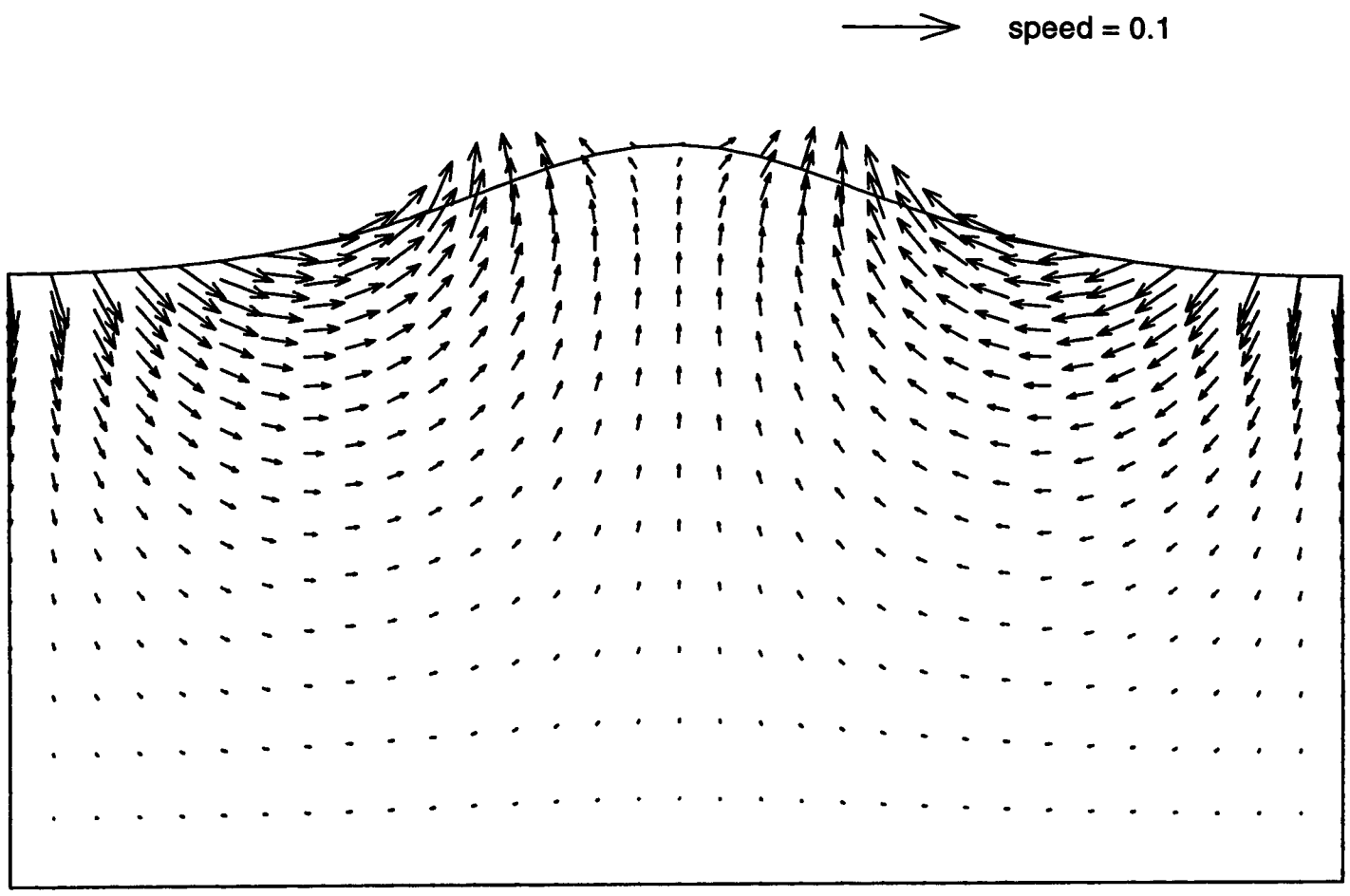

Figure 6.15 Velocity vectors at $t = 1.675$

Standing wave with initial amplitude, $a = 0.1$

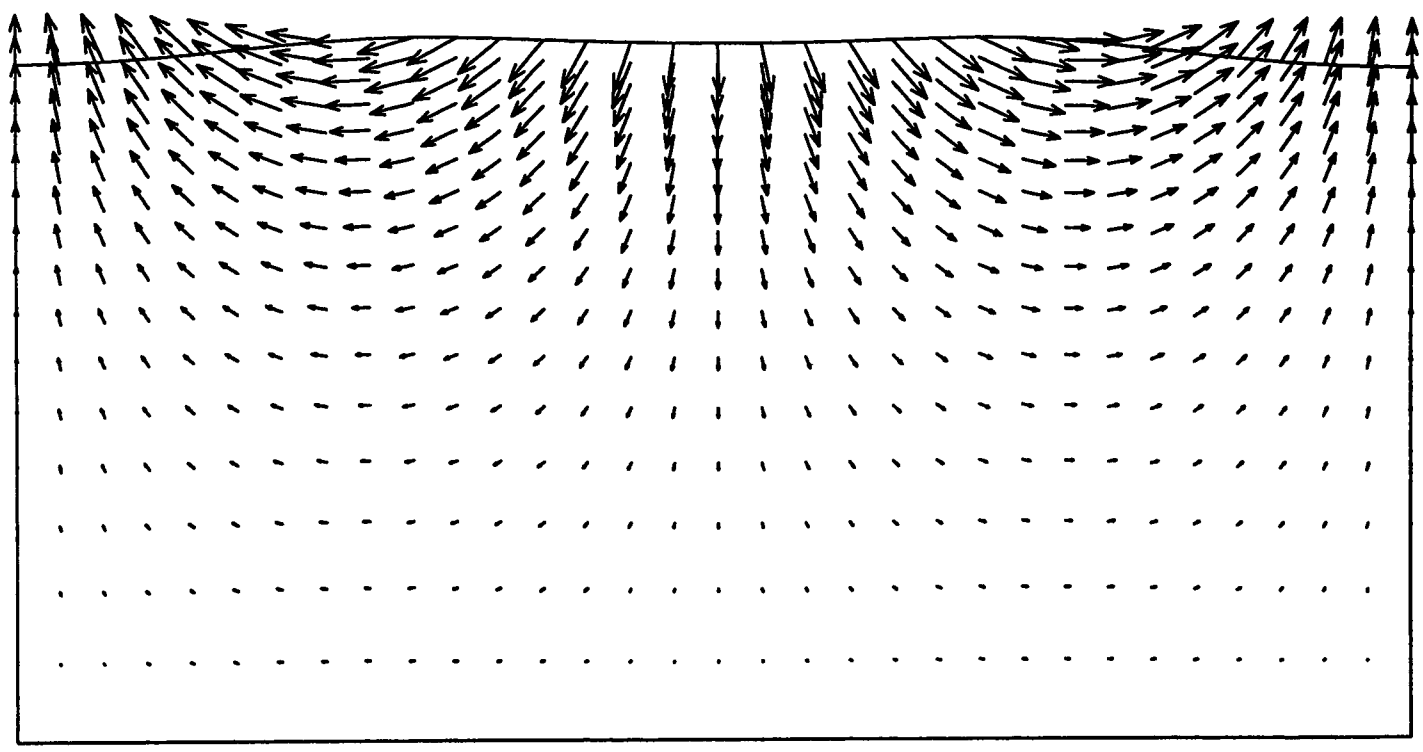

Figure 6.16 Velocity vectors at $t = 2.6$

Standing wave with initial amplitude, $a = 0.1$

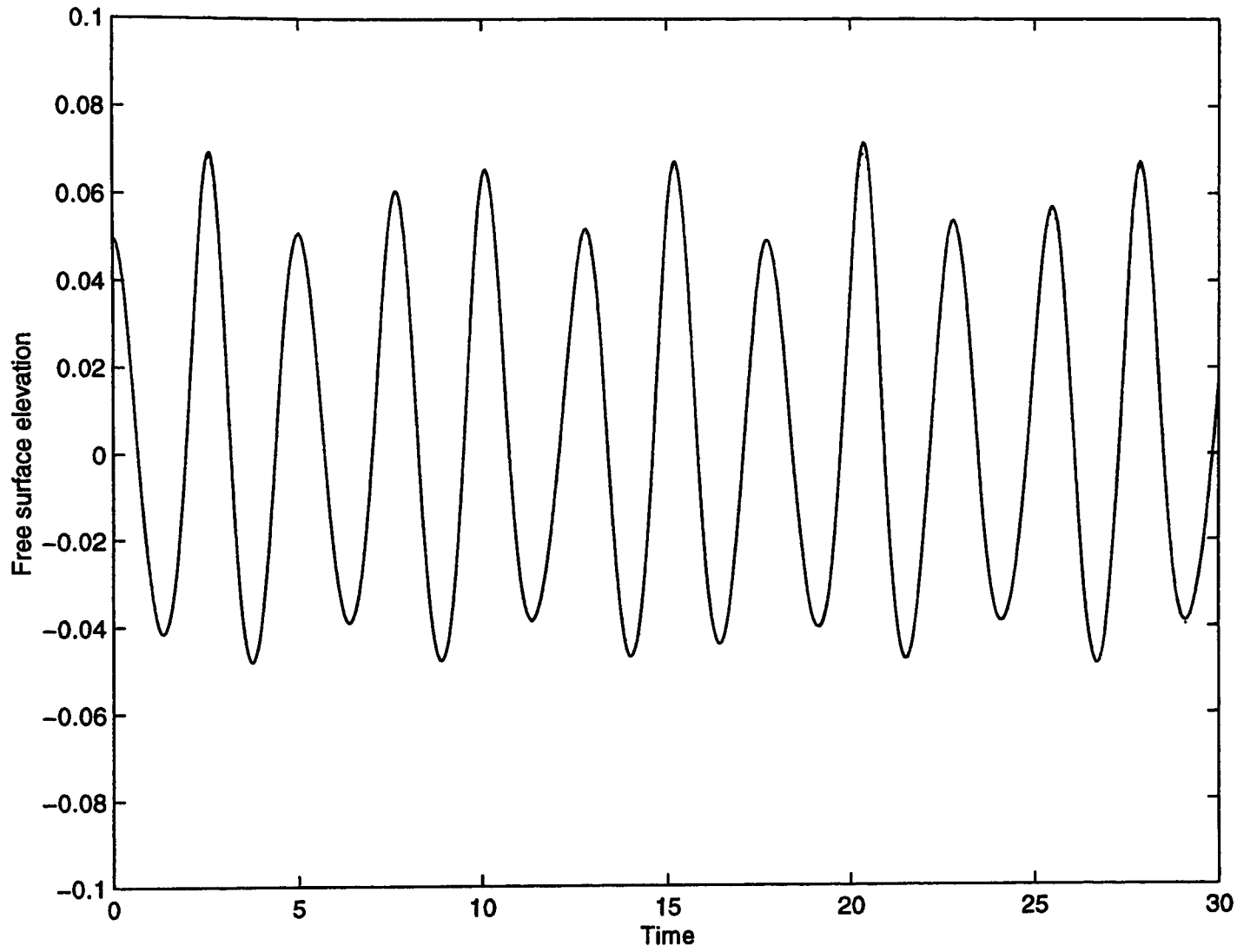

Figure 6.17 Time history of the free surface elevation at the centre of the tank

Double standing wave with initial amplitude, $a = 0.05$

Standard Finite Element Method

Dotted line : Time step = 0.1, Mesh : 128 by 32
Dashed line : Time step = 0.05, Mesh : 128 by 64
Solid line : Time step = 0.05, Mesh : 256 by 32

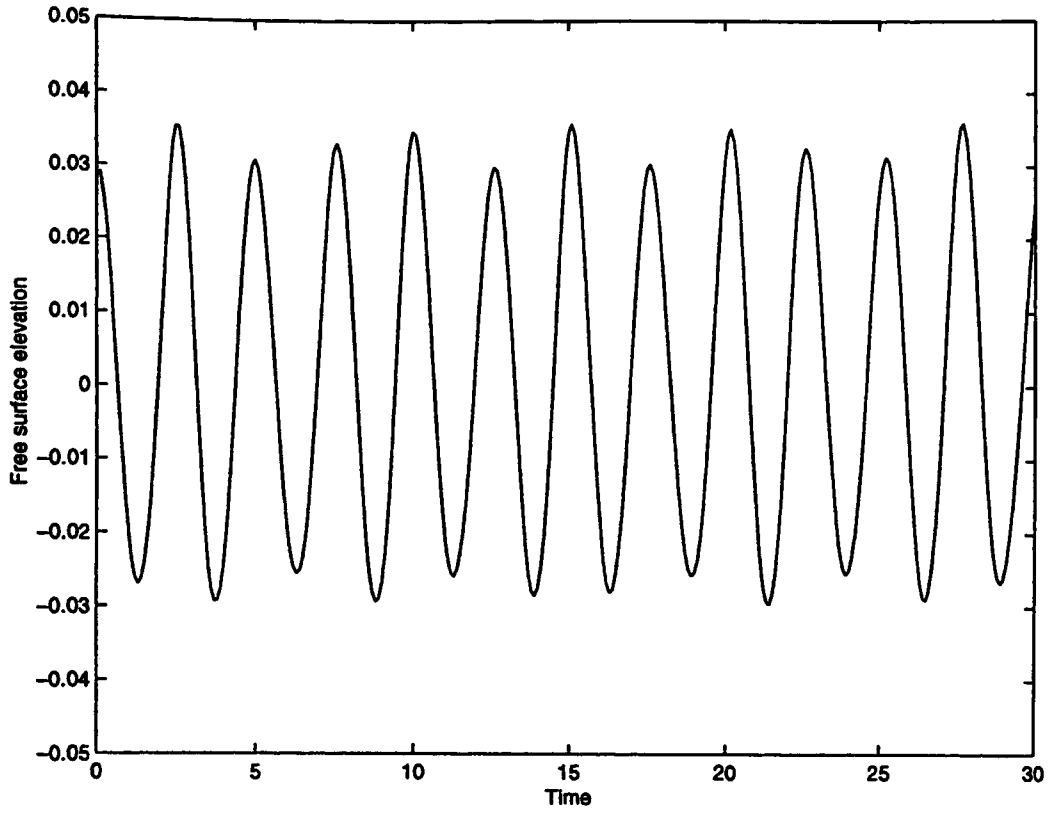

(*a*)

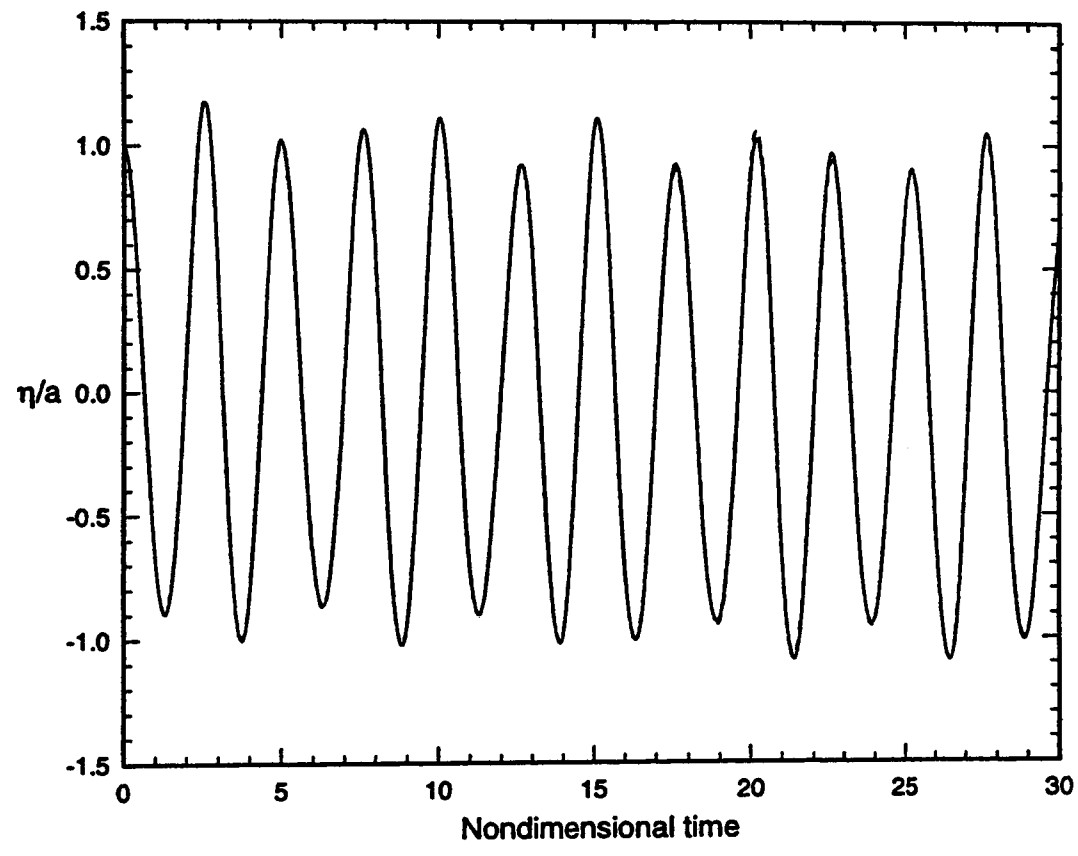

(*b*)

Figure 6.18 (*a*) Time history of the free surface elevation at the centre of the tank

Double standing wave with initial amplitude, $a = 0.03$

Standard Finite Element Method

Time step = 0.1, Mesh : 128 by 32

(*b*) Corresponding result of Chern *et al.* (1999)

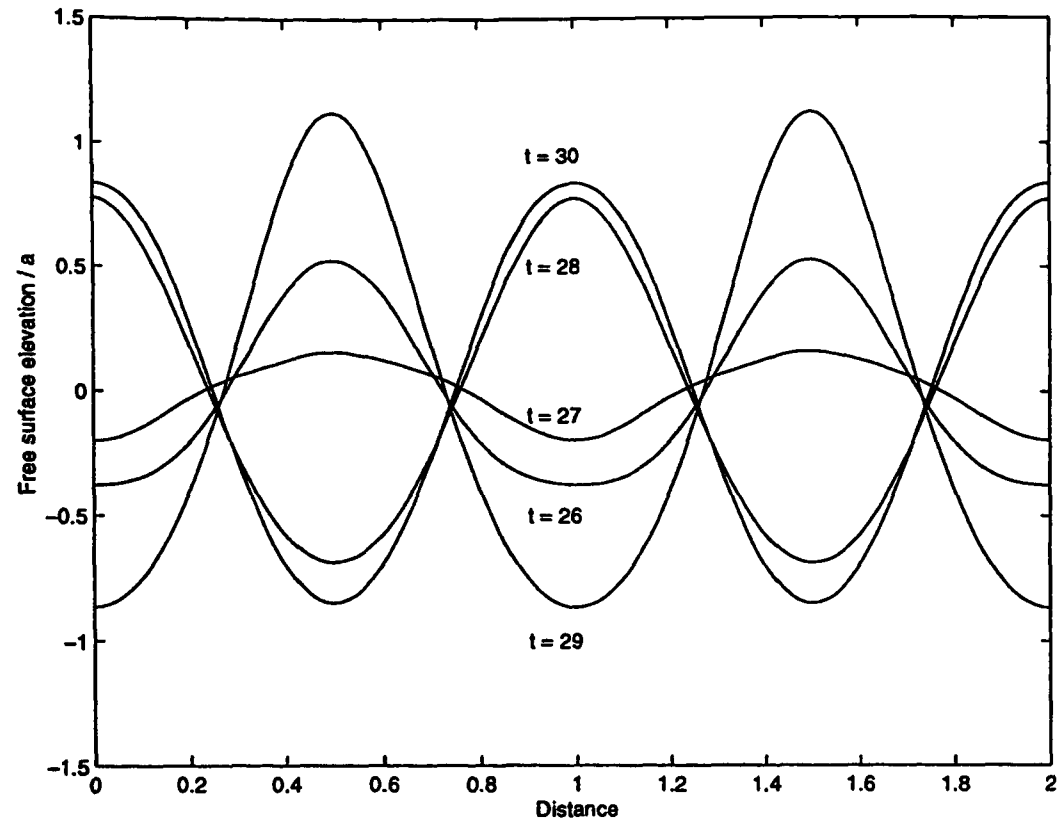

(*a*)

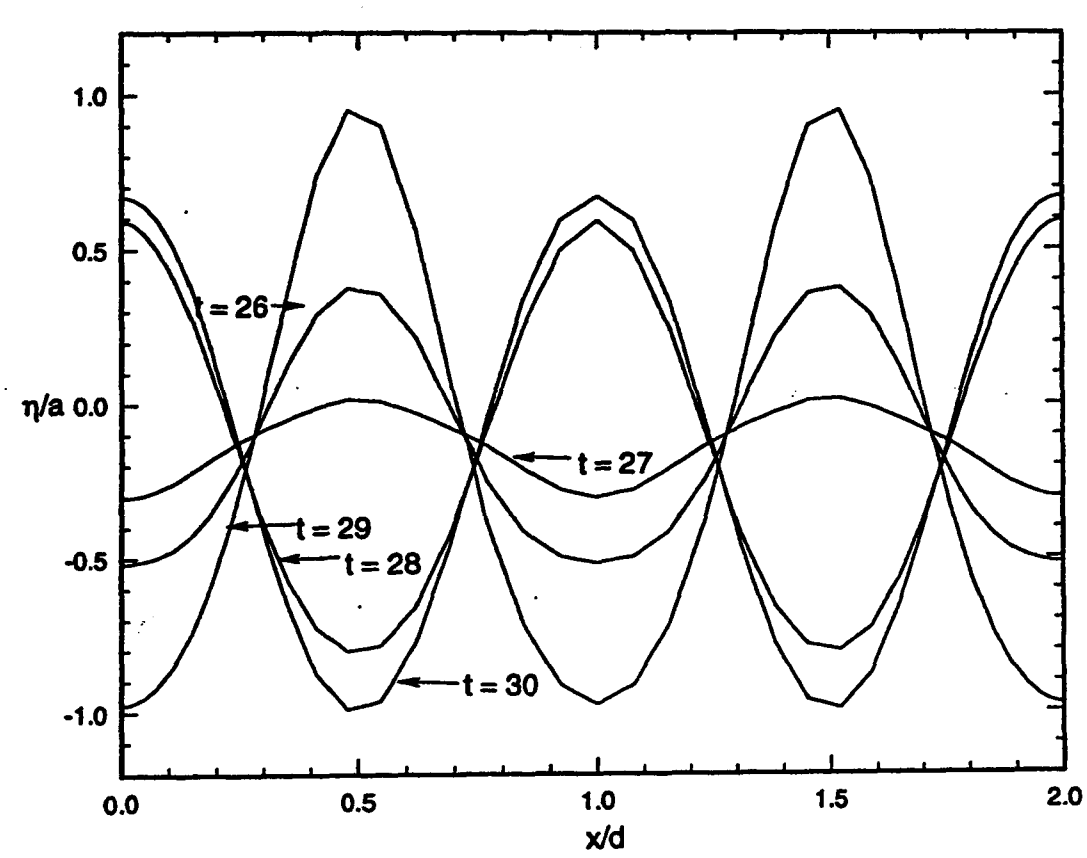

(*b*)

Figure 6.19 (*a*) A series of wave profiles from $t = 26$ to $t = 30$ Double standing wave with initial amplitude, $a = 0.03$

(*b*) Corresponding result of Chern *et al.* (1999)

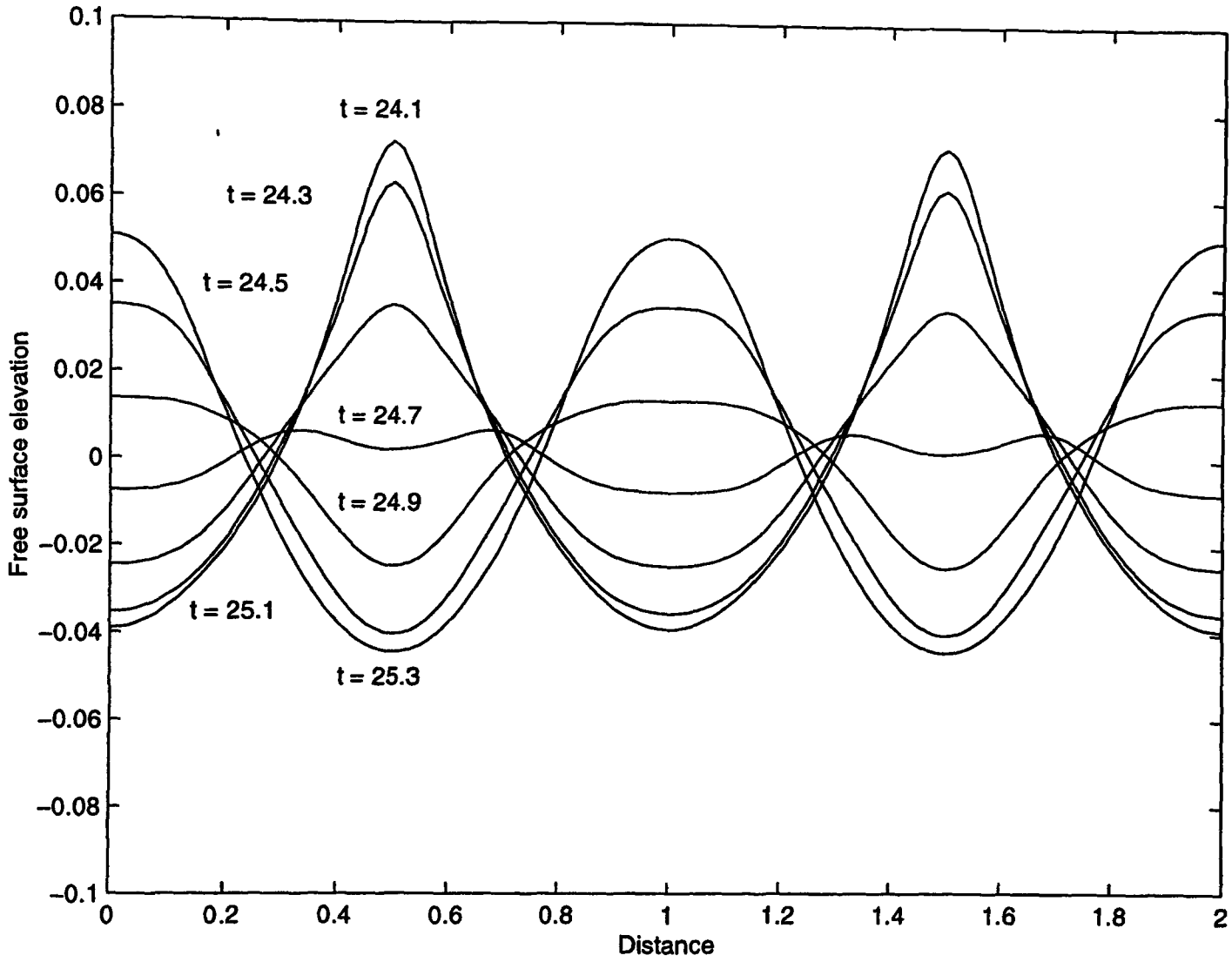

Figure 6.20 A series of wave profiles from $t = 24.1$ to $t = 25.3$

Double standing wave with initial amplitude, $a = 0.05$

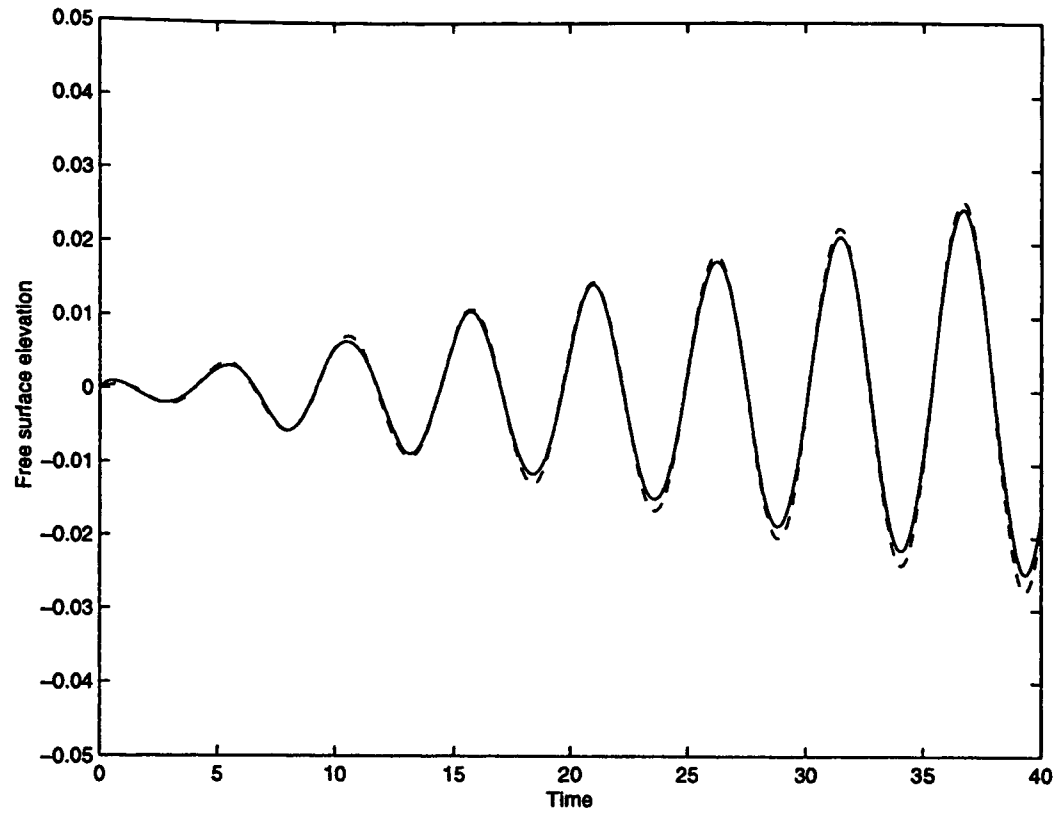

(*a*)

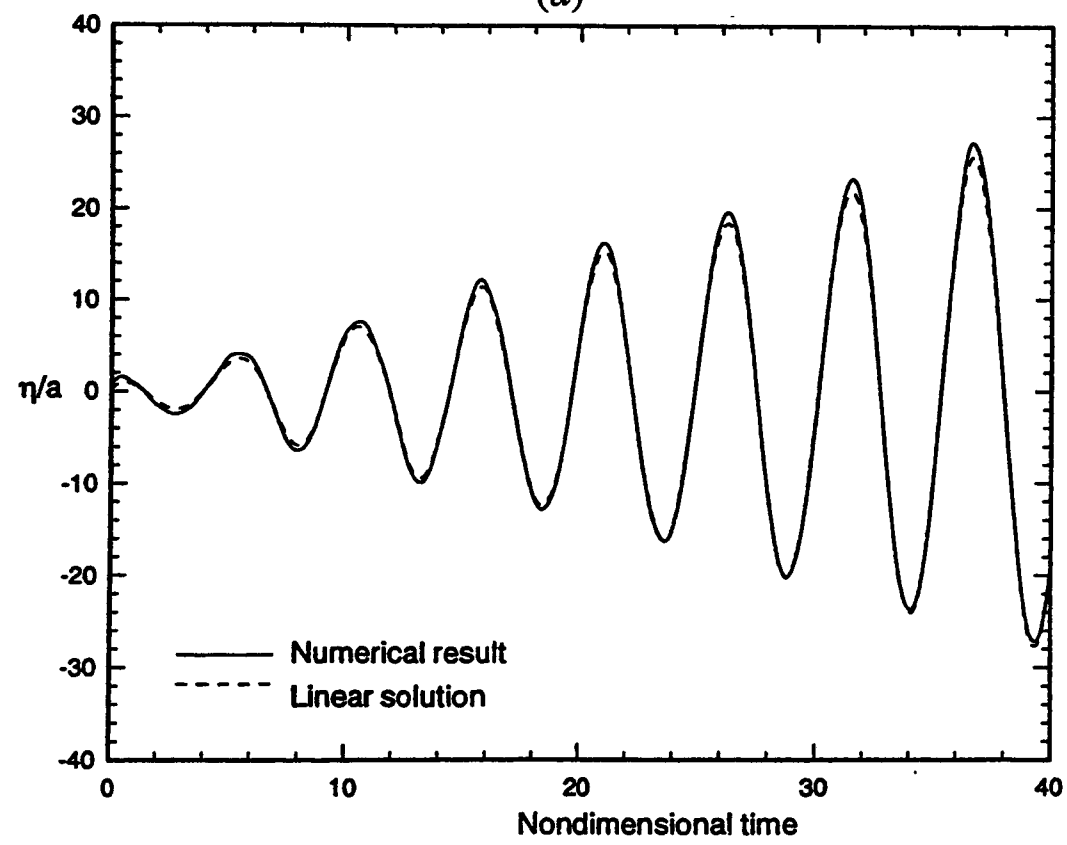

(*b*)

Figure 6.21 (*a*) Time history of the free surface elevation at the left hand wall of the tank

Sloshing wave motion, excitation frequency, $\omega = 0.999\omega_0$

Time step = 0.1 Mesh is 64 elements long and 32 elements deep

Dotted line : Analytical solution
Solid line : Standard Finite Element Solution

(*b*) Corresponding result of Chern *et al.* (1999)

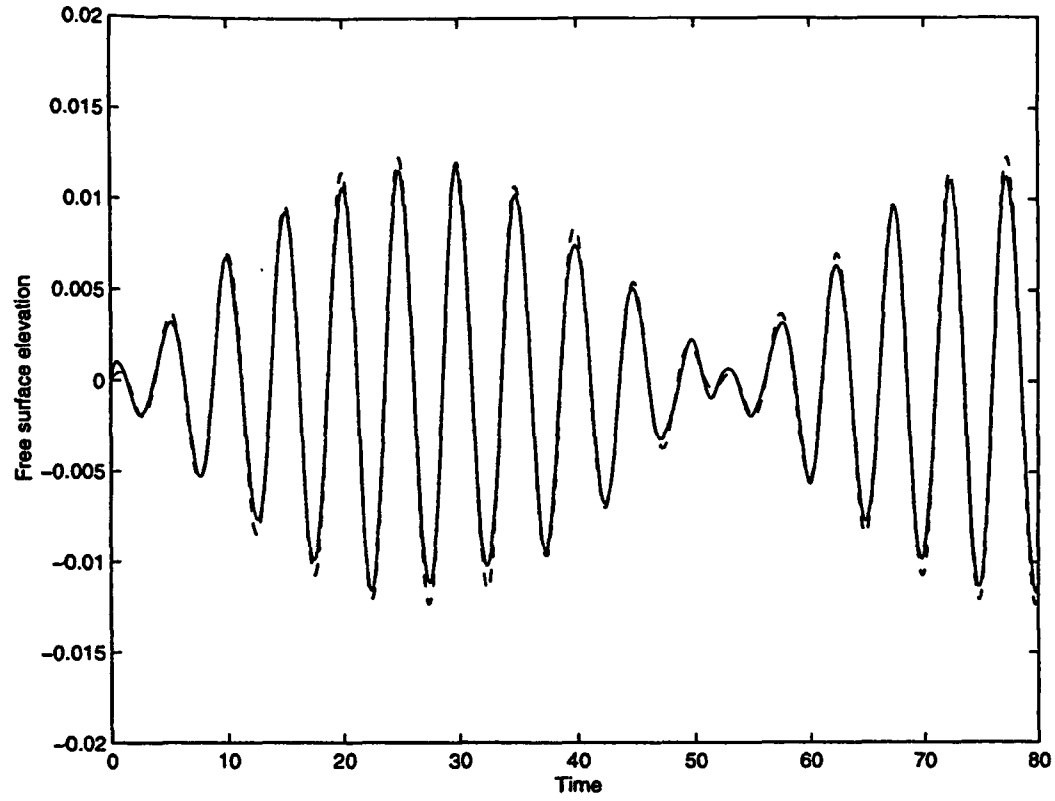

(*a*)

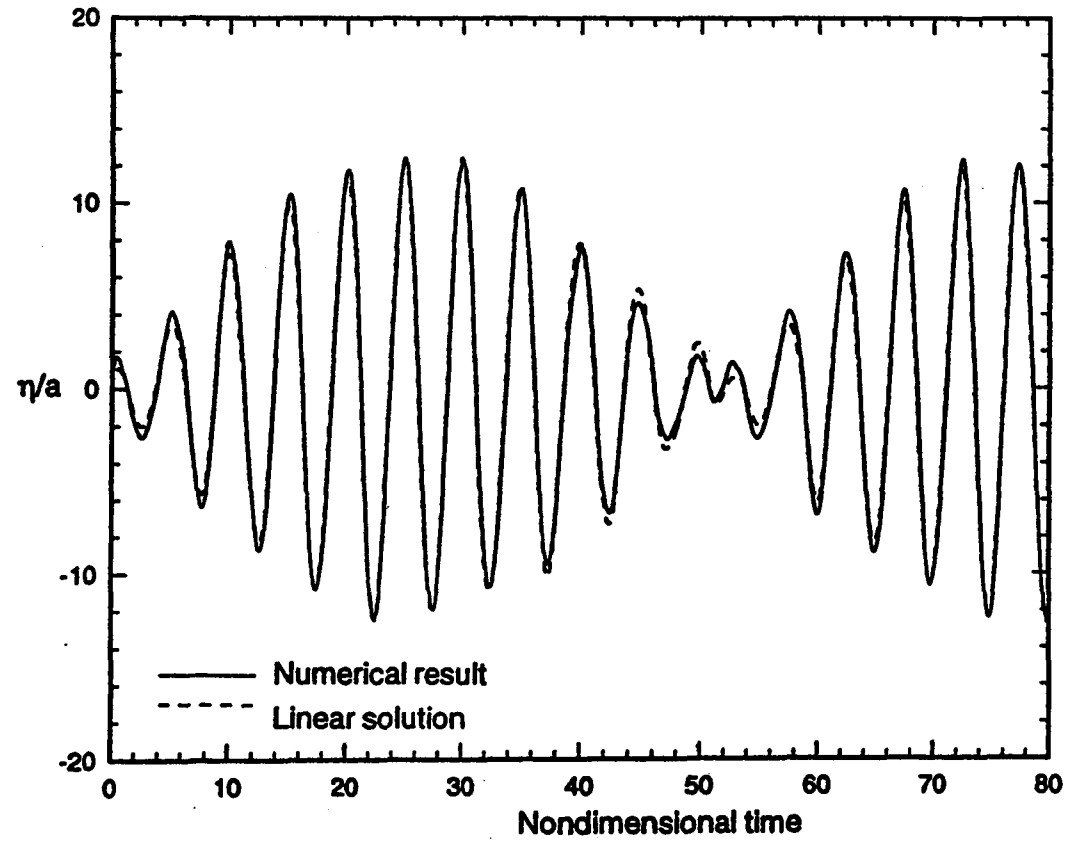

(*b*)

Figure 6.22 (*a*) Time history of the free surface elevation at the left hand wall of the tank

Sloshing wave motion, excitation frequency, $\omega = 1.1\omega_0$

Time step = 0.1 Mesh is 64 elements long and 32 elements deep

Dotted line : Analytical solution
Solid line : Standard Finite Element Solution

(*b*) Corresponding result of Chern *et al.* (1999)

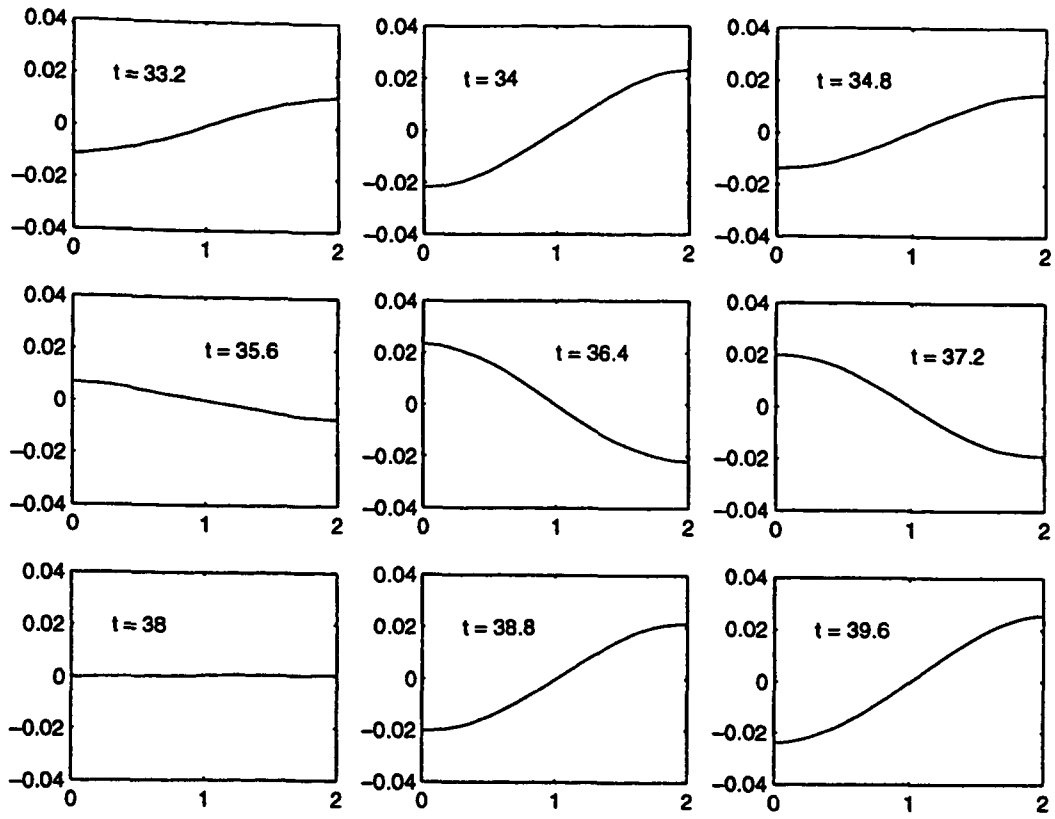

(*a*)

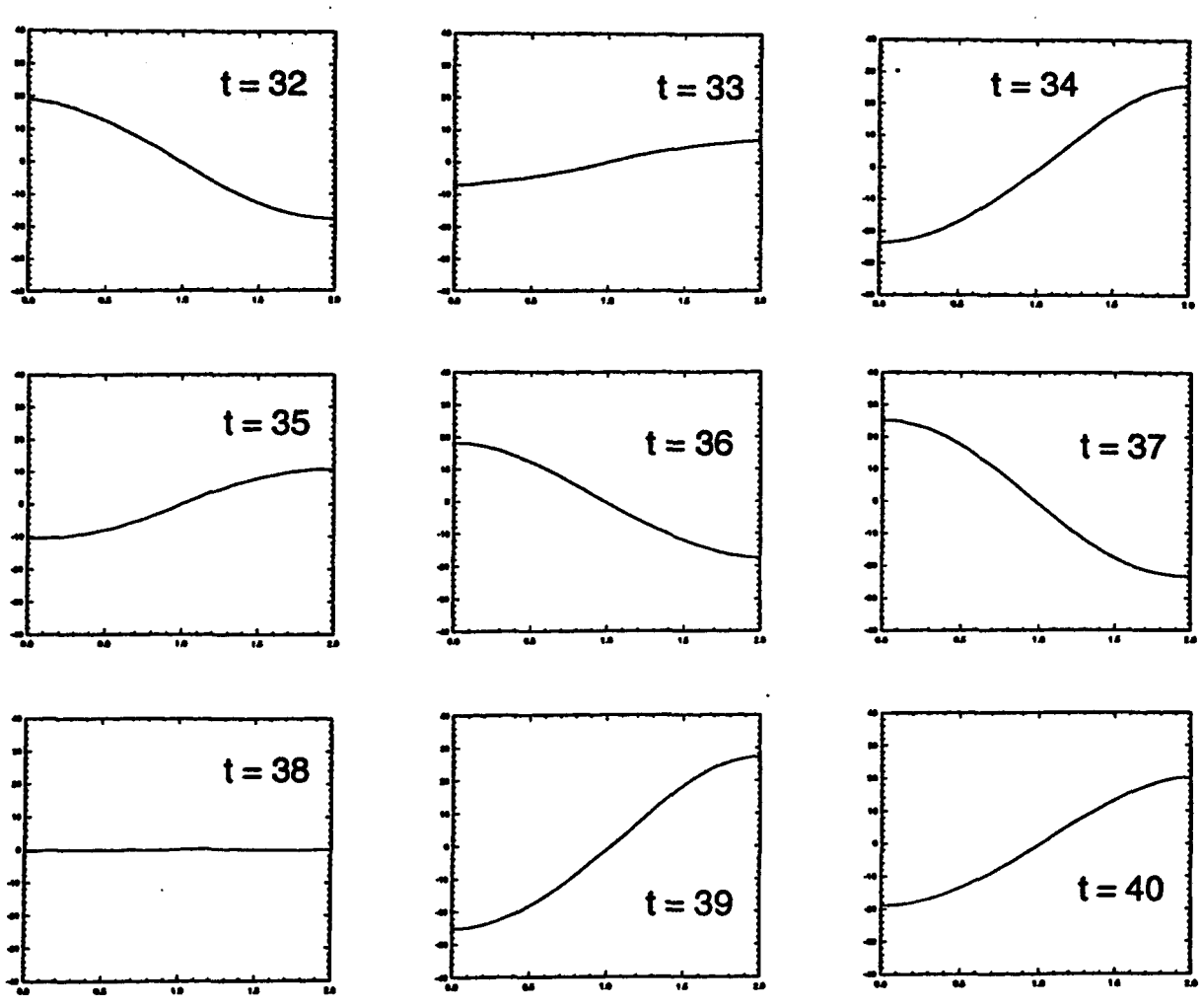

(*b*)

Figure 6.23 (*a*) A series of wave profiles from $t = 33.2$ to $t = 39.6$

Sloshing wave motion, excitation frequency, $\omega = 0.999\omega_0$

(*b*) Corresponding result of Chern *et al.* (1999)

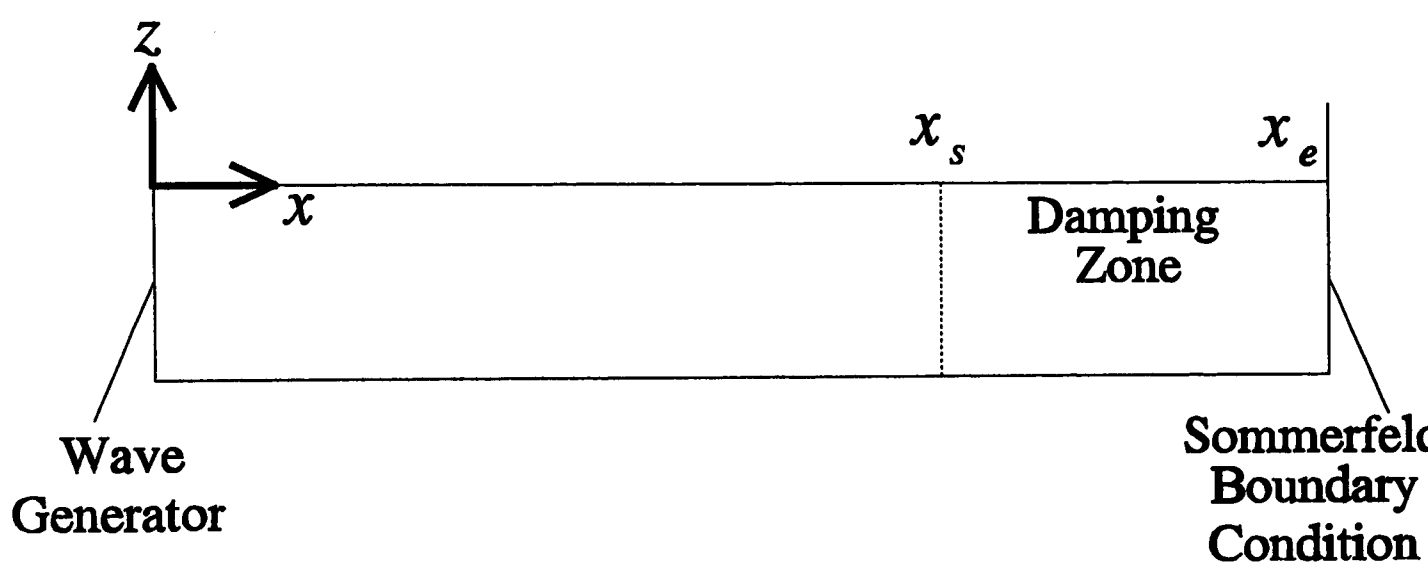

Figure 6.24

Model diagram for travelling wave case

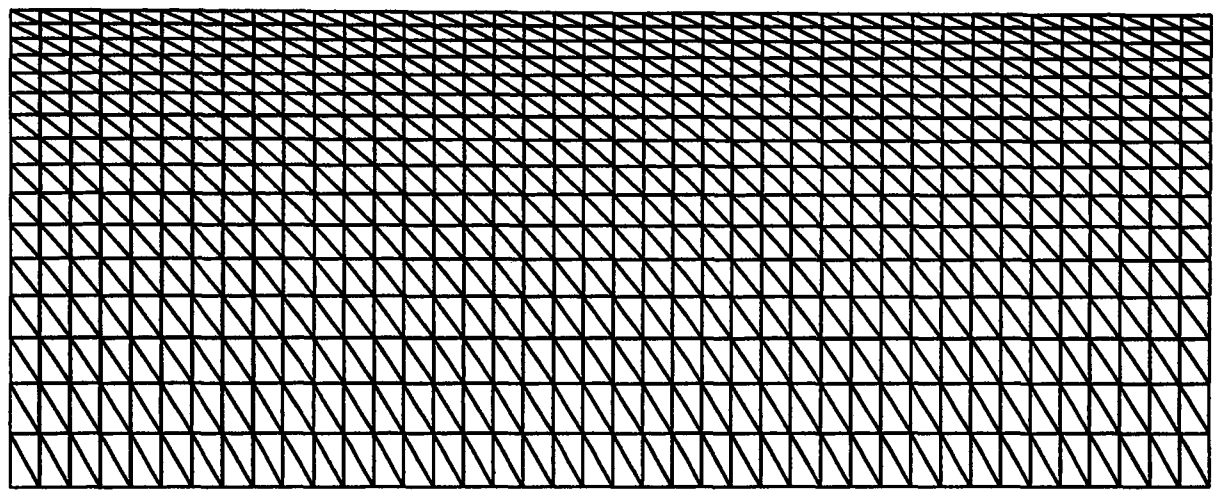

Figure 6.25 Section of initial structured mesh for travelling wave simulation

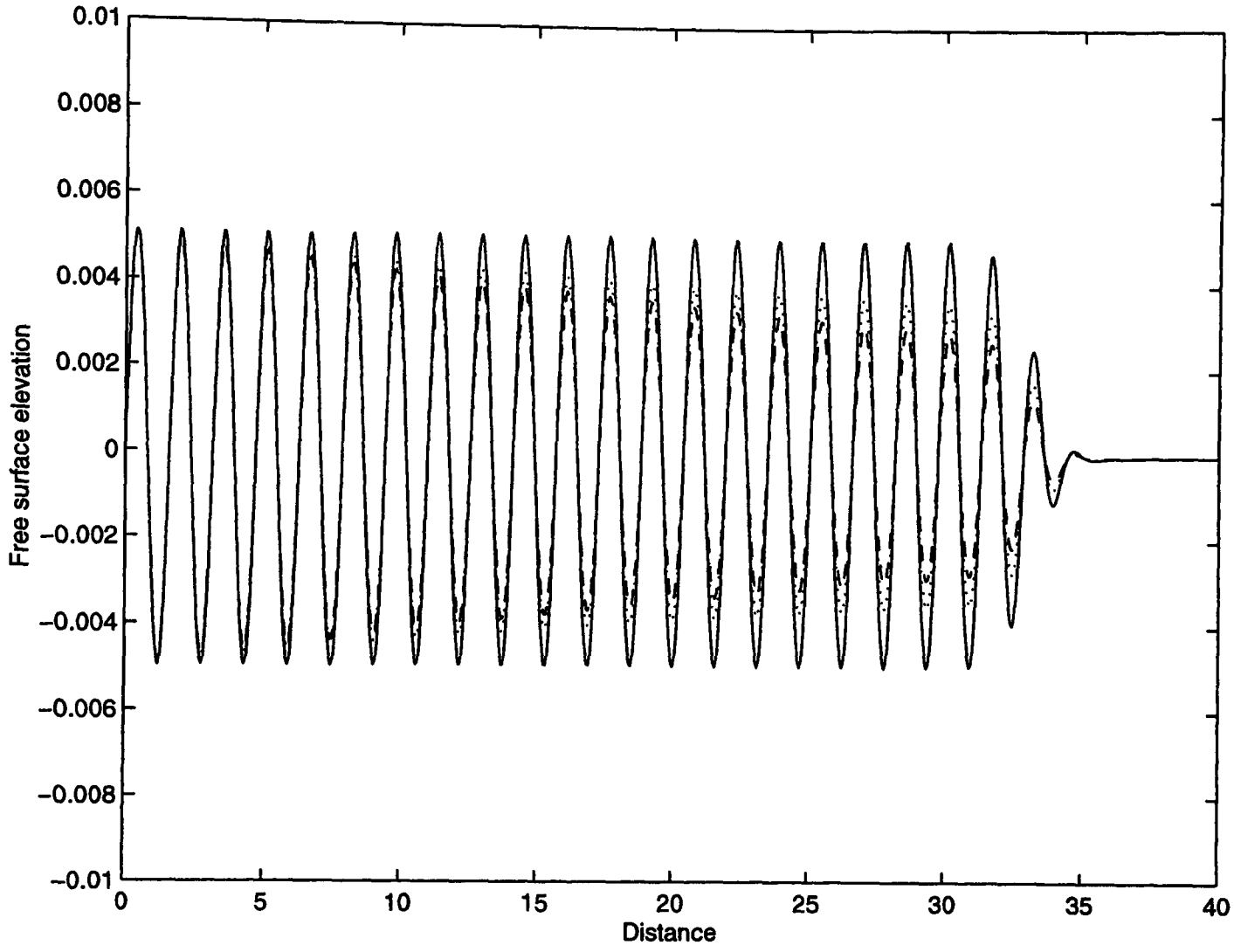

Figure 6.26 Space profile of the free surface elevation at $t = 60\pi = 188.4$

Wave generator velocity amplitude, $U_0 = 0.01$ Tank length = 40

Time step = $\pi/20 = 0.15707$ Mesh is 640 elements long and 16 elements deep

Dotted line : Interpolation and no Smoothing
Dashed line : Smoothing and no interpolation
Solid line : No interpolation and no smoothing

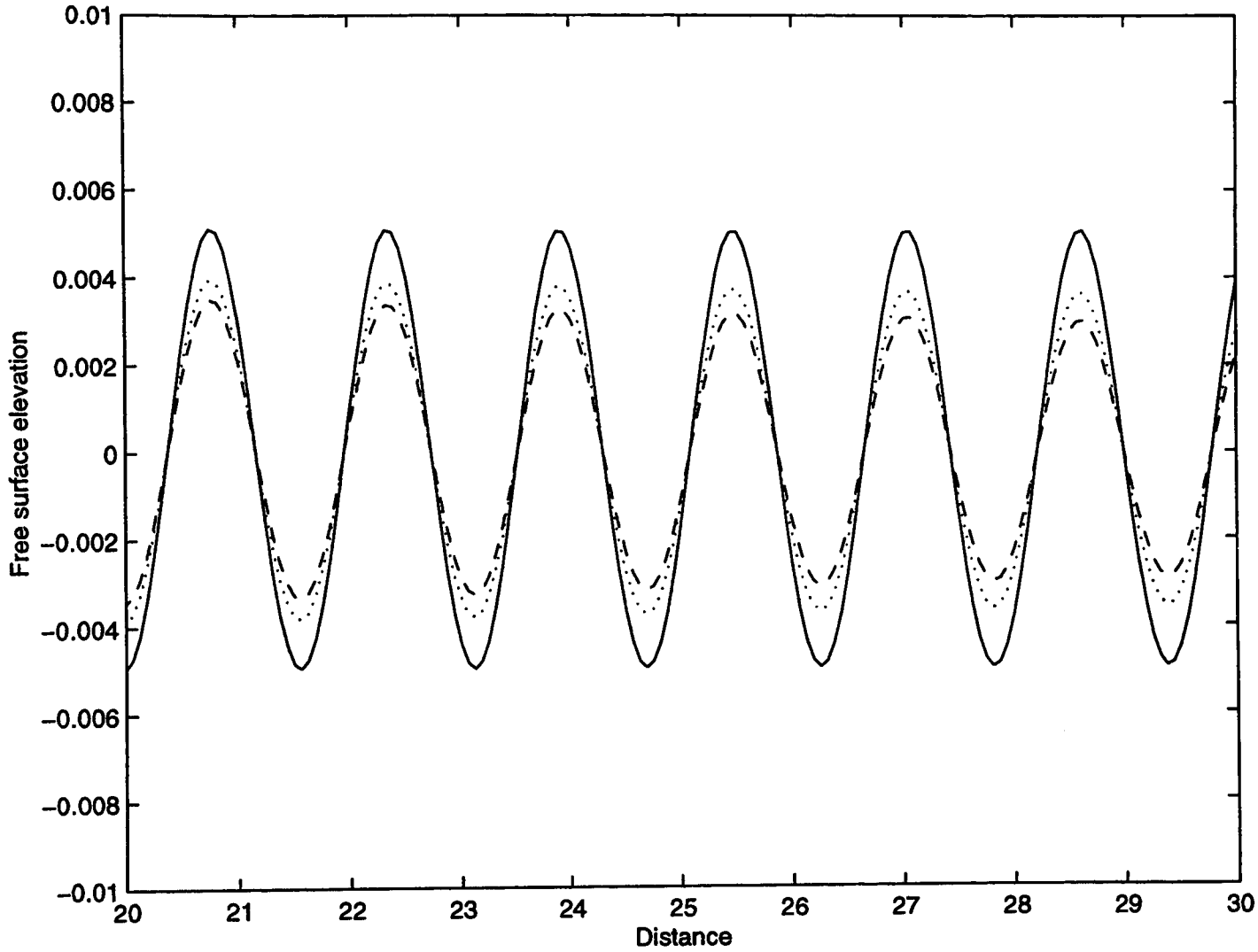

Figure 6.27 Space profile of the free surface elevation at $t = 60\pi = 188.4$

Wave generator velocity amplitude, $U_0 = 0.01$ Tank length = 40

Time step = $\pi/20 = 0.15707$ Mesh is 640 elements long and 16 elements deep

Dotted line : Interpolation and no Smoothing
Dashed line : Smoothing and no interpolation
Solid line : No interpolation and no smoothing

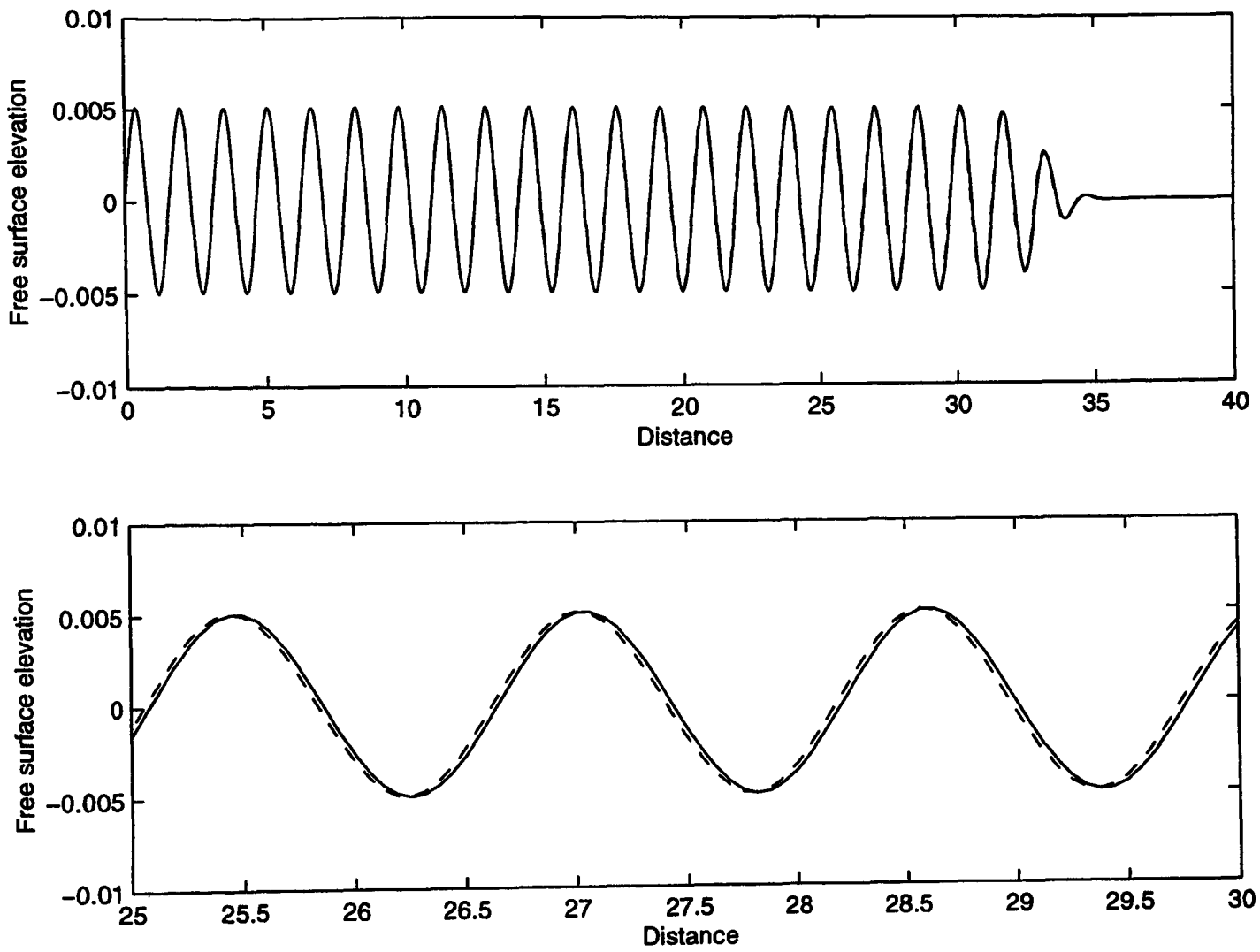

Figure 6.28 Space profile of the free surface elevation at $t = 60\pi = 188.4$

Wave generator velocity amplitude, $U_0 = 0.01$ Tank length = 40

Mesh is 640 elements long and 16 elements deep

Solid line : Time step = $\pi/20 = 0.15707$
Dashed line : Time step = $\pi/40 = 0.07854$

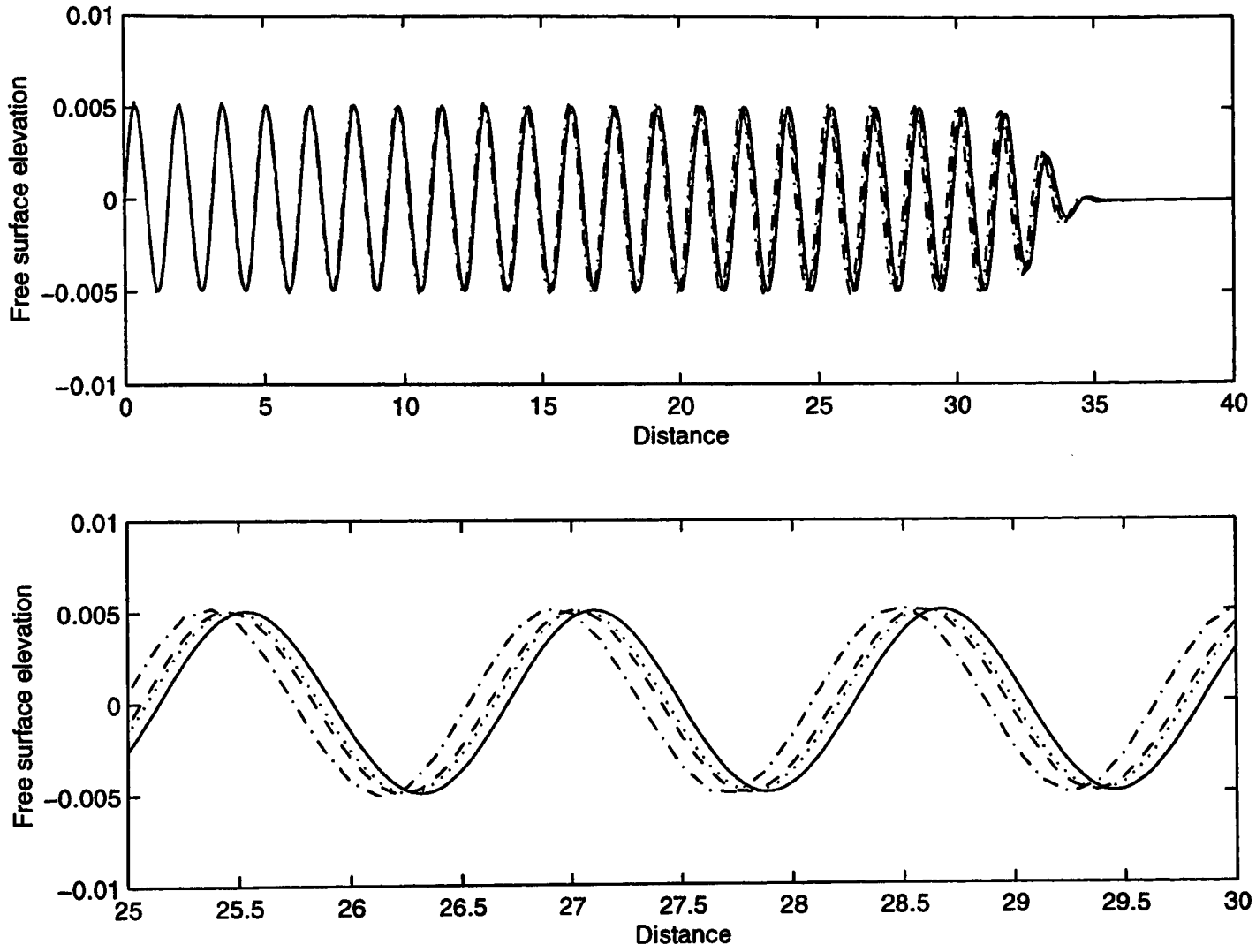

Figure 6.29 Space profile of the free surface elevation at $t = 60\pi = 188.4$

Wave generator velocity amplitude, $U_0 = 0.01$ Tank length = 40

Dot-dash line : Time step = $\pi/20 = 0.15707$ Mesh : 320 by 8
Dotted line : Time step = $\pi/20 = 0.15707$ Mesh : 640 by 16
Dashed line : Time step = $\pi/20 = 0.15707$ Mesh : 640 by 32
Solid line : Time step = $\pi/40 = 0.07854$ Mesh : 1280 by 16

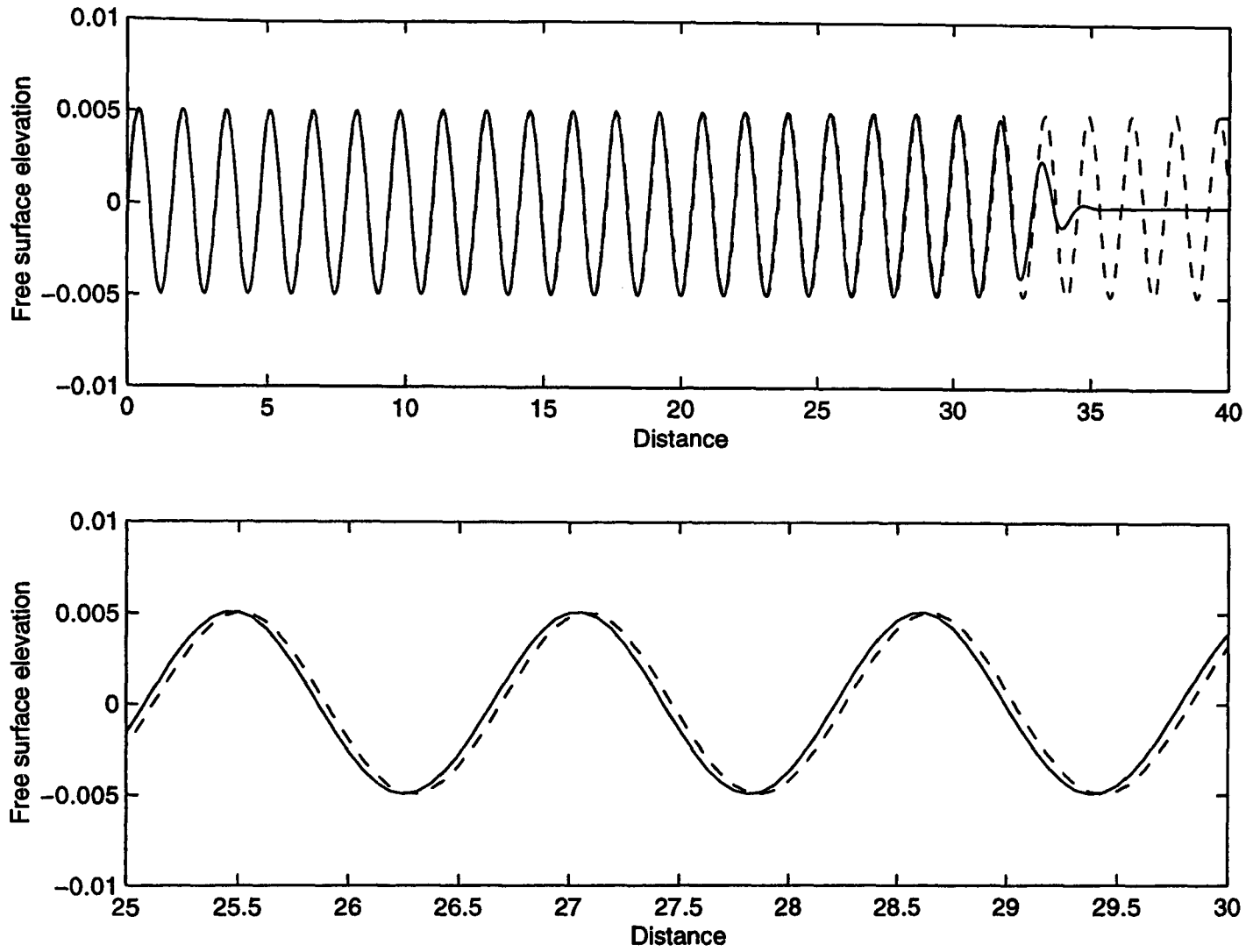

Figure 6.30 Space profile of the free surface elevation at $t = 60\pi = 188.4$

Wave generator velocity amplitude, $U_0 = 0.01$ Tank length = 40

Solid line : Finite Element Model. Time step = $\pi/20 = 0.15707$. Mesh : 640 by 16
Dashed line : Analytical solution

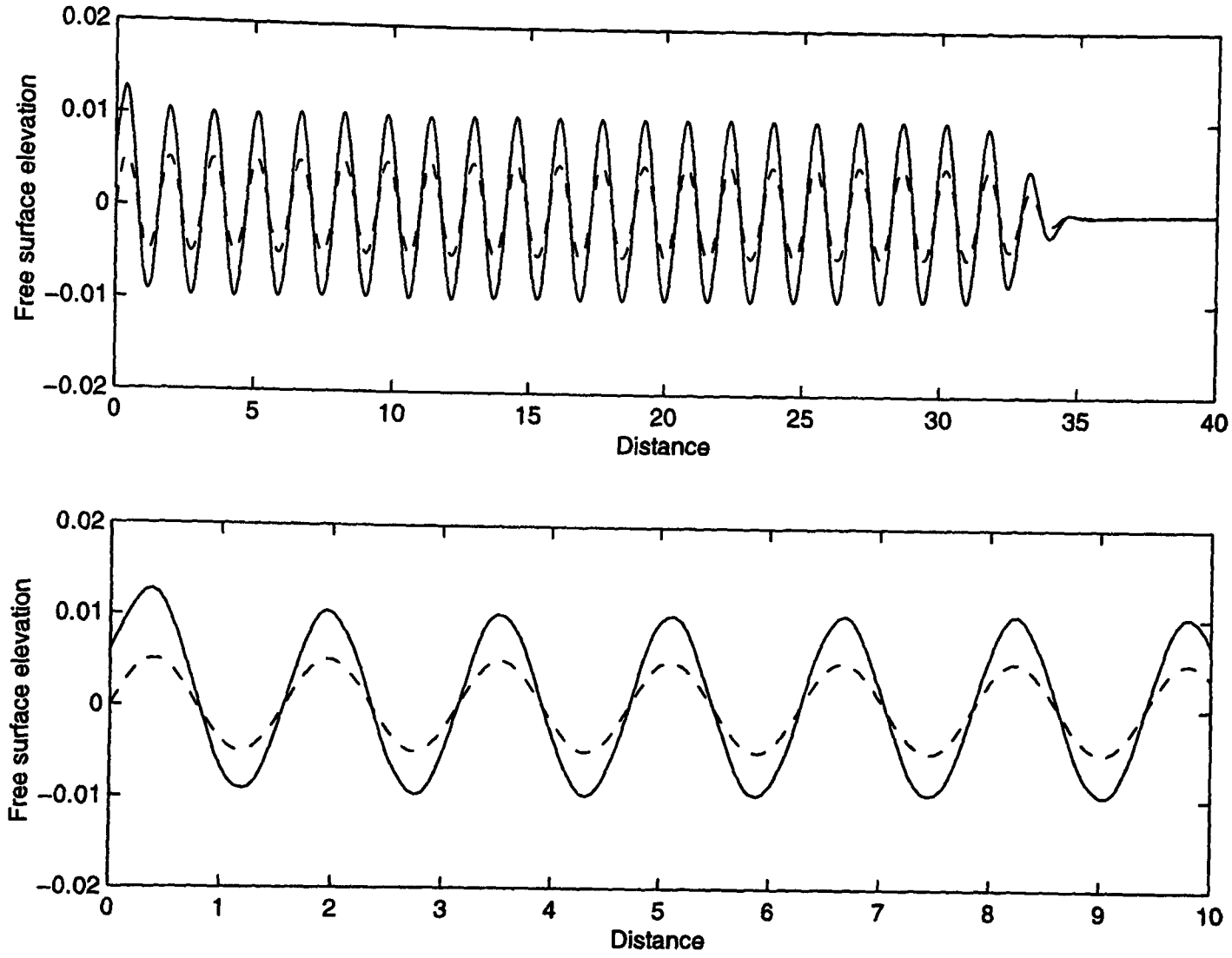

Figure 6.31 Space profile of the free surface elevation at $t = 60\pi = 188.4$

Wave generator velocity amplitude, $U_0 = 0.01$ Tank length = 40

Time step = $\pi/20 = 0.15707$ Mesh is 640 elements long and 16 elements deep

Solid line : Wave generator velocity is a function of time only
Dashed line : Wave generator velocity is a function of vertical position and time

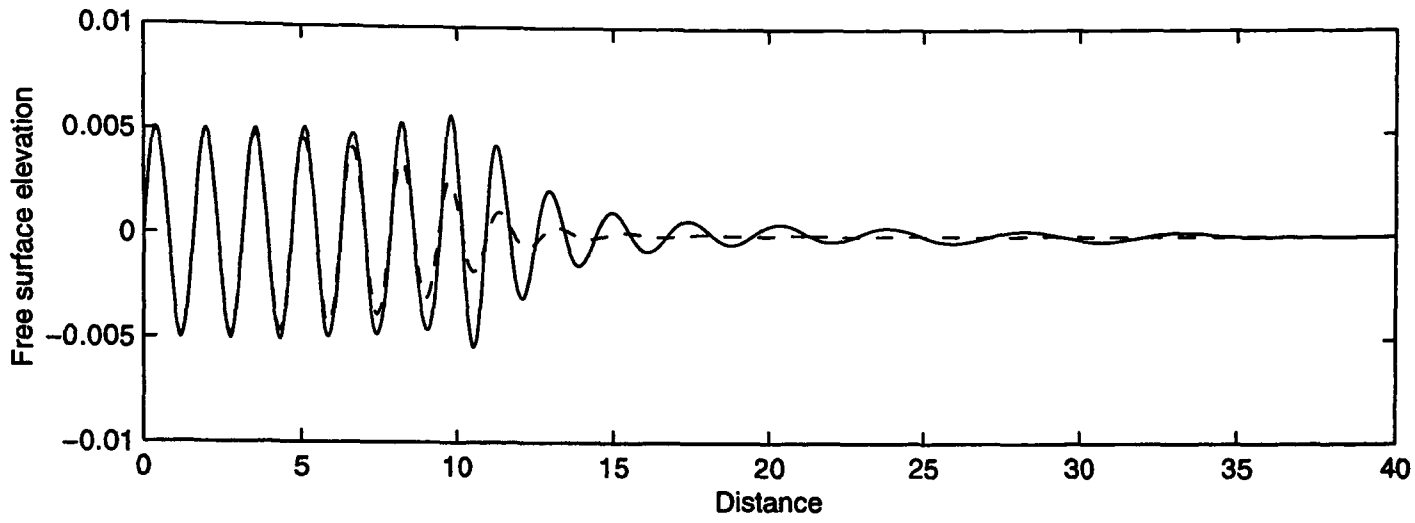

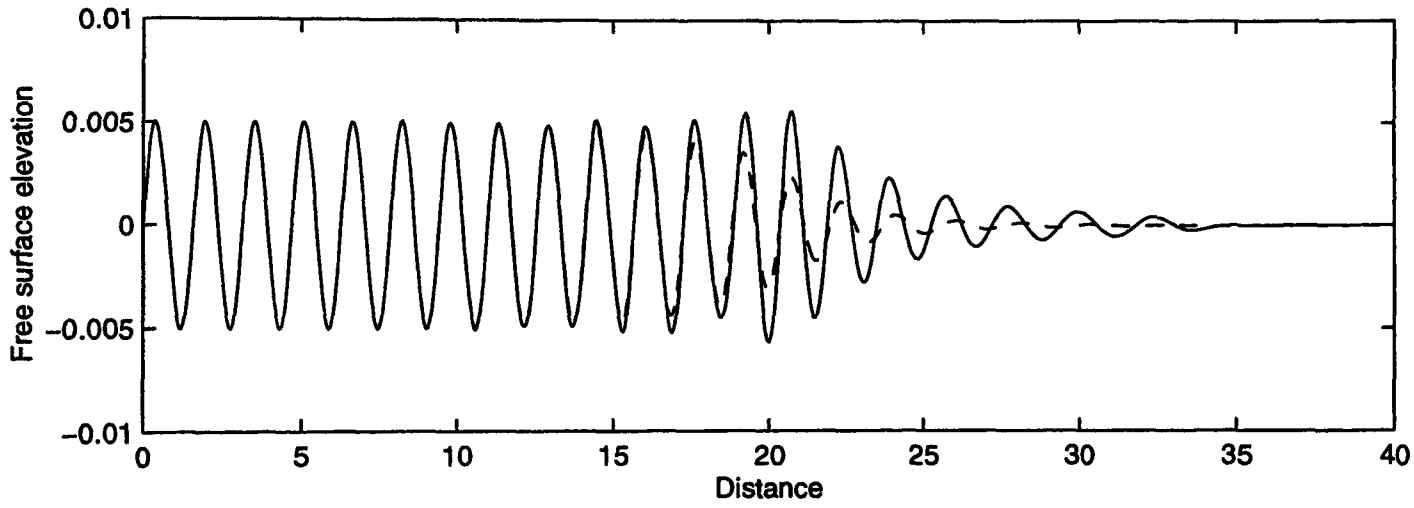

Figure 6.32 Space profiles of the free surface elevation

Wave generator velocity amplitude, $U_0 = 0.01$ Tank length = 40

Time step = $\pi/20 = 0.15707$ Mesh is 640 elements long and 16 elements deep

Dashed line : With ramp function
Solid line : Without ramp function

Top : $t = 16\pi = 50.3$
Bottom : $t = 30\pi = 94.2$

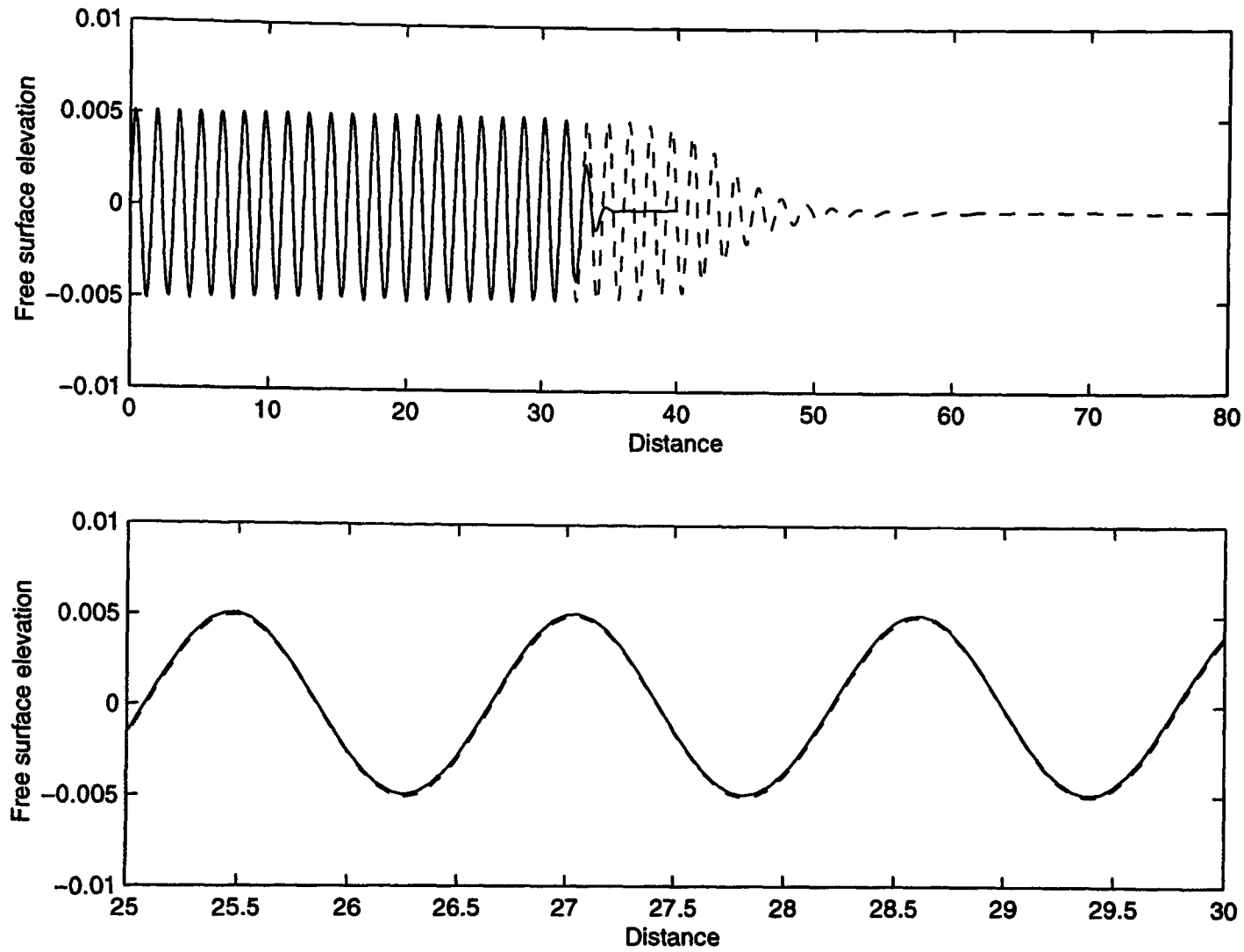

Figure 6.33 Space profile of the free surface elevation at $t = 60\pi = 188.4$

Wave generator velocity amplitude, $U_0 = 0.01$

Time step = $\pi/20 = 0.15707$

Dashed line : Tank length = 80 Mesh : 1280 by 16
Solid line : Tank length = 40 Mesh : 640 by 16

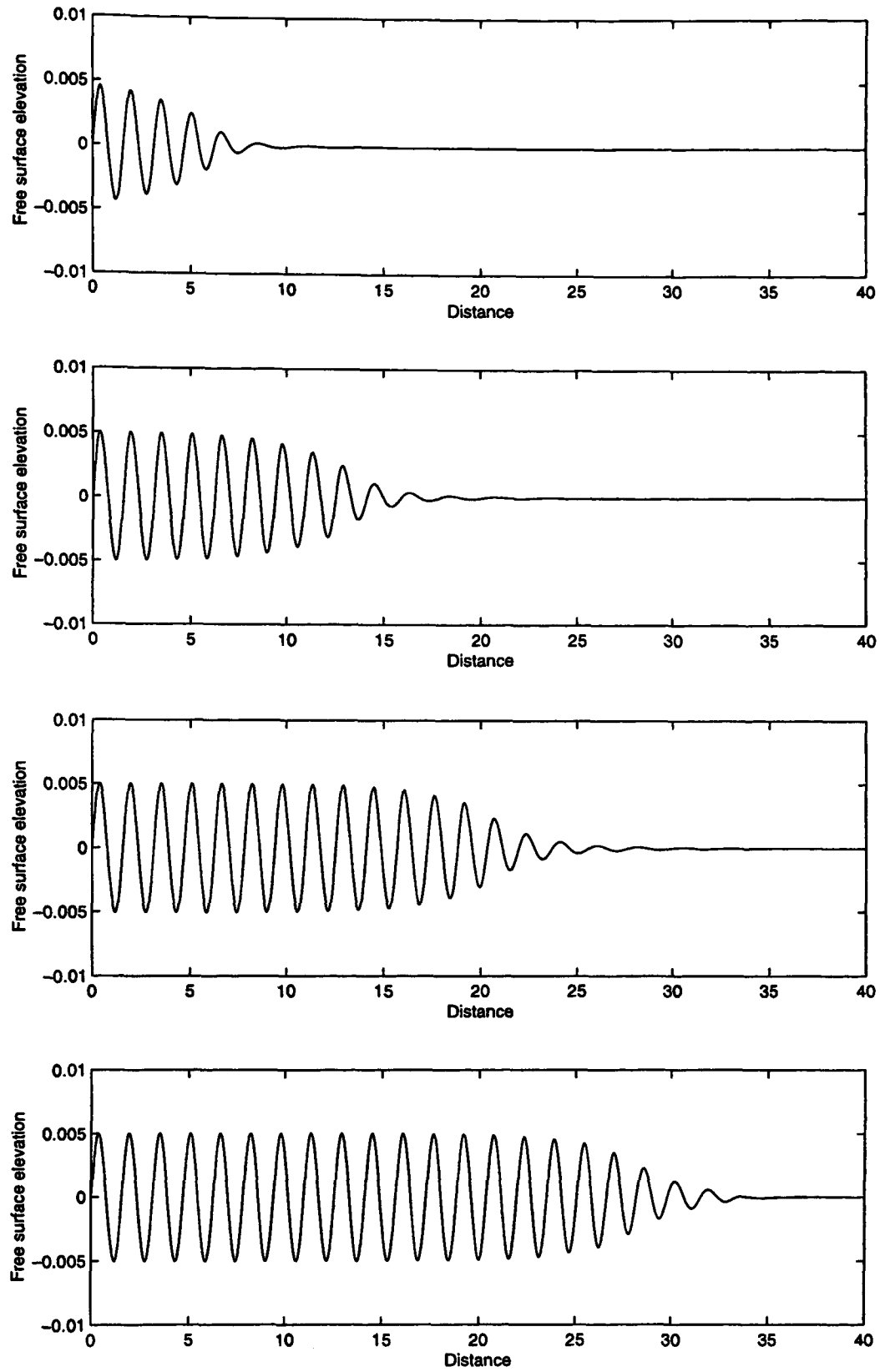

Figure 6.34 Space profiles of the free surface elevation

Wave generator velocity amplitude, $U_0 = 0.01$ Tank length = 40

From top to bottom:

$t = 10\pi = 31.4$, $t = 20\pi = 62.8$,
$t = 30\pi = 94.2$, $t = 40\pi = 125.7$

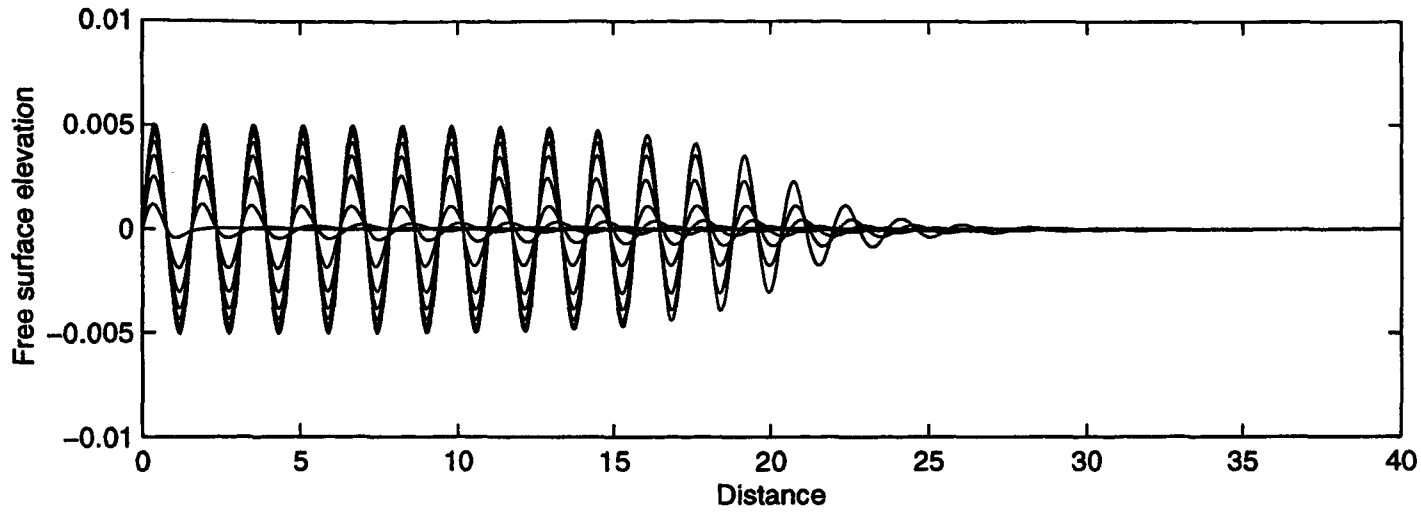

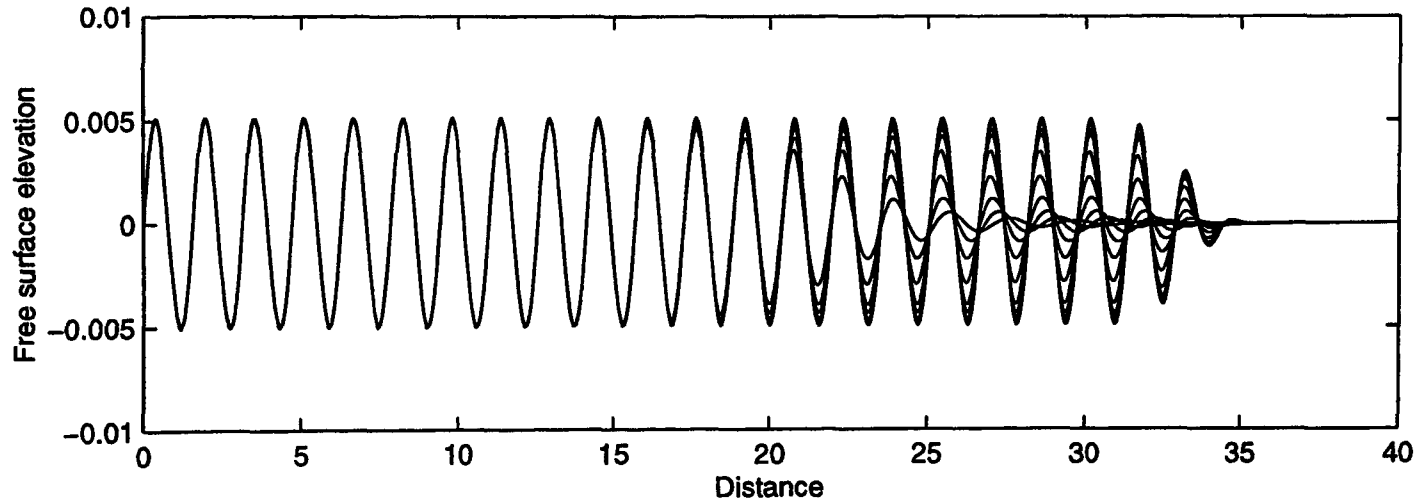

Figure 6.35 Space profiles of the free surface elevation

Wave generator velocity amplitude, $U_0 = 0.01$ Tank length = 40

Top : $t = 0$ to 30π at intervals of 2π
Bottom : $t = 30\pi$ to 60π at intervals of 2π

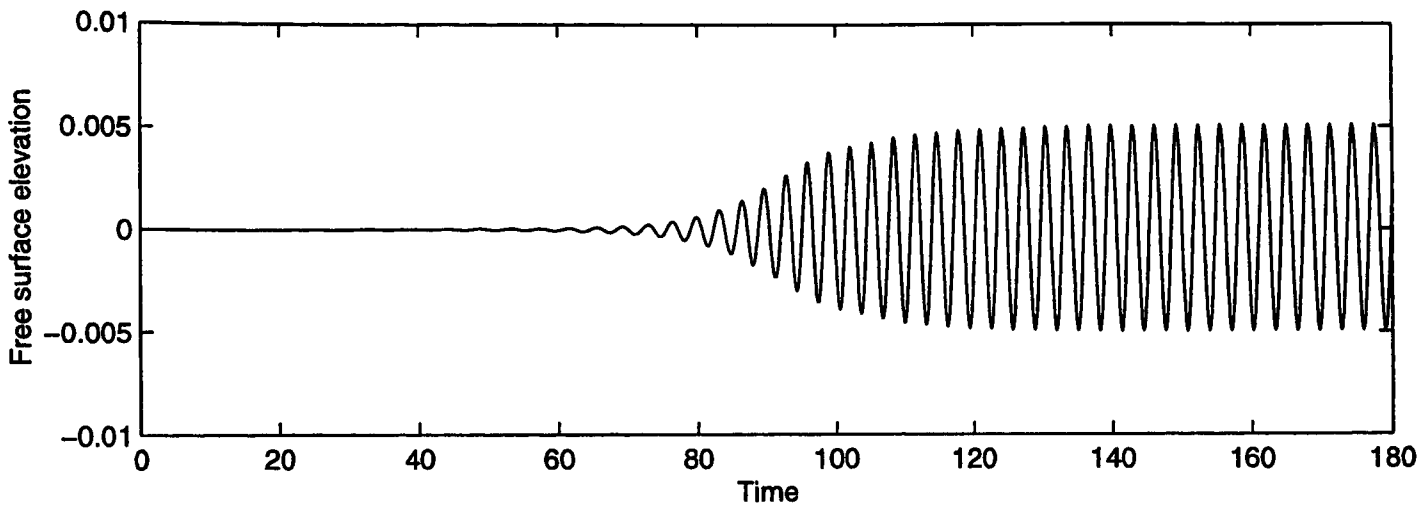

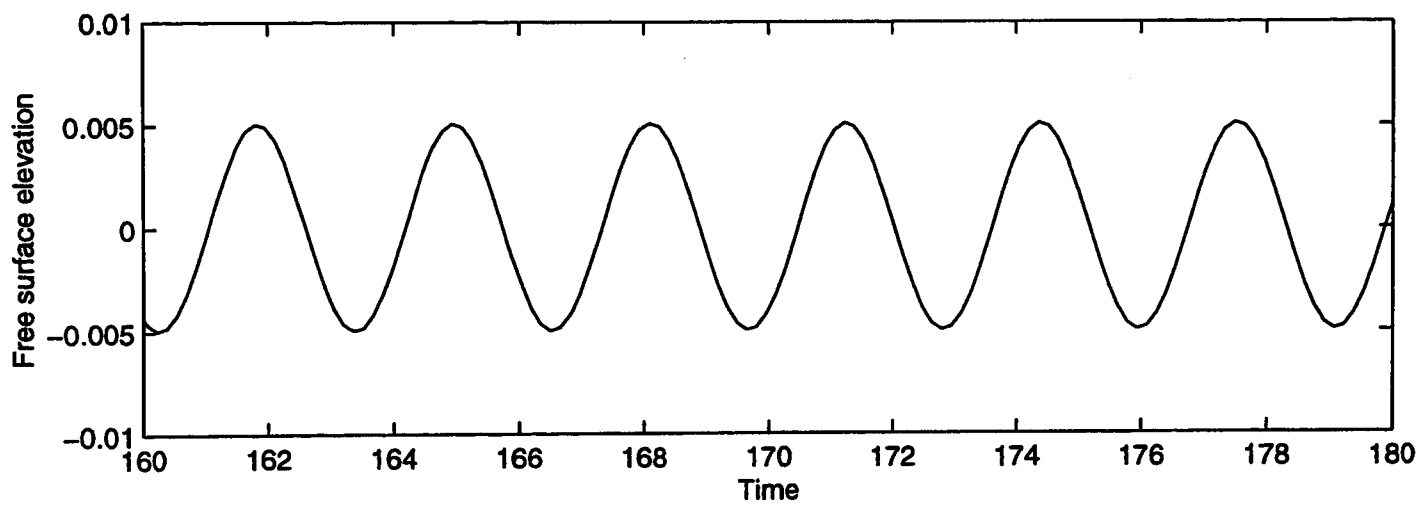

Figure 6.36 Time history of the free surface elevation at the centre of the tank (x = 20)

Wave generator velocity amplitude, U_0 = 0.01 Tank length = 40

Top : t = 0 to 180
Bottom : t = 160 to 180

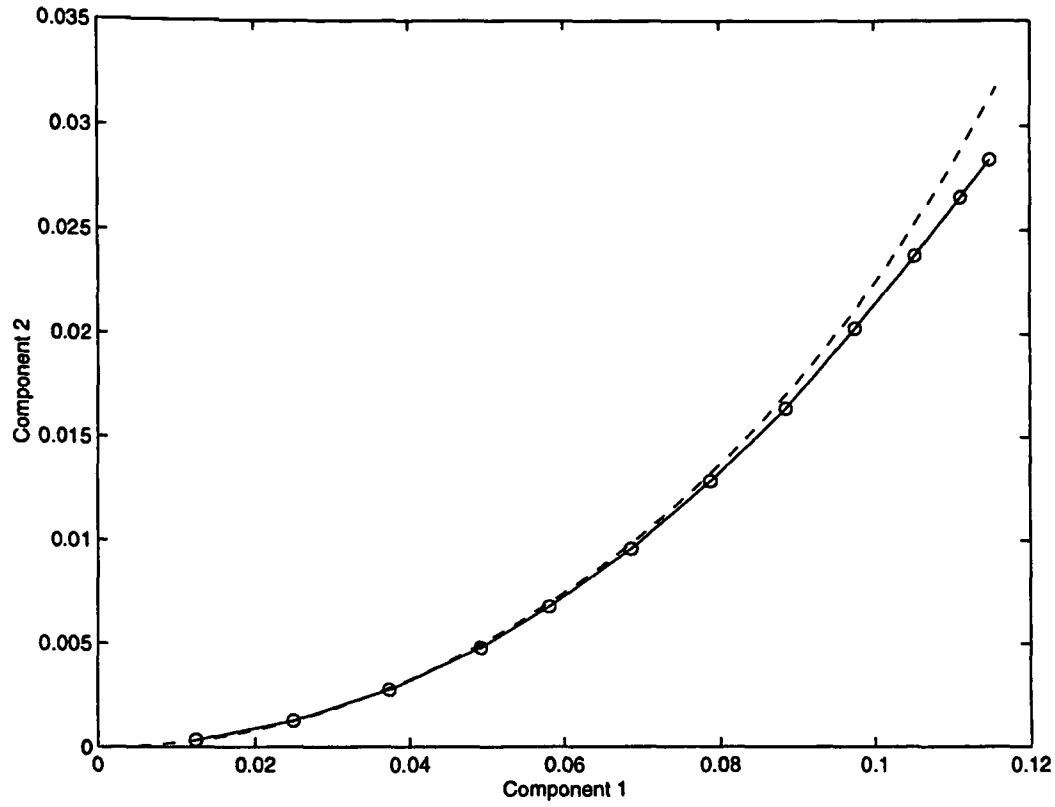

(*a*)

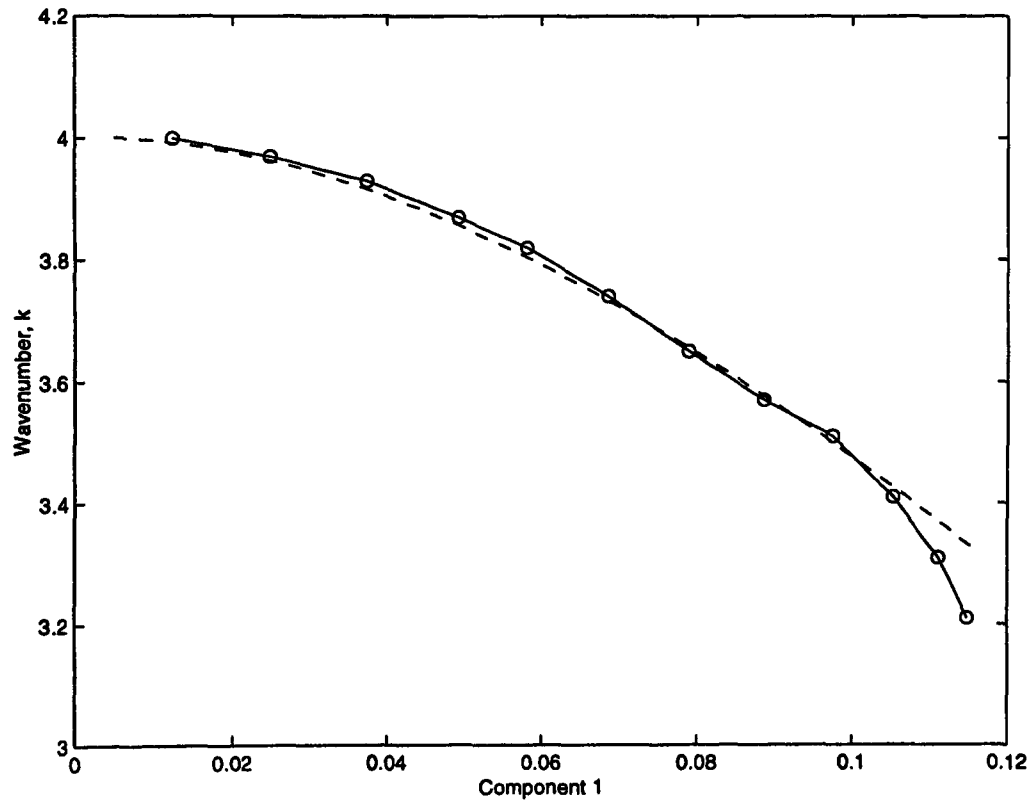

(*b*)

Figure 6.37 Comparison of sigma transform finite element solution with Stokes fifth order solution for regular travelling waves.

Components 1 and 2 are obtained from Fourier analysis of the free surface profile. Component 1 corresponds to the wavelength and component 2 to half the wave length. Circles joined by solid lines are the sigma transform results. The dashed line gives the values according to Stokes fifth order theory.

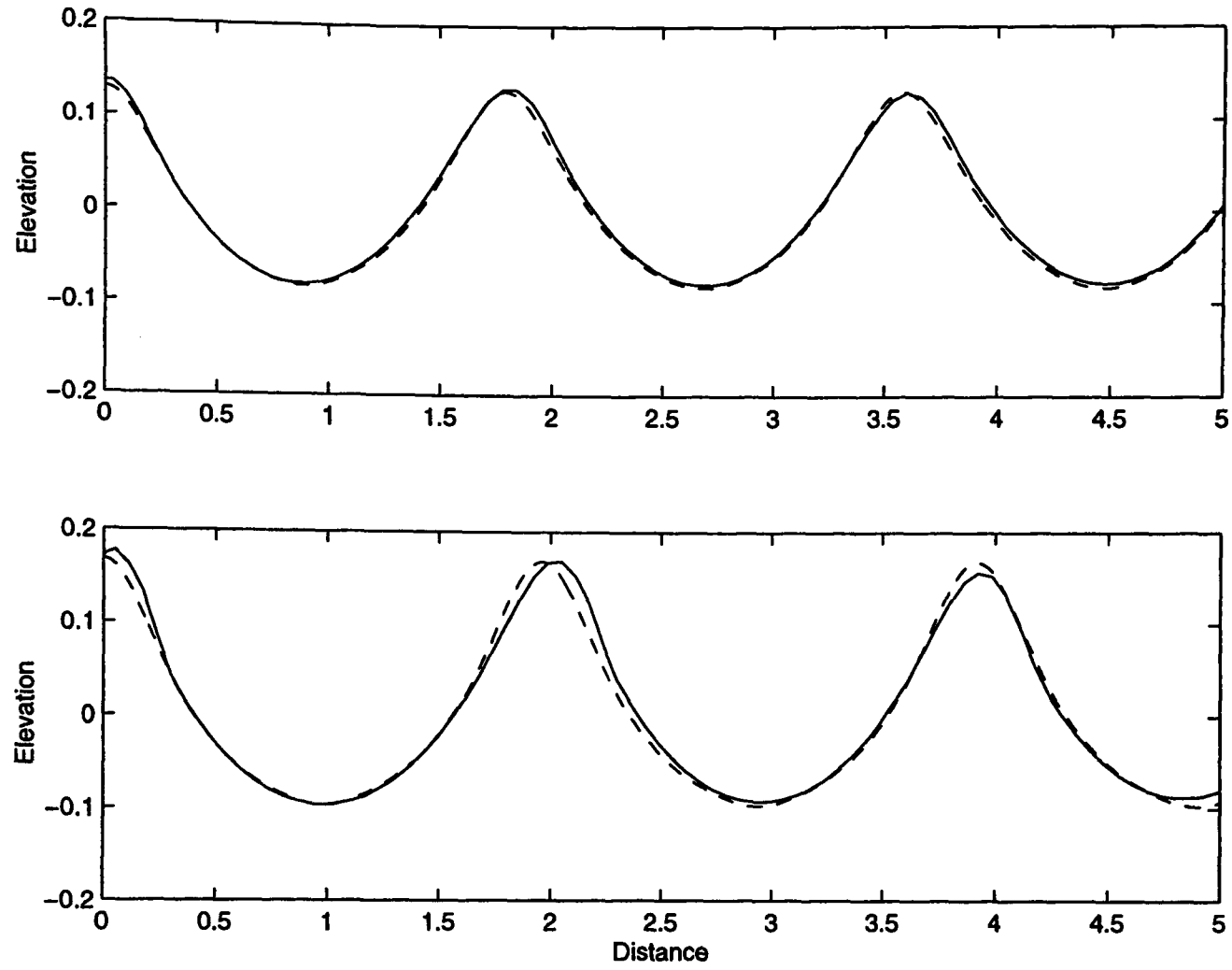

Figure 6.38 Comparison of sigma transformed finite element solution (solid) with Stokes fifth order theory (dashed).

Upper graph : Wave generator velocity amplitude, $U_0 = 0.225$
$H = 0.21$, $k = 3.51$, $kH/2 = 0.37$

Lower graph : Wave generator velocity amplitude, $U_0 = 0.3$
$H = 0.27$, $k = 3.21$, $kH/2 = 0.43$

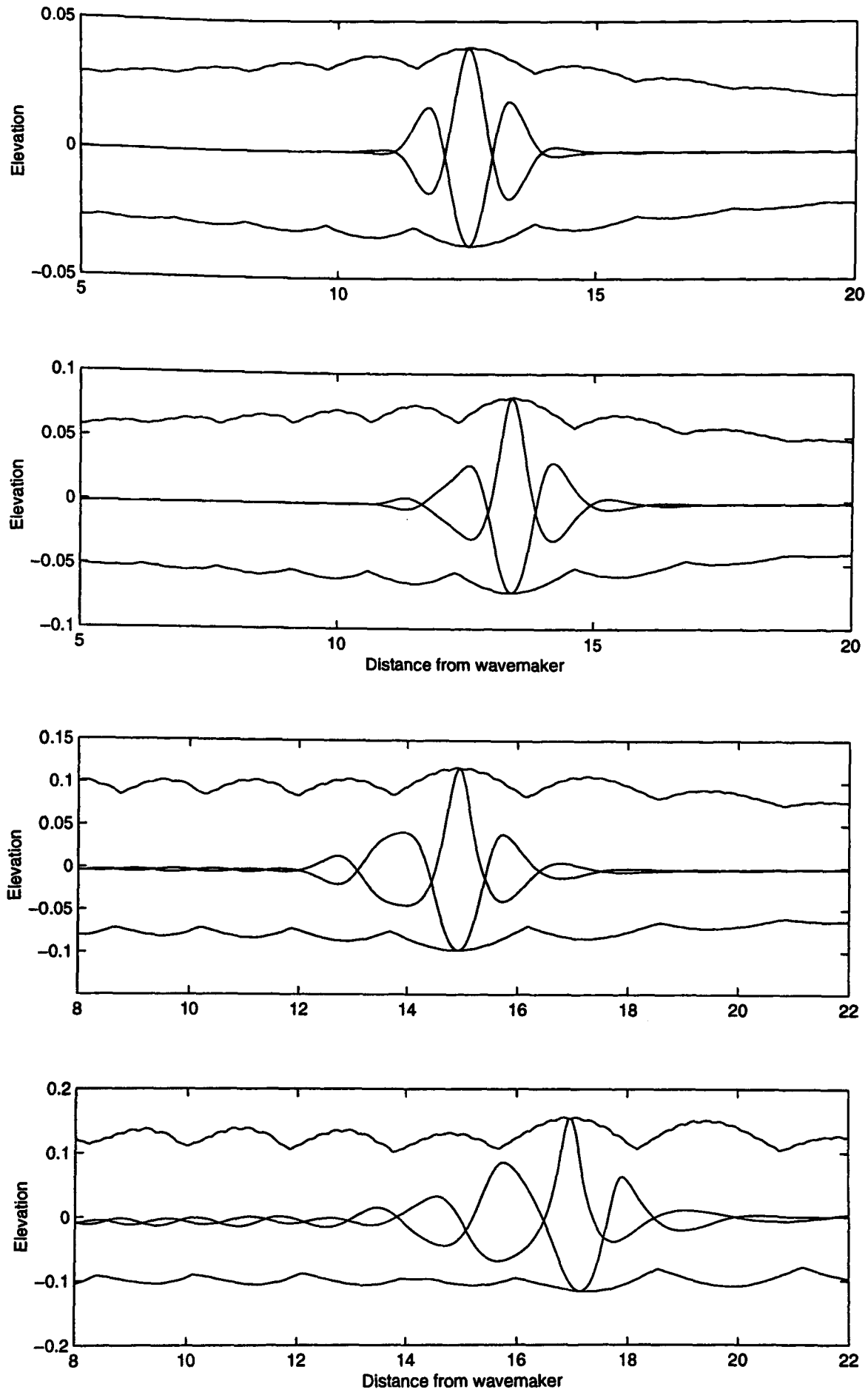

Figure 6.39 Free surface profiles at time of focus.

Results obtained using the standard finite element method. Each graph shows a focused peak and the corresponding focused trough result. The envelopes of maximum elevation over time for the peak case and minimum elevation for the trough case are shown. The four graphs correspond to wave generator velocity amplitudes of 1.0, 2.0, 3.0 and 4.0.

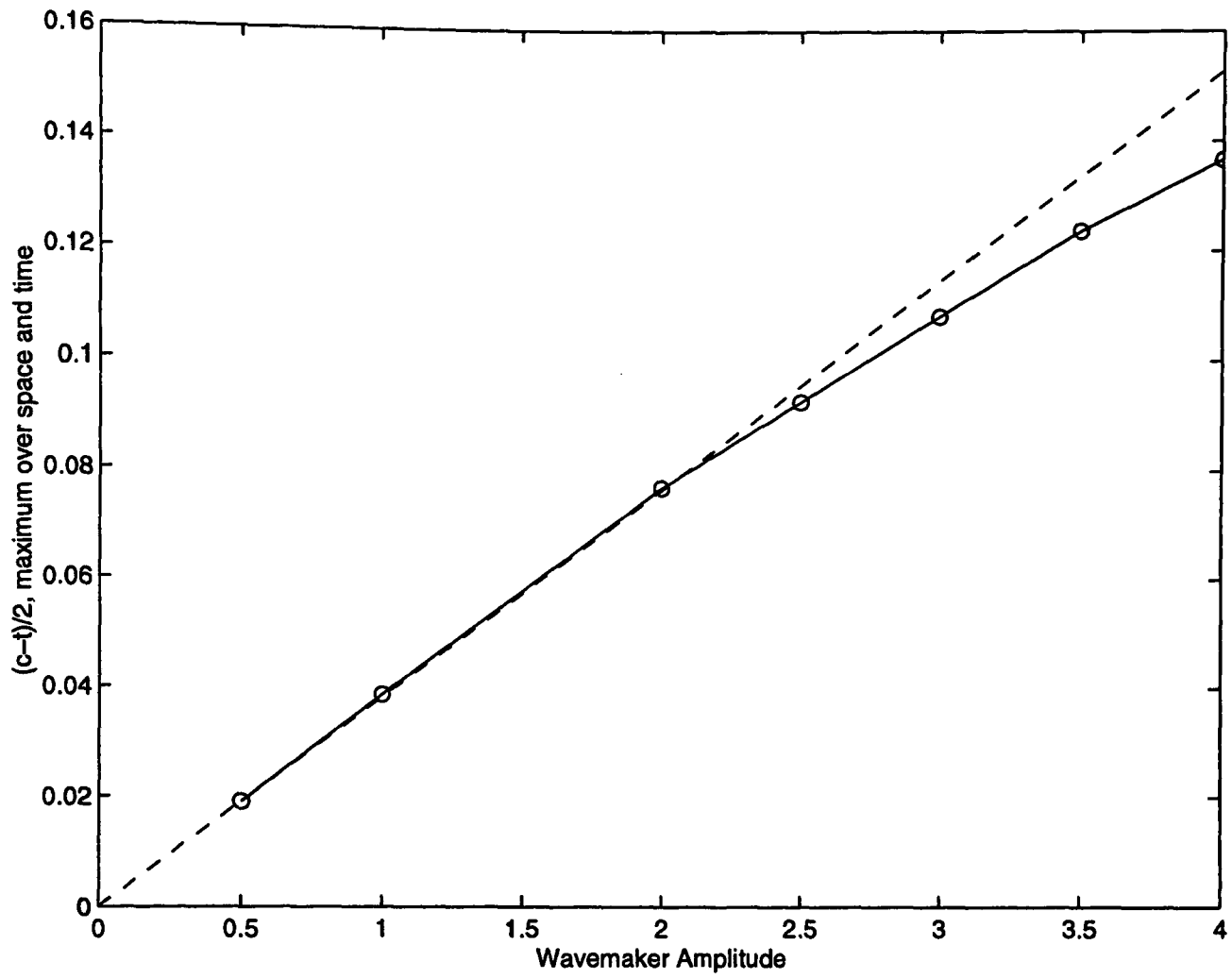

Figure 6.40 Graph of the maximum value of $(c\text{-}t)/2$ over all time and space against wave generator velocity amplitude for focused waves.

c is the elevation of the crest and t is the elevation of the trough

CHAPTER 7

RESULTS : THE FORCE ON A HORIZONTAL SUBMERGED CYLINDER DUE TO A TRAVELLING WAVE

7.1 Travelling Wave with Cylinder

The finite element program has been used to calculate the force exerted by travelling waves on a fixed submerged horizontal cylinder. For the results presented in the previous chapter, a purely structured mesh was used; for the following results the meshes are combinations of structured and unstructured sub-meshes. An example mesh containing a circular cylinder is shown in figure 7.1.

The force on the cylinder is calculated by integrating the pressure derived from Bernoulli's equation. The hydrodynamic pressure at any point in the flow is given by:

$$p = -\rho\frac{\partial\phi}{\partial t} - \rho\frac{1}{2}\left(\left(\frac{\partial\phi}{\partial x}\right)^2 + \left(\frac{\partial\phi}{\partial y}\right)^2\right) \quad . \tag{7.1}$$

Therefore, the corresponding force is given by the vector equation:

$$\begin{pmatrix} F_x \\ F_y \end{pmatrix} = -\rho\int_S \frac{\partial\phi}{\partial t}\begin{pmatrix} n_x \\ n_y \end{pmatrix} dS - \frac{\rho}{2}\int_S\left(\left(\frac{\partial\phi}{\partial x}\right)^2 + \left(\frac{\partial\phi}{\partial y}\right)^2\right)\begin{pmatrix} n_x \\ n_y \end{pmatrix} dS \ , \tag{7.2}$$

where the integrals are with respect to the distance around the cylinder surface S. The two terms on the right hand side of this equation will be referred to as terms $\mathbf{F}^a$ and $\mathbf{F}^b$, meaning,

$$\begin{pmatrix} F_x \\ F_y \end{pmatrix} = \begin{pmatrix} F_x^a \\ F_y^a \end{pmatrix} + \begin{pmatrix} F_x^b \\ F_y^b \end{pmatrix} \quad . \tag{7.3}$$

The total force can be considered to be the sum of first order components and second order components and so on. The first order component is proportional to the wave amplitude and oscillates at the wave frequency; the second order component is proportional to the square of the wave amplitude and comprises two subcomponents, a mean force and a component at twice the wave frequency, i.e. at 2ω. Similar statements can be made for higher order components. The velocity potential can be expressed as the perturbation expansion:

$$\phi = \epsilon\phi^{(1)} + \epsilon^2\phi^{(2)} + \epsilon^3\phi^{(3)} + \cdots\cdots \tag{7.4}$$

where $\phi^{(1)}$ is the first order component of the potential, $\phi^{(2)}$ is the second order component and so on; ε is a parameter related to the ratio of the wave amplitude and the wavelength. Likewise, the force on the cylinder is:

$$\begin{pmatrix} F_x \\ F_y \end{pmatrix} = \epsilon \begin{pmatrix} F_x^{(1)} \\ F_y^{(1)} \end{pmatrix} + \epsilon^2 \begin{pmatrix} F_x^{(2)} \\ F_y^{(2)} \end{pmatrix} + \epsilon^3 \begin{pmatrix} F_x^{(3)} \\ F_y^{(3)} \end{pmatrix} + \cdots\cdots \tag{7.5}$$

where the superscripts again refer to the order of the components.

Substituting equation 7.4 into equation 7.2 yields the following expressions for the first and second order force:

$$\begin{pmatrix} F_x^{(1)} \\ F_y^{(1)} \end{pmatrix} = -\rho \int_S \frac{\partial \phi^{(1)}}{\partial t} \begin{pmatrix} n_x \\ n_y \end{pmatrix} dS \tag{7.6}$$

and

$$\begin{pmatrix} F_x^{(2)} \\ F_y^{(2)} \end{pmatrix} = -\rho \int_S \frac{\partial \phi^{(2)}}{\partial t} \begin{pmatrix} n_x \\ n_y \end{pmatrix} dS - \frac{\rho}{2} \int_S \left(\left(\frac{\partial \phi^{(1)}}{\partial x} \right)^2 + \left(\frac{\partial \phi^{(1)}}{\partial y} \right)^2 \right) \begin{pmatrix} n_x \\ n_y \end{pmatrix} dS \quad . \tag{7.7}$$

Ogilvie (1963) provides the results of calculations for the first order force at the wave frequency on a submerged horizontal cylinder in water of infinite depth for a range of wave frequencies and cylinder radii. Figure 7.2 shows Ogilvie's results as a function of ν, h and a, where $\nu = \omega^2/g$, ω is the wave frequency, h is the distance from the centre of the cylinder to the mean free surface level and a is the cylinder radius. The graph gives a variable proportional to the magnitude of the first order force, which here will be called m_a. Ogilvie predicts that the magnitudes of the first order force in the x and y directions will be equal and 90 degrees out of phase. Therefore,

$$|F^{(1)}| = |F_x^{(1)}| = |F_y^{(1)}| = \frac{2\pi\rho g A}{\nu} m_a \quad . \tag{7.8}$$

Finite element simulations were performed using the standard method, in order to compare with Ogilvie's calculation of the first order force. Four cases have been examined, referred to as cases $A1$ to $A4$ and the relevant physical parameters are summarised in table 7.1. Table 7.1 gives the details of the various combinations of wave frequency, cylinder radius, and cylinder position, used for these four cases. The values of νa and $2\nu h$ are given in the table as these are the values needed to obtain m_a from figure 7.2. For the simulations corresponding to case $A1$, the domain is 15 units long, with a horizontal node spacing in the structured regions of 0.03125. The domain is 16 elements deep, with the node spacing such that it is eight times as large at the bottom of the tank as the top. A velocity varying with depth is imposed at the left boundary as described in chapter six; a ramp function is used to

build up the velocity gradually. The amplitude of the velocity is chosen such that the non-dimensional wave amplitude would be 0.005. The horizontal distance from the wave maker to the centre of the cylinder is 5 units; there are a further 5 units between the cylinder and start of the damping zone which is 5 units long. The Runge-Kutta time step is 0.0544; the time step is always chosen to be one fortieth of the wave period for the simulations described in this chapter. All simulations are run for 1600 Runge-Kutta timesteps, i.e. 40 wave periods. For case *A*2, the wavelength is approximately half that of case *A*1, therefore all the horizontal distance parameters just described are halved; for example, the total domain length for this case is 7.5. For these simulations, the domain length was approximately 20 times the wavelength and in the structured region, there are approximately 25 nodes per wavelength. For all the cases *A*1 to *A*4, the horizontal length of the unstructured mesh is 1.0.

The unstructured sections of the initial finite element mesh used for a number of these runs are displayed in figure 7.3. It can be seen that the mesh density varies; it is finer at the free surface and at the surface of the cylinder.

Time histories of the two components of the force, $\mathbf{F}^a$ and $\mathbf{F}^b$, obtained from the finite element simulations for case *A*3 are shown in figures 7.4 and 7.5 respectively. The force amplitude is initially zero. The amplitudes of F_x^a and F_y^a increase as the wave reaches the cylinder and build up to a steady value. F_x^b and F_y^b also increase from zero; after steady state has been reached, F_y^b is seen to oscillate at twice the wave frequency about a positive mean.

Fourier analysis of the time histories of F_x and F_y gives the magnitudes of the components at the wave frequency, ω and twice the wave frequency, 2ω. Neglecting third

order and higher components, these correspond to the first order oscillatory component and the second order oscillatory component in the x and y directions. Table 7.2 shows Ogilvie's prediction of the magnitude of the first order force per unit wave amplitude for the four cases. The values in the second and third columns multiply together to give the value in the fourth; ρ and g are taken to be unity in order to give non-dimensional results. Dimensional values for the force can be obtained by multiplying the non-dimensional values by $\rho g d^2$. Table 7.3 gives the results of the standard finite element method for the magnitude of first order force in the x and y directions. The term *segments* in the third column of the table refers to the number of segments around the cylinder in the finite element mesh. On the whole, there is reasonable agreement between the finite element results and Ogilvie, though the finite element results tend to be slightly smaller. It is possible that mesh refinement would improve the agreement. These runs were repeated using the sigma transform method in the structured regions. The results were indistinguishable from the standard finite element results to the level of accuracy used in the data presentation.

Ogilvie presents a graph allowing the mean second order vertical force to be calculated; this is a constant force in the y direction proportional to the square of the wave height. The graph is reproduced here as figure 7.6. The value m_b from this graph is related to the second order mean by the following equation:

$$\overline{F_y^{(2)}} = 2\pi\rho g A^2 m_b \quad . \tag{7.9}$$

Table 7.4 gives Ogilvie's prediction for the mean second order force per unit amplitude for cases $A1$ to $A4$. The results of the finite element method, obtained by taking the average

value of F_y^b for a section of the time history, once the system has reached steady state, are given in table 7.5. Fourth order and higher contributions to the mean force are assumed to be negligible. Close agreement can be seen between the finite element results and Ogilvie's predictions. Again, the sigma transform program gave identical results to those of the standard finite element scheme.

Wu and Eatock Taylor (1990) present results for the second order oscillatory component of the force on a submerged horizontal cylinder in water of finite depth. Figure 7.7 reproduces two of the graphs from Wu and Eatock Taylor's paper. The graphs show the factors m_c and m_d as functions of ν, a and d for the case where $h = 2a$. The second order force is given by the equation:

$$\begin{pmatrix} |F_x^{(2)}| \\ |F_y^{(2)}| \end{pmatrix} = \rho g A^2 \begin{pmatrix} m_c \\ m_d \end{pmatrix} \quad . \tag{7.10}$$

Four cases, referred to as cases $B1$ to $B4$, are examined using the standard and sigma transform versions of the finite element method, for the purpose of comparing with Wu and Eatock Taylor's results. These four cases are summarised in table 7.6. Table 7.7 presents the predictions of the force per unit amplitude on the cylinder of Wu and Eatock Taylor (1990). The results of the standard finite element method are given in table 7.8. The second order components were obtained from a Fourier analysis of the time history of the total force on the cylinder. For cases $B1$ and $B2$, three different runs were undertaken, each with a different number of segments around the cylinder. The initial unstructured meshes used for four of these runs is shown in figure 7.8. Case $B1$ shows reasonable agreement between Wu

and Eatock Taylor's results and the finite element results, and the mesh dependence is not great. Case $B3$ also shows reasonable agreement. However, good agreement is not found for cases $B2$ or $B4$. Case $B2$ shows a large degree of mesh dependence. $B2$ and $B4$ have higher frequencies than $B1$ and $B3$, and are effectively deep water cases. For this reason, the meshes chosen may not provide adequate vertical resolution close to the free surface. This is a possible explanation for inferior results for $B2$ and $B4$.

Chaplin (1984) obtained experimental results for the first and second order oscillatory components and the mean second order component of the force on a horizontal cylinder due to a travelling wave. Six of the test cases used by Chaplin are simulated here and are called cases C to H, the same labels used by Chaplin. Table 7.9 summarises the non-dimensionalised physical parameters for each case. Chaplin presented comparisons of his results with Ogilvie's for the first order force; this comparison is given here in table 7.10. The effect of mesh fineness around the cylinder has been investigated for cases C to F. Each case has been modelled with 32, 64 and 128 segments around the cylinder. Figures 7.9 and 7.10 show the initial unstructured section of the mesh for a number of cases.

Table 7.11 presents the results of the standard finite element program for the first order force on the cylinder. Some mesh dependence can be seen in the results, but it is not great. Reasonable agreement is found between the finite element results and Ogilvie's and Chaplin's results for the linear force. The values of the second order mean force given by Ogilvie and Chaplin for the six cases are given in table 7.12. These values can be compared with the finite element results in table 7.13. Again, good agreement can be seen. There is no mesh dependence in the results for case D, and the mesh dependence is largest for case

F.

Vada (1987) presents theoretical results for the second order oscillatory force and compares those results to the experimental results of Chaplin (1984). This comparison is given in table 7.14. The finite element results for the second order oscillatory force are presented in table 7.15. It can been seen that the mesh dependence for these results is greater than for the other two force components. Also, the agreement of the finite element results with Vada and Chaplin is not quite as great as with the other comparisons. However, clear correspondence can be seen between the finite element results and those of Vada and Chaplin.

All results for the force for cases *C* to *H* obtained using the sigma transform version of the program, were identical to those obtained from the standard version of the program.

Figures 7.11 to 7.14 give further details of the results for case *E*, where 32 segments around the cylinder have been used. Figure 7.11 shows the effect of the cylinder on the free surface. There is a phase shift of the wave as it passes over the cylinder, but no change in the amplitude. The wave before the cylinder is virtually unchanged. This is in agreement with the theoretical result of Dean (1948) that to first order, the reflection coefficient of a submerged cylinder is zero.

The velocity field around the cylinder is illustrated in figure 7.12 at four times during a wave period. Each velocity vector corresponds to a node in the mesh. In figure 7.12(*a*), the wave crest is over the cylinder and the fluid is moving from left to right. In the subsequent three figures it is seen that each quarter of a wave period the main direction of

fluid changes by an angle of 90 degrees.

Figure 7.13 illustrates the contours of the dynamic pressure field at the same four times as figure 7.12. In figure 7.13(*a*), the wave crest is over the cylinder; the dynamic pressure is larger above the cylinder than below it, and approximately equal either side of it. This results in a downward force on the cylinder. In figure 7.13(*b*), the force is to the left, in (*c*) upwards and in (*d*) to the right. This clockwise rotation of the force vector is also illustrated in figure 7.14 which shows the time history of the x and y components of the force. The circled points correspond to the times illustrated in figures 7.11 to 7.13.

7.2 Conclusions

The finite element models have been used to calculate the force on a submerged horizontal cylinder. Close agreement has been found with the theoretical results of Ogilvie (1963) and the experimental results of Chaplin (1984) for the first order force and the second order mean force. Agreement has also been found between the finite element results and the theoretical results of Wu and Eatock Taylor (1990) and Vada (1987) and the experimental results of Chaplin (1984) for the second order oscillatory force, although here the agreement is not as great. Where the best agreement between the finite element results and other theories was obtained, the results also showed the highest degree of mesh independence. Both versions of the finite element method have been found to be robust and reliable and should prove suitable for use in solving other non-linear problems involving waves and structures.

Table 7.1 Description of cases for comparison with Ogilvie (1963).

Case	ω	a	h	νa	$2\nu h$
A1	2.88675	0.06	0.075	0.5	1.25
A2	4.08248	0.06	0.075	1.0	2.5
A3	4.08248	0.06	0.12	1.0	4.0
A4	5.77350	0.06	0.0825	2.0	5.5

Table 7.2 First order force on cylinder - Ogilvie (1963).

Case	m_a	$2\pi\rho g/\nu$	$\lvert F_x^{(1)}\rvert/A = \lvert F_y^{(1)}\rvert/A$
A1	0.16	0.75398	0.121
A2	0.19	0.37699	0.0716
A3	0.12	0.37699	0.0452
A4	0.12	0.18850	0.0226

Table 7.3 First order force on cylinder - standard finite element results.

Run	Case	Segments	$\lvert F_x^{(1)}\rvert/A$	$\lvert F_y^{(1)}\rvert/A$
1	A1	32	0.113	0.118
2	A2	32	0.0639	0.0640
3	A3	64	0.0394	0.0427
4	A4	64	0.0200	0.0203

Table 7.4 Second order mean force on cylinder - Ogilvie (1963)

Case	m_b	$2\pi\rho g$	$F_y^{(2)}/A^2$ (mean)
A1	0.25	6.2832	1.57
A2	0.19	6.2832	1.19
A3	0.025	6.2832	0.157
A4	0.06	6.2832	0.377

Table 7.5 Second order mean force on cylinder - standard finite element results

Run	Case	Segments	$F_y^{(2)}/A^2$ (mean)
1	A1	32	1.52
2	A2	32	1.13
3	A3	64	0.158
4	A4	64	0.403

Table 7.6 Description of cases for comparison with Wu and Eatock Taylor (1990).

Case	ω	a	h	νa	$2\nu h$
B1	1	0.25	0.5	0.25	1.0
B2	2	0.25	0.5	1.0	4.0
B3	1	0.25	0.4375	0.25	0.875
B4	2	0.25	0.4375	1.0	3.5

Table 7.7 Second order oscillatory force on cylinder - Wu and Eatock Taylor (1990).

Case	$\lvert F_x^{(2)}\rvert/A^2$	$\lvert F_y^{(2)}\rvert/A^2$
B1	0.38	0.49
B2	0.05	0.04
B3	0.65	0.72
B4	0.13	0.12

Table 7.8 Second order oscillatory force on cylinder - standard finite element result.

Run	Case	Segments	$\lvert F_x^{(2)}\rvert/A^2$	$\lvert F_y^{(2)}\rvert/A^2$
5	B1	16	0.464	0.450
6	B1	32	0.453	0.426
7	B1	64	0.452	0.442
8	B2	16	0.133	0.0974
9	B2	32	0.0280	0.0294
10	B2	64	0.0119	0.111
11	B3	32	0.612	0.814
12	B4	32	0.0276	0.00949

Table 7.9 Description of cases for comparison with Chaplin (1984).

Case	ω	a	h	νa	$2\nu h$
C	1.8495	0.06	0.18	0.205	1.23
D	2.4660	0.06	0.18	0.365	2.19
E	1.8495	0.06	0.12	0.205	0.821
F	2.4660	0.06	0.12	0.365	1.46
G	3.0825	0.06	0.12	0.570	2.28
H	3.6990	0.06	0.12	0.821	3.28

Table 7.10 First order force on cylinder - Ogilvie (1963) and Chaplin (1984)

Case	$\lvert F_x^{(1)}\rvert/A = \lvert F_y^{(1)}\rvert/A$ - Ogilvie (1963)	$\lvert F_x^{(1)}\rvert/A = \lvert F_y^{(1)}\rvert/A$ - Chaplin (1984)
C	0.0430	0.0415
D	0.0450	0.0451
E	0.0576	0.0577
F	0.0691	0.0673
G	0.0642	0.0649
H	0.0513	0.0542

Table 7.11 First order force on cylinder - standard finite element results

Run	Case	Segments	$\|F_x^{(1)}\|/A$	$\|F_y^{(1)}\|/A$
13	C	32	0.0435	0.0429
14	C	64	0.0437	0.0433
15	C	128	0.0438	0.0433
16	D	32	0.0440	0.0461
17	D	64	0.0447	0.0460
18	D	128	0.0447	0.0460
19	E	32	0.0590	0.0584
20	E	64	0.0589	0.0586
21	E	128	0.0589	0.0582
22	F	32	0.0692	0.0722
23	F	64	0.0697	0.0713
24	F	128	0.0688	0.0708
25	G	128	0.0624	0.0624
26	H	128	0.0538	0.0512

Table 7.12 Second order mean force on cylinder - Ogilvie (1963) and Chaplin (1984)

Case	$F_y^{(2)}/A^2$ (mean) - Ogilvie (1963)	$F_y^{(2)}/A^2$ (mean) - Chaplin (1984)
C	0.0914	0.0944
D	0.102	0.101
E	0.190	0.187
F	0.273	0.268
G	0.255	0.230
H	0.195	0.194

Table 7.13 Second order mean force on cylinder - standard finite element results

Run	Case	Segments	$F_y^{(2)}/A^2$ (mean)
13	C	32	0.0930
14	C	64	0.0939
15	C	128	0.0941
16	D	32	0.106
17	D	64	0.106
18	D	128	0.106
19	E	32	0.205
20	E	64	0.203
21	E	128	0.199
22	F	32	0.301
23	F	64	0.293
24	F	128	0.285
25	G	128	0.248
26	H	128	0.209

Table 7.14 Second order oscillatory force on cylinder - Vada (1987) and Chaplin (1984)

Case	$\|F_x^{(2)}\|/A^2 = \|F_y^{(2)}\|/A^2$ - Vada (1987)	$\|F_x^{(2)}\|/A^2 = \|F_y^{(2)}\|/A^2$ - Chaplin (1984)
C	0.06	0.05
D	0.04	0.05
E	0.31	0.39
F	0.33	0.33
G	0.21	0.21
H	0.09	0.16

Table 7.15 Second order oscillatory force on cylinder - standard finite element results

Run	Case	Segments	$\|F_x^{(2)}\|/A^2$	$\|F_y^{(2)}\|/A^2$
13	C	32	0.0576	0.0551
14	C	64	0.0521	0.0617
15	C	128	0.0482	0.0609
16	D	32	0.0354	0.0164
17	D	64	0.0284	0.0348
18	D	128	0.0195	0.0304
19	E	32	0.424	0.225
20	E	64	0.349	0.288
21	E	128	0.301	0.276
22	F	32	0.446	0.227
23	F	64	0.279	0.365
24	F	128	0.230	0.314
25	G	128	0.176	0.164
26	H	128	0.0696	0.102

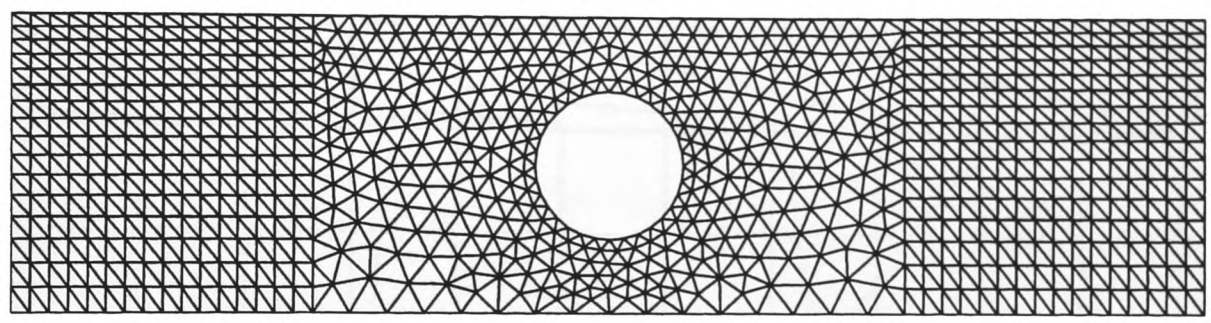

Figure 7.1 Combination of structured and unstructured mesh

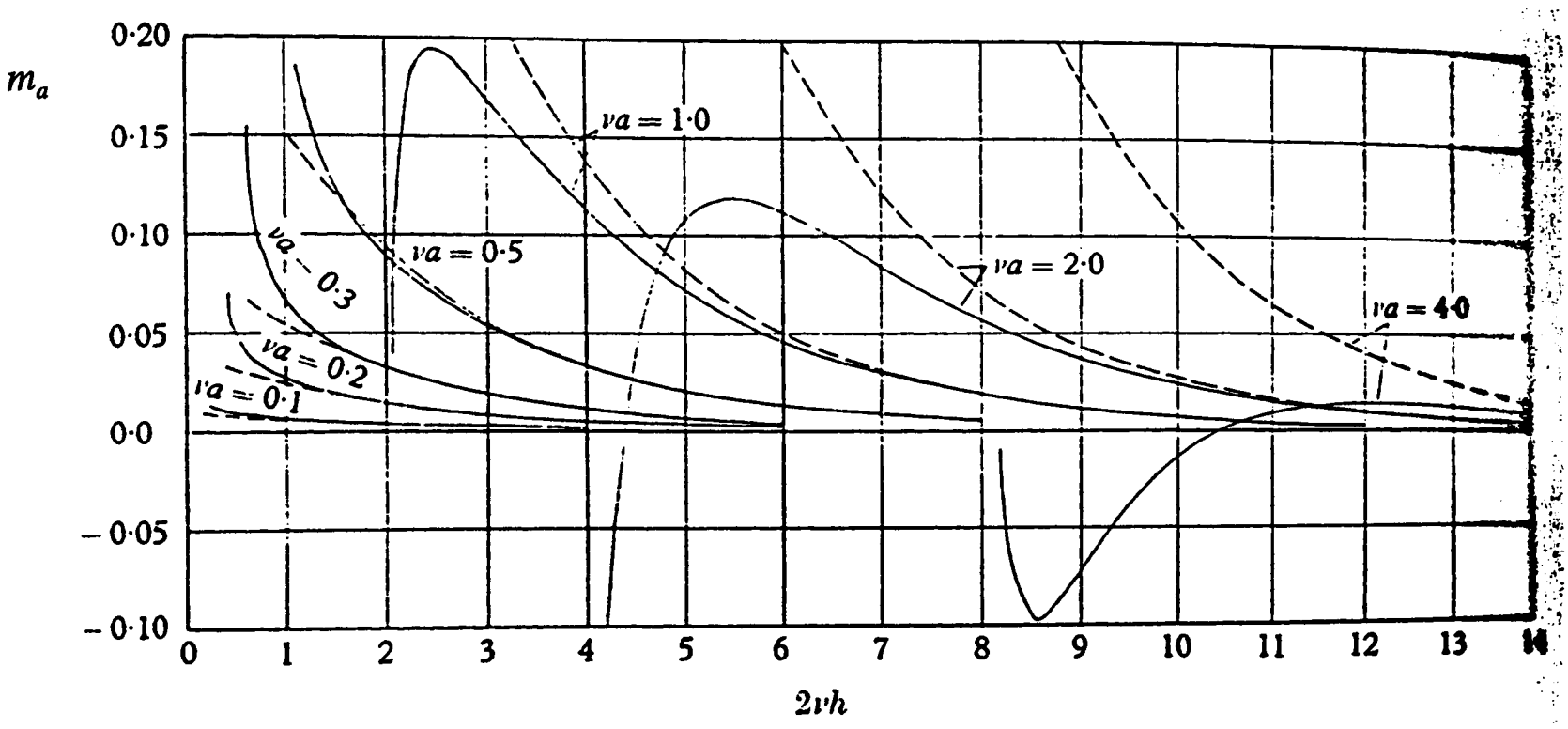

Figure 7.2 First order oscillatory force - Ogilvie (1963)

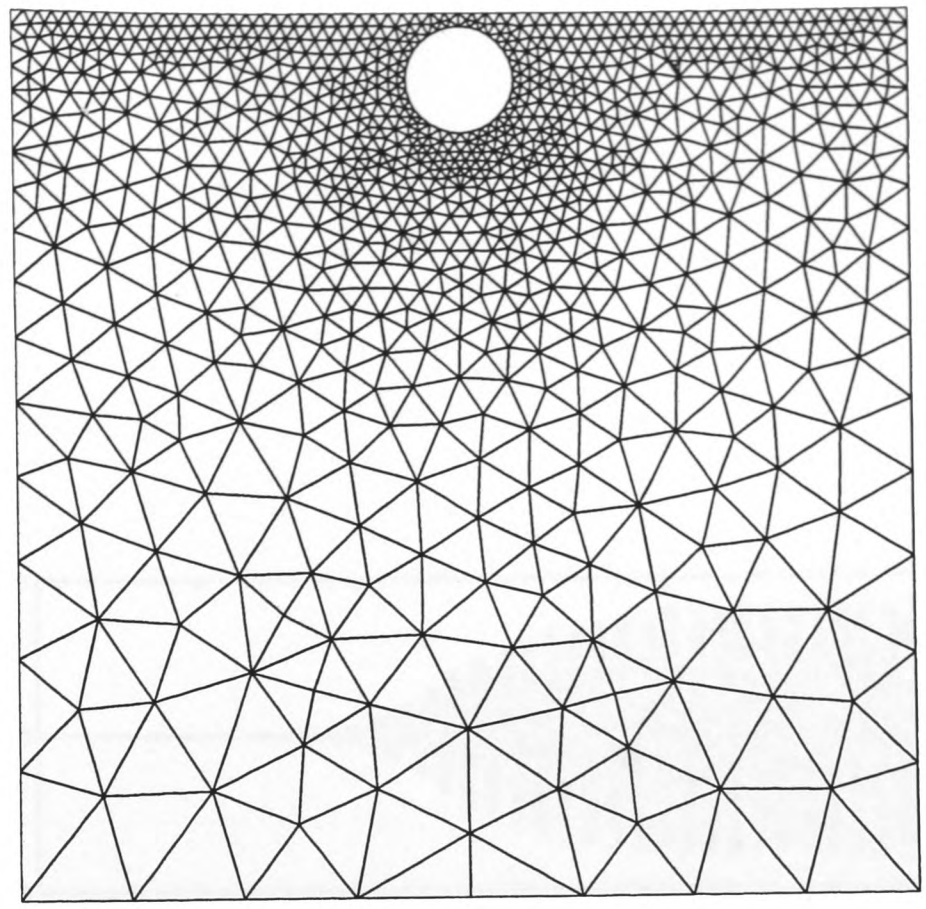

(*a*) Run 1, Case *A*1, 32 cylinder segments, $a = 0.06$, $h = 0.075$

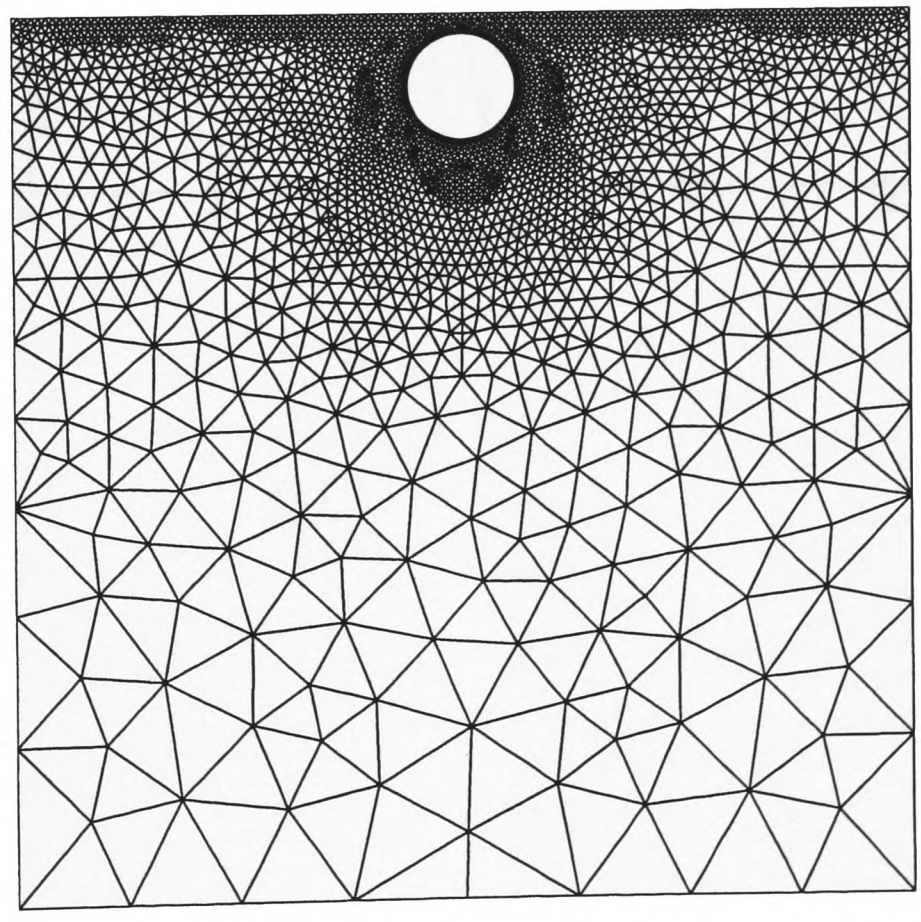

(*b*) Run 4, Case *A*4, 64 cylinder segments, $a = 0.06$, $h = 0.0825$

Figure 7.3 Unstructured sections of initial finite element meshes

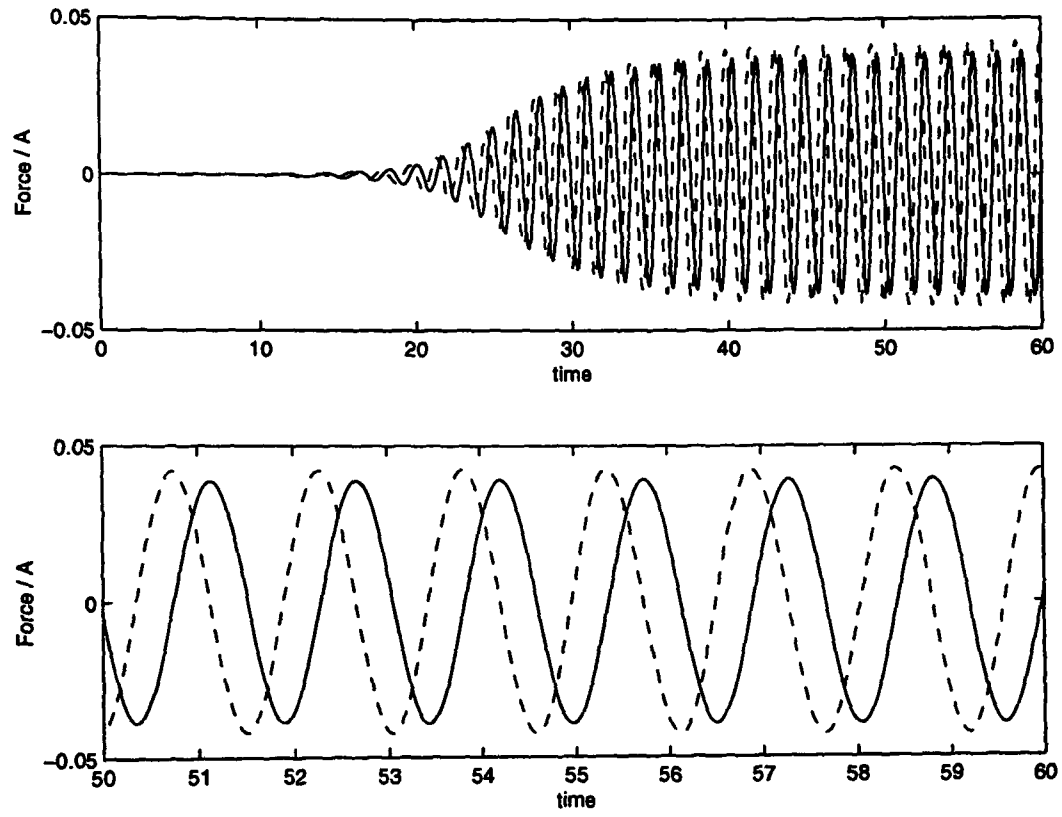

Figure 7.4 Force on cylinder. Component F^a for case $A3$

Solid line : x component
Dashed line : y component

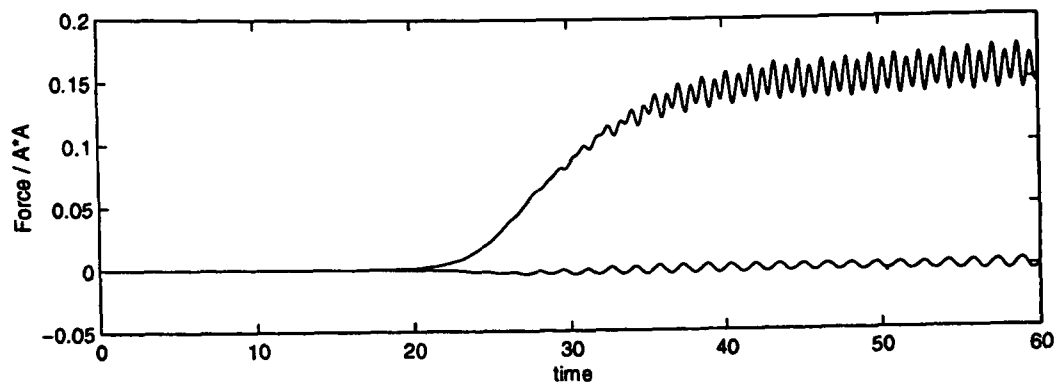

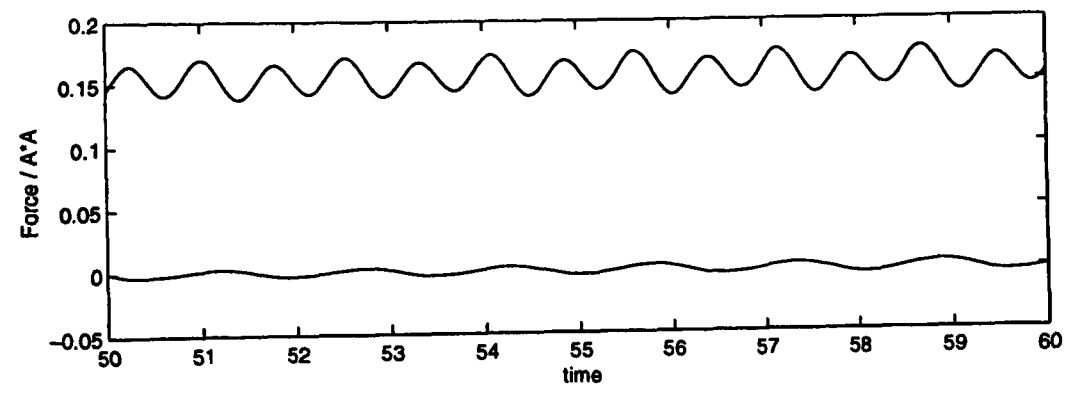

Figure 7.5 Force on cylinder. Component $\boldsymbol{F}^b$ for case $A3$

Lower line : x component
Upper line : y component

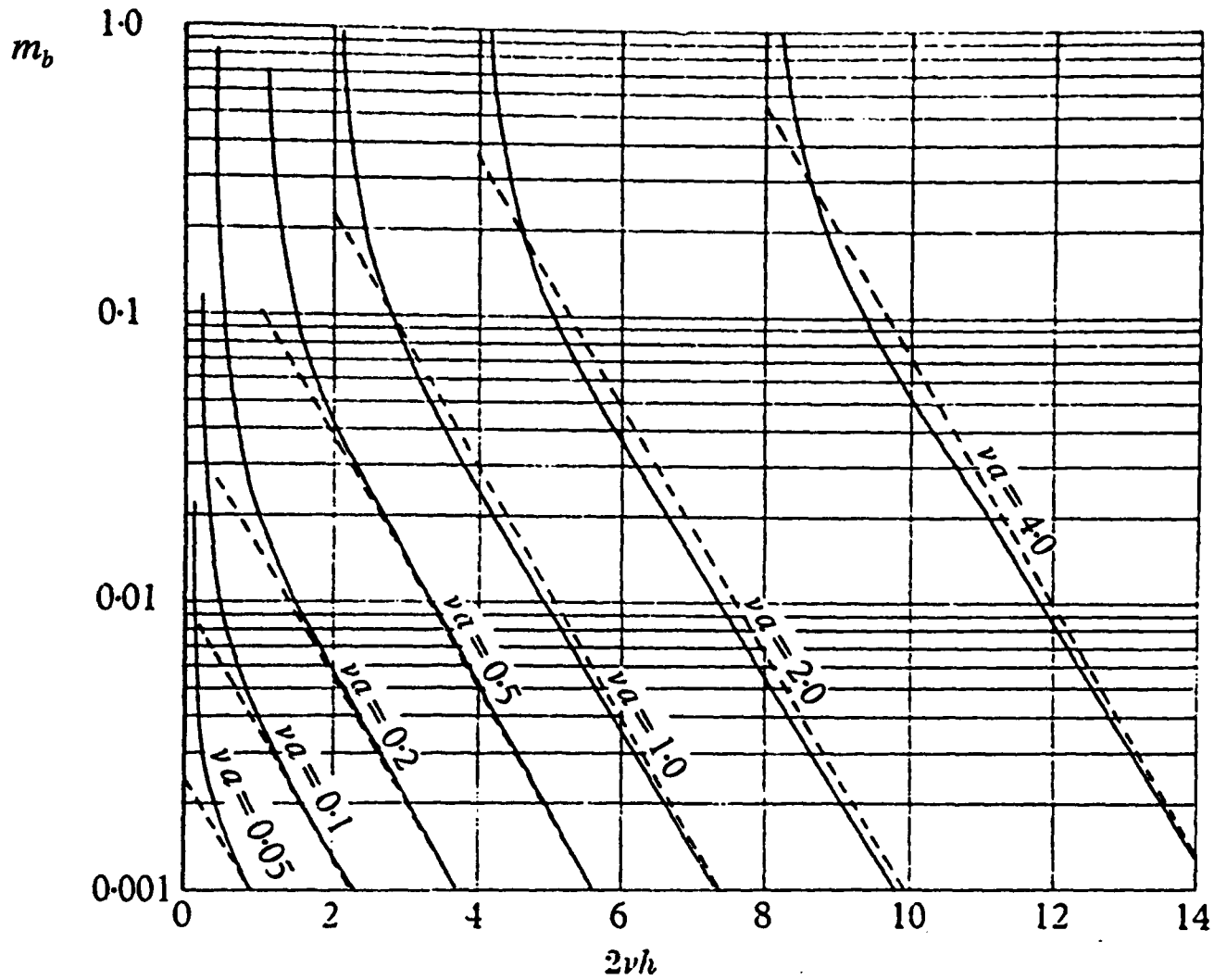

Figure 7.6 Second order mean force - Ogilvie (1963)

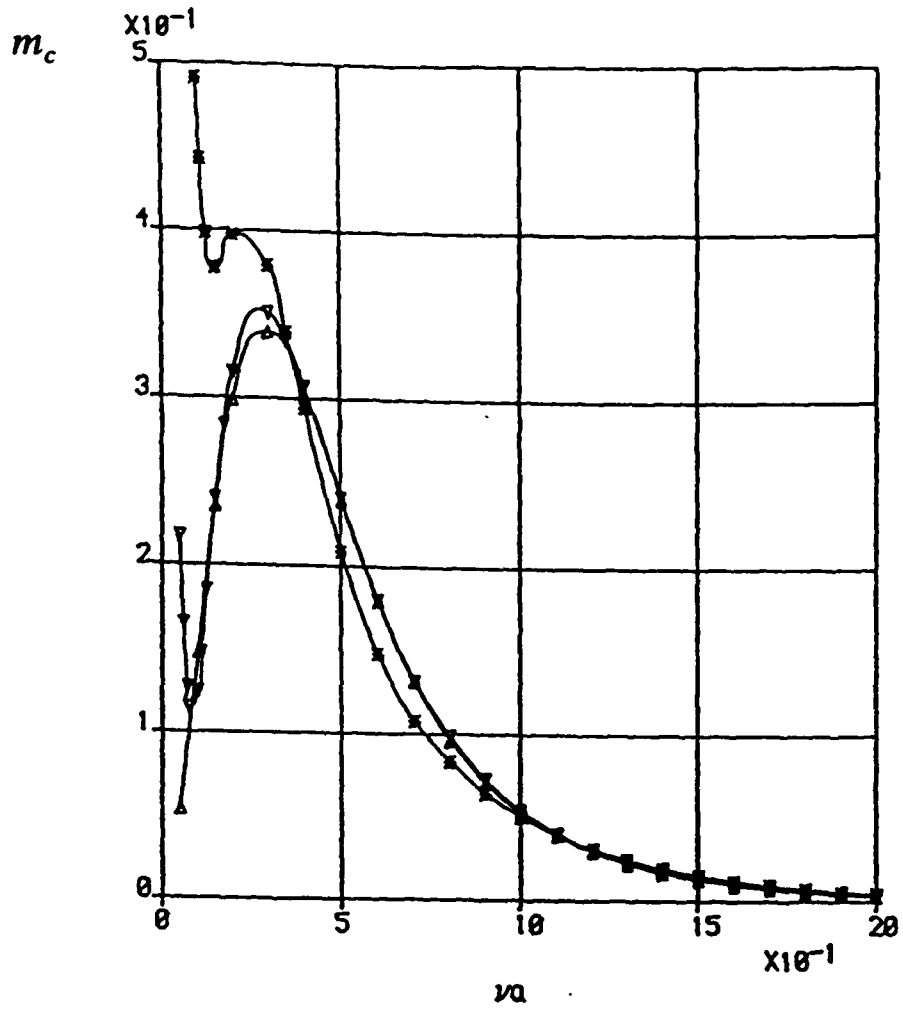

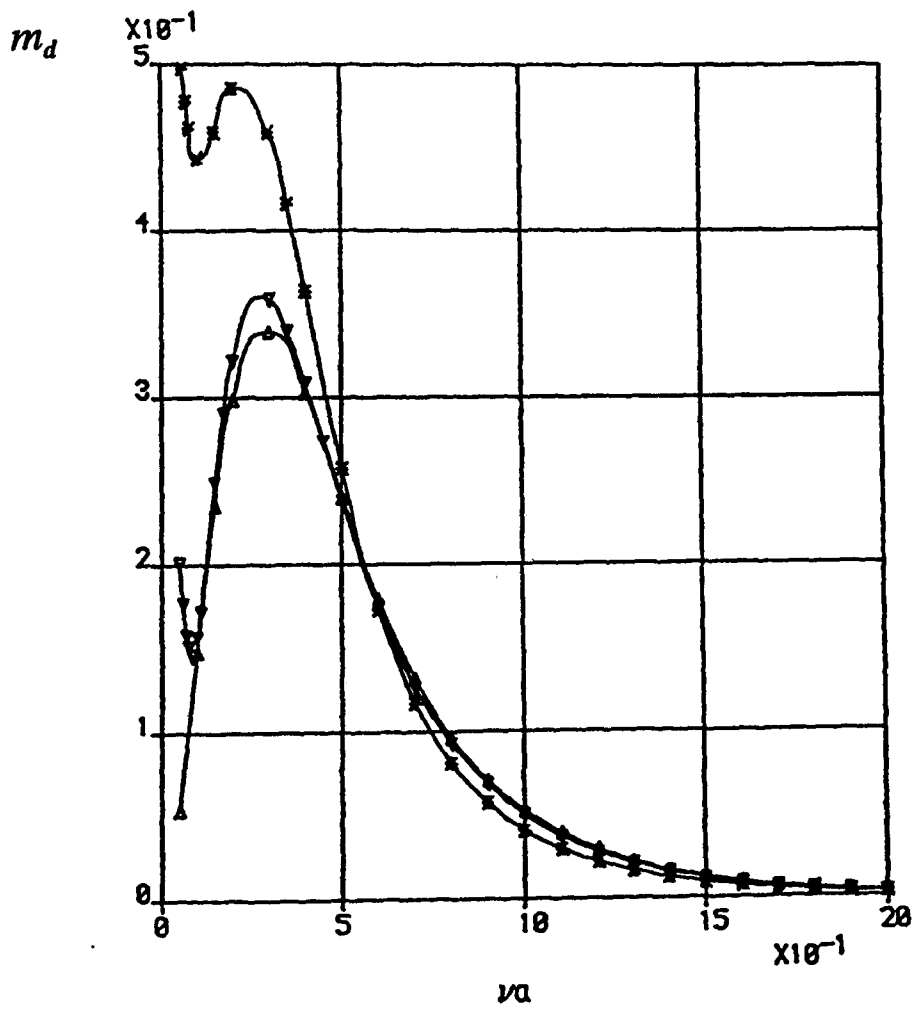

Figure 7.7 Second order oscillatory force - Wu and Eatock Taylor (1990)

Triangle : $d = \infty$, inverted triangle : $d = 7a$, star : $d = 4a$

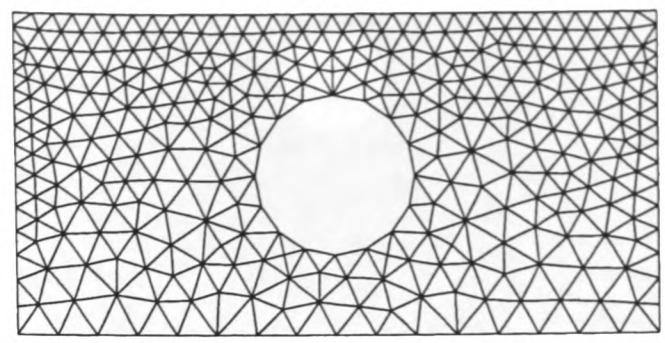

(*a*) Run 5, Case *B*1, 16 cylinder segments, $a = 0.25$, $h = 0.5$

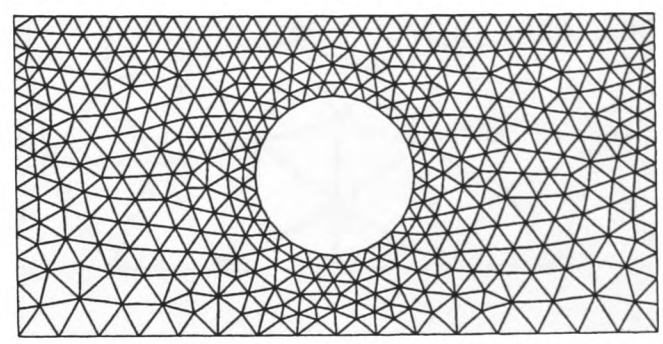

(*b*) Run 6, Case *B*1, 32 cylinder segments, $a = 0.25$, $h = 0.5$

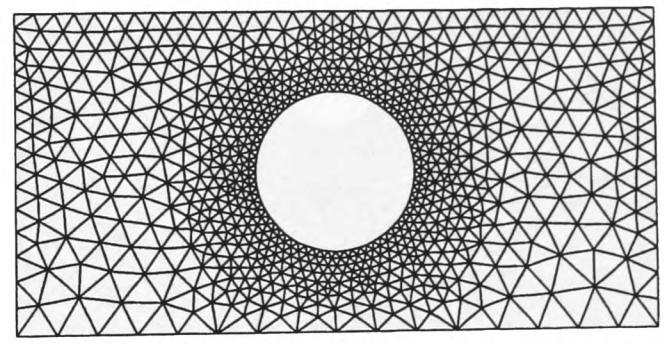

(*c*) Run 7, case *B*1, 64 cylinder segments, $a = 0.25$, $h = 0.5$

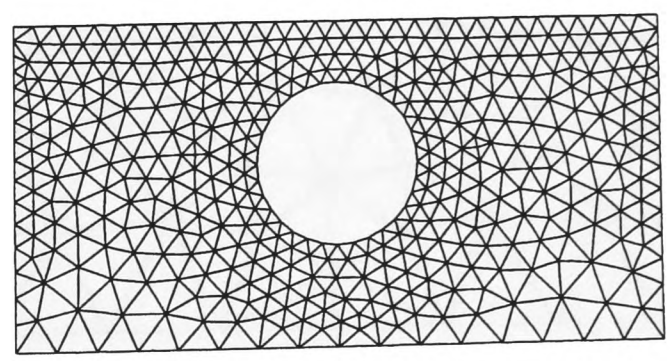

(d) Run 11, case *B*3, 32 cylinder segments, $a = 0.25$, $h = 0.4375$

Figure 7.8 Unstructured sections of initial finite element meshes

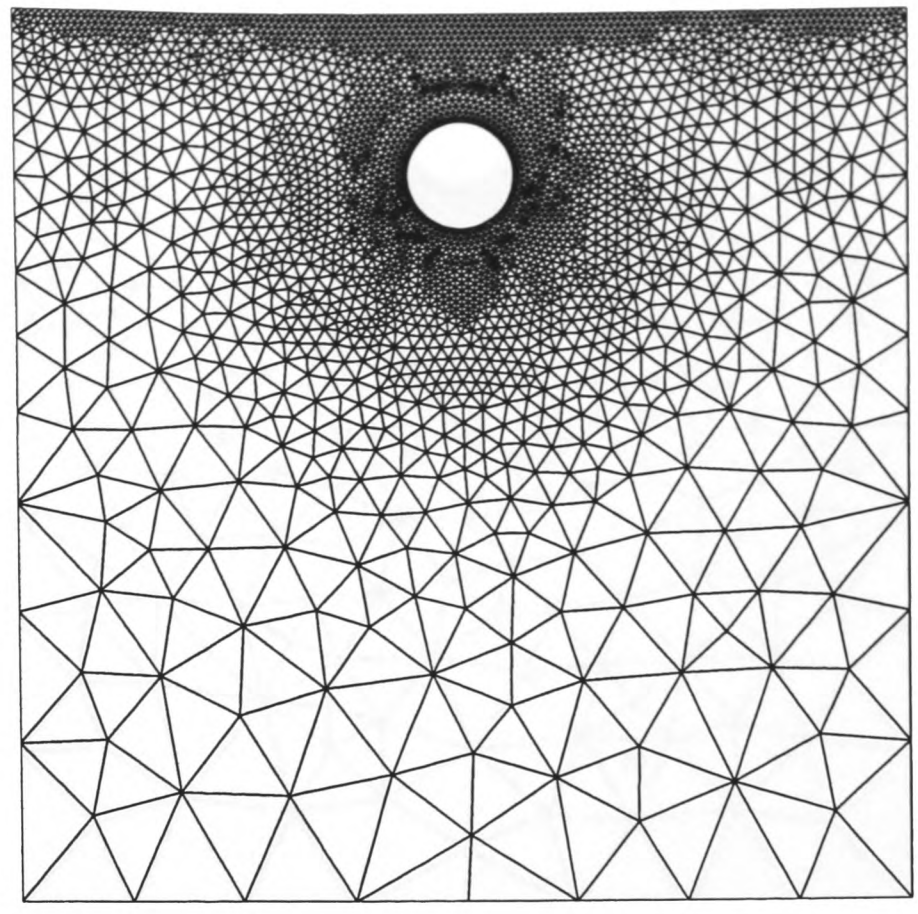

(*a*) Run 14, Case *C*, 64 cylinder segments, $a = 0.06$, $h = 0.18$

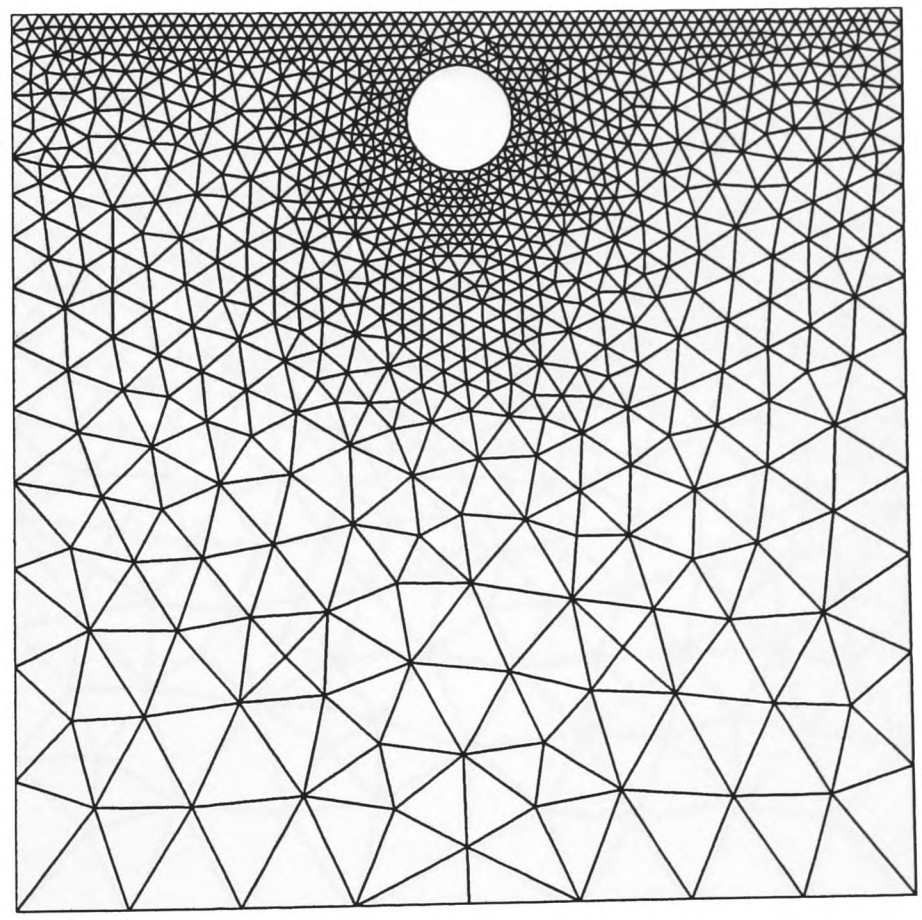

(*b*) Run 19, Case *E*, 32 cylinder segments, $a = 0.06$, $h = 0.12$

Figure 7.9 Unstructured sections of initial finite element meshes

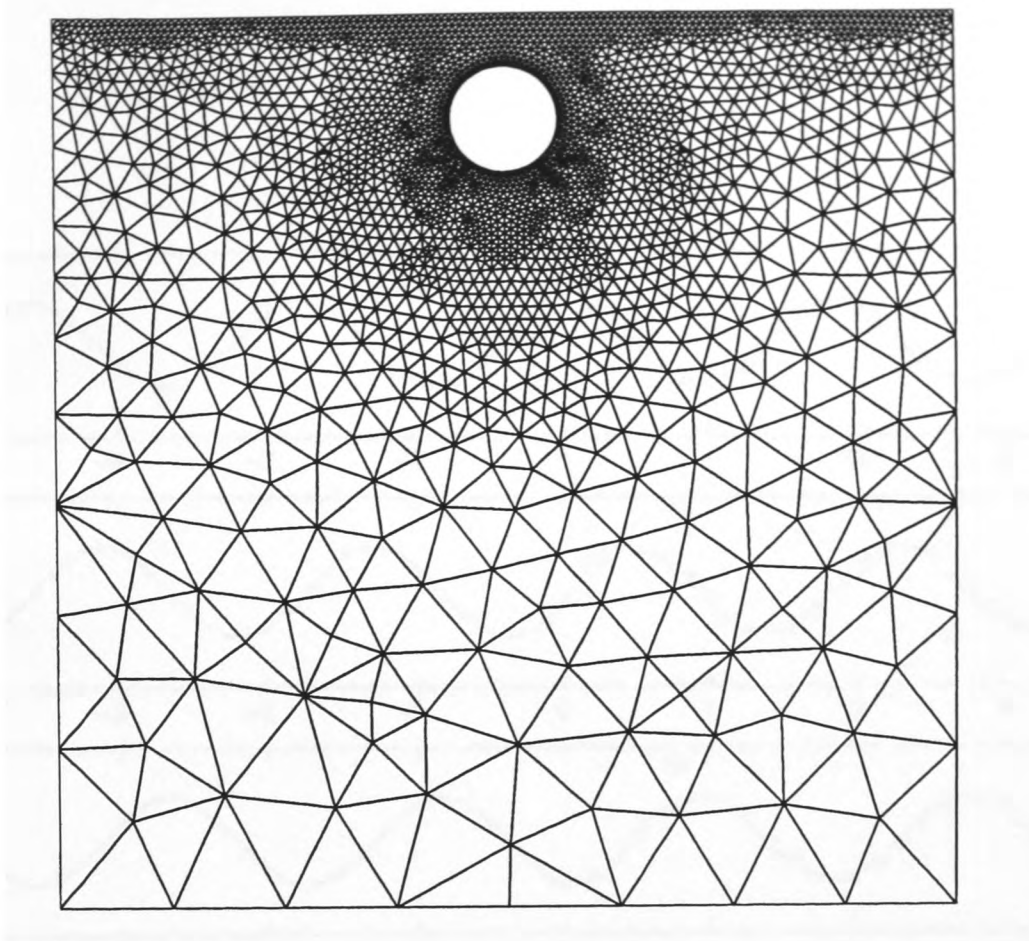

(*c*) Run 20, Case *E*, 64 cylinder segments, $a = 0.06$, $h = 0.12$

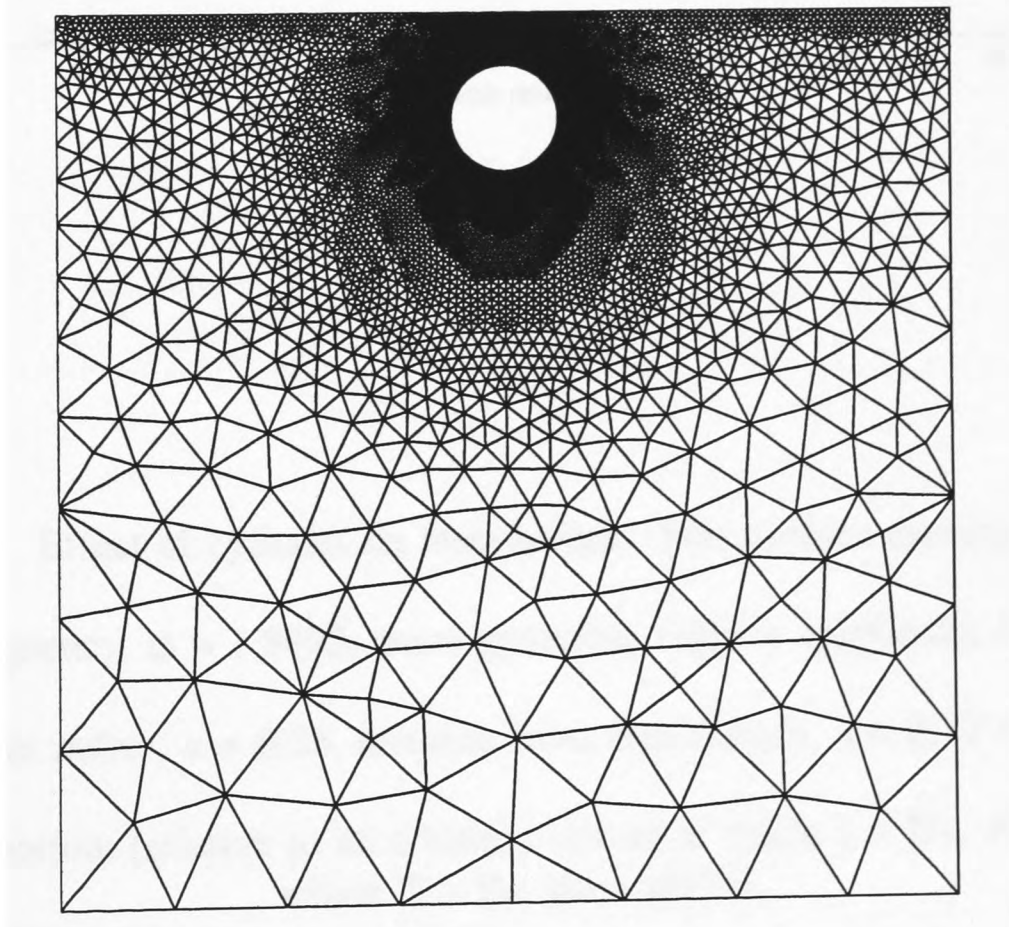

(*d*) Run 21, Case *E*, 128 cylinder segments, $a = 0.06$, $h = 0.12$

Figure 7.10 Unstructured sections of initial finite element meshes

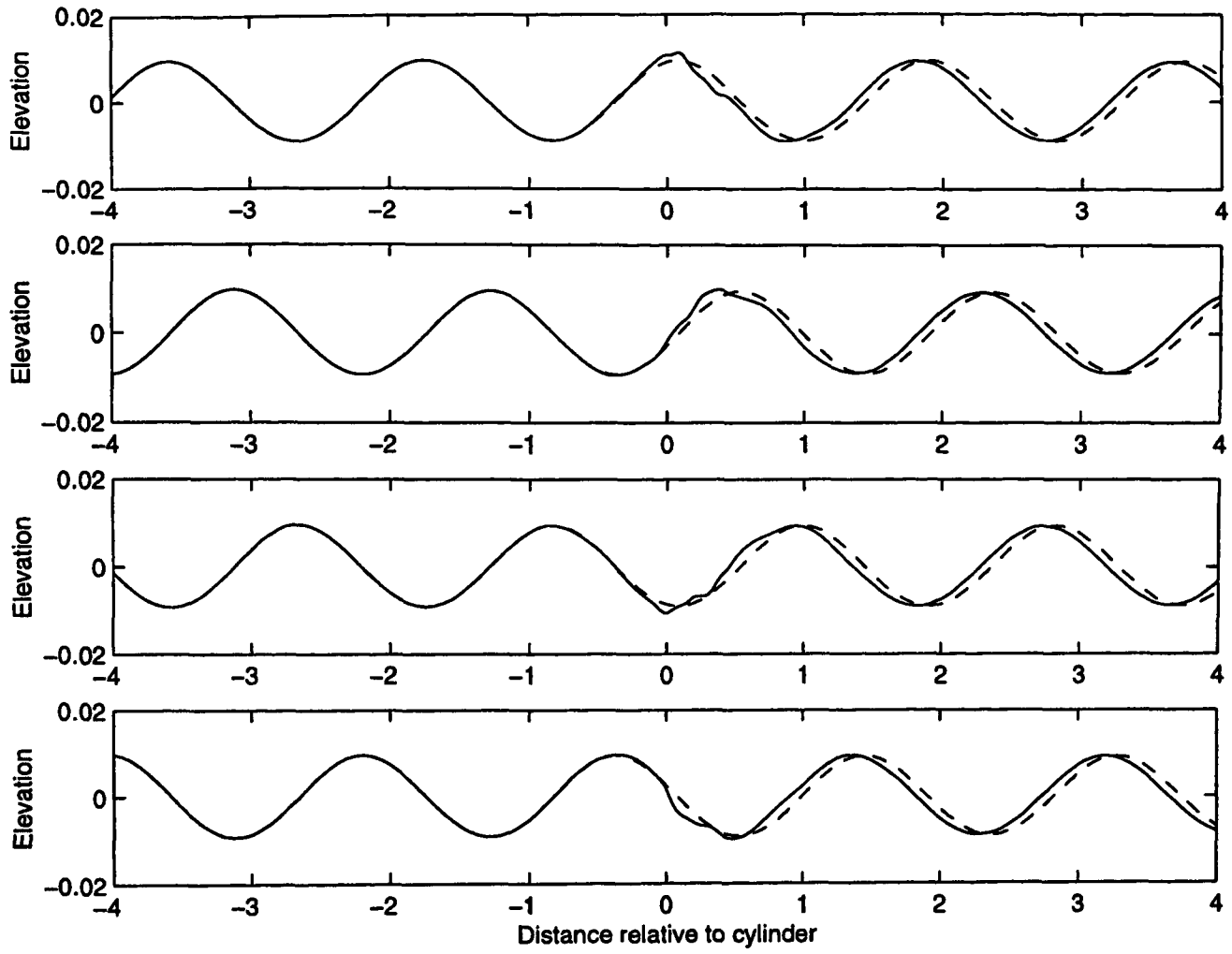

Figure 7.11 Effect of cylinder on free surface. Free surface elevation at cylinder.

Wave frequency, $\omega = 1.8495$, wave generator velocity amplitude, $U_0 = 0.009$.

Cylinder radius, $a = 0.06$, distance from free surface, $h = 0.12$ (case E).

From top to bottom (relative to an arbitrary reference time), $t = T/4$, $T/2$, $3T/4$ and T, where T is the wave period.

Solid line : Cylinder
Dashed line : No cylinder

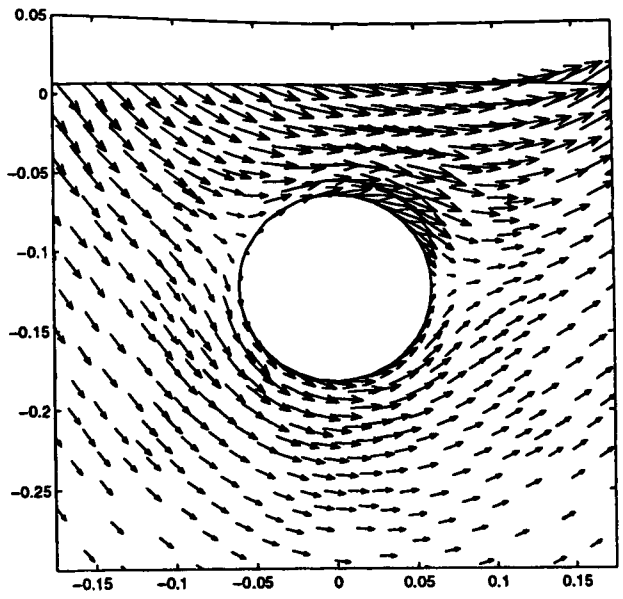

(*a*) $t = T/4$

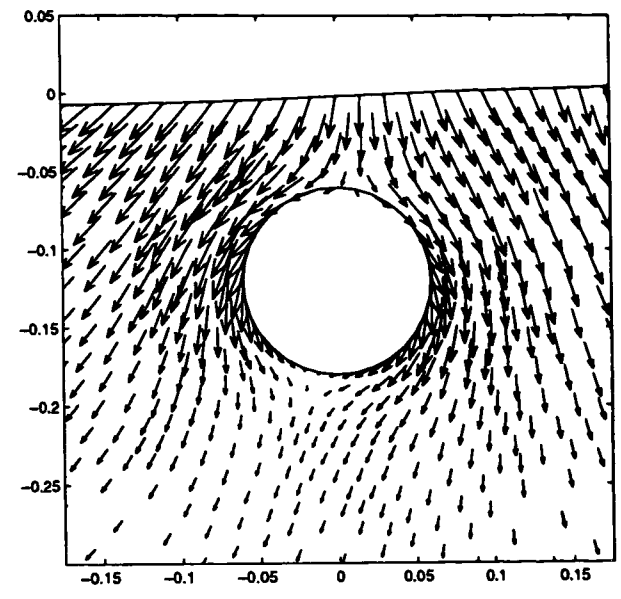

(*b*) $t = T/2$

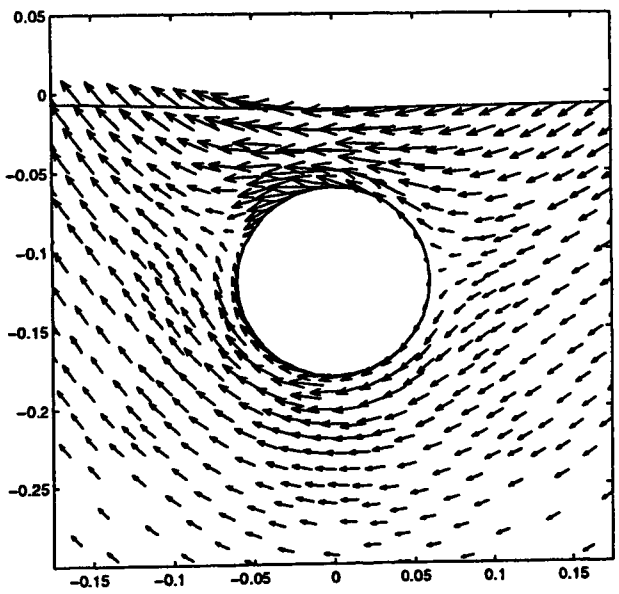

(*c*) $t = 3T/4$

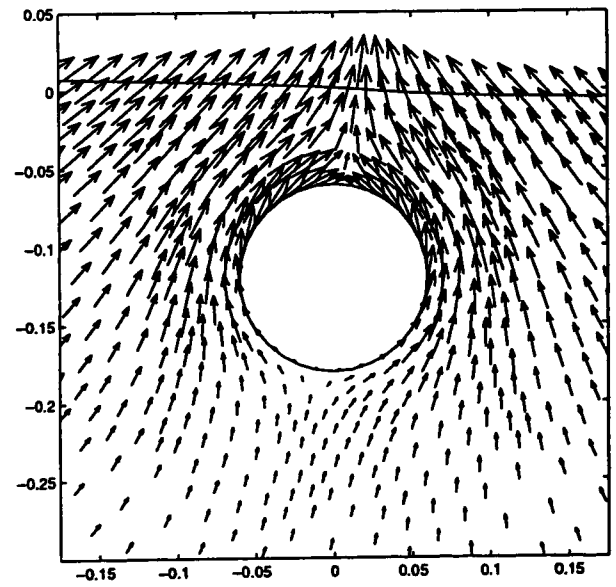

(*d*) $t = T$

Figure 7.12 Velocity vectors around the cylinder.

Wave frequency, $\omega = 1.8495$, wave generator velocity amplitude, $U_0 = 0.009$.

Cylinder radius, $a = 0.06$, distance from free surface, $h = 0.12$ (case *E*).

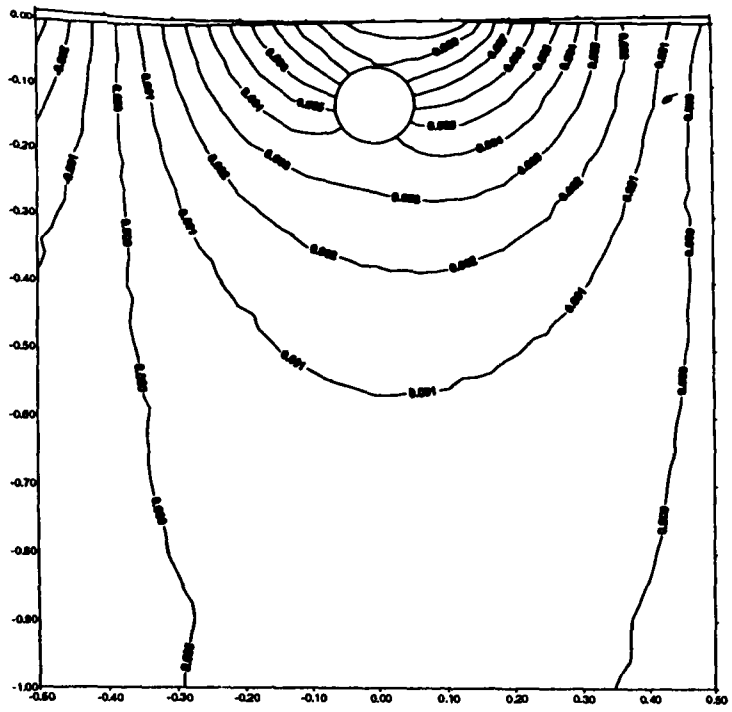

(a) $t = T/4$

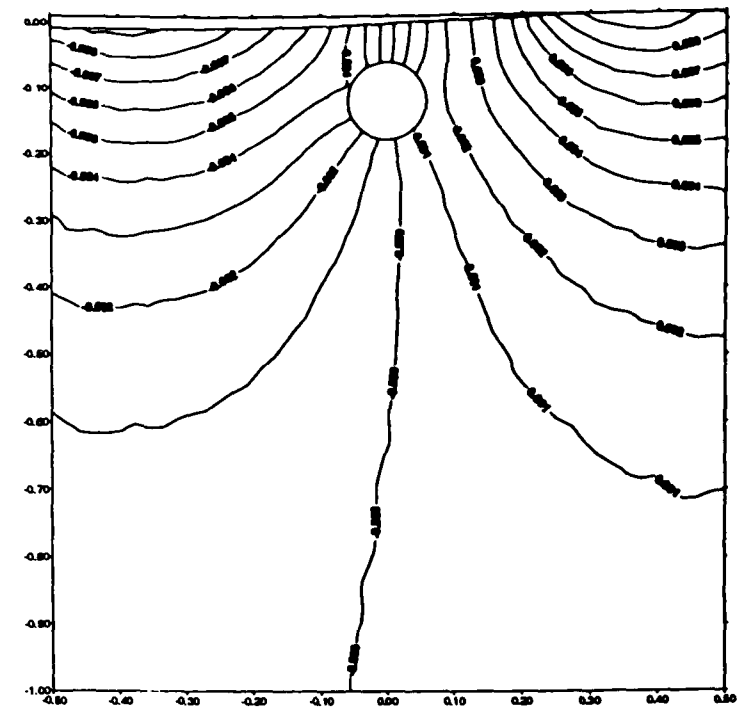

(b) $t = T/2$

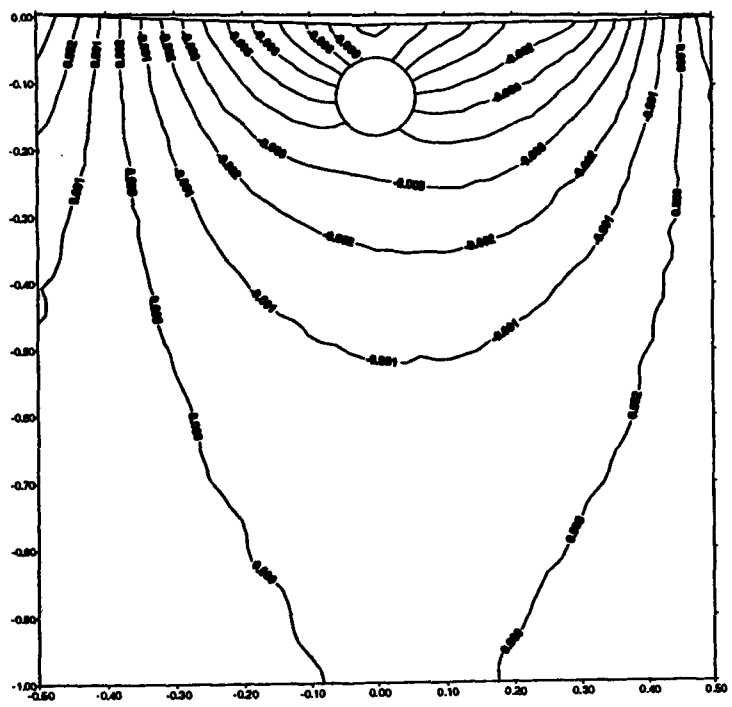

(c) $t = 3T/4$

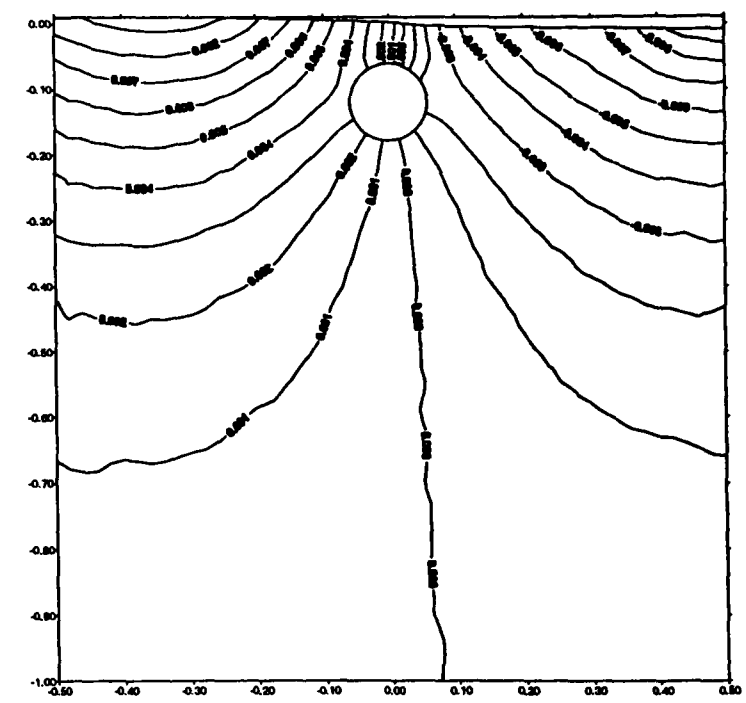

(d) $t = T$

Figure 7.13 Pressure field around cylinder.

Wave frequency, $\omega = 1.8495$, wave generator velocity amplitude, $U_0 = 0.009$.

Cylinder radius, $a = 0.06$, distance from free surface, $h = 0.12$ (case E).

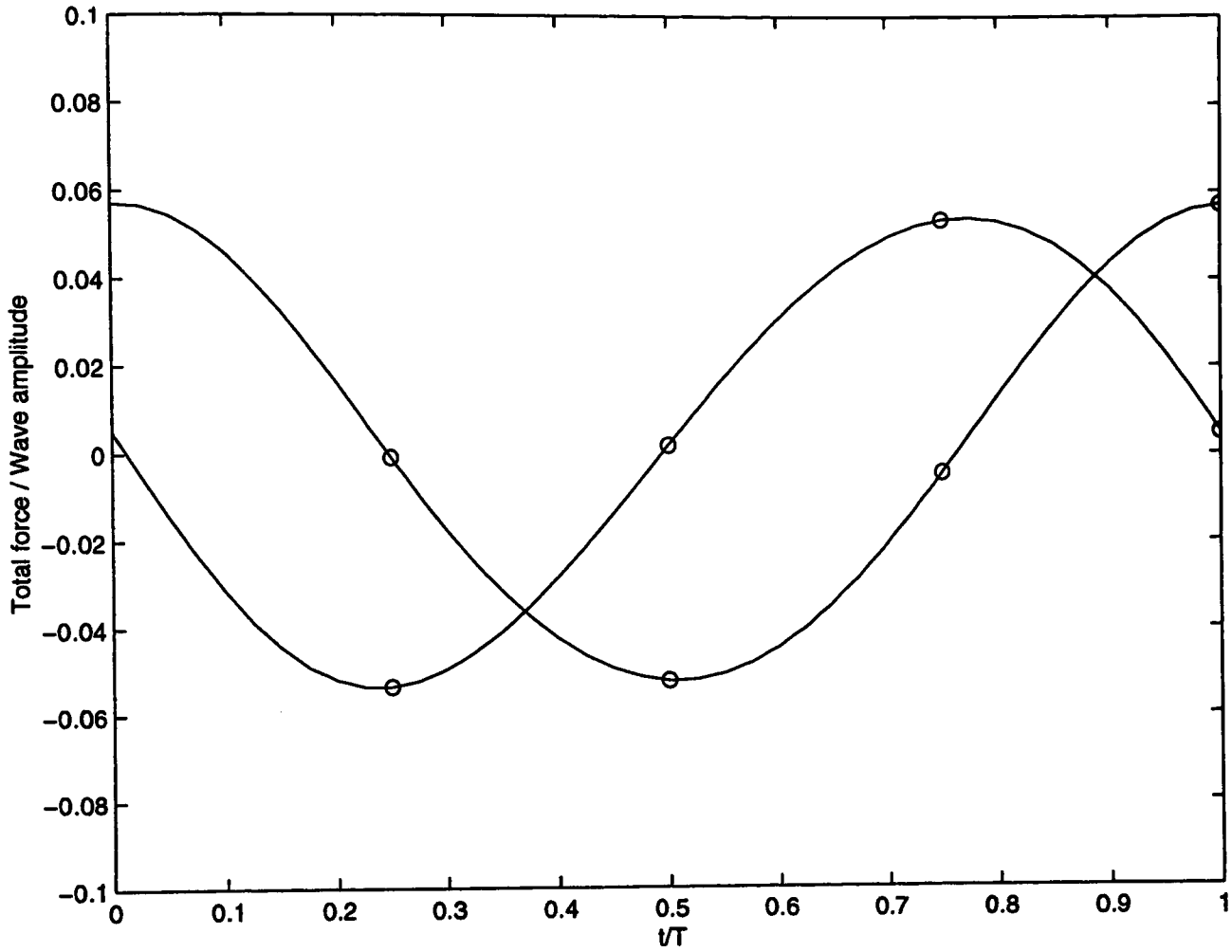

Figure 7.14 Force time history (x and y components) for one wave period.

Wave frequency, $\omega = 1.8495$, wave generator velocity amplitude, $U_0 = 0.009$.

Cylinder radius, $a = 0.06$, distance from free surface, $h = 0.12$ (case E).

x-component of total force is close to its maximum at $t = 0$
y-component of total force is close to zero at $t = 0$

Circles correspond to times for which velocity and pressure plots have been presented.

CHAPTER 8

CONCLUSIONS AND RECOMMENDATIONS

8.1 Introduction

Two unstructured mesh generators have been developed, based on advancing front and Voronoi methods. The Voronoi mesh generator has been used by two finite element programs to simulate inviscid free surface flow problems. Test cases where non-linear effects are important have been modelled, such as a standing wave of large amplitude, a base-excited tank and steep travelling waves. First and second order forces on a submerged horizontal cylinder due to travelling waves were calculated and compared with the theoretical results of Ogilvie (1963), Wu and Eatock Taylor (1990) and Vada (1987) and the experimental results of Chaplin (1984).

8.2 Mesh Generation

Two techniques for creating unstructured meshes for use with the finite element method have been successfully developed. Both the advancing front method and the Voronoi method have been found to mesh domains of arbitrary shape and size with varying mesh density. The mesh quality is good for both methods, there being very few or no elements deviating significantly from the equilateral ideal, i.e. the aspect ratio of the triangular elements is usually small. Both mesh generators were found to be robust, generally reliable and not prone to error. The mesh generators are automatic; the only input from the user is information about the boundary of the domain and the required mesh density within. This

is one of the reasons that the methods chosen are suitable for time domain simulations, where a different finite element mesh may be required at each time step, meaning an automatic method is essential.

The mesh generators produce high quality meshes for the case where a circle forms an internal boundary of the domain. This is a particularly important case in the present work as it is the kind of mesh needed when modelling a submerged horizontal cylinder. The unstructured mesh generators permit control of mesh density and so it is possible to make the mesh finer in the vicinity of the cylinder and at the free surface, and coarser elsewhere. By making the mesh coarse where extra resolution is not needed, it is possible to decrease significantly the run time of a simulation.

The advancing front method was found to be faster than the Voronoi method. On a few occasions, however, the advancing front method broke down, due to a problem encountered in checking overlapping elements. The Voronoi method does not have this difficulty; it is more reliable and therefore has been used for the finite element simulations herein where an unstructured mesh is needed.

8.3 Finite Element Simulations

Two finite element programs have been used to simulate free surface flow problems. The standard finite element method has been developed from a program written by Dr G. X. Wu of University College London; a number of improvements have been made to the efficiency of the method and a higher order velocity calculation technique has been implemented which

greatly improves the performance of the model. The other finite element model uses a sigma transformation to map the physical domain with a moving free surface boundary, on to a fixed regular computational domain.

Four free surface wave problems have been examined in the absence of an immersed structure; namely, a standing wave in a rectangular tank, a base-excited tank, progressive waves in a numerical wave flume and focused waves. A number of options were tested in order to optimise the performance of the model. It was found that the best results were obtained with the higher-order velocity calculation and updating the free surface using an mixed Euler-Lagrange technique. With this scheme, smoothing was not required, thus preventing damping of the solution. When simulating a travelling wave, a ramp function was used to increase the velocity at the wave generator boundary gradually from zero at the start of the simulation; this prevented spurious oscillations developing in the tank. A damping layer together with a Sommerfeld radiation condition was used at the open lateral boundary to absorb the waves; this method of wave absorption has been found to be very effective.

Both standing and travelling waves were modelled successfully. The large amplitude standing wave results agreed well with second order theory. Good agreement was also found with data presented by Greaves *et al.* (1997) and Chern *et al.* (1999). The travelling wave was generated with little or no loss of amplitude, often a problem with numerical simulations. The large amplitude waves agreed closely with Stokes fifth order theory. Results for the base-excited tank were found to be in agreement with the analytical theory of Wu *et al.* (1998) and the numerical results of Chern *et al.* (1999).

The first and second order forces on the horizontal cylinder were calculated for a number of combinations of cylinder diameter, location and wavelength. The cases chosen were ones where simple theories fail to produce accurate solutions. The first order force and the mean second order force were found to agree well with Ogilvie (1963) and Chaplin (1984). The second order oscillatory force was also found to agree with the results of others (Wu and Eatock Taylor (1990), Vada (1987) and Chaplin (1984)), but not as well as the other two force components.

8.4 Recommendations for Future Work

The finite element method used with unstructured meshes has been shown to be a successful technique for modelling steep waves interacting with structures. Many other cases could be examined using the same method, such as fully non-linear wave interaction with an array of cylinders. Problems where there is a sloping tank or a step change in the bottom of the tank could be examined. The method is readily applicable to arbitrarily shaped bodies, which may be partially submerged.

The higher order velocity technique should be extended so that it can be used on unstructured meshes, as well as structured meshes. In future, energy could be monitored as an accuracy check.

The model is readily extendable to three dimensions. In particular, the sigma transform technique should be useful in three dimensions as it would prevent the need for remeshing, which clearly would be more time consuming for a three dimensional unstructured

mesh generator. A three dimensional model could simulate waves travelling past a vertical cylinder, which is relevant to the important phenomenon of ringing. Multiply-connected cylinders could be considered if sufficient computer resource is available. The unstructured mesh generation would be useful for creating the two dimensional free surface mesh which would act as a template for the three dimensional structured mesh of tetrahedra extending beneath it.

In conclusion, two mesh generating techniques have been examined. The advancing front technique was found to be faster, but the Voronoi technique is more reliable. The higher order velocity calculation, a technique of the author's devising is very accurate and eliminates the need for smoothing except for the very steepest cases. The sigma transformed finite element method has been devised by the author and has been shown to give results of equal quality to the standard finite element method. For future work, three dimensional modelling of a surface piercing vertical cylinder using the sigma transform finite element method is recommended.

REFERENCES

Baker, T.J. (1989) "Automatic mesh generation for complex 3-dimensional regions using a constrained Delaunay triangulation", Engineering with Computers, Vol. 5, No. 3-4, pp 161-175.

Beck, R.F. (1994) "Time domain computations for floating bodies", Appl. Ocean Res. Vol. 16, pp 363-372.

Boo, S.Y. and Kim, C.H. (1996) "Fully non linear diffraction due to a vertical circular cylinder in a 3D HOBEM numerical wave tank ", Proc. 6th Int. Offshore and Polar Eng. Conf., Los Angeles, May 26-31.

Boo, S.Y., Kim, C.H. and Kim, M.H. (1994) "A numerical wave tank for non linear irregular waves by 3D HOBEM", J. of Offshore and Polar Engineering, Vol. 4. No. 4, pp 265-272.

Borthwick, A.G.L. and Kaar, E.T. (1993) "Shallow flow modelling using curvilinear depth-averaged stream function and vorticity transport equations", Int. J. Numer. in Fluids, Vol. 14, pp 1193-1217.

Borouchaki, H. and George, P.L. (1997) "Aspects of 2-D Delaunay Mesh Generation", Int. J. Numer. Methods Eng. Vol. 40, No. 11, pp 1957-1975.

Borouchaki, H., George, P.L. and Lo, S.H. (1996) "Optimal Delaunay point insertion", Int. J. Numer Methods Eng. Vol. 39, No. 20, pp 3407-3437.

Borouchaki, H. and Lo, S.H. (1995) "Fast Delaunay triangulation in three dimensions", Computer Methods in Applied Mechanics and Engineering, Vol. 128, No. 1-2, pp 153-167.

Bowyer, A. (1981) "Computing Dirichlet tessellations", Comput. J. Vol. 24, pp 162.

Buchmann, B., Skourup, J. and Cheung, K.F. (1998) "Run up on a structure due to second order waves and a current in a numerical wave tank", Appl. Ocean Res. Vol. 20, pp 297-308.

Burrows, R., Tickell, R.G., Hames, D. and Najafian, G. (1997) "Morison wave force coefficients for application to random seas", Appl. Ocean Res. Vol. 19, pp 183-200.

Cao, Y., Schultz, W.W. and Beck, R.F. (1990) "Three dimensional unsteady computations of non linear waves caused by underwater disturbance", Proc. 18th Symposium on Naval Hydrodynamics, Ann Arbor, Mich. pp 417-427.

Cao, Y., Schultz, W.W. and Beck, R.F. (1991) "Three dimensional desingularized boundary integral methods for potential problems", Int. J. Numer. Methods Eng. Vol. 12, pp 785-803.

Cao, Y., Lee, T., and Beck, R.F. (1992) "Computation of non linear waves generated by floating bodies", Proc. 7th Int. Workshop on Water Waves and Floating Bodies, France.

Cavendish, J.C. (1974) "Automatic triangulation of arbitrary planar domains for the finite element method", Int. J. Numer. Methods Eng. Vol. 8, pp 679-696.

Celebi, M.S. and Kim, M.H. (1997) "Non linear wave body interactions in a numerical wave tank", Proc. 12th Int. Workshop on Water Waves and Floating Bodies, France.

Celebi, M.S., Kim, M.H. and Beck, R.F. (1998) "Fully non linear three dimensional numerical wave tank simulation", Journal of Ship Research. Vol. 42. No. 1, pp 33-45.

Chan, C.T. and Anastasiou, K. (1997) "An automatic tetrahedral mesh generation scheme by the advancing front method", Communications in Numerical Methods in Engineering, Vol. 13, No. 1, pp 33-46.

Chaplin, J.R. (1984) "Nonlinear forces on a horizontal cylinder beneath waves", J. Fluid Mech. Vol. 147, p 449-464.

Chaplin, J.R., Rainey, R.C.T. and Yemm, R.W. (1997) "Ringing of a vertical cylinder in waves", J. Fluid Mech. Vol. 350, pp 119-147.

Chau, F.P. and Eatock Taylor, R. (1992) "Second-order wave diffraction by a vertical cylinder", J. Fluid Mech. Vol. 240, pp 571-599.

Chern, M.J., Borthwick, A.G.L., Eatock Taylor R. (1999) "A Pseudospectral sigma-transformation model of 2D nonlinear waves".

Cheung, K.F., Isaacson, M. and Lee, J.W. (1996) "Wave diffraction around a three dimensional body in a current", ASME Journal of Offshore Mechanics and Arctic Engineering, Vol. 118. No. 4, pp 247-252.

Conte, J.P. and Marshall, P.W. (1994) "Low frequency forces on tubular spaceframe towers - analysis of Cognac data", J. Offshore Mech. and Arctic Eng. - Trans. ASME, Vol. 116, No. 3, pp 122-126.

Couch, A.T. and Conte, J.P. (1997) "Field verification of linear and nonlinear hybrid wave models for offshore tower response prediction", J. Offshore Mech. and Arctic Eng. - Trans. ASME, Vol. 119, No. 3, pp 158-165.

Clement, A. (1996) "Coupling of two absorbing boundary conditions for 2D time domain simulations of free surface gravity waves", J. Comp. Phys. Vol. 126, pp 139-151.

Cokelet, E.D. (1977) "Steep gravity waves in water of uniform arbitrary depth", Phil. Trans. R. Soc. Lond. A Vol 286, pp 184-230.

Cointe, R. (1989) "Non-linear simulation of transient free surface flows", Fifth Intl Conf. on Numerical Ship Hydrodynamics, Hiroshima, September.

Cointe, R. (1990) "Numerical simulation of a wave channel", Eng. Anal. Bound. Elem. Vol. 7, pp 167-177.

Contento, G. and Casole, S. (1995) "On the generation and propagation of waves in 2D numerical wave tanks", Proc. 5th Int. Offshore and Polar Eng. Conf., The Netherlands, Vol. 3, pp 10-18.

Cook, W.A. (1974) "Body oriented coordinates for generating three dimensional meshes", Int. J. Numer. Methods Eng. Vol. 8, pp 27-43.

Cowper, G.R. (1973) "Gaussian quadrature formulas for triangles", Int. J. Num. Mech. Eng. Vol. 7, pp 405-408.

Dean, W.R. (1948) "On the reflection of surface waves by a submerged cylinder", Proc. Camb. Phil. Soc. Vol 44, pp 483-491.

Delaunay, B. (1934) "Sur la sphere vide", Bull. Acad. Sci. URSS Cl. Sci. Math. Nat. pp 793-800.

De Zeeuw, D. and Powell, K.G. (1993) "An adaptively refined Cartesian mesh solver for the Euler equations", J. Comp. Phys. Vol. 104, pp 56-68.

Dirichlet, G.L. (1850) "Uber die reduction der positiven quadratischen Formen mit drei unbestimmten gaizen Zahlen", J. Reine Angew. Math. Vol. 40, pp 209.

Dold, J.W. and Peregrine, D.H. (1986) "Water wave modulation", Proc. 20th Int. Conf. on Coastal Engineering, Taipei, pp 163-175.

Dommermuth, D.G. and Yue, D.K.P. (1987) "Numerical simulations of non linear axisymmetric flows with a free surface", J. Fluid Mech. Vol. 178, pp 195-219.

Dommermuth, D.G., Yue, D.P., Lin, W.M., Rapp, R.J., Chan, E.S. and Melville W.K. (1988) "Deep water plunging breakers: a comparison between potential theory and experiments", J. Fluid Mech. Vol. 189, pp 423-442.

Eatock Taylor, R., Borthwick, A.G.L., Greaves, D.M., Wu, G.X. and Ma Q.W. (1996) "Managed programme on uncertainties in loads on offshore structures. Project technical report. Project A3: Interaction of steep waves with structures."

Eatock Taylor, R. and Hung, S.M. (1987) "Second order diffraction forces on a vertical cylinder in regular waves" Applied Ocean Research, Vol. 9, pp 19-30.

Evans, A., Marchant, M.J., Szmelter, J. and Weatherill, N.P. (1991) "Mesh adaptivity with the quadtree method", in A.S. Arcilla, J. Hauser, P.R. Eiseman and J.F. Thompson eds, Numerical Grid Generation in Computational Fluid Dynamics and Related Fields, pp 67-78. Elsevier Science, North Holland.

Faltinsen, O.M. (1977) "Numerical solution of transient non linear free-surface motion outside or inside moving bodies", Proc. 2nd Intl Conf. on Num. Ship Hydro., U.C. Berkeley (ed. J.V. Wehausen and N. Salvesen), pp 347-357. University Extension Publications.

Faltinsen, O.M. (1990) "Wave Loads on Offshore Structures", Annu. Rev. Fluid Mech. Vol. 22, pp 35-56.

Faltinsen, O.M., Newman, J.N. and Vinje, T. (1995) "Nonlinear wave loads on a slender vertical cylinder", J. Fluid Mech. Vol. 289, pp 179-198.

Fenton, J.D. (1985) "A fifth-order Stokes theory for steady waves", J. Waterway Port Coastal and Ocean Engineering ASCE, Vol. 111, pp 216-234.

Ferrant, P. (1996) "Simulation of strongly non linear wave generation and wave-body interactions using a 3D MEL model", Proc. 21st ONR Symposium on Naval Hydrodynamics, Trondheim (Norway), pp 93-109.

Ferrant, P. (1997) "Non linear wave current interactions in the vicinity of a vertical cylinder", Proc. 12th Int. Workshop on Water Waves and Floating Bodies, France.

Frederick, C.O., Wong, Y.C. and Edge, F.W. (1970) "Two dimensional automatic mesh generation for structural analysis" Int. J. Numer. Methods Eng. Vol. 2, pp 133-144.

Frey, P.J., Borouchaki, H. and George, P.L. (1998) "3D Delaunay mesh generation coupled with an advancing front approach", Computer Methods in Applied Mechanics and Engineering, Vol. 157, No. 1-2, pp 115-131.

George, P.L. and Seveno, E. (1994) "The advancing front mesh generation method revisited", Int. J. Numer. Methods Eng. Vol. 37, No. 21, pp 3605-3619.

Gordon, W.J. and Hall, C.A. (1973) "Construction of curvilinear coordinate systems and apllications to mesh generation", Int. J. Numer. Methods Eng. Vol. 7, pp 461-477.

Greaves, D.M., Borthwick, A.G.L., Wu, G.X. and Eatock Taylor R. (1997) "A Moving Boundary Finite Element Method for Fully Nonlinear Wave Simulations", J. Ship Research. Vol. 41, No. 3, pp 181-194.

Greaves, D.M. and Borthwick, A.G.L. (1999) "Hierarchical tree-based finite element mesh generation", Int. J. Numer. Methods Eng. Vol. 45, pp 447-471.

Green, P.J. and Sibson, R. (1978) "Computing Dirichlet tessellations in the plane" Comput. J. Vol. 21, pp 168.

Grilli, S.T., Skourup, J. and Svendsen, I.A. (1989) "An efficient boundary element method for non linear water waves", Eng. Anal. Bound. Elem. Vol. 6, pp 97-107.

Grue, J. (1992) "Nonlinear water waves at a submerged obstacle or bottom topography", J. Fluid Mech. Vol. 244, pp 455-476.

Grue, J., Bjorshol, G. and Strand, O. (1993) "Higher harmonic wave exciting forces on a vertical cylinder", Institute of Mathematics, University of Oslo Preprint, No. 2. ISBN 82-553-0862-8.

Hammer, P.C. Marlowe, O.P. and Stroud, A.H. (1956) "Numerical integration over simplexes and cones", Math. Tables Aids Comp. Vol. 10, pp 130-137.

Hirt, C.W. and Nichols, B.D. (1981) "Volume of Fluid (VOF) method for the dynamics of free boundaries", J. Comp. Phys. Vol. 39, pp 201-225.

Isaacson, M. and Cheung, K.F. (1990) "Time domain solution for second order wave diffraction", ASCE Journal of Waterway, Port, Coastal and Ocean Engineering, Vol. 116, pp 191-210.

Isaacson, M. and Cheung, K.F. (1991) "Second order wave diffraction around two dimensional bodies by time domain method", Appl. Ocean Res. Vol. 13, pp 175-186.

Isaacson. M. and Cheung, K.F. (1993) "Time domain solution for wave current interactions with two dimensional body", Appl. Ocean Res. Vol. 15, pp 39-52.

Isaacson, M. and Ng, J.Y.T. (1993) "Time domain second order wave radiation in two dimensions", Journal of Ship Research, Vol. 37, pp 25-33.

Jin, H. and Tanner, R.I. (1993) "Generation of unstructured tetrahedral meshes by advancing front technique", Int. J. Numer. Methods Eng. Vol. 36, No. 11, pp 1805-1823.

Jeong, J.H. and Yang, D.Y. (1998) "Finite element analysis of transient fluid flow with free surface using VOF (Volume Of Fluid) method and adaptive grid", Int. J. Numer. Methods in Fluids. Vol. 26, pp 1127-1154.

Johnson, B.H. and Thompson, J.F. (1978) "A discussion of boundary-fitted coordinate systems and their applicability to the numerical modelling of hydraulic problems", Misc. Paper H-78-9, U.S. Army Engineer Waterways Experiment Station Hydraulics Laboratory, Vicksburg, Mississippi, U.S.A.

Kim, M.H., Celebi, M.S. and Kim, D.J. (1998) "Fully non linear interaction of waves with a three dimensional body in uniform currents", J. Appl. Ocean Res. Vol. 20, pp 309-321.

Kim, M.H. and Yue D.K.P. (1989) "The complete second-order diffraction solution for an axisymmetric body, Part 1: Monochromatic incident waves", J. Fluid Mech. Vol. 200, pp 235-264.

Kwak, S. and Pozrikidis, C. (1998) "Adaptive triangulation of evolving, closed, or open surfaces by the advancing front method", J. Comp. Phys. Vol. 145, No. 1, pp 61-88.

Lawson, C.L. (1972) "Generation of a triangular grid with application to contour plotting", California Institute of Technology, Jet Propulsion Lab. Tech. Memo. 299.

Lee, C.K. and Hobbs, R.E. (1999) "Automatic adaptive finite element mesh generation over arbitrary two dimensional domain using advancing front technique", Computers and Structures, Vol. 71, No. 1, pp 9-34.

Lighthill, M.J. (1979) "Waves and hydrodynamic loading", Proc. of the Second Int. Conf. Behaviour of Offshore Structures" pp 1-40.

Lighthill, J. (1986) "Fundamentals concerning wave loading on offshore strcutures", J. Fluid Mech. Vol. 173, pp 667-681.

Lin, W.M., Newman, J.N. and Yue, D.K.P. (1984) "Non linear forced motions of floating bodies", Proc. 15th Symp. on Naval Hydrodynamics, Hamburg, pp 33-49.

Lo, S.H. (1985) "A new mesh generation scheme for arbitrary planar domains", Int. J. Numer. Methods Eng. Vol. 21, pp 1403.

Lo, S.H. (1991) "Volume discretization into tetrahedra. 2. 3D triangulation by advancing front approach", Computers and Structures, Vol. 39, No. 5, pp 501-511.

Lohner, R. (1996) "Progress in grid generation via the advancing front technique", Engineering with Computers, Vol. 12, No. 3-4, pp 186-210.

Lohner, R. and Parikh, P. (1988) "Generation of 3-Dimensional unstructured grids by the advancing front method", Int. J. Numer Methods in Fluids, Vol. 8, No. 10, pp 1135-1149.

Longuet-Higgins, M.S. and Cokelet, E.D. (1976) "The deformation of steep surface waves on water, I: a numerical method of computation", Proc. Roy. Soc. Lond., A Vol 350, pp 1-25.

Malenica, S. and Molin, B. (1995) "Third-harmonic wave diffraction by a vertical cylinder", J. Fluid Mech. Vol. 302, pp 203-229.

Mavriplis, D.J. (1990) "Adaptive Mesh Generation for Viscous Flows Using Delaunay Triangulation", J. Comp. Phys. Vol. 90, No. 2, pp 271-291.

Mavriplis, D.J. (1995) "An advancing front Delaunay triangulation algorithm designed for robustness", J. Comp. Phys. Vol. 117, No. 1, pp 90-101.

Mellor, G.L. and Blumberg, A.F. (1985) "Modelling vertical and horizontal diffusivities with the sigma coordinate system", Monthly Weather Review, Vol. 113, pp 1379-1383.

Miyata, H. (1986) "Finite difference simulation of breaking waves", J. Comp. Phys. Vol. 65, pp 179-214.

Miyata, H., Kanai, A., Kawamura, T. and Park, J.C. (1996) "Numerical simulation of three dimensional breaking waves", J. Mar. Sci. Tech. Vol. 1, pp 183-197.

Molin, B. (1979) "Second order diffraction loads upon three-dimensional bodies", Applied Ocean Res. Vol. 1, pp 197-202.

Moller, P. and Hansbo, P. (1995) "On advancing front mesh generation in 3 dimensions", Int. J. Numer Methods Eng. Vol. 38, No. 21, pp 3551-3569.

Morison, J.R., O'Brien, M.P., Johnson, J.W. and Schaff, S.A. (1950) "The force exerted by surface waves on piles", J. Petroleum Engineering, Vol. 189, pp 149-157.

Muller, J.D., Roe, P.L. and Deconinck, H. (1993) "A frontal approach for internal node generation in Delaunay traingulations", Int. J. Numer. Methods in Fluids, Vol. 17, No. 3, pp 241-255.

Newman, J.N. (1996) "The second-order wave force on a vertical cylinder", J. Fluid Mech. Vol. 320, pp 417-443.

Ng, C.O. and Kot S.C. (1992) "Computations of water impact on a two dimensional flat bottomed body with a volume of fluid method", Ocean Eng. Vol. 19, pp 377-393.

Ng, J.Y.T. and Isaacson, M. (1993) "Second order wave interaction with two dimensional floating bodies by a time domain method" Appl. Ocean Res. Vol. 15, pp 95-105.

Ogilvie, T.F. (1963) "First- and second-order forces on a cylinder submerged under a free surface", J. Fluid Mech. Vol. 16, pp 451-472.

Park, J.C., Kim M.H. and Miyata, H. (1999) "Fully non linear free surface simulations by a 3D Viscous Numerical Wave Tank", Int. J. Numer. Methods in Fluids, Vol. 29, pp 685-703.

Peraire, J., Vahdati, M., Morgan, K. and Zienkiewicz, O.C. (1987) "Adaptive remeshing for compressible flow computations" J. Comp. Phys. Vol. 72, No. 2, pp 449-466.

Phillips , N.A. (1957) "A coordinate system having some special advantages for numerical forecasting", J. Meteorology, Vol. 14, pp 184-185.

Rassineux, A. (1998) "Generation of tetrahedral meshes by advancing front technique", Int. J. Numer. Methods Eng. Vol. 41, No. 4, pp 651-674.

Rebay, S. (1993) "Efficient unstructured mesh generation by means of Delaunay triangulation and Bowyer-Watson algorithm", J. Comp. Phys. Vol. 106, No. 1, pp 125-138.

Rivera, M.C. and Inostroza, P. (1997) "Using longest-side bisection techniques for the automatic refinement of Delaunay triangulations", Int. J. Numer. Methods Eng. Vol. 40, No. 4, pp 581-597.

Sibson, R. (1978) "Locally equiangular triangulations", Comput. J. Vol. 21, pp 243.

Stansberg, C.T., Huse, E., Krokstad, J.R. and Lehn, E. (1995) "Experimental study of non-linear loads on vertical cylinders in steep random waves", Proc. Fifth Intl Offshore and Polar Engng Conf. Vol. 1, pp 75-82.

Stansby, P.K. and Lloyd, P.M. (1995) "A semi-implicit Lagrangian scheme for 3D shallow water flow with a two-layer turbulence model", Int. J. Numer. Methods in Fluids, Vol. 20, pp 115-133.

Teigen, P. and Haver, S. (1998) "The Heidrun TLP : meaun TLP : ı
Appl. Ocean Res. Vol. 20, pp 27-36.

Thompson, J.F., Thames, F.C. and Mastin, C.W. (1974) **C.W.** (19
of body fitted curvilinear coordinate system for a field contar a field c
dimensional bodies", J. Comp. Phys. Vol. 15, pp 299-319., pp 299-3

Thompson, J.F., Warsi, Z.U.A. and Mastin, C.W. (19**in, C.W.**
systems for numerical solution of partial differential equaferential e
Vol. 47, no.1.

Thompson, J.F., Warsi, Z.U.A. and Mastin, C.W. (19**in, C.W.**
foundations and applications", North Holland. l.

Tsai, C.P. and Jeng, D.S. (1994) "Numerical Fourier solal Fourier
water depth." Applied Ocean Research, Vol. 16, pp 185-1!16, pp 18

Tsai, W.T. and Yue, D.K.P. (1996) "Computation of Non Iation of N
Rev. Fluid Mech. Vol. 28, pp 249.

Ursell, F. (1950) "Surface waves on deep water in the prester in the
Proc. Camb. Phil. Soc. Vol. 46, pp 141-152.

Vada, T. (1987) "A numerical solution of the second-ordhe second
submerged cylinder of arbitrary shape", J. Fluid Mech. Vduid Mech

Van Dommelen, L. and Rundensteiner, E.A. (1989) "E.A. (1989
forces in the two dimensional Poisson equation", J. Compion", J. C

Vinje, T. and Brevig, P. (1981) "Non linear ship motions ship moti
Hydro., Paris (Chairmen: J.C. Dern and H.J. Haussling),J. Haussli
Carenes, France.

Voronoi, G. (1908) "Recherches sur les parallelloedres rallelloedı
Vol. 134, pp 198.

Vugts, J.H., Dob, S.L. and Harland, L.A. (1998) "The ex1998) "Th
supported structures using an equivalent quasi-static desiasi-static
Res. Vol. 20, pp 37-53.

Wang, P., Yao, Y. and Tulin, M.P. (1995) "An efficient i'An effici
waves, based on the multi-subdomain approach with BEach with
Vol. 20, pp 1315-1336.

Wang, T. and Li, J.C. (1997) "Effect of nonlinear wavonlinear v
and hydrodynamic forces", Sci. China A - Math. Phys. Math. Phy

Watson, D.F. (1981) "Computing the N-Dimensional Delaunay tessellation with application to Voronoi polytropes", Computer Journal, Vol. 24, No. 2, pp 167-172.

Weatherill, N.P. (1992) "Delaunay triangulation in computational fluid dynamics", Computers and Mathematics with Applications, Vol. 24, No. 5-6, pp 129-150.

Weatherill, N.P. and Hassan, O. (1994) "Efficient 3-Dimensional Delaunay triangulation with automatic point creation and imposed boundary constaints" Int. J. Numer. Methods Eng. Vol. 37, No. 12, pp 2005-2039.

Wheeler, J.D. (1970) "Method for calculating forces produced by irregular waves" J. Petroleum Engineering, Vol. 10, pp 359-367.

Wille, S.O. (1992) "A structured tri-tree search method for generation of optimal unstructured finite element grids in 2 and 3 dimensions" Int. J. Numer. in Fluids, Vol. 14, No. 7, pp 861-881.

Wilson, J.K. and Topping, B.H.V. (1998) "Parallel adaptive tetrahedral mesh generation by the advancing front technique", Computers and Structures, Vol. 68, No. 1-3, pp 57-78.

Wolfram, J. and Naghipour, M. (1999) "On the estimation of Morison force coefficients and their predictive accuracy for very rough circular cylinders", Appl. Ocean Res. Vol. 21, pp 311-328.

Wu, G.X. and Eatock Taylor R. (1990) "The second order diffraction force on a horizontal cylinder in finite water depth", Appl. Ocean Res. Vol. 12, No. 3. pp 106-111.

Wu, G.X. and Eatock Taylor R. (1994) "Finite Element analysis of two-dimensional non-linear transient water waves", Appl. Ocean Res. Vol. 16, pp 363-372.

Wu, G.X. and Eatock Taylor R. (1995) "Time stepping solutions of the two dimensional non-linear wave radiation problem", Ocean Eng. Vol. 22. No. 8, pp 785-798.

Wu, G.X., Ma, Q.W. and Eatock Taylor R. (1998) "Numerical simulation of sloshing waves in a 3D tank based on a finite element method", Applied Ocean Research, Vol. 20, pp 337-355.

Xu, X., Pain, C.C., Goddard, A.J.H. and de Oliveira, C.R.E. (1998) "An automatic adaptive meshing technique for Delaunay triangulations", Computer Methods in Applied Mechanics and Engineering, Vol. 161, No. 3-4, pp 297-303.

Yang, C. and Ertekin, R.C. (1992) "Numerical simulation of non linear wave diffraction by a vertical cylinder", Transactions, ASME, Vol. 114, pp 36-44.

Yerry, M.A. and Shephard, M.S. (1983) "A modified quadtree approach to finite element mesh generation", IEEE Computer Graphics Appl. Vol. 3, no. 1, pp 39-46.

Yerry, M.A. and Shephard, M.S. (1984) "Automatic 3D mesh generation by the modified octree technique", Int. J. Numer. Methods Eng. Vol. 20, no. 11, pp 1965-1990.

Yiu, K.F.C., Greaves, D.M., Cruz, S., Saalehi, A. and Borthwick A.G.L. (1996) "Quadtree generation: Information handling, boundary fitting and CFD applications", Computers and Fluids, Vol. 25, No. 8, pp 759-769.

Young, D.P., Melvin, R.G., Bieterman, M.B., Johnson, F.T. and Samant, S.S. (1991) "A locally refined rectangular grid finite element method: Application to computational fluid dynamics and computational physics", J. Comp. Phys. Vol. 92, no. 1, pp 1-66.

Zienkiewicz, O.C. and Phillips, D.V. (1971) "An automatic mesh generation scheme for plane and curved surfaces by isoparametric coordinates", Int. J. Numer. Methods Eng. Vol. 3, pp 519-528.

Zienkiewicz, O.C. and Taylor R.L. (1994) "The Finite Element Method", Vol. 1 and Vol. 2, McGraw-Hill Book Company.